UNIVERSITY OF Southampton

University of Southampton Research Repository
ePrints Soton

Copyright © and Moral Rights for this thesis are retained by the author and/or other copyright owners. A copy can be downloaded for personal non-commercial research or study, without prior permission or charge. This thesis cannot be reproduced or quoted extensively from without first obtaining permission in writing from the copyright holder/s. The content must not be changed in any way or sold commercially in any format or medium without the formal permission of the copyright holders.

When referring to this work, full bibliographic details including the author, title, awarding institution and date of the thesis must be given e.g.

AUTHOR (year of submission) "Full thesis title", University of Southampton, name of the University School or Department, PhD Thesis, pagination

http://eprints.soton.ac.uk

**UNIVERSITY OF SOUTHAMPTON**

FACULTY OF ENGINEERING, SCIENCE AND MATHEMATICS

School of Ocean and Earth Sciences

# The North Atlantic Heat Budget: An Argo Based Study

Thesis for the degree of Doctor of Philosophy

by

Rachel Elaine Hadfield

October 2007

# Abstract

The Argo dataset is used to obtain estimates of the heat storage and heat divergence with the aim of the assessing the usefulness of the Argo array for investigating the North Atlantic heat budget. The accuracy of the Argo-based mixed layer heat storage varies significantly throughout the North Atlantic. Errors are smallest, around 10-20 $Wm^{-2}$ on monthly timescales for 10° x 10° boxes, reducing to 5-10 $Wm^{-2}$ on seasonal scales in the subtropics and eastern basin. Heat storage errors over a fixed 300 m layer are higher, but typically remain below 20 $Wm^{-2}$ on seasonal timescales away from the western boundary.

The heat budget is closed (using net heat fluxes from the NCEP climatology and NOC reanalysis) within the estimated error throughout the subtropical and eastern North Atlantic, indicating the value of the Argo dataset in studies of this nature. However, within the western boundary the heat budget residual typically exceeds 50 $Wm^{-2}$, with the heat storage overestimated or the heating from the net heat flux and/or advective and diffusive divergence underestimated. Assuming that heat storage error estimates are accurate and considering results in the literature regarding the bias in net heat flux products, it is likely that heating from divergence is underestimated. The heating contribution from this term may be large on scales that cannot be resolved using Argo. In the eastern and subtropical North Atlantic, the errors in the Argo-based heat budget terms are smaller than the uncertainty in the net heat flux products and can thus be used to provide insight into which atmospheric dataset (the NCEP reanalysis or the NOC climatology) may be more accurate. The NOC net heat flux is more accurate than that from NCEP throughout the year in the subtropics and during the first half of the year in the eastern mid-latitudes.

The errors in the mixed layer heat storage are smaller than the interannual variability in this term. Thus Argo can be used to investigate variability on this scale. While the current Argo dataset is on the short side for studies of this nature, continued funding of the array is expected to provide more insightful results.

# Author's Declaration

I Rachel Hadfield, declare that the thesis entitled 'The North Atlantic Heat Budget: An Argo Based Study' and the work presented in it are my own. I confirm that

- this work was done wholly or mainly while in candidature for a research degree at the University;

- where I have consulted the published work of others, this is always clearly attributed;

- where I have quoted work from others, the source is always given. With the exception of such quotations, this thesis is entirely my own work;

- I have acknowledged all my main sources of help;

- parts of this work have been published as Hadfield, et al. (2007).

Signed: ……..

Date: ……

# Acknowledgements

I am very grateful to my supervisors, Dr Neil Wells and Dr Simon Josey, for their help, advice, optimism and encouragement throughout the course of my PhD and to my panel chair, Professor Harry Bryden for his support.

I would like to thank Dr Joel Hirschi for his guidance and the many hours he has dedicated to running weekly discussion groups. This opportunity to informally discuss work with other postgraduate researchers has been incredibly helpful.

I would also like to thank the members of the Rapid climate change project, in particular Dr Meric Srokosz. The project has funded my PhD and provided several opportunities to present work at annual meetings. These meetings have been interesting and great fun.

I am grateful to Dr Elaine McDonagh for making the 36°N data available for use in this study and to Dr Beverly DeCuevas and Dr Andrew Coward for providing OCCAM output. Also many thanks to Dr Steven Alderson for providing access to his Argo-based sea surface height fields and to Dr Josh Willis for sharing his knowledge on the derivation of the velocity field from Argo displacements.

This work was supported by the NERC Rapid climate change project, grant no. NER/S/S/2003/11906. The Argo data were collected and made freely available by the International Argo Project and the national programmes that contribute to it (http://www.argo.ucsd.edu, http://argo.jcommops.org). Argo is a pilot programme of the Global Ocean Observing System.

# Contents

# LIST OF TABLES

# LIST OF FIGURES

# ACCOMPANYING MATERIAL

A CD containing matlab optimal interpolation programmes, written for use in this study, accompanies this thesis.

# APPENDICES

# Acronyms and Abbreviations

ACCE Atlantic Circulation and Climate Experiment
ALACE Autonomous Lagrangian Circulation Explorer
C Central subduction buoy
CGFZ Charlie Gibbs Fracture Zone
COADS Comprehensive Ocean Atmosphere Dataset
COARE Coupled Ocean-Atmosphere Response Experiment
CTD Conductivity Temperature Depth
DACs Data Assemble Centres
DMQC Delayed Mode Quality Control
DSOW Denmark Strait Overflow Water
DWBC Deep Western Boundary Current
EAP East Atlantic Pattern
ECMWF European Centres for Medium-range Weather Forecast
GCM General Circulation Model
GDACs Global Data Assembly Centres
GFDL Geophysical Fluid Dynamics Laboratory
GIN Greenland-Iceland-Norwegian
ISOW Iceland-Scotland Overflow Water
lNADW lower North Atlantic Deep Water
LSW Labrador Sea Water
MAR Mid-Atlantic Ridge
MBT Mechanical Bathythermograph
MLD Mixed Layer Depth
MOC Meridional Overturning Circulation
MODE Mid-Ocean Dynamics Experiment
MOM Modular Ocean Model
MW Mediterranean Water
NAC North Atlantic Current
NADW North Atlantic Deep Water
NAO North Atlantic Oscillation
NCEP National Centres for Environmental Prediction
NCEP/NCAR National Centres for Environmental Prediction/ National Centre for Atmospheric Research
NE Northeastern subduction buoy
NOC National Oceanography Centre
NW Northwestern subduction buoy
NWP Numerical Weather Prediction
OCCAM Ocean Circulation and Climate Advanced Model
OGCM Ocean General Circulation Model
OHC Ocean Heat Content
OHT Ocean Heat Transport
OI Optimal Interpolation
RMS Root Mean Square

RTM Radiative Transfer Models
RTQC Real Time Quality Control
SeaWiFS Sea-viewing Wide Field-of-view Sensor
SNR Signal to Noise Ratio
SPMW Subpolar Mode Water
SSH Sea Surface Height
SST Sea Surface Temperature
STMW Subtropical Mode Water
XBT Expendable Bathythermograph
UOR Undulating Ocean Recorder
VOS Voluntary Observing Ships
WGASF Working Group on Air-Sea Fluxes
WMO World Meteorological Organisation
WOA World Ocean Atlas
WOCE World Ocean Circulation Experiment

**Table A1** Variables used throughout the thesis

| **Variable** | **Definition** | **Value and/or Units** |
|---|---|---|
| $g$ | Gravity | 9.8 $m^2s^{-1}$ |
| $f$ | Coriolis force: $2\Omega sin\phi$ | $s^{-1}$ |
| $\Omega$ | Earths Rotation | Rad $s^{-1}$ |
| $\phi$ | Latitude | Radians |
| $T_a$ | Mixed layer temperature | °C |
| $T_{-h}$ | Entrainment temperature | °C |
| $h$ | Mixed layer depth | m |
| $u$, $v$, | Eastward and Northward velocity components | $ms^{-1}$ |
| $\upsilon$ | The horizontal velocity field | $ms^{-1}$ |
| $w$ | Vertical velocity field | $ms^{-1x,m}$ |
| $q$ | Vertical heat flux | $Wm^{-2}$ |
| $t$ | Time | Seconds |
| $\rho$ | Density of seawater | 1027 kg $m^{-3}$ |
| $C_p$ | Specific heat capacity of sea water | 3986 J $kg^{-1}$ $°C^{-1}$ |
| $HS_{full}$ | Heat storage from the model temperature field | $Wm^{-2}$ |
| $HS_{sub}$ | Heat storage from the subsampled model temperature field | $Wm^{-2}$ |
| $A_v$ | Coefficient of turbulent viscosity | $m^2s^{-1}$ |
| $\beta$ | Latitudinal variation | $m^{-1}s^{-1}$ |
| $Z_e$ | Ekman boundary layer thickness | m |
| ^ | Mean | |
| $k_{x,y}$ | Eddy diffusion coefficient | $m^2s^{-1}$ |
| $k_z$ | Vertical diffusion coefficient | $m^2s^{-1}$ |

# CHAPTER 1. Introduction

## 1.1 Motivation

During the 20th century the global climate has shown a considerable warming with a reported increase in the global average sea surface and land surface air temperature of 0.61±0.16 °C (Jones et al., 2001; Folland et al., 2002). The amount of heat stored in the ocean has also steadily increased (Barnett et al, 2005). Levitus et al. (2005) examined the warming signal in global heat content over different depths. Their results, plotted in Fig1.1 indicate that a large part of the observed change in heat content can be accounted for by warming in the upper 700 m. In addition, the global average sea level has risen due to thermal expansion and melting of ice reservoirs at an estimated rate of 1.8±0.1 mm $yr^{-1}$ from global tide gauge data (Douglas, 1997) or 2.1±1.2 mm $yr^{-1}$ from altimeter data (Nerem, 1999). These observed changes have important environmental and social-economic impacts that cannot be ignored. The recent Stern report on the economics of climate change (October, 2006) and the 4th Assessment of the Intergovernmental Panel on Climate Change provide further evidence for the reality of climate change.

To improve our ability to predict future changes, it is necessary to monitor the global climate system and the mechanisms responsible for transporting heat around the globe. The relative importance of the ocean and atmosphere for redistributing heat from low to high latitudes has been the subject of much research (Vonder Haar and Oort, 1973; Oort and Vonder Haar, 1976; Carrisimo et al., 1985; Bryden, 1993; Trenberth and Solomon, 1994; Trenberth and Caron, 2001). Estimates of the ocean and atmosphere heat transports made by Trenberth and Caron (2001) suggest that poleward Ocean Heat Transport (OHT) is dominant only between 0-17°N. However, as shown in Fig. 1.2, atmospheric energy transport and latent heat transport associated with the meridional water transport indicates that the oceans and atmosphere may contribute about equally in maintaining the global heat balance (Bryden and Imawaki, 2001).

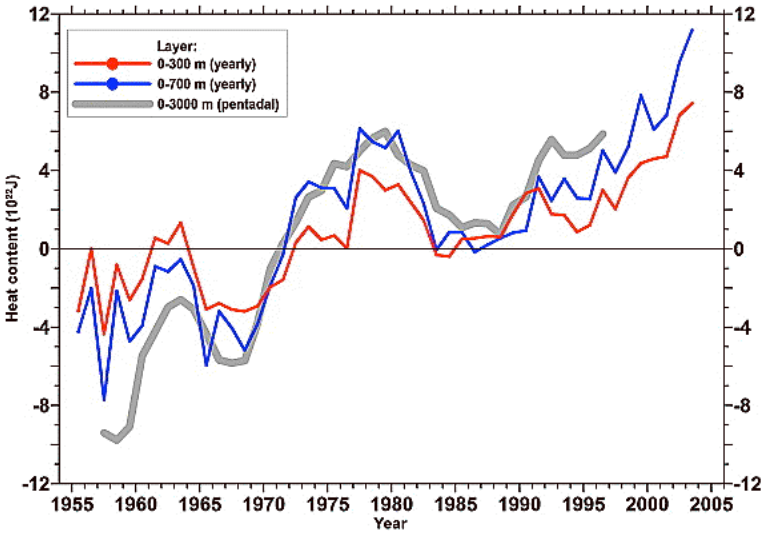


**Figure 1.1** Time series of yearly ocean heat content ($10^{22}$ J) for the upper 300 and 700m and pentadal (5-year running composites) ocean heat content ($10^{22}$ J) for the upper 3000 m of the global ocean (Levitus et al., 2005).

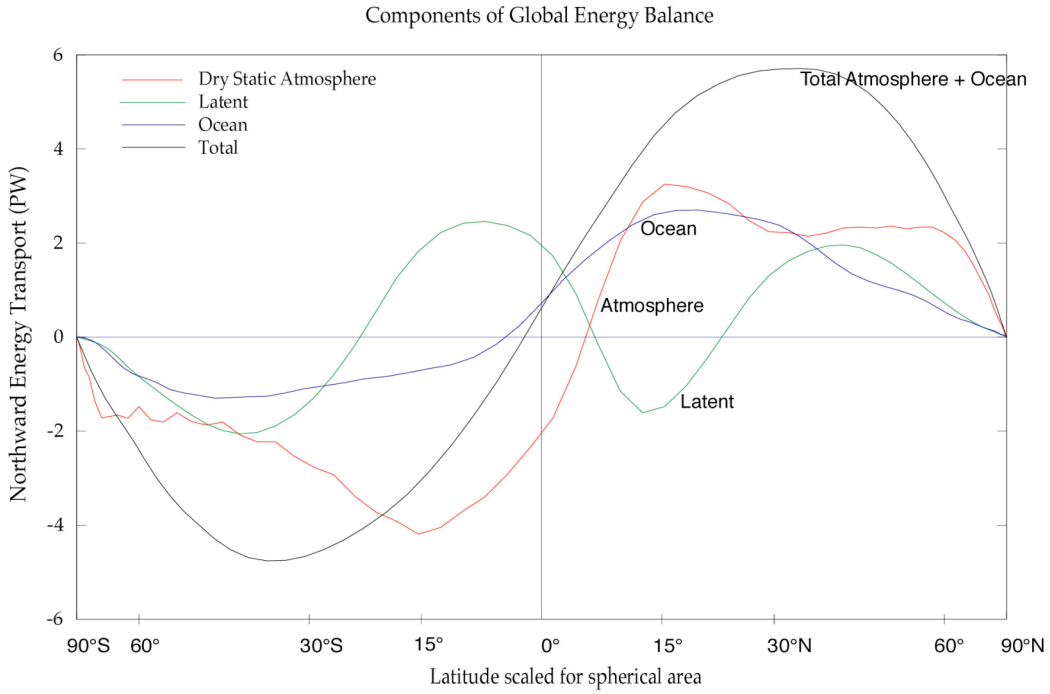


**Figure 1.2** Components of global energy balance showing the dry static atmosphere heat transport (red), the latent heat transport (green), the ocean heat transport (blue) and the total heat transport (black). Figure created by Bryden and Imawaki (2001) using data from Keith (1995).

Investigation of variations in the Ocean Heat Content (OHC), the exchange of heat across the air-sea interface and the OHT can improve understanding of the role of the ocean in the global climate system. Although in principle if two of these terms are known the third can be derived, in practice closure may not be achieved due to observational errors and inaccuracies arising from necessary assumptions made to obtain these terms. Quantification of all three terms is therefore useful for improved understanding of the ocean's role in climate.

### 1.2 Aims and objectives

The main aim of this thesis is to investigate the accuracy with which the Argo dataset can be used to quantify the seasonal heat storage and heat divergence components of the heat budget. It is anticipated that the Argo dataset may be usefully employed to examine the range, seasonal cycle and the variability in these components.

This study is focussed on the North Atlantic Ocean. There are several reasons for this focus. First the relatively high coverage of historical datasets in this region has enabled previous observational analyses of the climatological heat budget. These analyses can be used to help verify results obtained in this study. Second, the North Atlantic plays an important role in maintaining present day global climate through its overturning circulation driven by deep convection and sinking at high latitudes. Thus this ocean basin, with its varied dynamics, provides an ideal opportunity to identify the regions where the Argo dataset can and cannot be used for investigations of the nature outlined above. Third, the North Atlantic OHC is sensitive to changes in global climate (Banks and Wood, 2001) indicating that some interannual variability can be expected in this region. The regions of the North Atlantic where this interannual variability can be captured and studied using the Argo dataset is investigated.

Thus the objective of this study is to identify the regions of the North Atlantic where the Argo dataset can be usefully used to further our understanding of the mechanisms responsible for the transfer of heat from the equator to the poles. The upper ocean is of particular interest due to its close coupling with the atmosphere above. Although there are published studies that have investigated the North Atlantic heat budget of the upper ocean (refer to section 1.6 for a review), it is anticipated that use of the Argo dataset in such an

analysis may be useful for identifying interannual variations in the heat budget components (previous observational analysis on this scale present climatological values only). In addition, this study differs from previous analyses since an attempt is made to quantify each heat budget component individually (rather than inferring any term from knowledge of the others) and careful consideration is given to the errors associated with each heat budget component.

In order to accomplish the aims of this thesis it is essential to have an understanding of the study region. To this end, in this introductory chapter a description of the North Atlantic is first given. In the following, the North Atlantic circulation is discussed in section 1.3 and a review of the literature on North Atlantic variability is given in section 1.4. In addition, it is useful to introduce the fundamental equations required for calculating the heat budget terms (section 1.5). Existing heat budget studies are described in section 1.6. A review of studies that use the Argo dataset is given in section 1.7 and the structure of this manuscript is briefly outlined in section 1.8.

### 1.3 The North Atlantic Ocean: Circulation and structure

The large-scale circulation of the North Atlantic Ocean comprises two main components; the horizontal circulation and the vertical Meridional Overturning Circulation (MOC). Although these components of the flow are interlinked, they are described separately here.

A schematic of the horizontal circulation in the North Atlantic Ocean is shown in Fig. 1.3. The horizontal circulation is characterized by the presence of two gyres; the anticyclonic subtropical gyre centered on 24°N and the cyclonic subpolar gyre centered around 50°N. The subtropical gyre is bordered to the west by the North American continent until about 36°N, where the Gulf Stream turns east. At the Grand Banks the Gulf Stream splits into 3 sub-branches; one branch recirculating water clockwise, closing the gyre; one continuing east forming the Azores Current and the remainder forming the North Atlantic Current (NAC). The NAC continues as a well-defined boundary current along the eastern slope of the Grand Banks. At about 51°N it divides feeding into the Irminger and Nordic Seas. The current velocities in these branches of the NAC are much lower than in the NAC

itself with mean speeds of ~2 $cms^{-1}$ and 15-20 $cms^{-1}$, respectively (Tourre et al., 1998). The Labrador, Greenland and Mediterranean basins all exhibit mean cyclonic circulation.

The complex topography of the North Atlantic influences the circulation. Exchange between the eastern and western basins of the North Atlantic occurs preferentially over deep gaps in the Mid-Atlantic Ridge (MAR), for example over the Charlie Gibbs Fracture Zone (CGFZ) at ~52°N, the Faraday Fracture Zone at ~50°N and, to a lesser extent, the Maxwell Fracture Zone (~48°N). Tourre et al. (1998) suggest that this topographic steering, evident even in near surface flows, may limit the oceans response to climate variations locking cross ridge transports of heat and freshwater to a certain latitude band. This is supported by Cunningham and Alderson (2006), who found changes of opposing sense in the thermocline waters on either side of the MAR.

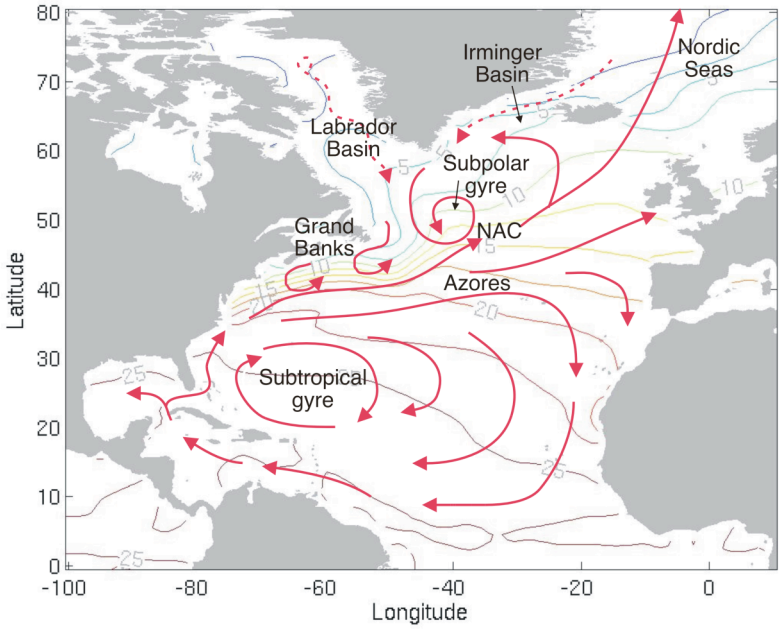


**Figure 1.3** Schematic of the North Atlantic circulation. Red arrows indicate the large-scale surface flow regime, broken arrows indicate deep flow. Contours, with 2.5°C intervals, show the 10 m climatological temperature for June from the World Ocean Atlas.

The vertical MOC is driven by the formation of deep-water masses in the Greenland – Iceland - Norwegian (GIN) Seas and the Labrador Sea of the North Atlantic. A study by

Pickart et al. (2003) suggested that the Irminger Basin is also a site of deep-water formation, although direct observations have yet to be made. In these deep-water formation regions dense surface waters lose buoyancy through cooling during winter, triggering sinking.

Deep-water masses formed in the GIN Seas enter the North Atlantic over sills in the ridge between Greenland and Great Britain (Iceland-Scotland Overflow Water (ISOW)) and the Denmark Strait (Denmark Strait Overflow Water (DSOW)). DSOW and ISOW comprise the bulk of lower North Atlantic Deep Water. DSOW has a cold and relatively fresh signal flowing at depths of more than 3500 m, while ISOW is warmer and saltier and is centred at 2500-3500 m. Water formed in the Labrador Sea (Labrador Sea Water (LSW)) comprises the upper NADW flowing at depths of 1600-2500 m. The estimated 15±2 Sv (1 Sv = $10^6$ $m^3$ $s^{-1}$) of NADW (Schmitz and McCartney, 1993) is transported south in the Deep Western Boundary Current (DWBC).

Other water masses found in the North Atlantic include Mediterranean Water (MW) and Mode Waters. These are typically formed during winter-time by convection. MW is formed in the Mediterranean basin with waters preconditioned for convection through meteorological forcing (Marshall and Schott, 1999). MW, characterized by high salinity and temperature, is found in the North Atlantic at depths of around 1000 m. Mode waters exhibit uniform properties. The main mode waters in the North Atlantic are the Subtropical Mode Waters (STMW) and the Subpolar Mode Waters (SPMW). STMW, commonly referred to as "Eighteen Degree Water" is characterized by temperatures close to 18°C and can be traced throughout the western subtropical gyre at depths of up to 300 m (Marshall et al., 1993). Subpolar Mode Water (SPMW) is found along the branches of the NAC at depths of up to 500 m and is characterized by low potential vorticity (Perez-Brunius et al., 2004).

The MOC is responsible for carrying most of the heat transported from the equator to the poles in the North Atlantic Ocean (Roemmich and Wunsch, 1985). Estimates of poleward ocean heat transport in the North Atlantic are shown in Fig. 1.4. Values of 1.2 PW (1 PW = $10^{15}$ W), 1.3±0.3 PW, 1.2±0.1 PW, 0.6 ± 0.09 PW and 0.3 PW have been estimated at latitudes of 14°N (Klein et al., (1995), 24°N (Lavin et al., 1998), 36°N (McDonagh, personal comm.), 47°N (Ganachaud and Wunsch, 2003) and 55°N (Bacon,

1997), respectively. All estimates given here are derived using hydrographic section data and all contain some element of error.

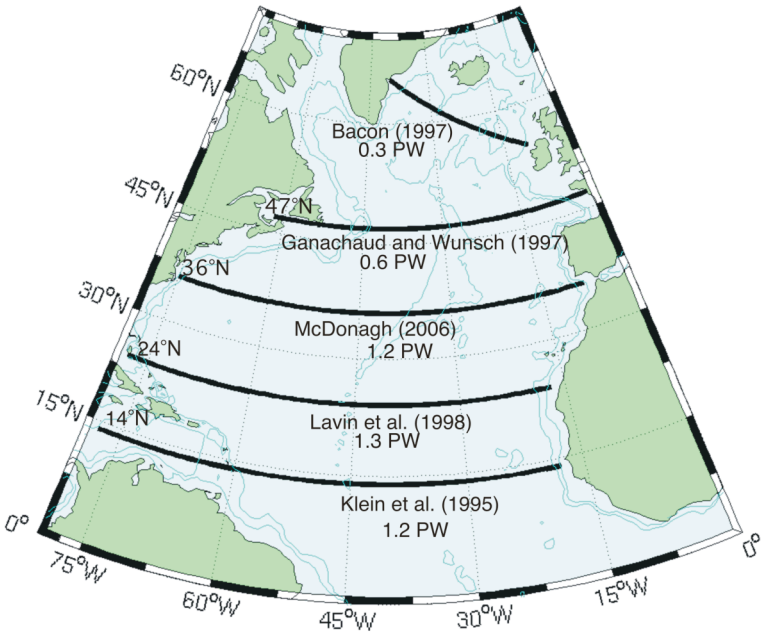


**Figure 1.4** Estimates of poleward heat transport at different latitudes in the North Atlantic Ocean.

### 1.4 Temporal Variability in the North Atlantic

Over the past century, improved ocean monitoring has enabled temporal trends in both the circulation and properties of the North Atlantic to be identified. In this section the literature on these changes is reviewed. Variability in the circulation is discussed in section 1.4.1. A review of observed temperature changes follows in section 1.4.2. Before examining the trends in the North Atlantic, it is instructive to first introduce the leading modes of North Atlantic climate variability, the North Atlantic Oscillation (NAO) and the East Atlantic Pattern (EAP).

The anomalous sea level pressure for positive states of the NAO and EAP have been calculated using atmospheric fields from the National Oceanography Centre (NOC) climatology and are shown in Fig.1.5. The NAO is characterised predominantly by cyclical fluctuations of air pressure between the high-pressure system near the Azores and the low-pressure system near Iceland. States of positive NAO exhibit a stronger than normal subtropical high pressure and a deeper than normal Icelandic low. This increased pressure

difference results in enhanced storm activity and a more northerly storm track. The sea-level pressure pattern associated with the EAP is dominated by anomalously low pressure centred approximately midway between the two centres of the NAO dipole. The EAP is most prominent in winter and non-existent in summer. Both the NAO and EAP have exhibited an upward trend, with the NAO switching to positive values in the 1970s and the EAP switching to positive values slightly later.

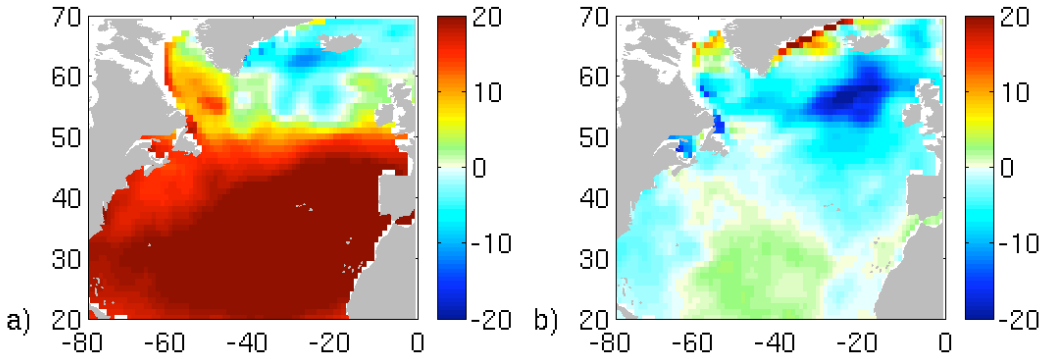


**Figure 1.5** Sea Level Pressure anomaly (December to March averages) for a) Positive NAO state and b) positive EAP state, based on the NOC climatology pressure field. Anomalies relative to weak NAO and EAP states. Units in mbar.

### 1.4.1 Variability in the North Atlantic Circulation

Changes in water mass formation and the horizontal gyre circulation have been recorded in the observational record. Curry and McCartney (2001) presented observational evidence for interannual to interdecadal variability in the intensity of the North Atlantic gyre circulation. They found a correlation between observed changes and the state of the NAO, with weakened Gulf Stream and NAC circulation corresponding to periods of low NAO. In addition, a positive correlation between LSW formation and the NAO has been documented. This relationship can be explained by the stronger winds associated with periods of high NAO index and the more north-easterly orientation of the winter storm track. Intense low-pressure centres thus pass over the southern Labrador Sea drawing cold, dry air from the Labrador Continent over the relatively warm surface waters of the sea, driving extreme heat loss and deeper convection. There is a lag of perhaps 2-4 years

between the atmospheric NAO and LSW thickness, indicative of the ocean's slower response time (Clarke and Gascard, 1983). Freshwater pulses from the Arctic and the conditions of past winters also influence deep convection and water mass properties (Pickart et al., 2002). In the eastern basin Mediterranean Water plays an influential role in determining water mass properties (Lozier et al., 1995).

Due to the difficulty in obtaining direct measurements of the MOC strength, little is known about its variability. Past changes in MOC strength have been investigated using a limited set of observations, while climate models have been used to predict future changes under different global warming and greenhouse gas scenarios. It should be noted that in addition to anthropogenic changes in the MOC, natural multidecadal oscillations in overturning strength have also been modelled (Knight et al. 2005).

From observations along a repeat transatlantic section at 24°N the Atlantic MOC appears to have slowed by about 30 % between 1957 and 2004 (Bryden et al., 2005). This result is based on snap-shots of data and may therefore reflect natural variability in the MOC and not a long-term trend. In order to distinguish which of these two possibilities is responsible for changes in the MOC, continuous monitoring of the flow is required. This has only been possible since the inception of the Rapid climate change MOC monitoring array deployed in 2004 (Rapid, 2006). The array consists of 22 moorings across 26°N. Preliminary results from the monitoring array indicate that the natural variability exhibits fluctuations of 5-6 Sv on timescales of less than one year (Kanzow et al., 2007). It is therefore possible that the slow down of the MOC observed by Bryden et al. (2005) is a feature of natural variability.

Most General Circulation Model (GCM) projections into the 21$^{st}$ Century show a reduction in the strength of the overturning with increasing concentrations of greenhouse gasses (IPCC, 2001). There is a broad range in the magnitude of this reduction in strength. The MOC in the Geophysical Fluid Dynamics Laboratory (GFDL) GCM showed a complete collapse (Rahmstorf, 1995) while there was no significant change in the MOC in the Max-Plank Institute (MPI) coupled model (Latif et al., 2000). Some models exhibit a partial collapse. For example the Hadley Centre HadCM3 model shows no convection in the Labrador Sea but persistent deep-water formation in the GIN seas (Wood et al., 1999) and the GFDL coupled climate model showed a 40% reduction in the MOC strength

(Dixon and Lanzante, 1999). This multitude of results highlights our inability to accurately predict how the ocean circulation will be affected by global warming.

### 1.4.2 Variability in Water Mass Properties

Barnett (2005) and Levitus et al. (2005) documented a long-term global mean increase in upper-ocean heat content. Superimposed on this mean trend are shorter periods and smaller regions of warming and cooling. Some of the changes in the North Atlantic are discussed here.

In the subtropics (south of 32°N) a general warming trend was observed to persist throughout much of the 20$^{th}$ Century (Roemmich and Wunsch, 1984; Parilla et al., 1994; Bryden et al., 1996; Joyce and Robbins, 1996; Arbic and Owens, 2001; Vargas-Yáñez et al., 2004). This warming was centred at a depth of 600-3000m. Hydrographic data collected from research cruises and the long-term hydrographic station at Bermuda indicate that the warming trend extends back to at least 1922 (Joyce and Robbins, 1996).

The rate of warming between 1957 and 1981 at 24°N was 0.08°C per decade (Roemmich and Wunsch, 1984), this slowed to 0.02°C per decade between 1981 and 1992 (Parilla et al., 1994). Hydrographic sections along 52°W and 66°W occupied in 1997 indicated that in the western basin the warming trend has ended with a subsequent cooling observed (Joyce et al., 1999). However, sampling of the eastern part of the 24.5°N section in 2002 revealed that the warming in the eastern Atlantic continued at a higher rate of 0.4°C per decade (Vargas-Yáñez et al., 2004). Below 3000 m, a general cooling trend has been observed at an order of magnitude less than the observed upper ocean warming (Parilla et al., 1994; Arbic and Owens, 2001).

In the subpolar North Atlantic, cooling at a rate of ~0.3°C per decade between the 1950s to the late 1980s was documented (Arbic and Owens, 2001). This cooling trend was found to be more pronounced in the west than the east (Read and Gould, 1992). Lazier et al. (2002) and Yashayaev and Clarke (2005) observe a subsequent warming within the Labrador Sea, beginning in the mid-1990s.

Joyce et al. (1999) and Koltermann et al. (1999) attribute the observed temperature trends in the subpolar and subtropical regions to changes in LSW properties. A strong negative correlation between the thickness of Labrador Sea Water in its source region and

temperature anomalies at Bermuda with a time lag of 6 years were found (Joyce and Robbins, 1996). This change in properties is thought to be caused by a combination of changing renewal rates and changing properties of water from which LSW is formed (Read and Gould, 1992). This hypothesis is consistent with the observed increase in salinity on isotherms at a nearly constant rate of 0.010 psu per decade between 1957-1992 in the subtropical gyre (Bryden et al., 1996). In addition to these long-term trends in temperature, significant variability on shorter timescales has also been identified.

### 1.5 The Heat Budget

In this study the form of the heat budget is given in terms of the heat balance equation (Stevenson and Niiler, 1983; Foltz and McPhaden, 2005) with only a brief derivation provided here; refer to Appendix 1 for further details. The equations governing the conservation of heat and mass in the upper ocean are

$$\rho C_p \left( \frac{\partial T}{\partial t} + \upsilon \cdot \nabla T + w \frac{\partial T}{\partial z} \right) = \frac{\partial q}{\partial z} \tag{1.1a}$$

$$\nabla \cdot \upsilon + \frac{\partial w}{\partial z} = 0 \tag{1.1b}$$

where $T$ is temperature, $\upsilon$ horizontal velocity with eastward and northward components $u$ and $v$, $w$ vertical velocity, $q$ vertical heat flux, $\rho C_p$ the specific heat capacity per unit volume, $\nabla \equiv (\partial/\partial x, \partial/\partial y)$ is the horizontal gradient, $x$, $y$ and $z$ are the eastward, northward and vertical coordinates respectively and $t$ is time.

Vertically integrating from depth $h$ to the sea surface (1.1b) becomes

$$w_{-h} + v_{-h} \cdot \nabla h = \nabla \cdot h v_a \tag{1.2}$$

the subscripts $-h$ and $a$ indicate the variables at depth $h$ and the variables averaged between depth $-h$ and the sea surface, respectively. The vertical velocity at the sea surface is assumed to be equal to zero (rigid lid approximation) and changes in mass due to

precipitation and evaporation have been neglected. Using (1.1b) and (1.2) and including diffusive heat fluxes, the heat conservation equation (1.1a) vertically integrated from depth $h$ to the sea surface can be written

$$h\frac{\partial T_a}{\partial t} + hv_a \cdot \nabla T_a + \nabla \cdot \int_{-h}^{0} \hat{v}\hat{T}dz + (T_a - T_{-h})\left(\frac{\partial h}{\partial t} + v_{-h} \cdot \nabla h + w_{-h}\right) + hk_{x,y} \cdot \nabla^2 T_a + k_{z,-h}\frac{\partial T}{\partial z} = \frac{Q + Q_{-h}}{\rho C_p} \tag{1.3}$$

where $\hat{v}$ is the deviation from the vertically averaged velocity field $\left(v = v_a + \hat{v}\right)$, $\hat{T}$ is the deviation from the vertically averaged temperature $\left(T = T_a + \hat{T}\right)$, $k_{xy}$ the horizonal and diffusion coefficient, $k_{z,-h}$ the vertical diffusion across the depth surface $-h$, $Q$ the surface heat flux and $Q_{-h}$ the penetrative heat flux at depth $h$. The terms from left to right represent the local heat storage, the horizontal advective heat flux, the velocity shear covariance, the entrainment and the horizontal and vertical diffusion on the left hand side of the equation. The entrainment term comprises three components, arising from (left to right) 1) temporal changes in $h$, 2) horizontal gradients in $h$ and 3) vertical advection. The term on the right hand side is the absorbed net air-sea heat flux. The methods used to quantify each of these heat budget terms are outlined in chapter 5.

### 1.6 Previous Analyses of the North Atlantic Heat Budget

There are many published studies, which have attempted to quantify the North Atlantic heat budget components. The aim here is to provide some details on the datasets used in earlier studies to quantify the heat budget and to briefly summarise their findings. Thus, the limitations of these studies will be revealed, and the need for additional investigation of the role of the oceans in global climate and energy budgets is highlighted. It should be noted here that the change in heat content is referred to, simply as the heat storage.

Gabites (1950) carried out one of the earliest studies of the broad-scale mean seasonal heat storage. Due to the lack of subsurface temperature observations at that time, he utilised a sea surface temperature dataset combined with a simplified model of the seasonal

thermocline. Over the subsequent decades the number and quality of subsurface temperature soundings steadily increased. Bryan and Schroeder (1960) examined the seasonal heat storage between 20-65°N in the North Atlantic using 20,000 bathythermograph observations. Some 15 years later Oort and Vonder Haar (1976) (henceforth OV76) examined the seasonal heat storage of the upper 275 m in the Northern Hemisphere oceans using around 400,000 historical hydrographic station soundings and 700,000 bathythermograph casts. Lamb and Bunker (1982) (henceforth LB82) utilised data collected between 70°N and 20°S in the Atlantic, over a period of a decade. This provided 233,957 soundings, enabling quantification of the seasonal heat storage over the upper 300 and 500 m. Air-sea flux climatologies were used alongside the heat storage estimates to infer heat transport divergence as a residual. Hsiung at al. (1989) (henceforth H89) used the Levitus climatology (1982) alongside a naval dataset giving a total of 3.8 million observations. As in LB82, H89 infer heat transport divergence as a residual of the heat storage estimates and the net heat flux.

The heat storage results for the upper 275 m of the Northern Hemisphere from OV76 for the upper 300 m from LB82 and H89 exhibit similar seasonal cycles in heat budget components. Values from Lamb and Bunker (1982) are plotted in Fig. 1.6. Each study indicates maximum warming during May to August, maximum cooling in November and December and transitional periods, which generally are close to zero, for March, April, September and October. The largest annual range in heat storage is found at around 40-50°N, where maximum summer values are 150-200 $Wm^{-2}$. Wintertime heat loss is of the same magnitude. Slightly smaller hemispheric heat storage values were found in OV76, than the Atlantic values of LB82 and H89. The inferred heat transport from LB82 and H89 is northwards throughout most of the year in the extratropical North Atlantic (north of 20°N). There is a seasonal cycle, with maximum values in spring (H89). Southwards heat transport is observed in November and December (LB82).

The studies discussed above are affected by a spatial sampling bias due to concentration of observations along shipping routes and coastal regions. Bryan and Schroeder (1960) observed that some locations in the North Atlantic only had data collected during one or two years and that this could lead to a temporal bias due to decadal changes in OHC. In addition, the accuracy of the XBT dataset is dependent on application

of corrections to fall rates (Willis et al., 2004). None of the above studies include extensive estimates of the associated errors. However, both OV76 and LB82 suggest a mean standard error in the range 10 – 20 $Wm^{-2}$. Another limitation of these studies is that only the heat storage and the net heat flux are quantified; the advective and diffusive heat divergence is then inferred from the imbalance of these terms. None of these earlier studies consider interannual variability in heat storage.

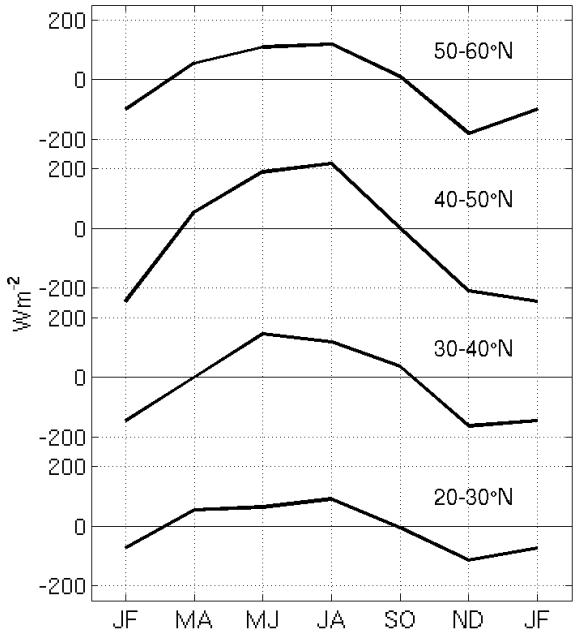


**Figure 1.6** Subsurface heat storage over the upper 300 m in the North Atlantic. Figure created using data from Lamb and Bunker (1982), $Wm^{-2}$.

Satellite data have been used alongside subsurface observations to try and overcome the spatial and temporal bias inherent in subsurface observational data alone (White and Tai, 1995; Chambers et al., 1997, Willis et al., 2003). Such studies use the correlation between steric height (which can be extracted from altimetric height observations) and subsurface temperature observations to obtain estimates of the subsurface temperature with improved spatial coverage. However, this regression method is of limited accuracy in regions where steric height signals are weak. Guinehut et al. (2004) found that using the regression method on sea surface temperature and altimeter data could explain less than

40% of the signal variance at a depth of 200 m in the North Atlantic subtropical and subpolar gyres.

Sarmiento (1986), Böning and Herrmann (1994), Jones and Leach (1999), Wang and Carton (2002), Stammer et al. (2003) and Dong and Kelly (2004) (henceforth DK04) used Ocean General Circulation Models (OGCMs) to investigate the components of the North Atlantic heat budget. These studies indicate a primary balance between the net surface heat flux and local storage in the mid-latitude oceans. In addition, DK04 noted that the contribution of advection and diffusion to the mixed layer temperature tendency can be significant spatially and temporally. Results from Böning and Herrman (1994) and DK04 are consistent with the observational studies of LB82 and H89, exhibiting a seasonal cycle in poleward heat transport, with maximum values in spring and summer. Results from Wang and Carton (2002) are in contention with minimum heat transport in January – June. However, these latter results are based on an analysis of the full ocean depth.

DK04 also investigated the interannual variability in heat storage, with a focus on the Gulf Stream region of the North Atlantic. Their results indicated that interannual variations in the mixed layer temperature are dominated anomalous advection. Results from these studies are dependent on the observational data assimilated into the model and application of accurate ocean physics in the applied models.

To date, only a few studies have utilised the Argo subsurface temperature dataset (chapter 2) to examine the heat storage of the North Atlantic. Lavender (2001) and Centurioni and Gould (2004) used float data to quantify heat storage in the Labrador and Irminger Seas, respectively. Willis et al. (2004) used float data alongside XBT and altimeter data to quantify OHC on a global scale. Although Willis et al. (2004) examined variability in OHC between 1993-2003, they did not give a break down into different ocean basins and none of the studies considered the annual cycle in OHC. More details on Argo-based studies follow in the review in section 1.7.

### 1.7 Review of Previous Argo-Based Studies

More than 170 papers and reports based on data collected by autonomous floats have been written in the past seven years, many appearing in peer-reviewed journals. These studies cover a broad range of purposes, including investigation of sea surface height fields, salinity structure, mixed layer depth, subsurface circulation and oxygen concentration. Only

studies that use float data to quantify changing ocean temperatures and heat content are discussed here. For a full list of published studies based on autonomous drifter data refer to the Argo website (2006).

For the past 3 years, the Argo project, discussed in detail in chapter 2, has provided the largest single source of subsurface temperature data in the global oceans. As such it is valuable for quantifying the oceans role in the climate system, through investigation of changing ocean temperatures. There are several existing studies in the literature that use Argo data, both independently and alongside additional datasets, to this end.

Willis et al. (2004) published the earliest study of this nature. In their study, data from profiling floats was combined with other historically available subsurface temperature data and satellite altimetric height fields using the method of Willis et al. (2003). A global warming in the upper 750 m during 1993 – 2003 was observed at an average rate of 0.86 ± 0.12 $Wm^{-2}$. Levitus et al. (2005) used Argo data alongside additional historical temperature data collected using Expendable BathyThermographs (XBTs), shipboard Conductivity Temperature Depth (CTDs) and moored buoys to calculate the heat content over a deeper depth (0 – 3000 m) and over a longer time period, spanning 1955 – 2003. They observed an average warming rate of 0.2 $Wm^{-2}$ over this period. Gille (2002) used data from floats deployed during the World Ocean Circulation Experiment (WOCE) to examine heat content changes in the Southern Ocean. These early floats did not record temperature profiles during ascent but do provide temperature data from the drift depth, which ranged from 700 to 1100 m. The float temperature records, which provide data throughout the 1990s, were compared to earlier hydrographic temperature measurements from the region. Gille reported an increase in Southern Ocean mid-depth temperatures by around 0.17 °C between the 1950s and the 1980s.

While the studies discussed above incorporate data from autonomous drifters, they are not exclusively based upon it. On the contrary a large proportion of the time periods considered in these studies predate the Argo project. In addition, the depth over which heat content is quantified in Levitus (2005) extends below the depth of Argo float profiles. There are several studies in the literature that rely solely on Argo data to quantify changes in subsurface temperature and heat content. Such studies typically focus on select regions of the World Ocean. The earliest studies of this nature investigated the subpolar oceans

(Lavender, 2001; Centurioni and Gould, 2004; Wirts and Johnson, 2005). WOCE float deployments were typically concentrated in such regions to exploit the unique resource of wintertime hydrographic observations provided by autonomous drifters.

Lavender (2001) examined the general circulation and temperature and salinity variability in the Labrador Sea using more than 200 floats deployed between 1994 and 1998. The hydrographic data was used to investigate deep convection and the one dimensional heat budget during the winter of 1996-97 and 1997-98. Changing subsurface temperatures were investigated in the Irminger basin using 7725 profiles taken between November 1994 and June 2003 (Centurioni and Gould, 2004). A general warming trend was evident with temperatures of 2.85 ± 0.1 °C in 1997 rising to 3.07 ± 0.08°C in 2003. Wirts and Johnson (2005) observed a warming trend in the southeast Bering Sea using data collected between May 2001 and October 2004. The warming was reported to be of the order 1°C between May 2001 and September 2003. A slight cooling was also observed during the winter of 2003/2004, although this was entirely reversed by warming near the end of the record.

More recent studies on subsurface temperature changes inferred exclusively from Argo data have focussed on the North Atlantic (Ivchenko et al., 2006) and the sea south east of Japan (Yoshida and Hoshimoto, 2006). Ivchenko et al. (2006) estimated the heat content anomaly over different layers in the upper 1500 m using profile data obtained from autonomous floats between January 1999 and December 2005. Over 400 profiles per month were used in this analysis. An average warming over the upper 1500 m during the study period at a rate of 0.88 $Wm^{-2}$ was observed. Despite this general warming, periods and regions of cooling were identified. In particular, cooling occurred at low latitudes after 2003 and throughout the North Atlantic in the 1000 – 1500 m layer. Ivchenko's dataset includes some Argo floats with pressure sensor problems (Appendix 2), thus some of the observed trends may be spurious. The heat content change in a warm core ring in the sea east of Japan was investigated using 90 profiles obtained from one Argo float (Yoshida and Hoshimoto, 2006). Surface heat flux values were found to be consistent with changes in the heat content in the surface isothermal layer.

In addition to studies based on quantifying temporal changes in subsurface temperature, the Argo dataset has been used to investigate the potential temperature –

salinity (θ-S) relationship (King and McDonagh, 2005; Johnson, 2006), the upper ocean temperature structure (Molinari, 2004) and seasonal and interannual variations in heat transport (Straneo, 2006).

King and McDonagh (2005) used data from 30 floats in the vicinity of 32°S in the Indian Ocean to examine changes in the θ-S relationship of the Subantarctic mode water. Relative to shipboard CTD data sampled in 1987 the salinity was observed to increase on temperature levels, consistent with findings from shipboard CTD data sampled in 2002. Changes in θ-S have also been investigated over shorter time periods using Argo data. For example, an isopycnal potential temperature-salinity anomaly in the South Pacific was investigated using 2 profiling floats in austral winter 2004 (Johnson, 2006). The anomaly had a signal of more than 0.35 psu in salinity and 0.9 °C in temperature. Molinari (2004) examined the temperature structure of the upper 750 m in the north western subtropical North Atlantic using data collected between 1950-2003. Most of the data consists of bathythermograph readings, but some float profiling data is included during the period 1998-2001. It was found that the interannual variability in the position of the 18° isotherm observed with XBT data could be reproduced using float data (Molinari, 2004). Straneo (2006) examined the variations in heat and freshwater transport through the central Labrador Sea using profiling float data from 1996 to 2000 and data collected by the Ocean Weather Station Bravo between 1964 and 1974. The float dataset consisted of more than 800 float profiles. Heat divergence was found to have increased between the two periods considered.

### 1.8 Structure

Here a short description of the structure of this manuscript is given. In this thesis the Argo dataset, which is used to investigate the North Atlantic heat budget is introduced in chapter 2. Suitable interpolation methods and lengths are explored in chapter 3. In chapter 4, an analysis of the accuracy of the Argo-based temperature and heat storage fields is carried out. In chapter 5, the variables used to obtain estimates of the different heat budget components are quantified providing essential grounding for the heat budget analysis. The seasonal cycle in individual heat budget components is presented in chapter 6 and the closure obtained is discussed. Interannual variability is investigated in chapter 7. The aim

here is to provide insight into the mechanisms responsible for recent observed changes in the North Atlantic temperature field and to yield further understanding of the limitations and capabilities of current atmospheric and oceanic observing systems.

# CHAPTER 2. Datasets

## 2.1 Introduction

In the research described here a variety of datasets and model outputs are exploited to investigate the North Atlantic heat budget. In particular subsurface temperature and drift datasets from the Argo program and atmospheric variables from the National Centers for Environmental Prediction/National Center for Atmospheric Research (hereafter referred to as NCEP) reanalysis and the National Oceanography Centre (NOC) climatology are used to quantify the heat budget components. An Ocean General Circulation Model (OGCM), the Ocean Circulation and Climate Advanced Model (OCCAM) is used to examine the validity of assumptions made and to estimate errors in the heat budget terms (Chapter 4). The 2001 World Ocean Atlas (WOA) monthly climatological temperature field provides a first-guess during interpolation of the Argo temperature data (Chapter 3). In addition, the WOA salinity field is used in calculations of potential temperature and geostrophic velocity.

In this chapter these different datasets are discussed starting with the Argo dataset in section 2.2. The atmospheric datasets are described in section 2.3. Section 2.4 gives details on the OCCAM model and in section 2.5 derivation of the WOA temperature and salinity fields is briefly outlined.

## 2.2 Argo

The International Argo program, which began in 1998, aims to deploy a global array of 3000 profiling floats to monitor the state of ocean temperature and salinity. The technological development of the Argo floats is outlined in the first sub-section. Quality control procedures are described in section 2.2.2 and in section 2.2.3, the Argo sampling density is discussed.

### 2.2.1 Float development

The earliest neutrally buoyant floats invented in 1955 were developed to investigate subsurface circulation (Swallow, 1955; Swallow, 1957). Tracking involved the use of a dual hydrophone array to determine the floats azimuth relative to the ship. Despite success

with the Aries experiment, in which Henry Stommel's model for deep circulation was verified (Swallow, 1971), the 6 km tracking range limited the utility of these early floats. However, during the late 1960's long-range tracking using the SOFAR channel and moored sound receivers (Rossby and Webb, 1970) rectified this issue and enabled systematic exploration of mesoscale features over a substantial part of the ocean basin, paving the way for the 1973 Mid-Ocean Dynamics Experiment (MODE) (MODE Group, 1978). In the subsequent generation of floats, the transmitter and receiver positions were reversed so that the floats listened to moored sound sources (Rossby et al., 1983). Data was then transmitted through the Argos Satellite System at the end of the mission.

The first autonomous (i.e. not requiring an acoustic tracking network) float was the Autonomous Lagrangian Circulation Explorer (ALACE). ALACE floats were developed in the late 1980s and tested in the Drake Passage in the early 1990's (Davis et al., 1992). The ALACE float cycles from the surface to pre-programmed depths with buoyancy changes accomplished by moving hydraulic fluid between an internal reservoir and external bladder. These floats relay their position to the Argos Satellite System upon surfacing, thus discarding the need for communications with underwater transmitters or receivers. During WOCE in the 1990s, ALACE floats were fitted with temperature, and later, salinity sensors in order for profiles to be taken during ascent and these were called Profiling ALACE, or PALACE floats.

Based on the experience in WOCE, in 1998 a plan was presented to develop a global array of profiling floats on a 3° grid throughout the ice-free areas of the deep ocean. It was anticipated that these floats would provide measurements of subsurface currents, temperature and salinity. The float plan, called Argo, is a multinational collaboration with 27 countries involved. The first Argo floats were deployed in late 1999 and over the past 7 years there has been a steady increase in the number of active floats. Since mid 2003 Argo has been the largest single source of ocean profiling data, collecting more profiles than the previous largest source, XBTs. As well as being more numerous, the Argo data go deeper than the 750 m XBTs, measure temperature more accurately and also provide conductivity, enabling determination of salinity and density, and ocean current data. The status of the array in December 2005 is shown in Fig. 2.1. At this time there were 2090 active floats in

the World Ocean. Note that by March 2007, this figure had reached more than 2800. The floats have a design life of around 4 years requiring that 800 floats are deployed per year to maintain the 3° x 3° array of 3000 floats. The floats deployed by the Argo program typically drift at a depth of 1000 m and profile to 2000 m every ten days.

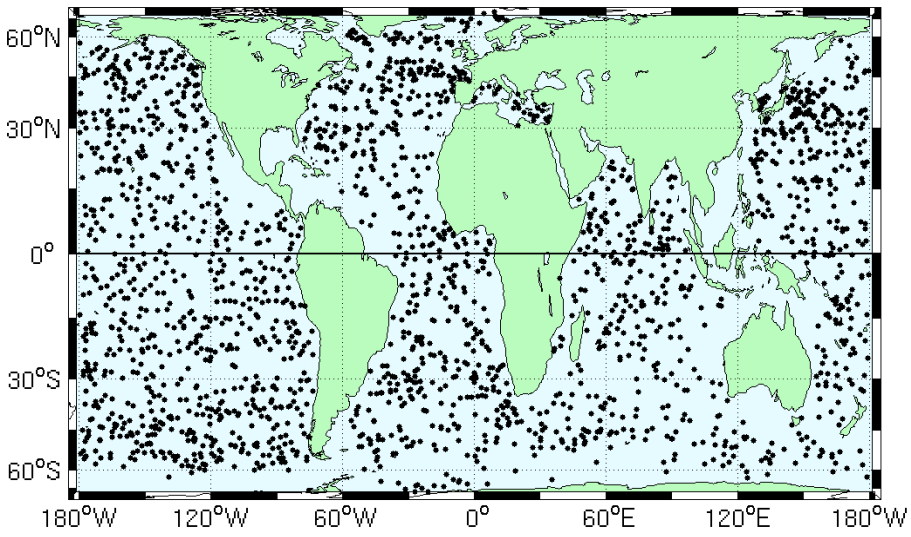


**Figure 2.1** The Global Argo float distribution, December 2005 showing 2090 active floats.

The accuracy of float temperature readings is ± 0.005 °C in the early float models (Davis et al., 2001), improving to ±0.002 °C for the later models (Oka, 2005). Similarly, the accuracy of the pressure readings varies among models and is subject to a hysteresis error of ±2 to ± 5 dbar. Salinity data are generally accurate to ± 0.01 psu. Typically the drift in the pressure and temperature is assumed to be negligible, while the conductivity sensor is vulnerable to biofouling, causing long-term salinity drifts (Davis, 1998).

Oka (2005) recovered three profiling floats after 2 – 2.5 years of operation and recalibrated their sensors to determine the temperature, pressure and salinity offsets. The temperature drift for the recovered floats varied between +0.001 to +0.002 °C which is within the precision of the calibration. However, both the pressure and salinity exhibited significant drifts of +5.92 ± 0.93 dbar and -0.0125 psu respectively. The surface pressure recorded by the float revealed a jump of a few dbar after the first dive and a gradual drift

thereafter. Oka (2005) applied the surface pressure as a correction to the pressure throughout the water column and found this reduced the offset to an accuracy of 2-3 dbar, close to the precision of the calibration. The offset in salinity was primarily caused by drift in the conductivity sensor, with an observed drift nearly proportional to the operating period of the floats.

There are several studies that aim to correct salinity errors in the float data (Freeland, 1997; Bacon et al., 2001; Durand and Reverdin, 2005; Böhme and Send, 2005). However, at the time of writing, such corrections had not been routinely applied to Argo salinity data. Due to the complexity in applying non-uniform adjustments to correct for salinity drift, the Argo salinity profiles are not considered in this study. Since the main focus of this work is the heat budget, the aims of the study are not compromised.

Data is recovered from the floats via the Argos satellite system and transmitted to regional Data Assembly Centres (DACs). The floats typically spend 7-8 hours transmitting on the surface at an average rate of one message every 50 seconds. Float data is transmitted from the DACs to Argo's 2 Global Data Assembly Centres (GDACs) in Brest, France (Coriolis) and Monterey, California where they are made freely available online. The GDACs synchronise their data holdings to ensure consistent data is available on both sites.

In this study, Argo profile data are accessed via ftp on the Coriolis website (Coriolis, 2006). A total of 49,599 float profiles were collected in the North Atlantic Ocean (0-70°N, 0-100°W) during the period 01/01/99 - 31/12/05. The monthly time series of the number of temperature profiles obtained by Argo is shown in Fig. 2.2. Although the first Argo floats were not deployed until late 1999, around 400 profiles were collected per month throughout 1999. These profiles are from floats deployed during WOCE and the Atlantic Circulation and Climate Experiment (ACCE) (Bower et al., 2002). The lowest sampling occurs in mid-2000, when the ACCE and WOCE floats near the end of their lifetime and the number of Argo deployments is low. This minimum is followed by a steady increase in profile numbers as Argo deployments begin in earnest, with less than 200 profiles collected in May 2000 to more than 800 profiles collected per month by the end of 2005. There is a jump in the number of profiles from 509 in November 2000 to 800 in December 2000, dropping

again to around 500 in January 2001. This is due to a large number of duplicate profiles placed on the server during December 2000.

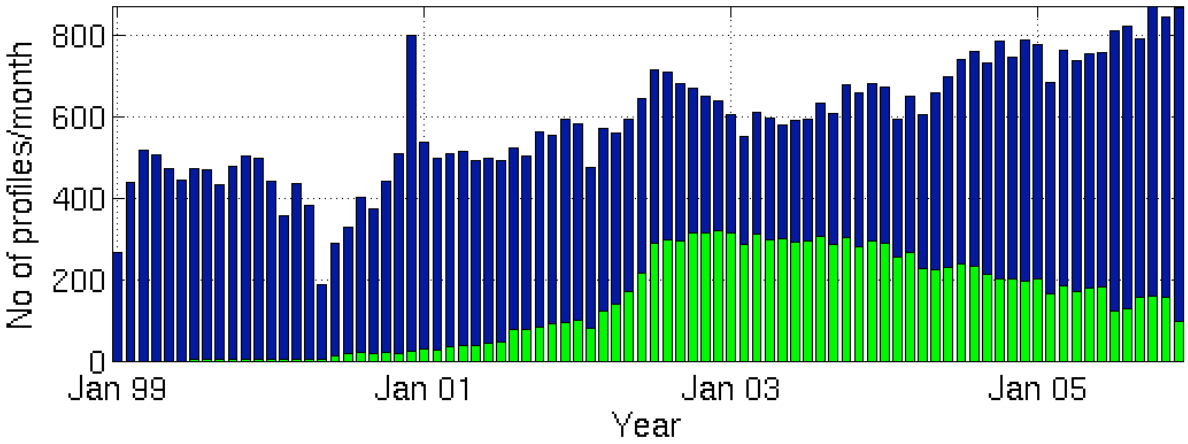


**Figure 2.2** Time series of the number of profiles collected each month by Argo in the North Atlantic. The colours indicate the total number of profiles (blue) and profiles which have undergone Argo delayed mode quality control (green).

### 2.2.2 Quality control

To assure the standard of the profile data, quality control is required. The data centre performs real time and delayed mode quality control procedures and provides flags for each profile. Additional quality control procedures are performed in this study. After application of both the Argo and additional quality control procedures 43,127 profiles remain in the North Atlantic dataset. This is 87 % of the original number. Table 2.1 shows the numbers of profiles failing the different checks applied. Note that the total number of these profiles (6,547) is greater than the number of omitted profiles (6,472), indicating that some profiles failed more than one quality check. Details on the applied quality control checks follow below.

**Table 2.1** Quality control statistics for the Argo dataset

| **Total number of profiles in dataset prior to quality control = 49,599** | | |
|---|---|---|
| **Quality Check** | **No. failed** | **Action taken** |
| a) and b) Argo quality control (RTQC and DMQC) | 3424 | All removed |
| c) Argo grey list | 127 | All removed |
| d) No readings in top 100m | 619 | All removed |
| d) <10 readings in profile | 396 | All removed |
| d) Gaps in upper 100m | 4240 | 1321 removed, 2932 extrapolated, after extrapolation 24 profiles out of range and removed |
| e) Range check on T and P | 403 | Visual Inspection: 235 removed, 93 T jumps removed, 75 identified as ok |
| f) Visual check | 77 | 37 removed, 40 T jumps removed |
| g) Duplicate | 364 | All removed |
| **Total number of profiles in dataset after quality control = 43,127** | | |

a) Real-Time Quality Control (RTQC)

The GDAC aims to apply RTQC within 24 hours of the float returning to the surface. In order to meet this deliverable, RTQC procedures are automatic and limited to simple checks. For example, the location cannot be on land, the date must be sensible (i.e. year greater than 1997, month in range 1 to 12, etc) and the temperature readings must be within global limits. All profiles have undergone RTQC.

b) Delayed Mode Quality Control (DMQC)

The DMQC involves manual subjective assessment of plots of temperature versus pressure and of salinity versus temperature. This assessment is done in relation to nearby floats and historical data. For more information on Argo quality control procedures refer to the Argo Quality Control Manual (Wong et al., 2002).

The monthly time series of the number of profiles undergoing delayed mode quality control is shown in Fig. 2.2. As of March 2006, these quality control procedures had been applied to only 24% of the North Atlantic data. This number does not satisfy the Argo target of applying DMQC within 4-5 months of sampling. However, the DMQC procedures were not finalised until April 2005, by which time over 43,000 profiles had been collected in the North Atlantic alone. Once this backlog of data has been cleared it is hoped that the Argo target for DMQC can be met.

During real time and delayed mode quality control, all collected Argo profiles are flagged to indicate their reliability, for full details refer to the Argo data management users handbook (Carval et al., 2006). Any profiles flagged as 'bad' or 'probably bad' are not used in this study. Around 7 %, 3424 profiles, are thus omitted from the North Atlantic dataset. At the time of accessing the Argo data (March, 2006) it was general practice to flag a profile as bad if a data point at any depth throughout the profile was identified as bad. It is therefore likely that some omitted profiles may have been correctable. In April 2006 the Argo quality control procedure was updated so that the profile flag reflects the number of bad data points in each profile.

c) The Argo grey list

In addition to applying RTQC and DMQC, the GDACs maintain a 'grey' list of all floats with reported sensor problems. One hundred and twenty seven profiles from 14 floats (out of 780 floats) on the grey list are removed from the dataset used in this study.

d) Additional quality control: Missing readings

Profiles with readings at less than 10 vertical levels throughout the water column and without data in the upper 100 m are not used in this study. Consequently 1015 (partial) profiles are omitted.

During quality control all pressure readings are converted to depth using the UNESCO routine (UNESCO, 1983) and temperature values are interpolated onto standard depth surfaces. The original vertical resolution varies between profiles. Some have a resolution of 5 m in the top 200 m, 10 m at 200-500 m and 20 m at 500-2000 m while others have a lower vertical resolution of 10 m, 20 m and 50 m over the same depth increments. In view of this original vertical resolution, the spacing of interpolated depth

surfaces is set to vary from 5 m at 10-200 m, to 10 m at 200-500 m, 20 m at 500-1000 m and 50 m at 1000-1500 m. There are a total of 104 depth surfaces.

Profiles with their first reading below 10 m and above 100 m are inspected to determine if extrapolation can be used to estimate the temperature at 10 m. If the gradient in the temperature field is less than a critical value this is considered possible. This value is chosen to vary with the depth of the shallowest profile observation and is calculated as 0.2 $(B-1)^{-1}$ ° C $m^{-1}$, where B is the depth bin of the shallowest reading; B=1 at 10 m. The extrapolation of profiles allows 69 % of the 4240 profiles without readings at 10 m, but with readings in the upper 100 m, to be included in this study.

e) Additional quality control: Range check

The temperature readings are subjected to a range check with flags applied to profiles containing temperature readings outside of a given range at any depth. The considered range varies spatially and is calculated using the monthly WOA climatological temperature fields (Stephens et al., 2001). It is defined as five times the standard deviation in a 10-degree box centred on the profile location, or 10 °C, whichever is more. Profiles with negative pressure readings or with pressure greater than 2100 dbar are also flagged. All flagged profiles undergo visual inspection, and where possible adjustments are made to the temperature field. Correctable profiles typically show temperature 'jumps', where the temperature appears bad at only one or two depths throughout the water column. An example of temperature spikes in a profile collected at 48.5°N, 22.5°W during February 2003 is shown in Fig. 2.3. The erroneous readings are removed from the profile and gaps are filled by linear interpolation. It is believed that temperature jumps are caused by transmission errors and not problems with the sensors. Erroneous profiles that cannot be adjusted are removed from the dataset. In this way 235 profiles are omitted.

f) Additional quality control: Visual inspection

Visual inspection of all remaining temperature profiles helps identify and correct or remove erroneous data points not identified by the automated checks. This visual quality control involves plotting temperature profiles for different months and 5° x 5° subregions and subjectively identifying outliers. A total of 37 profiles are thus omitted and temperature spikes are removed from 40 profiles.

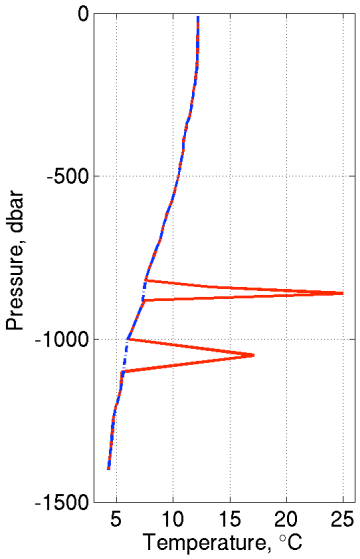


**Figure 2.3** Example of temperature spikes in a profile sampled at 48.5°N, 22.5°W on the 3rd of February 2003. Both the original profile (solid red) and the updated profile (dashed blue) are shown.

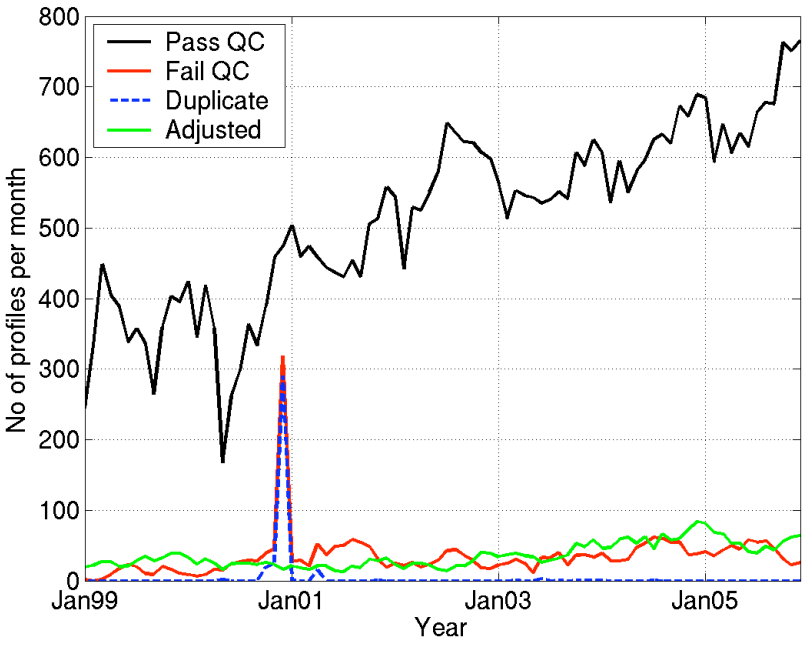


**Figure 2.4** Monthly time series of Argo profiles collected in the North Atlantic. Time series of the total number of profiles passing all quality control checks (black), failing the quality control (red), duplicated (broken blue) and adjusted (green) are plotted.

g) Additional quality control: duplicated profiles

Duplicate profiles are identified and removed from the dataset. Only one month, December 2000, is affected. Almost 80 % of temperature profiles are duplicated during this month. A time series of the number of profiles passing, failing and updated by the additional quality control procedures is plotted in Fig. 2.4. The total number of profiles remaining after quality control varies from a minimum of 167 in May 2000 to a maximum of 765 in December 2005.

2.2.3 Data distribution

The average sampling density provided by Argo during each year between 1999-2005 is mapped in Fig. 2.5 (10 m) and Fig. 2.6 (1000 m). Values are normalised by the Argo target sampling density, thus values greater than or equal to 1 indicate that the Argo target resolution has been achieved.

During 1999-2001 the Argo coverage at 10 m is mostly constrained to a few select regions covering areas of about 1000 $km^2$ (Fig. 2.5). By 2002 the coverage is more widespread, nearing its target resolution across large areas of the North Atlantic. The region 30-50°N, 20-40°W and the area off the east coast of North America at 20-40°N are particularly well sampled. During all years the sampling in the region off the west coast of Africa and south of 20°N is poor. In these areas the sampling density is less than 50% of the Argo target.

Comparison of the Argo coverage at 1000 m and 10 m indicates a temporal trend in the number of profiles extending to 1000 m. During the early Argo years, 1999-2001, the sampling at 1000 m is notably lower than that at 10 m, with only 53% of profiles extending to 1000 m. Floats deployed during WOCE were programmed to sample only the upper 1000 m (Davis and Zenk, 2001). Post 2002, the sampling density at 1000 m is similar to that at 10 m with 85 % of profiles extending to 1000 m. It should be noted that the area of the North Atlantic deeper than 1000 m is only 86 % of the area covered by the surface of the North Atlantic.

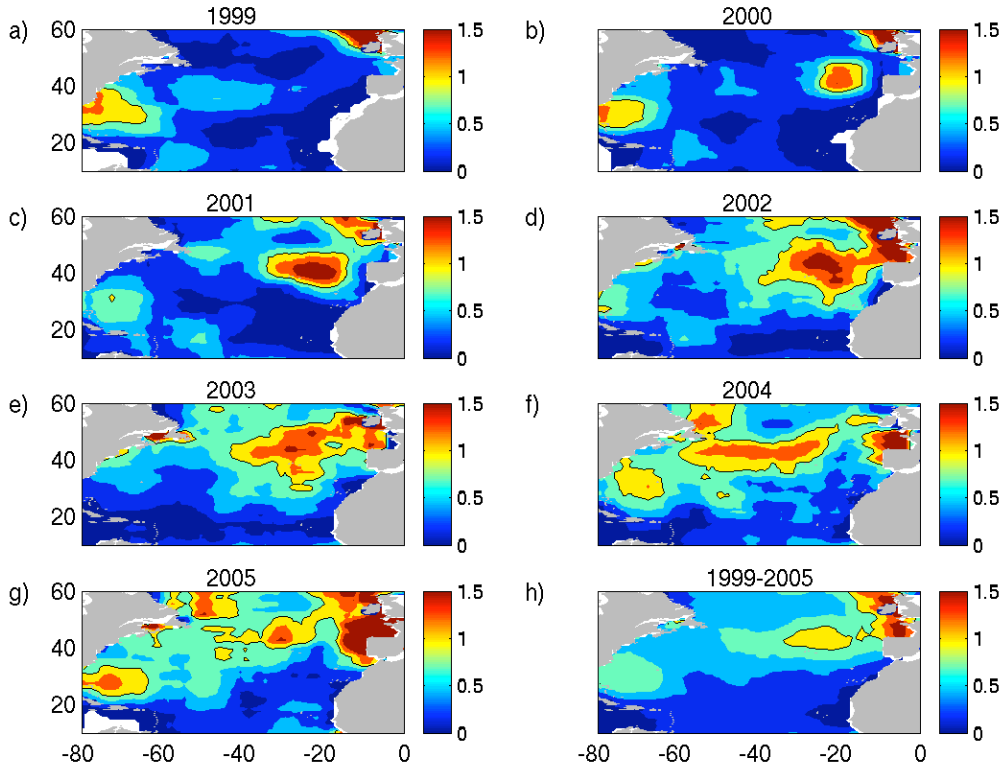


**Figure 2.5** Argo sampling density at 10 m for a) 1999, b) 2000, c) 2001, d) 2002, e) 2003, f) 2004, g) 2005 and h) 1999-2005. Values are scaled so that one (contoured) is Argo target resolution, i.e. one float in 3°x3° area, which sampling every 10 days provides 36 profiles per year. Contour intervals are 0.25 °C.

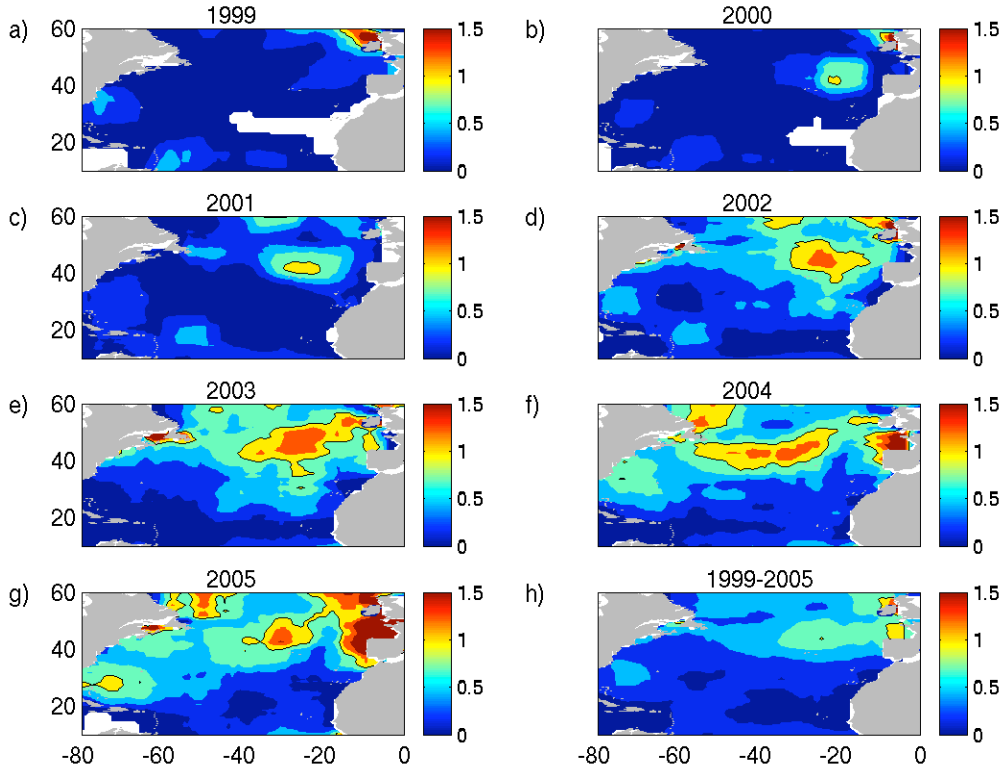


**Figure 2.6** Caption as for Fig. 2.5 but at a depth of 1000 m

## 2.3 Atmospheric fields from climatology

### 2.3.1 Derivation of fields

The net heat flux across the air-sea interface is the sum of four components; net short-wave (solar) radiation, net long-wave radiation and latent and sensible heat fluxes. Direct measurements of heat fluxes, using heat flux sensors, are difficult and expensive and hence only provide limited datasets at a few locations. Generation of global heat flux fields is therefore reliant on alternative methods. One of the most widely applied methods, referred to as the 'Bulk Formula method' in the literature, uses semi-empirical formulae to determine air-sea exchanges from measurements of several oceanographic and atmospheric variables. These measurements, which include near surface air temperature, wind speed, relative humidity, cloud cover, sea level pressure and Sea Surface Temperature (SST), are

obtained from Voluntary Observing Ships (VOS), buoys, satellite remote sensing and from outputs of Numerical Weather Prediction (NWP) models.

The shortwave ($Q_s$) and the longwave ($Q_L$) flux parameterisations are relatively crude (WGASF, 2000). Quantification of $Q_s$ from bulk formulae requires knowledge of the surface albedo, the cloud cover and the local noon solar elevation. $Q_L$ is dependent on the water vapour pressure, the difference between the sea and air temperatures and the fractional cloud cover. NWP models use Radiative Transfer Models (RTM) to calculate the radiative fluxes. This requires knowledge of the radiation at the top of the atmosphere (obtained from satellites) and parameterisations of processes such as scattering, absorption and diffusion of radiation at different levels in the atmosphere. The limiting factor in most RTMs is the representation of clouds and their radiative effects.

The bulk formulae for the latent heat flux ($Q_E$) and the sensible heat flux ($Q_H$) have the general form given in equations 2.1 and 2.2 respectively.

$$Q_E = \rho C_E U(q_s - q_{10}) \tag{2.1}$$

$$Q_H = \rho C_p C_H U(SST - T_{10}) \tag{2.2}$$

$\rho$ is the air density, $U$ is the wind speed at 10 m above sea level, $q_s$ and $q_{10}$ are mixing ratios of the air in contact with the water and at 10 m, $L$ is the latent heat of vaporisation of water, $C_p$ is the specific heat capacity of water, $SST$ and $T_{10}$ are the sea surface and 10 m air temperatures and $C_E$ and $C_H$ are variable exchange coefficients for latent and sensible heat respectively.

Direct flux measurements are required for determination of the exchange coefficients. Before the mid-1970's, due to the low number of direct flux measurements, there was limited knowledge of how exchange coefficients varied with wind speed. Values for the coefficients, $C_E$ and $C_H$, were therefore taken to be constant and equal, ranging from 1.4 – 2.3 x $10^{-3}$ (e.g. Budyko, 1963). Bunker (1975; 1976) studied the variability of exchange coefficients with wind speed and stability and produced charts for these values, showing an increase in exchange coefficients with wind speed. The derived coefficients were based on

a small number of observations, especially at higher wind speed values, and hence the coefficients obtained were still of limited accuracy. This was an important issue in bulk parameterisations for many years. As larger and more accurate calibration datasets have become available, several studies focused on improving the bulk parameterisations have been published (Webster and Lukas, 1992; DeCosmo et al., 1996; Fairall et al., 2003). The new parameterisations provide a better estimation of fluxes for a wider range of wind speeds and the roughness of the sea surface.

One of the most widely used algorithms in the air-sea interaction community at present is that of the Coupled Ocean-Atmosphere Response Experiment (COARE) developed by Fairall et al. (1996). Updated versions of this algorithm are still being published to further increase it's applicability. The most recent updates include an increase to the sensible and latent fluxes in light winds, as well as high wind conditions using a database covering 7200 hours of observations, 800 hours of which were for wind speeds above 10 $ms^{-1}$ (Fairall et al., 2003). The COARE algorithm is currently accurate to within 5 % for wind speeds of 0-10 $ms^{-1}$ and within 10 % for wind speeds up to 20 $ms^{-1}$, compared to the 30 % uncertainty of twenty years ago (Fairall et al., 2003). However, as noted in the final report of the Working Group on Air-Sea Fluxes (WGASF, 2000), further improvements to the flux formulae are necessary if the accuracy required for identifying interannual variability and obtaining near global heat balance is to be met.

Other issues with using the bulk method for estimating air-sea exchange involve the accuracy of ship observations, the uneven distribution of these observations (concentrated along shipping routes and with limited observations at high latitudes) and the difficulty of obtaining error estimates. The bias arising in measurements is not constant over time but instead changes with observational methods. For example, there has been a shift to engine intake temperature readings over bucket temperatures and changes in height of wind speed measurements have occurred due to changes in ship height. Recent efforts have attempted to identify and correct such uncertainties (Kent et al., 1999).

The zonal ($\tau_x$) and meridional ($\tau_y$) wind stress components are calculated using

$$\tau_x = \rho C_D u_x \left(u_x^2 + u_y^2\right)^{1/2} \quad (2.3a)$$

$$\tau_y = \rho C_D u_y \left(u_x^2 + u_y^2\right)^{1/2} \quad (2.3b)$$

where $C_D$ is the variable exchange coefficient for momentum and $u_x$ and $u_y$ are the zonal and meridional 10 m wind velocities. The exchange coefficient for momentum varies with wind speed and the surface roughness of the ocean. However, the dependence of the surface roughness of the ocean on the sea state (i.e. height and steepness of waves) remains a subject of debate (Taylor and Yelland, 2001). Dependencies of surface roughness on wave slope, significant wave height and wave age have all been proposed in the literature. Taylor and Yelland (2001) provide a review of the literature on this subject.

### 2.3.2 The NOC climatology and the NCEP reanalysis

In this thesis atmospheric fields from the NOC climatology and the NCEP reanalysis are used to quantify the net heat flux and the wind-driven advective heat divergence. These particular products are currently the only available fields covering the period 1999 – 2005. Other products, such as the European Centre for Medium Range Weather Forecasting (ECMWF) 40-year reanalysis, which finishes in 2002, have not been employed.

The National Oceanography Centre (NOC) climatology version 1.1, formerly the SOC climatology (Josey et al., 1999), is based on meteorological data from an enhanced version of the Comprehensive Ocean Atmosphere Dataset (COADS; Woodruff et al., 1993). COADS comprises data from voluntary observing ships (merchant, ocean research, fishing, navy etc) and moored and drifting buoys, with around 30 million meteorological reports available between 1980-1993 (the original COADS temporal coverage). The NOC 1.1 climatology is based on this period but fields for individual months are now available for the longer period 1980-2005. The fields for 1994-2005 have been developed using the same method as that adopted for the NOC 1.1 climatology, applied to updates of the COADS. Biases in the COADS arising from variations in the observing method (Kent et al., 1993) are corrected using additional information regarding observing procedures from

the World Meteorological Organisation (WMO, 1993) report 47 which details ship instrumentation. These corrected observations are then averaged onto monthly 1° x 1° grids using a successive correction method (Josey et al., 1999). The applied corrections were found to be complex with changes of up to 15 $Wm^{-2}$ in monthly mean net heat flux. The NOC 1.1 climatology does not exhibit closure of the global ocean heat budget, as it has a net global oceanic gain of 30 $Wm^{-2}$.

A linear inverse analysis of the NOC climatology (referenced to as version 1.1a) for the years 1980-1993, which uses ten hydrographic ocean heat transport constraints to help close the heat budget is also available (Grist and Josey, 2003). Despite a reduction in the global net heat imbalance to a 2 $Wm^{-2}$ loss, the applied spatially fixed parameter adjustments led to poorer agreement between the adjusted fluxes at certain buoy deployments. For example, the subduction buoy array deployment (situated in the subtropical North Atlantic) showed heat flux differences of 45 $Wm^{-2}$ when compared to the climatology after adjustment, but only 8 $Wm^{-2}$ before. This highlights the need for regional instead of global adjustments. Only the NOC 1.1 climatology is considered in this study, since the NOC 1.1 a) climatology adjustments are based on the inversion for the period 1980-1993. In addition, the NOC 1.1 heat fluxes show larger differences with the NCEP heat fluxes, providing a better idea of the likely range of error in surface flux products.

The National Centers for Environmental Prediction/National Centre for Atmospheric Research (NCEP/NCAR) reanalysis assimilates land surface, ship, radar and wind radiosonde (rawinsonde), pilot balloons (pibal), aircraft and satellite data into a Numerical Weather Prediction (NWP) model to improve flux estimates in regions of sparse data coverage. The model has T62 resolution, corresponding to a roughly 2° x 2° grid and 28 sigma levels in the vertical. Fields are available on 6-hourly, daily and monthly time scales. Kalnay et al. (1996) and Kistler et al. (2001) describe the reanalysis data assimilation system in detail. Gridded variables are freely available for download from the NCEP website (2006).

Many studies have compared NCEP and NOC fluxes to high quality observations from buoys and research vessels to identify regions of existing bias (Gulev, 1995; Moyer and Weller, 1997; Smith et al., 2001; Josey, 2001; Moore and Renfrew, 2001; Renfrew et

al., 2002; Yu et al., 2004). The NOC 1.1 climatology underestimates turbulent heat fluxes in areas of large temperature gradients across the air-sea boundary, probably due to an overestimation of the atmospheric humidity (Josey et al., 1999). However, comparisons with buoy data in the subduction region in the subtropical North Atlantic Ocean found that the NOC 1.1 fluxes agree to within 10 $Wm^{-2}$. The NCEP reanalysis underestimated the heat gain due to overestimation of latent heat losses and underestimation of the shortwave radiation at the same location (Josey, 2001). The averaged net heat gain in NCEP is less than the corresponding buoy value by 35±12 $Wm^{-2}$.

Moore and Renfrew (2001) and Renfrew et al. (2002) found significant overestimation in the reanalysis latent and sensible heat loss over the Gulf Stream and the Labrador Sea. Errors were particularly pronounced during high flux events, sensible and latent heat fluxes overestimated by up to 100 % and 50 % respectively (Moore and Renfrew, 2001). This overestimation of fluxes in the NCEP reanalysis is thought to be due to the application of inappropriate roughness length formulations that result in overestimation of ocean heat losses during moderate and high winds.

The global mean ocean surface energy balance obtained from the NCEP reanalysis is 6 $Wm^{-2}$. This value is lower than the energy balance in the NOC climatology. However, on the basis of the comparisons discussed above, it is thought that this reduced imbalance is partly due to the application of inappropriately high transfer coefficients in the bulk formulae which lead to overestimation of turbulent fluxes (Renfrew et al., 2002).

Comparisons of the wind stress fields from the NCEP reanalysis and the NOC climatology with buoy data have been made by Josey et al. (2002). In the subduction region of the subtropical North Atlantic, the error in monthly mean NOC wind stress fields ranged from 0.004 to 0.008 $Nm^{-2}$, corresponding to 5-10 % of the mean stress. The NCEP wind stress fields were noticeably weaker than those from NOC in the Tropics; the zonal average wind stress magnitude at the equator is 0.022 $Nm^{-2}$ for NCEP and 0.031 $Nm^{-2}$ for NOC.

## 2.4 OCCAM

The Ocean Circulation and Climate Advanced Model (OCCAM) is based on the Bryan - Cox - Semtner general ocean circulation model (Bryan 1969; Semtner, 1974; Cox, 1984) and is a development of the GFDL Modular Ocean Model (MOM) code (Pacanowski et al., 1990). The model run used in this study has full surface forcing based on a modified set of atmospheric variables (wind speed, air temperature, specific humidity, sea level pressure, cloudiness, precipitation and short wave radiation) from the NCEP reanalysis (Kalnay et al., 1996) and the model top level temperature. The surface salinity is relaxed to monthly mean observations to account for runoff and inaccuracies in the precipitation observations. For more details on the model run refer to Coward and de Cuevas (2005).

The model run spans 1985-2003, has a horizontal resolution of 1/4° x 1/4° and 66 levels in the vertical, 14 of which are in the upper 100m. The eddy permitting resolution supports narrow boundary currents such as the Gulf Stream and frontal features. Several recent analyses have demonstrated that this model can be usefully employed to study the circulation of the North Atlantic (e.g. Marsh et al., 2005, Hirschi et al., 2006).

The model has a two-grid scheme to avoid an artificial island at the poles and Fourier filtering at high latitudes. A rotated latitude-longitude grid with pseudo poles on the equator in the Pacific and Indian Oceans was used for modelling the Arctic and North Atlantic while the rest of the world is modelled using a regular latitude-longitude grid. A simple channel model is used to connect the two grids through the Bering Strait (Coward et al., 1994). For use in this study, the temperature field for the North Atlantic was rotated onto a North-South grid using a bilinear interpolation in both longitudinal and latitudinal directions.

## 2.5 The 2001 World Ocean Database

The World Ocean Database contains many observations of different ocean variables including in-situ temperature, salinity, oxygen, dissolved inorganic nutrients and chlorophyll. Atlases of the data have been produced by interpolation of observations onto standard depth levels and gridding by objective analysis. Only monthly 1° x 1° temperature and salinity climatological fields are used in this study. These fields extend from the

surface to 1500 m on 24 depth levels, with 10 m resolution in the upper 30 m, reducing to 100 m resolution between 300 m and 1500 m.

Over seven million temperature casts collected over the period 1772-2001 from a range of oceanographic instrumentation are used to produce monthly climatological temperature fields. Despite some data being available from over 200 years ago, 50 % of the profiles used in the 2001 WOA were sampled after 1979. Around 1.5 million salinity profiles are used in the salinity climatological monthly field. Bottle data, CTD data and data collected by XBT, Mechanical Bathythermograph (MBT), moored and drifting buoys, profiling floats and Undulating Ocean Recorders (UOR) are all included in the WOA. For further details on the 2001 WOA refer to Stephens et al., (2001) and Conkwright et al. (2002).

# CHAPTER 3. Investigation of Interpolation Methods

## 3.1 Introduction

The Argo dataset contains many thousands of temperature profiles randomly distributed in space and time (chapter 2). In order to use this dataset to investigate the North Atlantic heat budget it is necessary to first interpolate the observations onto regular grids. Despite the relatively large number of observations in the Argo dataset there is a limit to the length and timescales that can be resolved. In this chapter these scales and a variety of interpolation schemes are investigated. The aim here is to determine a method that can be employed for the subsequent heat budget analysis.

In the following, the length and time scales that the Argo dataset is capable of resolving are considered in section 3.2. In section 3.3 interpolation methods are discussed, these methods are then tested in section 3.4. A discussion of results is provided in section 3.5.

## 3.2 Statistics of the North Atlantic Temperature field

In order to carry out interpolation of randomly distributed data, length and time scales need to be defined. These applied scales will depend on the resolution of the observations and on the dominant scales of variability to be resolved. In this section the length scales imposed by the Argo dataset are first investigated. These imposed scales are then briefly discussed in the context of the ocean processes that can be resolved.

For interpolation to be successful it is necessary that the applied interpolation distances and times are larger than the separation between data points. Thus there is a trade off between the temporal and spatial resolution that can be achieved. As outlined in chapter 1, this study aims to investigate the seasonal cycle in the heat budget. It is therefore a requirement that the temporal scale is short enough to enable the seasonal signal to be resolved. In view of this the temporal scale is set to 30 days. The imposed spatial scale is investigated by determining the percentage of 2° x 2° grid points in the North Atlantic for which there is at least one observation within the defined one-month period and different

distances. The results are plotted in Fig. 3.1. Values are shown for each year between 1999 and 2005.

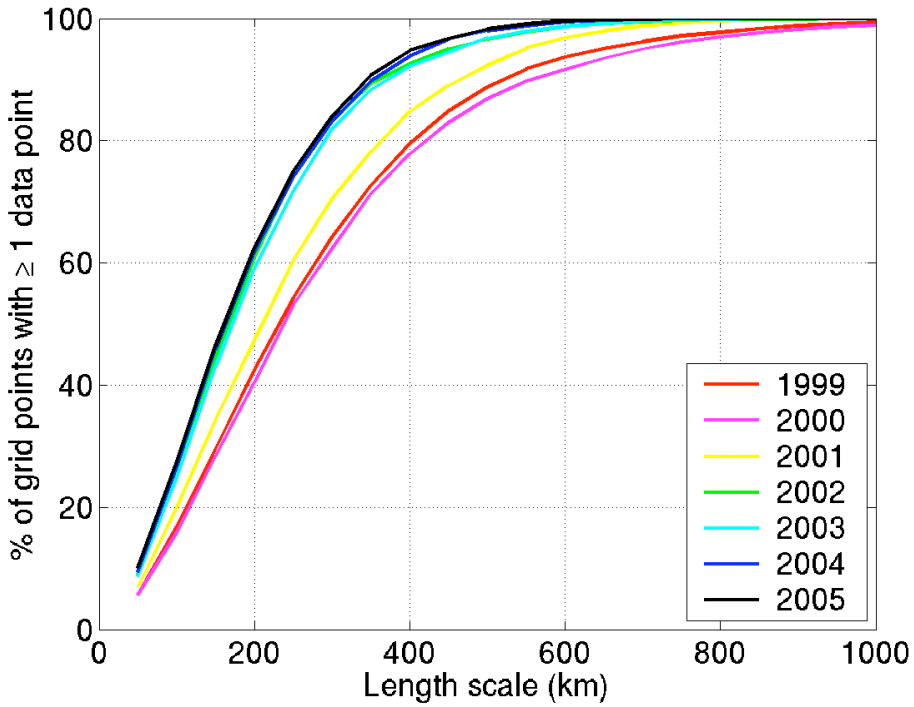


**Figure 3.1** The percentage of 2° x 2° grid points in the North Atlantic (0-70°N, 0-100°W) that lie within the distances specified on the x-axis and a one month period of at least one data point.

On average 20 % of North Atlantic grid points have data collected within 100 km and one month. In comparison, 70 % (90 %) of grid points have data collected within 300 km (500 km) and the same timescale. There is a temporal trend reflecting the variability in the number of active floats in the North Atlantic over time. Eighty nine percent of grid points are located within 500 km and one month of an observation in 1999, compared to 98 % in 2005. This result suggests that it should be possible to resolve length scales of 500 km throughout much of the North Atlantic between 1999 and 2005 using the Argo dataset. It is undesirable to apply interpolation length scales less than 500 km when a monthly temporal

scale is used. In well sampled regions and following the completion of the Argo array it may be possible to resolve scales of 300 km or less.

Processes in the ocean act on a multitude of scales from micro-scale turbulence to gyre and basin scale circulation. Given the target resolution of Argo (3° x 3°) and the results presented above, it is apparent that the mesoscale cannot be fully resolved using Argo. White (1995) examined the correlation length scales of the global ocean using a thirteen-year dataset containing some 500,000 temperature observations with a focus on the decorrelation scales of interannual signals at gyre-to basin scales. He suggested decorrelation scales of 5° in longitude (corresponding to 390 km at 45°N) and 2.5° in latitude (roughly 220 km) in the global ocean. Decorrelation scales were calculated at three different depth levels; the sea surface, 200 m and 400 m. A decrease in the length scales with increasing depth was observed, while time scales remained relatively constant. These length scales suggested by White are slightly lower than the 500 km length scales imposed by Argo. However, correlation scales of up to 1000 km (Böhme and Send, 2005) have been applied in the literature during similar studies. In addition Zang and Wunsch (2001) give evidence for the existence of a climatological scale which extends beyond 500 km. Thus, the choice of 500 km employed here is reasonable.

## 3.3 Interpolation Methods

The interpolation method used to obtain regularly spaced products from sets of irregularly spaced observations demands attention. In meteorology and oceanography there are two main methods commonly used to this end; distance weighting schemes and optimal interpolation. Details on these two methods are given in section 3.3.1 and section 3.3.2, respectively.

### 3.3.1 Distance Weighting Schemes

Distance weighting schemes calculate the values for weights either as a function of separation between analysis and observing stations, as a function of the accuracy of one observation relative to another, or as a combination of both (Thiebaux and Pedder, 1987).

Discrete values for distance weighting are calculated using some prescribed distance function *w(D),* where *D* is the distance between the grid point and the observing location. Weights are normalised so that the sum of the weights is equal to unity.

$$X_{grid} = X_m + \sum_i (X_i - X_m) \bullet \left( \frac{w_i(D_i)}{c} \right) \tag{3.1}$$

$$c = \sum_i w_i(D_i) \tag{3.2}$$

where $X_i$ are the observation values, $X_m$ is the first guess field and $X_{grid}$ is the interpolated value. The first guess field, $X_m$, can be taken as a mean value of all input data points (Gellers-Barkman and Wells, 1992), as a climatological value (Lavender, 2001) or as a value from a map produced at an earlier time step (Alderson and Killworth, 2005). The choice of the first guess field introduces a certain degree of subjectivity into the analysis. This is particularly true in regions of low sampling density, where the interpolated field will relax to the first guess.

Typically all weights are set to zero beyond a radius of influence, *L*. This radius determines the amount of smoothing; if *L* is too small, interpolation errors are introduced in response to observation errors. Conversely, if *L* is too large the analysis field is over-smoothed. An obvious constraint on the value of *L* is that it shouldn't be smaller than the largest distance between a grid point and the nearest neighbouring observations. In practice, this might be much longer than the average distance between neighbouring observations so that the lower limit for *L* could still result in over-smoothing in some areas. In this case a successive correction in which repeated analyses are carried out with successively smaller values for *L* might be more effective than single-scan analysis. The successive correction process results in variable resolution of the interpolated field with smaller scale features being transferred to the analysis field in areas of high observing density.

Distance weighting functions applied in the literature have various forms. Thiebaux and Pedder (1987) give an overview of some of these functions, mostly applied in a meteorological context. Barnes (1964) describes successive correction methods, modifications to the method are provided by Maddox (1980) and Buzzi et al. (1991).

### 3.3.2 Optimal Interpolation

The main limitation of empirical weight formulations is that they cannot properly take into account the spatial inhomogeneity of observations. This inhomogeneity can cause large analysis uncertainty in regions where sampling is highly variable. Statistically optimal interpolation overcomes this limitation by considering not only the distance of an observation from the grid point but also the distance between different observations. Optimal Interpolation (OI) methods were first used for interpolating atmospheric observations by Gandin (1963), for ocean observations by Bretherton et al. (1976) and for subsurface float velocity data by Davis (1998). The method is based on the Gauss-Markov theorem which gives a linear estimate that is unbiased, is optimal in the least squares sense and provides an estimate of the error variance.

The analysis field, $X_{grid}$ is obtained from

$$X_{grid} = X_m + \sum_{i=1}^{N} w_i (X_i - X_m) \tag{3.3}$$

where $X_m$ is the first guess field, $X_i$ are the observations of the field and $w$ is the weighting matrix given by

$$w = Cdg \bullet Cdd^{-1} \tag{3.4}$$

$Cdg$ is the covariance between the analysed value at the observation point and the grid point and $Cdd^{-1}$ is the inverted covariance matrix between the observation points. Due to the paucity of observations in most ocean regions and the requirement that the function be

positive definite (i.e. the matrix needs to have positive eigenvalues so that the matrix is diagonally dominant) and symmetrical, it is often not possible to obtain covariance functions from the data. Instead, the covariance functions are typically obtained by fitting, or assuming, an analytical model.

Many different forms of covariance functions have been used in the literature. Lynch and McGillicuddy (2001) give an overview of some of these forms. Several studies concerned with the interpolation of Argo data assume a Gaussian function (Davis, 1998; Wong et al., 2003; Lavender et al., 2005; Böhme and Send, 2005). Exponential and algebraic fits (e.g. Davis, 1998) have also been applied for interpolation of oceanographic datasets. Thiebaux and Pedder (1987) and Piterbarg et al. (1991) investigated the sensitivity of interpolated fields to the form of the covariance function used in the OI. Both studies found that the detailed form of the covariance function did not greatly affect the interpolated field.

### 3.4 Testing Interpolation Methods

In order to assess the accuracy of different interpolation methods, the temperature field from the OCCAM model (section 2.5) is subsampled to the Argo resolution and interpolated onto regular grids using a range of methods. This subsampling involves extracting the model temperature profile closest to each location sampled by Argo between July 2001 and June 2003. Interpolated fields are produced for January and July 2002 at 10m and 1000m. Comparisons between the interpolated temperature fields and the full model temperature field are then made. Although the resolution of the OCCAM model is 1/4° x 1/4°, the model temperature field has been subsampled to 2° x 2° to reduce computational load during interpolation. This is necessary particularly when using an OI, which involves computationally demanding matrix inversion. The subsampled 2° x 2° model temperature field will be referred to as the full model temperature field to avoid confusion with the model temperature field subsampled to the Argo resolution (referred to as the subsampled temperature field).

Simple averaging schemes, distance-weighting schemes and optimal interpolation schemes are all tested. The latter two schemes use the WOA as a first guess field, no first

guess is used in the simple averaging scheme. The Root Mean Squared (RMS) difference between the full and subsampled field interpolated using each method, averaged over the area 20-60°N, 80-0°W, are given in Table 3.1. It can be seen that provided a suitable length scale is applied, the OI methods produce a more accurate interpolated temperature field than either the simple averaging or distance weighting schemes. RMS differences are typically 0.10 – 0.20 °C lower when such an OI scheme is employed over the other interpolation methods. Despite this reduction, RMS differences typically remain in excess of 0.75 °C. This large value reflects the large differences between the full temperature field and the interpolated temperature field in regions of high mesoscale activity. There are many areas throughout the North Atlantic where the combined sampling and interpolation errors are much less than 0.5°C. Errors are discussed in more detail in chapter 4.

The values presented in the table are discussed in more detail below. Additional details on the success of these different interpolation schemes are given in the subsections 3.4.1, 3.4.2 and 3.4.3 for simple averaging methods, distance weighting schemes and OI schemes, respectively.

**Table 3.1** RMS temperature differences (°C) between the full model temperature field and the subsampled temperature field gridded using different methods.

| **Gridding method** | **Jan** | **July** |
|---|---|---|
| Averaging | 0.81 | 0.78 |
| Averaging + correction for position | 0.84 | 0.81 |
| Distance weighting, Cressman | 0.79 | 0.76 |
| Distance weighting, extended Cressman, $\alpha=4$ | 0.81 | 0.74 |
| OI Gaussian: *Lx=100km, Δt=30 days* | 1.36 | 1.35 |
| OI Gaussian: *Lx=500km, Δt=30 days* | 0.75 | 0.74 |
| WOA climatological field | 1.64 | 1.69 |

### 3.4.1 Simple Averaging schemes

In this method, the temperature at each grid point is obtained by averaging all profiles obtained from the month of interest and within 500 km of the grid point. There are gaps in the interpolated field in regions of low Argo coverage. The differences between the interpolated temperature field and the full model temperature field (referred to as the interpolation error) for winter (January) and summer (July) at 10 m and 1000 m are shown in Fig. 3.2.

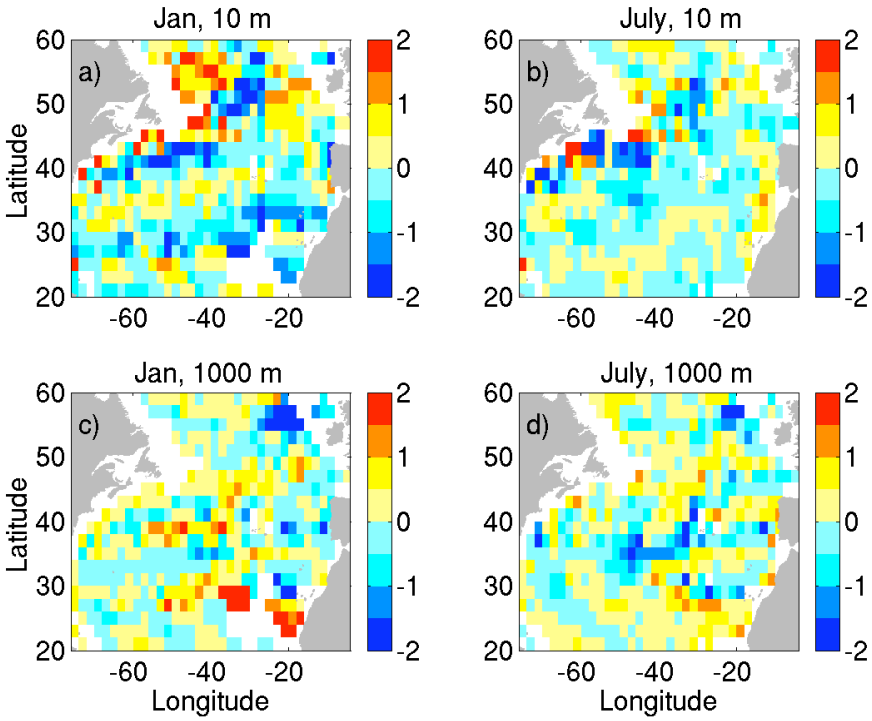


**Figure 3.2** Difference plot (the interpolation error) between the full model temperature field and the subsampled temperature model field interpolated using a simple averaging scheme for a) January 10m, b) July 10m, c) January 1000m and d) July 1000m. Red indicates the interpolated field is too warm, blue too cold. Values in °C.

Largest interpolation errors are evident in the vicinity of the western boundary current, with regions of neighbouring warm and cold bias exceeding 2 °C at 10 m. This structure suggests that the interpolated temperature field is over-smoothed at this location,

i.e. the temperature structure of the western boundary current is not fully resolved. Errors are also large in areas of low sampling such as off the west coast of Africa. Elsewhere in the North Atlantic the bias is typically less than 1 °C. Lower interpolation errors are apparent in July (typically less than 0.5 °C) than in January. This difference is likely a reflection of the higher sampling density in July 2002, relative to January 2002. In July 648 profiles were available, compared to 542 in January. These observed trends are supported by the RMS differences which are 0.81 °C in January and 0.78 °C in July. Differences are also smaller at 1000 m than at 10 m. This is due to the smaller spatial and temporal variability in the temperature field at deeper depths.

The mean position of the data used to obtain an estimate of the temperature at the grid point $x_g,y_g$ is generally not centred on the grid point itself. Using information from the WOA01 temperature field a correction is applied to the interpolated field to account for this discrepancy between the mean position, $x_{mean},y_{mean}$ and the grid point. The correction is simply the difference between the WOA temperature at $x_{mean},y_{mean}$ and $x_g,y_g$. This correction does not lead to an improvement in the accuracy of the interpolated field. The RMS difference actually increased from 0.81 °C to 0.84 °C during January and from 0.78 °C to 0.81 °C during July.

### 3.4.2 Distance weighting schemes

The Cressman (1959) distance-weighting model is also used to interpolate the subsampled OGCM temperature field. The model is defined using equations (3.1 - 3.2) with the following weighting function

$$w(D) = \frac{L^2 - D^2}{L^2 + D^2} \tag{3.5}$$

where $D$, the distance between the observation and the grid point, is less than $L$, the radius of influence, $w(D)=0$ where $D \geq L$. An extension of the Cressman model with an extra exponent parameter $\alpha$ is also tested.

$$w(D) = \left( \frac{L^2 - D^2}{L^2 + D^2} \right)^{\alpha} \tag{3.6}$$

with $\alpha > 1$. The effect of increasing α is to increase the weight given to observations where $D$ is small relative to the weight given to observations where $D$ is large. This decreases the amount of smoothing applied to the observed field. $L$ is set to 500km. The first guess field is taken to be the monthly temperature field from the 2001 WOA.

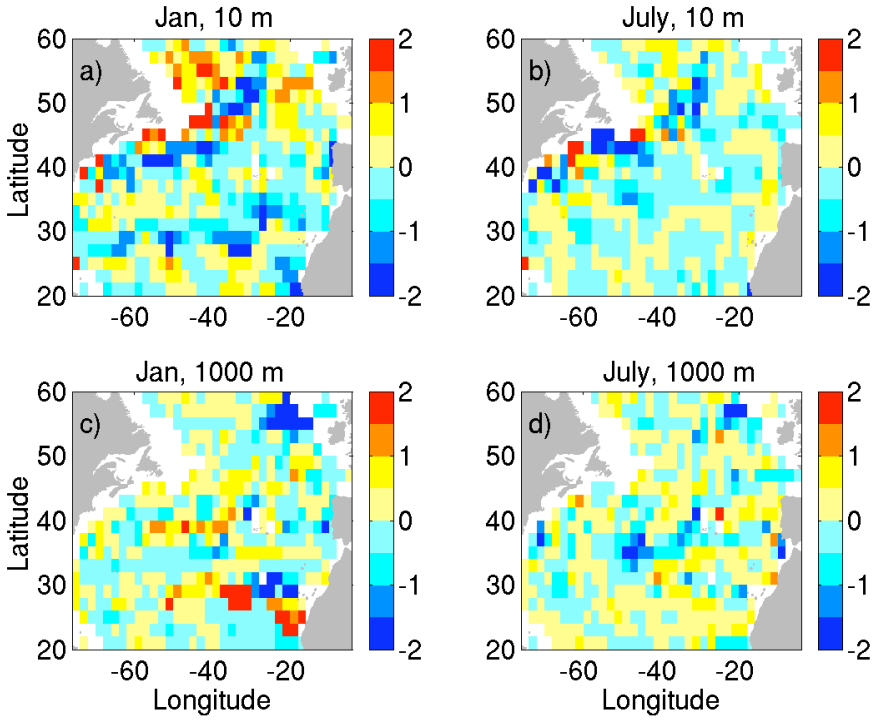


**Figure 3.3** Difference plot (the interpolation error) between the full model temperature field and the subsampled temperature model field interpolated using the Cressman distance weighting scheme for a) January 10m, b) July 10m, c) January 1000m and d) July 1000m. Red indicates the interpolated field is too warm, blue too cold. Values in °C.

The differences between the interpolated temperature field based on the Cressman distance weighting and the full model temperature field are plotted in Fig. 3.3. The differences shown here are typically slightly lower than the differences shown for the

interpolated temperature field based on the simple averaging scheme (compare Fig. 3.2 and Fig. 3.3), thus indicating a reduction in the interpolation error. However, this difference is not large. RMS differences for the distance-weighted interpolated temperature field are 0.02°C lower than those from the averaged field for both January and July. Using the extended Cressman scheme (Thiebaux and Pedder, 1987) led to no significant difference over the original Cressman scheme (not shown).

### 3.4.3 Optimal Interpolation Schemes

The subsampled temperature field is now interpolated using an OI scheme. A Gaussian covariance function is used. In each case considered, four correlation parameters set the decay scale of the correlation function: a longitudinal scale ($Lx$), a latitudinal scale ($Ly$), a cross-isobath scale ($\Phi$) and a temporal scale ($\Delta t$). The values of $Lx$ and $Ly$ are assumed to be equal in all cases since $\Phi$, the cross isobath scale accounts for anisotropy.

The cross-isobath scale is included to account for the effects of topography on water mass properties and circulation. In this study, the method of Wong et al. (2003) is adopted with the cross-isobath separation, *F,* defined as the fractional distance in potential vorticity,

$$F_{ab} = \frac{|PV(a) - PV(b)|}{\sqrt{PV^2(a) + PV^2(b)}} \tag{3.7}$$

where $PV$ is the barotropic potential vorticity, $f/H$, where $f$ is the Coriolis parameter ($2\Omega \sin(\phi)$, $\Omega$ the rotation rate of Earth, $\phi$ the latitude in radians) and $H$ is the full ocean depth, $a$ and $b$ refer to locations, which are discussed in more detail later in this section.

The optimal estimate of the temperature at each grid point and on each depth surface is obtained using equation 3.3. $X_i$ are taken to be the 40 temperature profiles with the shortest separation factor (the spatial, temporal and cross-isobath separation relative to the prescribed length scales). Different values for the number of profiles included in the OI are also considered. The interpolated field is found to be sensitive to the chosen number of profiles for values much less than 40, but relatively insensitive to values above this. To

illustrate the typical spread of the data the Argo profile positions used to interpolate to the grid point 30°N, 60°W for February 2003 are shown in Fig. 3.4 a).

The monthly climatological value of the 2001 World Ocean Atlas, $X_{WOA}$, is taken to be the first guess field. The Gaussian data-grid covariance is defined as

$$Cdg_i = \left\langle s^2 \right\rangle .\exp\left\{ -\left[ \frac{Dx_{i,g}^2}{Lx^2} + \frac{Dy_{i,g}^2}{Ly^2} + \frac{F_{i,g}^2}{\Phi^2} + \frac{Dt_{i,g}^2}{\Delta t^2} \right] \right\} \tag{3.8}$$

and the Gaussian data-data covariance,

$$Cdd_{i,j} = \left\langle s^2 \right\rangle .\exp\left\{ -\left[ \frac{Dx_{i,j}^2}{Lx^2} + \frac{Dy_{i,j}^2}{Ly^2} + \frac{F_{i,j}^2}{\Phi^2} + \frac{Dt_{i,j}^2}{\Delta t^2} \right] \right\} \tag{3.9}$$

where $Dx$, $Dy$ are the spatial separations and $Dt$ the temporal separation. The subscripts *i* and *j* refer to pairs of Argo profiles while the subscript *g* refers to the grid point being mapped to. The schematic in Fig. 3.4 b) shows these different terms. $s^2$, the signal variance, is calculated from

$$s^2 = (1/N)\sum_i \left( T_i - T_{WOA} \right)^2 \tag{3.10}$$

while $\eta^2$, the noise variance is calculated from

$$\eta^2 = (1/2N)\sum_i \left( T_i - T_n \right)^2 \tag{3.11}$$

$N$ is the number of profiles included in the OI, set to 40 here and $T_n$ is the data point which has the shortest distance from $T_i$. For example in Fig 3.4 c), for $i=1$, $n=2$ while at $i=3$, $n=1$. The noise is added to the leading diagonal of the data-data covariance.

For use in *Cdg*, $a$ and $b$ in $F$ (Eq. 3.7) represent float profile positions, $i$, and the grid position, $g$, respectively. For use in *Cdd*, the data-data covariance, $a$ and $b$ represent pairs of floats, $i$, $n$, with the shortest spatial-temporal separations. For example, in Fig. 3.4 c), in the calculation of *Cdd* for $i=1$, the pairs are $a=X_1$ and $b=X_2$, for $i=2$ the pairs are $a=X_1$ and $b=X_2$ and for $i=3$ the pairs are $a=X_1$ and $b=X_3$. Values of $F$ lie between 0 and 1, with a mean of 0.23.

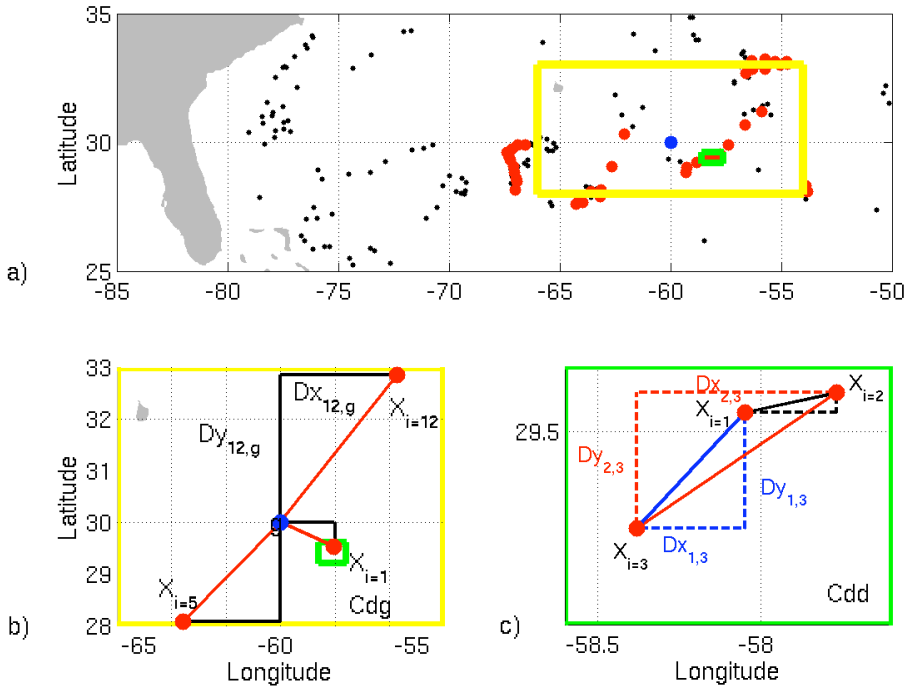


**Figure 3.4** OI explanatory figure, a) shows the float distribution with the 40 floats which would be used to interpolate to the grid point 30°N, 60°W Feb '03 (blue) marked in red. All profile positions within a 180 day time frame of Feb '03 are also plotted (black). b) shows a close up on the region boxed in yellow using three of the floats to explain the terminology used for calculating *Cdg* and c) shows a close up on the region boxed in green using three of the floats to explain the terminology used for calculating *Cdd*. Note that not all points plotted in a) are shown on b) and c).

For simplicity all scales are set as constant values on a given depth level throughout the North Atlantic. However, length scales are set to decrease linearly to half the surface value at 500 m, while time scales increase linearly to three times the surface values at 500 m. Beneath 500 m all scales remain constant. The correlation scales are set to vary with depth in view of results presented in White (1995). These results are discussed in section 3.2 above. Although no increase in time scales with depth was observed by White (1995), in this study the time scales are set to increase downwards through the water column to compensate for the applied decrease in length scales. Time scales are set to 30 days at the surface and increase linearly to 90 days at 500 m. This could introduce some smoothing of the seasonal cycle in upper ocean heat storage, particularly when examining the heat storage at high latitudes, where the wintertime mixed layer is deep.

The OI is first applied using correlation length scales of 100 km. This length scale was chosen to represent the mesoscale. The timescale is set to 30 days and the cross-isobath scale is set to 0.10. These length scales are applied to illustrate the inability of the Argo dataset to resolve such small spatial scales on monthly timescales. The difference field between the optimally interpolated temperature and the full model temperature field is plotted in Fig 3.5.

The interpolation errors are larger than those from the simple averaging scheme, particularly at 1000 m (compare Fig. 3.5 with Fig. 3.2). At this depth the interpolation error exceeds 1.5 °C throughout much of the North Atlantic, with the interpolated field cooler than the full temperature field. The RMS differences between the full sampled and subsampled temperature field are 1.36 °C and 1.35 °C for January and July, respectively. Comparison of the difference plots with the sampling density plots (Fig. 2.5 and 2.6) presented in chapter 2 indicates that the highest errors typically correspond to the regions of lowest sampling. In data sparse regions, application of the 100 km length scale results in an interpolated field, which is simply the first guess field, in this case the WOA. As shown below, the WOA field is generally cooler than the model at 1000 m. Hence the interpolated field is cooler than the model when unrealistically small values for the length scales are employed.

The difference between the WOA temperature and the model temperature is plotted in Fig. 3.6. Comparison of this figure with Fig. 3.5 reveals a good level of agreement between the two, especially at 1000 m. This improved agreement at depth likely reflects the reduced weighting given to the dataset with increasing depth. Thus the interpolation error for the OI method when a 100 km length scale is applied is dominated by the error in the first guess field. The RMS difference between the full model temperature field and the temperature from the WOA is 1.64 °C in January and 1.69 °C in July.

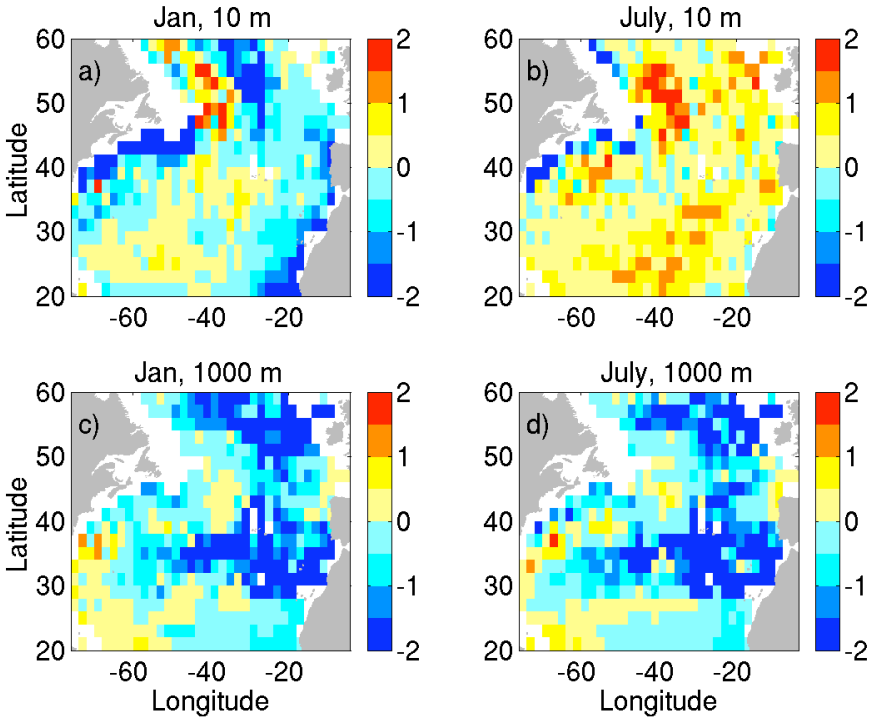


**Figure 3.5** Difference plot between the full model temperature field and the subsampled temperature model field interpolated using an OI scheme with Gaussian covariance, $Lx$=$Ly$=100km and $\Delta t$=30 days for a) January 10m, b) July 10m, c) January 1000m and d) July 1000m. Red indicates the interpolated field is too warm, blue too cold. Values in °C.

The model temperature field is warmer than that of the WOA, possibly reflective of an observed warming trend in the North Atlantic, which extends back to the 1920s (the OCCAM temperature field is for 2002 while the WOA is an average of data collected throughout the last century). It can therefore be expected that when interpolating Argo

observations, use of the WOA as a first guess field could result in a cold bias in the temperature field in regions of low sampling density.

The OI is now applied using longer length scales of 500 km. The cross isobath correlation is increased to 0.25 so the effects of the bathymetry do not become too important relative to the effects of spatial separation. A factor of 4 in the difference *f/H* contributes to the separation parameter in an approximately equivalent way to a 500 km separation in space. The cross-isobath length scale is selected to make the same contribution to the weighting as given by Böhme and Send (2005) during interpolation of salinity data in the North Atlantic.

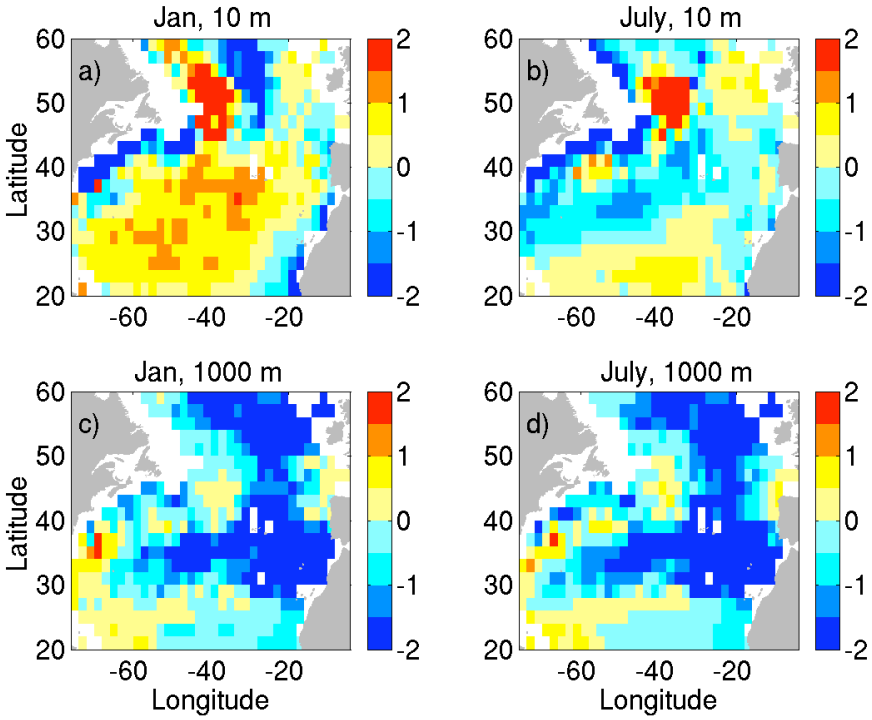


**Figure 3.6** Difference plot between the full model temperature field and WOA temperature field for a) January 10m, b) July 10m, c) January 1000m and d) July 1000m. Red indicates warmer WOA temperatures than OCCAM and blue indicates cooler WOA temperatures than OCCAM. Values in °C.

The temperature field interpolated using the OI scheme, length scales of 500 km, time scales of 30 days and cross isobath scales of 0.25 is plotted in Fig. 3.7. At 10 m,

differences only exceed 0.5 °C within the western boundary, where variability is high, and off the west coast of Africa, where sampling is low. The errors are more randomly distributed at 1000m, but remain high in the eastern subpolar North Atlantic. In comparison to Fig. 3.2 and Fig. 3.3, which show the interpolation error for the averaging and distance weighting schemes, the interpolation error in Fig. 3.7 is reduced. This improvement in the accuracy of the interpolated field is also apparent by examination of the RMS differences in Table 3.1. The RMS difference for this interpolated temperature field is 0.75 and 0.74 °C for January and July, respectively. The small difference between the January and July RMS values suggests that the OI scheme is less sensitive to under-sampling than the other tested interpolation schemes.

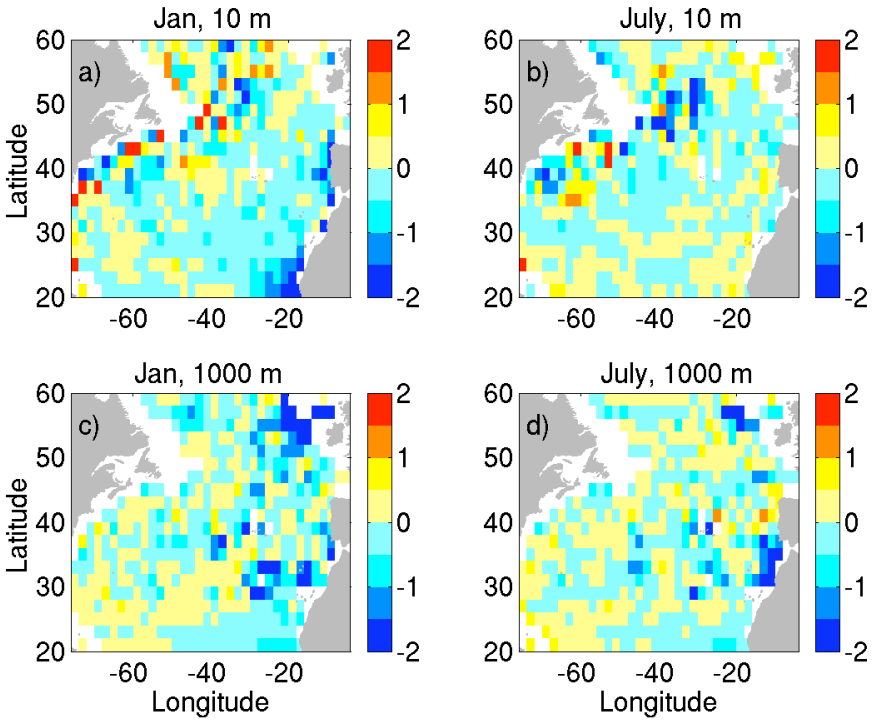


**Figure 3.7** Difference plot between the full model temperature field and the subsampled temperature model field interpolated using an OI scheme with Gaussian covariance, $Lx$=$Ly$=500km and $\Delta t$=30 days for a) January, 10m, b) July, 10m, c) January 1000m and d) July 1000m. Red indicates the interpolated field is too warm, blue too cold. Values in °C.

### 3.5 Summary

The interpolated temperature fields presented above indicate that the OI scheme is capable of achieving a more accurate representation of the full temperature field from a subsampled dataset than either a simple averaging scheme or a distance weighting scheme. However, the success of the OI scheme is dependent on the application of correlation scales that give appropriate weighting to the data. Where the length scales are too short the interpolated field relaxes to the first guess field. This is undesirable since the first guess field may be quite different to the actual temperature field and, in addition, the first guess field does not contain interannual variability. Since one of the aims of this work is to investigate this interannual variability, this may pose a limitation.

Alternative options for the first guess field include the Argo dataset itself, or an interpolated field from a previous time-step. The problem with the former option is that in regions where an accurate first guess field is most important (i.e. in data sparse regions), the first guess field will be most erroneous while the problem with the latter is that any errors in the initial field will propagate through subsequent interpolated fields. Thus, while it is recognised that the WOA is not an ideal first-guess field, it is considered to be the best option of available fields.

In view of the findings presented above, an OI scheme is used in this study to interpolate the Argo data. A Gaussian function is used to model the covariance. Use of a Gaussian model in the covariance matrices is consistent with other studies that use OI schemes to interpolate Argo float data (e.g. Wong et al., 2003; Böhme and Send, 2005). Length scales of 500 km, time scales of 30 days and a cross isobath scale of 0.25 are applied during interpolation. The length scales are set to decrease through the water column, while the time scales increase. The length scales decrease linearly to 250 km at 500 m and the temporal scales increase linearly to 90 days at 500 m. All scales remain constant below 500 m. The cross isobath scale is set to 0.25, so that a factor of 4 in the difference $f/H$ contributes to the separation parameter in an approximately equivalent way to a 500 km separation in space. The OI programs used in this study can be found on the accompanying CD.

# Chapter 4. Accuracy of Argo Temperature and Heat Storage Fields

## 4.1 Introduction

This study utilises subsurface data with a relatively high sampling density and atmospheric fields corrected for known bias to quantify the heat budget terms. Despite careful application of quality control procedures to minimise observational errors (chapter 2) and an appropriate mapping scheme to minimise interpolation error (chapter 3), errors arising from under-sampling of the field are unavoidable. In climate change and variability studies it is important to include estimates of such errors in order to determine the significance of observed signals.

This chapter focuses on quantifying the errors associated with using the Argo dataset to estimate the temperature (section 4.2) and heat storage (section 4.3) fields. The availability of independent observational subsurface temperature data in the North Atlantic enables estimation of likely errors in the Argo based temperature field. In this study, hydrographic data across a zonal section is used for this purpose. Independent observational estimates of heat storage are more limited. A model-based approach is therefore adopted to quantify the combined sampling and interpolation errors in Argo-based heat storage estimates. This involves subsampling an eddy-permitting model (OCCAM, chapter 2.3) to the nominal Argo resolution. Section 4.4 highlights the relationship between errors in heat storage estimates and 1) sampling density in the context of past and likely future numbers of available float profiles, and 2) the length of time over which storage is calculated (from one to six months). Independent error estimates, which can be used in the absence of ground-truth information, are presented in section 4.5. A summary follows in section 4.6. The main bulk of this chapter has been published in a peer-reviewed journal (Hadfield et al., 2007). A copy of the paper can be found in Appendix 3.

## 4.2 Accuracy of an Argo Derived Temperature Section

The errors associated with using the Argo dataset to estimate the upper ocean temperature are now investigated. There is a focus on whether the dataset can usefully be

employed to determine temperature across a typical North Atlantic hydrographic section. One of the aims here is to obtain some idea of the likely errors in the Argo based temperature field during periods when sections are unoccupied for studies of temporal variability.

For this analysis Argo float temperature profiles are interpolated, using the method described in chapter 3 with the May WOA climatological temperature field as a first guess, to positions of cruise CTD stations to obtain an Argo based temperature section. Comparisons are made between the interpolated Argo section and the actual cruise CTD section. Although only a single example cruise section is analysed, it is expected that results will be generally applicable to other sections in regions with similar Argo sampling density. In the following, the cruise data is described in section 4.2.1. Comparisons between the cruise section and the Argo-based section are made in 4.2.2 and altimeter data is analysed in section 4.2.3.

### 4.2.1 The Hydrographic Section

The cruise section considered is along 36°N, sampled in May and June of 2005 (McDonagh et al., 2006). The cruise track is shown in Fig. 4.1. Positions of Argo float profiles interpolated to create the Argo-based estimate of the temperature section are also shown. The spatial and temporal spread of Argo data used in the interpolation covers an area of more than $2.5 \times 10^6$ km$^2$ and a period of more than 5 months.

The average station separation of cruise CTDs is 50 km, with highest resolution of around 3 km in the western boundary current and lowest resolution of around 80 km in the middle of the section. The cruise section is therefore likely to resolve internal waves and mesoscale eddies. Mesoscale eddies are common in the region, particularly west of 65°W (Richardson, 1983). Although the Argo dataset may sample some of these features, the Argo array, with a target resolution of 3° x 3°, is not capable of fully resolving them.

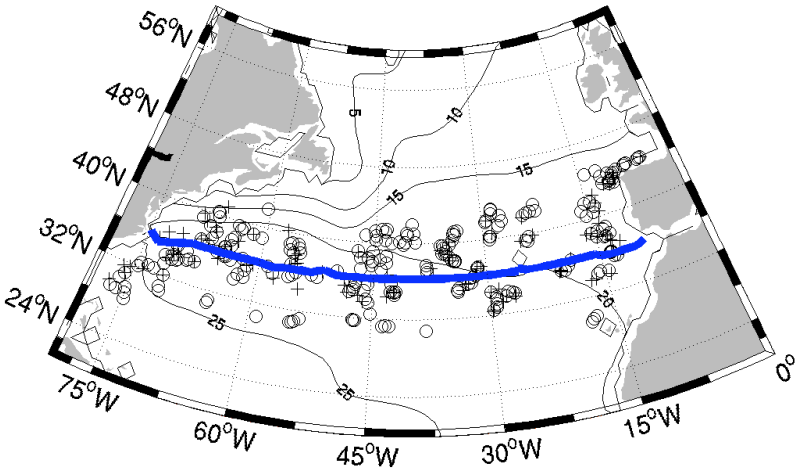


**Figure 4.1** The cruise section across 36°N sampled during May and June 2005. Positions of Argo profiles used to obtain the interpolated Argo-based hydrographic section are shown as circles (sampled within 30 days of the cruise CTD) and crosses (sampled more than 30 days before or after the cruise CTD). The contoured field is the WOA 10 m temperature in May.

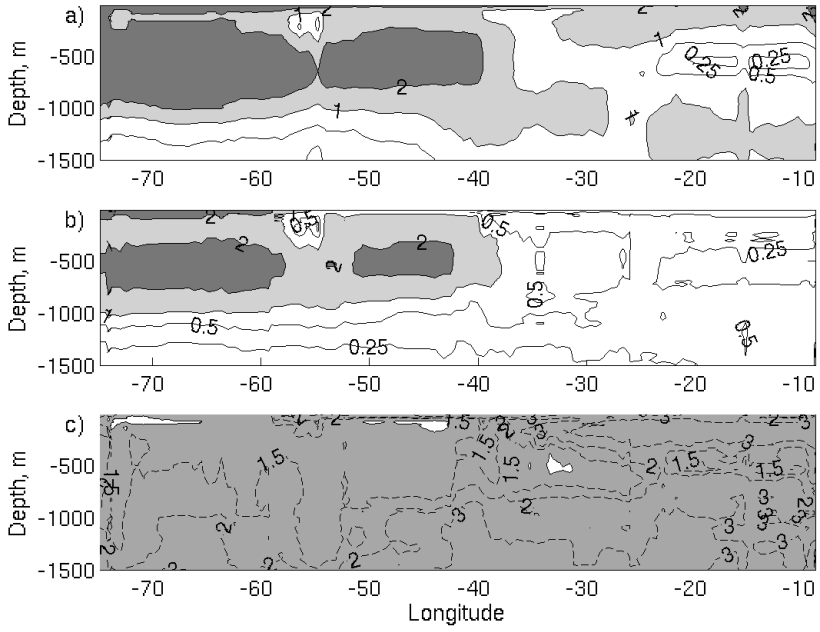


**Figure 4.2** Optimal interpolation statistics across the cruise section showing a) the signal, b) the noise and c) the signal to noise ratio. Shading shows values > 1 °C with contours of 0.5, 1, 2 and 5 °C drawn in a) and b) and contours of 1.5, 2 and 3 in c).

The signal (*s,* equation 3.10, chapter 3) and noise ($\eta$, equation 3.11, chapter 3) statistics across the cruise section are shown in Fig. 4.2 a) and b), respectively. Both the signal and noise exhibit highest values in the western basin at a depth of 500-1000 m. The signal and noise exceed 4 °C and 2 °C respectively in this location. In the eastern basin and deeper than 1000 m, the signal and noise are much smaller, with typical values less than 1.5 °C and 0.5 °C respectively. The signal generally exceeds the noise. This is apparent from the Signal-to-Noise Ratio (SNR), Fig. 4.2c, with values of more than one throughout most of the North Atlantic. Schiller et al., (2004) tentatively suggest that a SNR of one or more provides statistically significant and useful information about Argo-sampled data in the ocean.

### 4.2.2 Cruise and Argo Section Inter-comparison

Isotherms across 36°N based on the cruise CTD data and the interpolated Argo-based estimate of the temperature field are plotted in Fig. 4.3a) and b), respectively. The Argo data is able to resolve the main features in the section with good agreement in isotherm depths between the two (quantified in more detail below). However the isotherm structure is smoother in the Argo based section than in the cruise section. This is particularly evident in the western basin where the cruise data resolves several features with length scales of the order 200 km. The Gulf Stream, characterised by the steep shoaling of isotherms at 74°W, is also well resolved in the cruise section but less so in the Argo section. Neither the present, nor target, Argo array enables mesoscale features to be resolved. In addition, the 500 km length scales applied in the Optimal Interpolation (OI) smooth many mesoscale features that are sampled by Argo. Reduction of the length scales in the western boundary is unlikely to yield a better agreement between the Argo and cruise temperature sections due to the low Argo sampling in this region (Fig. 4.1).

Isotherms across 36°N have also been plotted using temperature data from the WOA for the month of May (Fig. 4.3c). For each hydrographic station position the closest WOA temperature profile is extracted. No interpolation is applied to the extracted WOA profile to account for the discrepancy in position between the cruise CTD and WOA position. There are therefore discontinuities in the WOA temperature section caused by shifts in the

latitude of extracted profiles, for example at 69°W and 14°W. The WOA climatological isotherms are much smoother than those in the cruise and Argo derived sections.

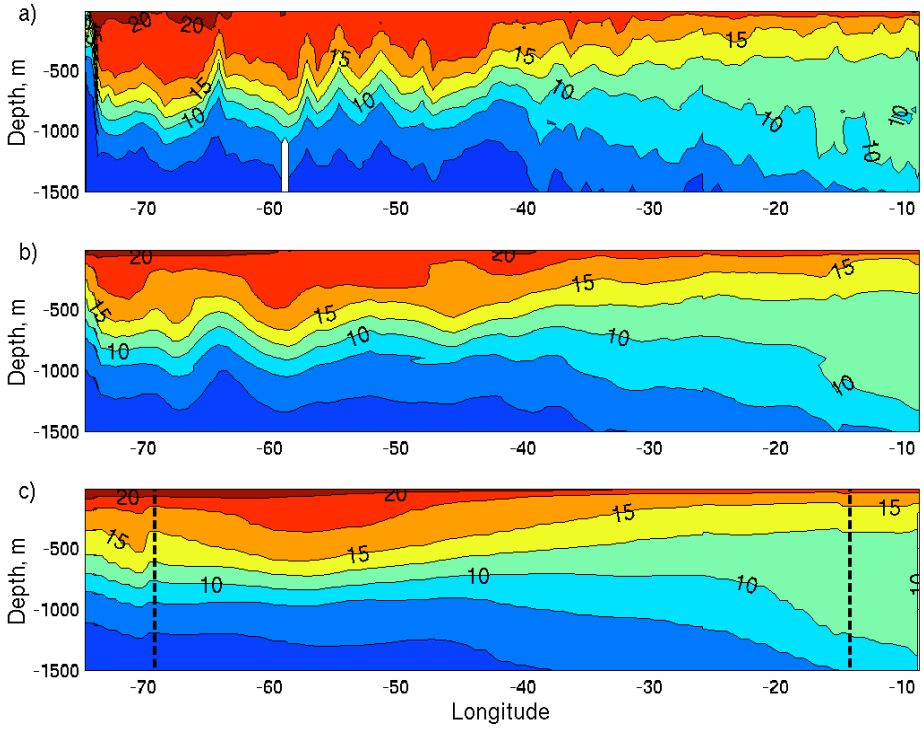


**Figure 4.3** The temperature section across 36°N for a) the hydrographic CTD section, b) the Argo-based temperature section and c) the WOA temperature section. Contour intervals of 2.5 °C.

In order to quantify the level of agreement between the Argo derived temperature field and the hydrographic measurements, difference plots of the Argo based and WOA temperature fields relative to the cruise values are shown in Fig. 4.4 a) and b), respectively. For each subplot, there are two panels; the upper panel shows the differences over the upper 100 m and the lower panel shows the differences between 100 and 1500 m. This method of plotting is employed to show the results over the upper 100 m in more detail. Before differencing, a 300 km running average was applied to the cruise data. This averaging removes some of the finer-scale structure captured by the hydrographic section, which the Argo dataset cannot resolve. The difference between the hydrographic section and a temperature field obtained by applying the OI scheme to all the CTD station data (with the

WOA as a first guess) in place of Argo profile data is also shown. The latter calculation was carried out to give an indication of the errors associated with the OI scheme.

Over much of the section, the Argo based estimates of temperature agree with the cruise measurements to within 0.5 °C. The agreement between the cruise and Argo-based temperature section is particularly good in the upper 100 m (Fig. 4.4a, upper panel). However, there are several regions, particularly in the 500 – 1000 m layer west of 40°W where the differences exceed 0.5 °C (Fig. 4.4a, lower panel). Furthermore at the western boundary, west of 72°W, the temperature is more than 2 °C warmer in the Argo section than in the cruise section. The climatological values from the WOA typically show larger differences from the cruise section than the Argo based sections, particularly in the surface waters across the section (Fig. 4b, upper panel) and the upper 1200 m at 65-73°W.

The difference field in Fig. 4.4c provides a measure of the uncertainty introduced by application of the OI scheme; the differences are much smaller than those resulting from the use of the Argo or WOA datasets, with values less than 0.5 °C across the basin, except in the region west of 72°W. This suggests that most of the error results from under-sampling and not from smoothing in the interpolation scheme. The larger values in the western boundary are caused by smoothing of temperature features with scales shorter than the length scales applied in the interpolation.

The level of agreement between the cruise temperature field and the Argo estimate of the temperature field has been further quantified by calculating the RMS difference as a function of station number averaged over both the 0-1500 m and the 0-100 m depth interval (Fig. 4.5a). The mean RMS difference between 0 – 1500 m and across the whole section for the Argo based estimate is 0.58 °C, while RMS differences at hydrographic stations in the Gulf Stream are more than 2 °C. These RMS differences are lower than those found when the hydrographic data are compared with the WOA climatological values, for which the section average RMS difference is 0.81 °C. For the upper 100 m, the improvement with Argo is more dramatic, the RMS differences being 0.56 °C compared to 1.13 °C for the WOA. Thus, the Argo based temperature estimates across the section are in better agreement with the hydrographic measurements than the WOA climatology indicating that

they are capable of providing useful information about temperature variability at this latitude. As a measure of the uncertainty introduced by the interpolation, the RMS difference of the interpolated cruise section relative to the original measurements is typically 0.29 °C, with largest differences in the western basin.

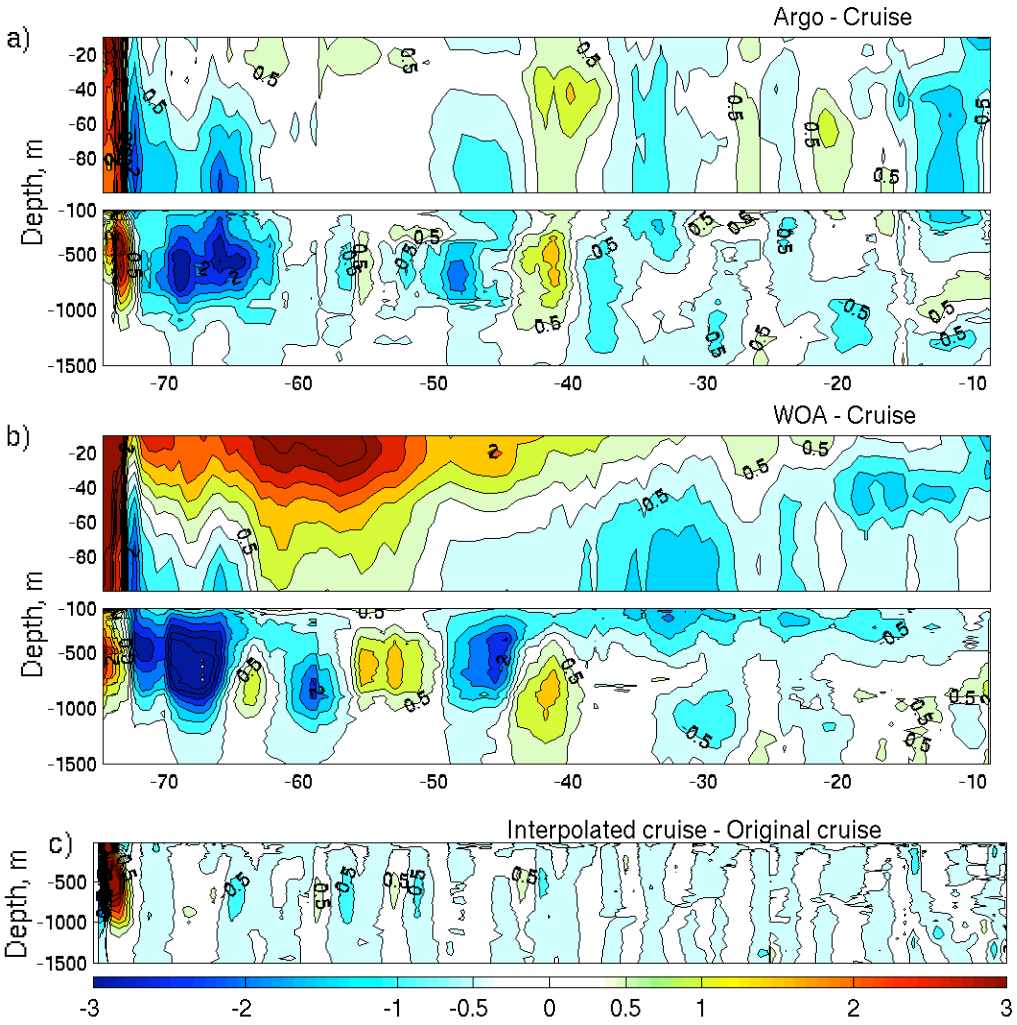


**Figure 4.4** Temperature section difference plots with respect to the hydrographic section data for a) Argo – hydrographic temperature data, b) WOA based estimates – hydrographic temperature data and c) hydrographic section created by applying the OI scheme to the cruise CTD section – original hydrographic section. Contours are -4 °C to 4 °C in 0.5 °C increments.

To test for bias in the Argo-based temperature field, the depth averaged temperature difference between the Argo and cruise section is considered (Fig. 4.5c). The temperature difference fluctuates around zero, with regions of both positive and negative values. The mean difference between 65-10°W (i.e. ignoring the western part of the section which Argo is incapable of fully resolving) is small, only -0.05 °C. The mean difference in this part of the section over the upper 100 m is also small, 0.07 °C.

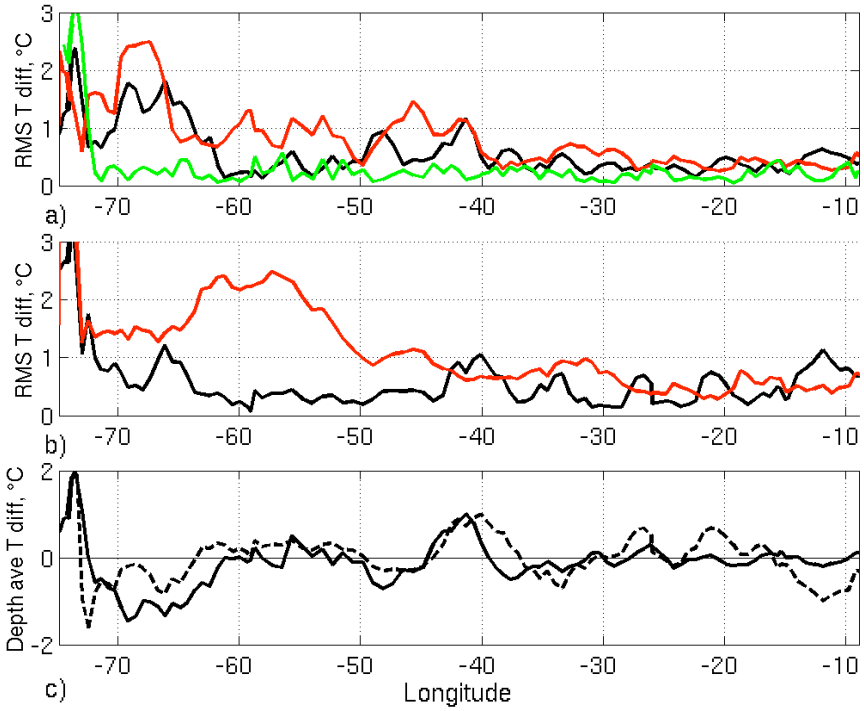


**Figure 4.5** Depth-averaged differences across the section showing a) RMS difference over 0 – 1500 m between the cruise section and i) the Argo based section (black), ii) the WOA based section (red) and iii) the interpolated cruise CTD section (green), b) RMS difference over 0 – 100 m between the cruise section and i) the Argo based section (black) and ii) the WOA based section (red) and c) the mean difference between the cruise section and Argo based section over 0-1000 m (solid black) and the upper 100 m (broken black).

This above analysis reveals agreement between the hydrographic and Argo based temperature fields to within 0.5 °C in the eastern basin but with higher differences in the

western basin. Differences were particularly high within the boundary current, exceeding 2 °C. Nevertheless, the difference between the hydrographic and Argo values was smaller than the difference between hydrography and values from the WOA climatology. This improvement was particularly large in the upper 100 m, where the WOA RMS differences were more than twice as large as those from Argo, 1.13 °C, compared to 0.56 °C. This result indicates that Argo data is useful for capturing variability in the temperature field across zonal sections in the absence of a dedicated research cruise and thus demonstrates the potential for using Argo to monitor changes in ocean properties. It is anticipated that this result will hold for other regions of the North Atlantic with similar sampling densities and thus that Argo offers exciting possibilities for investigating temperature variability in the upper ocean, which may be linked to changes in the meridional overturning circulation (Bryden et al., 2005).

### 4.2.3 Satellite Data Analysis

Both the hydrographic section and the Argo dataset may sample mesoscale features, but such features cannot be fully resolved by Argo. The combined sampling and interpolation errors estimates of the Argo based temperature field discussed above therefore represent an upper limit. The infrequency of repeat hydrographic sections restricts quantification of errors arising from this source. However, examination of satellite fields can provide some indication of the mesoscale variability during periods when hydrographic sections are occupied and this is briefly considered here.

A longitude-time plot of altimeter data (Aviso live access server, 2006) at 36°N throughout 2005 is shown in Fig. 4.6. The plot reveals anomalously low Sea Surface Height (SSH) centered on 64°W and 72°W during the cruise period. These features are 200-300 km across, persist for a period of around 2 months and exhibit negative SSH anomalies of more than 10 cm. These characteristics are consistent with cyclonic circulation and anomalously cool ocean temperatures resulting from the doming of isothermal surfaces. Such temperature features can be observed in the cruise section (Fig. 4.3a) and to a lesser extent, in the Argo-based section (Fig. 4.3b). The doming of isotherms at 64°W is particularly notable, doming at 72°W is less distinct. Weaker negative SSH

anomalies (of around 5cm) are evident at 51°W and 54°W and also correspond to doming isothermal surfaces in the cruise section. These individual features are smoothed in the Argo-based section. These observed features are consistent with cold-core eddies or meanders of the Gulf Stream (Richardson, 1983).

Thus it is evident that the larger temperature errors in the western basin arise from mesoscale eddies resolved by the cruise section, which cannot be fully resolved by Argo. Such features are transient features and do not represent an annual or seasonal mean. It is therefore argued that the lower temperature errors of 0.3 °C in the eastern basin (where mesoscale eddies are not present) provide a truer representation of the sampling errors associated with using the Argo dataset to obtain the temperature field on annual time scales.

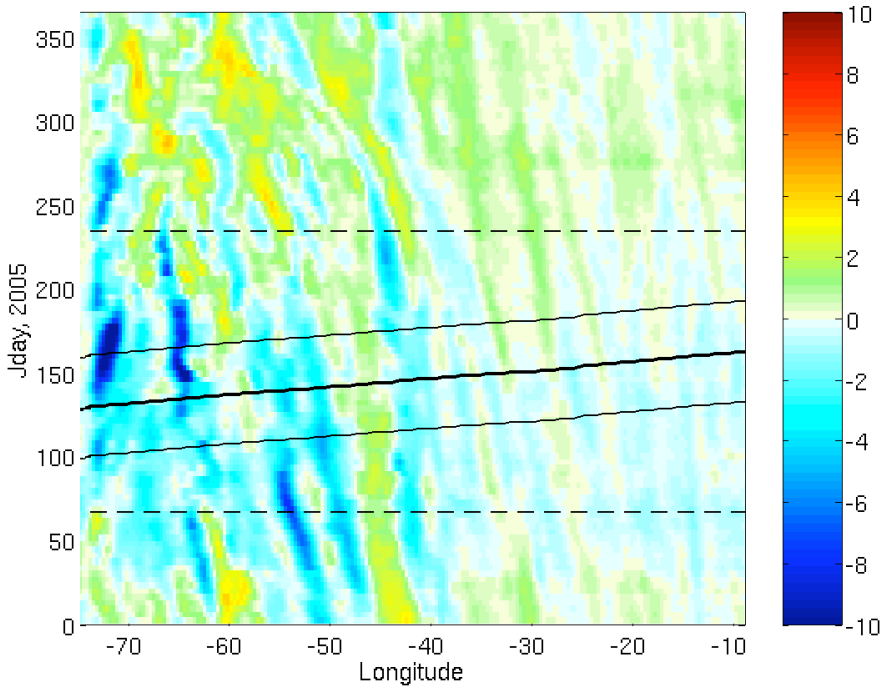


**Figure 4.6** Hovmöller plot (longitude-time) of altimeter sea surface height anomaly at 36°N, units in cm. The lines indicate the period of the cruise (thick solid) ± 30 days (thin solid) and the time span (dashed lines) of the Argo floats interpolated to estimate the temperature across the section.

## 4.3 Accuracy of Argo Derived Heat Storage Estimates

### 4.3.1 Introduction

The analysis of the 36°N cruise section provided an indication of likely errors in Argo based estimates of the ocean temperature in relatively well sampled regions. In this section, the accuracy of Argo based estimates of heat storage is investigated. In the absence of detailed observational estimates of heat storage, a model-based approach is adopted, using the eddy permitting Ocean Circulation and Climate Advanced Model (OCCAM) (chapter 2).

As in chapter 3, the full model temperature field is subsampled to the Argo resolution and then interpolated onto a regular monthly 2° x 2° grid using the OI scheme with the WOA monthly fields as a first guess. This is done for all months between January 2000 and December 2003. The subsampled interpolated temperature field and the full OCCAM temperature field are then used to obtain estimates of the upper ocean heat storage. The difference between the heat storage estimated from the full and subsampled, interpolated temperature field is indicative of the combined error associated with the sampling limitations of Argo and the OI scheme. Errors arising from sensor drift will not be included. It was shown in the previous section that this error is small in comparison to other sources of error.

Although the version of the OCCAM model used in this study has a horizontal resolution of 0.25°, in view of the computationally demanding matrix inversion performed in the OI and the resolution of the Argo array, the subsampled data was interpolated onto a 2°. For consistency the full OCCAM temperature field was also subsampled to a 2° grid, henceforth this field is referred to as the fully sampled field to avoid confusion with the subsampled and then interpolated field (referred to simply as the subsampled field). Both the fully sampled and the subsampled heat storage estimates (henceforth referred to as $HS_{full}$ and $HS_{sub}$) are averaged into 10° x 10° boxes before comparisons are made. In the following, calculations of upper ocean heat storage are discussed in section 4.3.2 and comparisons of $HS_{full}$ and $HS_{sub}$ are detailed in section 4.3.3.

4.3.2 Estimating the upper ocean heat storage

In this section the error associated with estimating the monthly upper ocean heat storage from a dataset with the spatial and temporal sampling of Argo is investigated. That is the error associated with

$$\rho C_p \left[ h \frac{\partial T_a}{\partial t} + \frac{\partial h}{\partial t}(T_a - T_{-h}) \right] \tag{4.1}$$

where $h$ is the depth of the upper layer; $t$ time; $T_a$ the temperature vertically averaged between the sea surface and depth -$h$; $T_{-h}$ the temperature at depth -$h$; $\rho$ the potential density and $C_p$ the specific heat capacity. In this study, $\rho$ and $C_p$ are set to constants of 1027 kg m$^{-3}$ and 3986 J kg$^{-1}$ °C$^{-1}$, respectively. For simplicity, this term is referred to as the heat storage, although it is strictly speaking heat storage tendency plus the entrainment of heat arising from temporal variations in the depth of the defined upper ocean (the first entrainment term identified in equation 1.3, chapter 1). As will become apparent in later chapters, with the exception of the net heat flux these two terms are the largest contributors to the seasonal heat budget throughout the North Atlantic.

In the literature, different definitions for the depth of the upper layer, *h,* have been utilised in heat budget analyses. Foltz and McPhaden (2005), Foltz et al. (2003) and Wang and McPhaden (1999) prescribe *h* to be the depth of the mixed layer. Moisan and Niiler (1998) tested two different values for *h*, in the first *h* was set to a constant 300 m, while in the second *h* was the time varying depth of an isothermal surface which is deeper than the mixed layer throughout the year. Various other studies of the upper ocean heat budget have also set *h* to an isothermal surface (Stevenson and Niiler, 1983, Godfrey et al., 1999 and Roemmich et al., 2005) and a fixed depth (Lamb and Bunker, 1982; Hsiung et al., 1989).

There are advantages to each of these definitions of the upper ocean. Taking *h* to be the Mixed Layer Depth (MLD) is expected to minimise errors in $\rho C_p h \frac{\partial T_a}{\partial t}$. This is because both the fixed depth and isothermal surface are defined as being deeper than the mixed layer depth throughout the year. Thus, the mixed layer method integrates

temperature errors (which are generally correlated throughout the water column, Fig. 4.4a) over a shallower depth. Despite larger errors in $\rho C_p h \frac{\partial T_a}{\partial t}$ when $h$ is defined as the depth of an isothermal surface, such a surface approximates a material surface so that entrainment terms are minimised. Defining $h$ in this way therefore allows these terms, which are difficult to quantify accurately, to be neglected (Stevenson and Niiler, 1983). Setting $h$ as a fixed depth, avoids difficulties that arise in defining and identifying the mixed layer and isothermal layer depths and enables comparison with existing studies in the North Atlantic. When considering the heat budget over a fixed layer it is important to consider the part of the water column over which seasonal heating and cooling occurs.

In this analysis, each of these definitions for $h$ is considered. For the MLD case, $h$ is defined as the depth at which the temperature is 0.2 °C cooler than the temperature at 10 m. This is the MLD definition proposed by Montegut et al. (2004) after visual inspection of profiles with global coverage and from all seasons. Montegut et al. (2004) tested a range of threshold temperature values including 0.5 °C and 0.8 °C. Their results indicated that the 0.5 °C and 0.8 °C MLD criterion were not sensitive enough to capture the spring restratification. It should be noted that at high latitudes (north of 50°N), where the MLD is controlled by salinity and temperature, the MLD defined by temperature variations alone is likely to be erroneous. Montegut et al. (2004) found MLD from a temperature criterion was underestimated in the subpolar North Atlantic, with respect to MLD defined using a density criterion.

The MLD is estimated from individual profiles for both the subsampled and full sampled model temperature fields. The subsampled MLD field is interpolated onto a regular grid using the MLD of all profiles within the correlation length scale (500 km) as the first guess. There are therefore gaps in the interpolated MLD at grid points with no data within this radius. These gaps are filled using a mean seasonal cycle MLD (calculated from the 4 year time series). Any remaining gaps are then filled by spatial interpolation.

For the isothermal analysis, the chosen isotherm is defined for individual 10° x 10° boxes as the shallowest isotherm which remains deeper than the MLD throughout the year and which does not outcrop locally. For example, the isothermal layer is defined as the

upper water column to the depth of the 15 °C isotherm at 30-40°N, 45-35°W and to the 0 °C isotherm at 50-60°N, 55-45°W. The fixed depth is defined here as the upper 300 m since the effects of the seasonal cycle are largely restricted to this layer in the North Atlantic (Curry and McCartney, 2001).

### 4.3.3 Results

a) Annual Mean Comparison

In order to show the spatial variation of the error associated with subsampling, the RMS differences between the monthly heat storage determined from the subsampled and fully sampled OCCAM temperature fields is calculated for 10° x 10° boxes centred on 2° x 2° boxes within the study region. The mean spatial RMS differences over a one year period (2002) are shown in Fig. 4.7. For the heat storage over the mixed layer, the RMS difference shown is the combined heat storage and heat entrainment RMS difference. The RMS differences between $HS_{full}$ and $HS_{sub}$ are lowest in the subtropical North Atlantic using the MLD definition for *h*, with values of less than 10 $Wm^{-2}$ at 15-25°N, 70-50°W and less than 20 $Wm^{-2}$ south of 35°N and west of 30°W. In comparison, RMS differences for the heat storage over the upper ocean to an isothermal layer and a fixed depth are typically larger, between 20 and 50 $Wm^{-2}$ in the same region.

The annual mean RMS difference between $HS_{full}$ and $HS_{sub}$ typically shows an increase with latitude and highest values in the western basin for all definitions of the upper ocean. The RMS differences over the mixed layer exceed 100 $Wm^{-2}$ in the Labrador and Irminger Seas. In this region the RMS differences are lowest for the heat storage calculated over the upper 300 m (Fig. 4.7b). The RMS differences for the heat storage over the isothermal layer are large in this region due to the large depth of the chosen isothermal surface. The mean MLD is not particularly deep in the Labrador and Irminger Seas with values around 300 m. However, the annual range in MLD is of a similar magnitude to this. Thus, it is anticipated that the high RMS differences between the mixed layer $HS_{full}$ and $HS_{sub}$ in this region and elsewhere in the subpolar North Atlantic arise from difficulties in estimating both the temperature and the MLD.

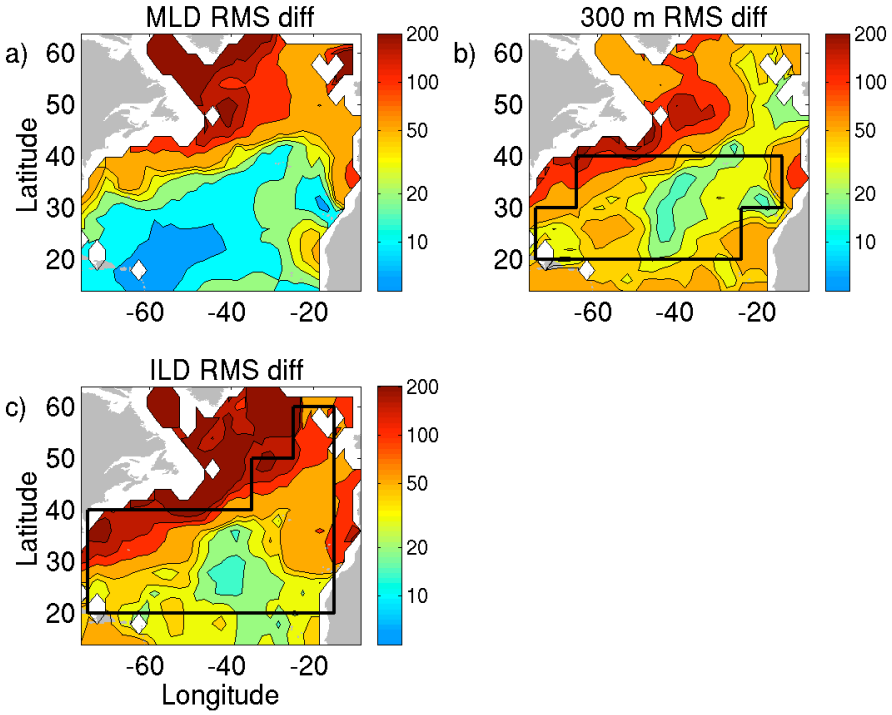


**Figure 4.7** Annual mean RMS difference between the subsampled and fully sampled OCCAM temperature field estimates of monthly heat storage for 2002 over a) the mixed layer, b) the upper 300 m and c) the isothermal layer. The scale is logarithmic, with values in $Wm^{-2}$. The contour intervals are 10, 20, 30, 40, 50, 100, 150 and 200 $Wm^{-2}$. The 10° x 10° boxes contained by the subtropical subset and the main North Atlantic region are outlined in b) and c), respectively.

b) Comparisons of $HS_{full}$ and $HS_{sub}$ Throughout One Seasonal Cycle

Time series of heat storage obtained from the fully sampled and subsampled temperature fields for each 10° x 10° box in the North Atlantic are shown in Fig. 4.8. Only the mixed layer heat storage is considered in this section. A clear seasonal cycle in the mixed layer heat storage is evident in the majority of the boxes considered with small increases during summer and larger reductions during winter. The physics of the seasonal cycle are discussed in more detail in chapter 6. In many regions, differences between the heat storage over the mixed layer calculated from the subsampled and the fully sampled OCCAM temperature fields are small, of the order 10-20 $Wm^{-2}$. This indicates that the

lower resolution associated with the Argo based subsampling does not introduce serious errors into the retrieved heat storage. RMS differences are particularly low in the area 20-30°N, 75-25°W and 30-40°N, 55-15°W (outlined in Fig. 4.7 b), henceforth referred to as the subtropical subset. However, further north and west the differences may exceed 50 $Wm^{-2}$, particularly in the winter when the mixed layer is deep. In view of expected underestimate of the MLD in this region (due to the use of a temperature criterion to define the MLD), it is likely that these errors are underestimated.

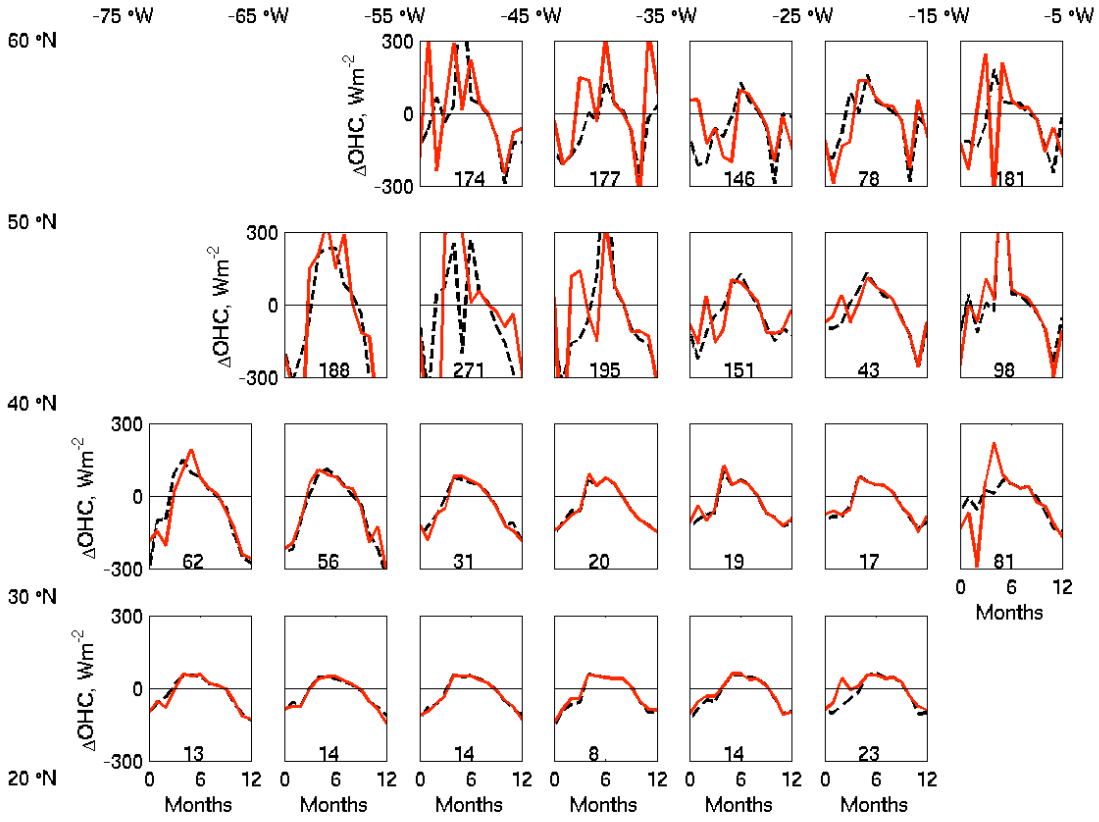


**Figure 4.8** Time series of mixed layer heat storage in $Wm^{-2}$ for different 10°x10° boxes in the North Atlantic. The red line is based on model temperature data which was subsampled at the Argo float locations and interpolated, while the broken line is based on fully sampled model data. The annual mean RMS difference between $HS_{full}$ and $HS_{sub}$ is given on each subplot.

The boxes covering the region 40-50°N, 65-35°W and 50-60°N, 55-25°W show largest differences between heat storage estimated from the 2 different temperature fields. The heat storage in this region extends off the vertical scale in Fig. 4.8 with values exceeding 900 $Wm^{-2}$ and 600 $Wm^{-2}$ based on the subsampled and fully sampled temperature fields, respectively. In view of these large errors, it is unlikely that the Argo dataset will be useful for heat budget investigations on these scales in this region, with errors in the heat storage larger than the annual range.

## 4.4 The Relationship Between the Accuracy of Argo-Based Heat Storage Estimates and Sampling

Having examined the likely uncertainty in heat storage estimates due to sampling at the Argo resolution, the relationship between this uncertainty and the number of Argo profiles available for analysis is now investigated in more detail. In order to do this, the OCCAM model has been randomly subsampled to different data densities. The sampling densities considered span the range 50 – 480 profiles per 10° x 10° box per year. This is equivalent to 42 - 420 floats in the North Atlantic. This range was chosen to cover the Argo float density during 1999 (110 floats) and the Argo target float density (344 floats). A total of ten sampling densities are considered at regular intervals (42 floats, 84 floats…, 420 floats). For each of the ten sampling densities, the OCCAM temperature field is randomly subsampled ten times and interpolated onto the full model grid using the OI scheme. RMS differences between $HS_{full}$ and $HS_{sub}$ were then calculated for each of the sampling densities to give some indication of the likely heat storage errors. These calculations were carried out for 10° x 10° degree boxes in the main North Atlantic region and in the subtropical subset, outlined in Fig. 4.8 b) and c), respectively. The subtropical subset includes the majority of 10° x 10° boxes south of 40°N, excluding only the eastern-most boxes and the box at 20-30°N, 75-65°W, through which the Gulf Stream flows. The main North Atlantic region excludes those areas where errors in mixed layer heat storage exceed 100 $Wm^{-2}$, covering the 10° x 10° boxes at 20-40°N, 75-15°W, 40-50°N, 35-15°W and 50-60°N, 25-15°W. This analysis is only carried out for the heat storage over the mixed layer. While the errors in the heat storage over a fixed- and isothermal- layer are expected to be higher, it is

anticipated that the relationship between the sampling rate and the magnitude of the errors will be qualitatively similar for other definitions of the upper ocean. The results are shown in Fig. 4.9.

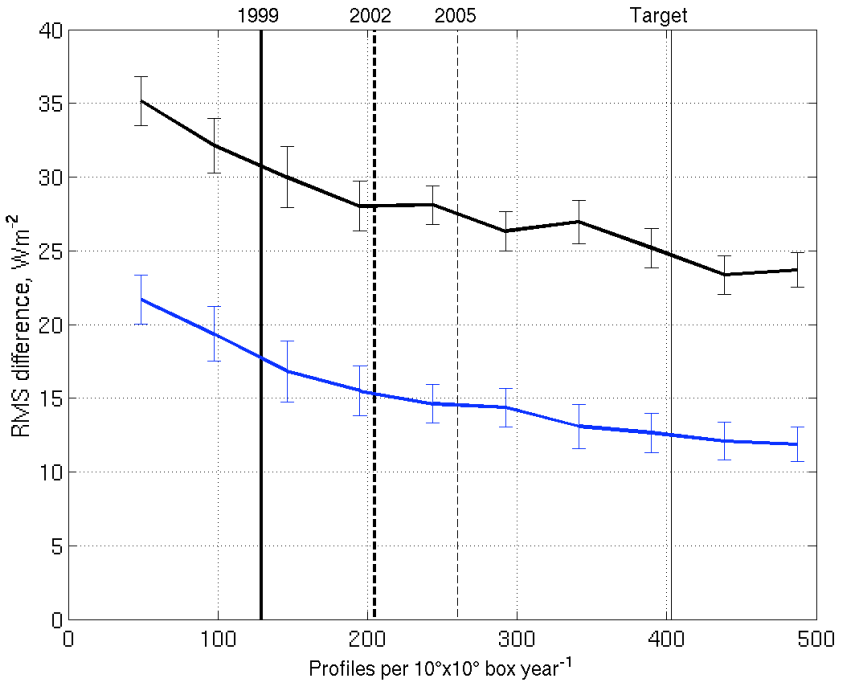


**Figure 4.9** Variation in RMS difference between $HS_{full}$ and $HS_{sub}$ over the mixed layer, with number of profiles for the main North Atlantic (black) and the subtropical subset (blue). Note the 1999 (thick), 2002 (thick broken), 2005 (thin broken) and target Argo profile numbers (thin) are also shown. Error bars are two times the standard error.

The RMS difference between $HS_{full}$ and $HS_{sub}$ for the main North Atlantic region at the Argo target density is 25 ± 1 $Wm^{-2}$. In contrast, the RMS differences for the subtropical subset are smaller and fall by about a third from 18 $Wm^{-2}$ at the 1999 Argo distribution to 12 $Wm^{-2}$ at the target number of Argo floats. The error bars at each given sampling density typically span 3-4 $Wm^{-2}$, indicating that the spatial distribution of profiles, as well as the number of profiles, affects the accuracy of Argo based heat storage estimates. The difference in sampling uncertainty obtained for the main North Atlantic region and the subtropical subset highlights the need for an array which is not simply random in nature but

which addresses the requirements of a higher sampling density in regions of higher temperature variability.

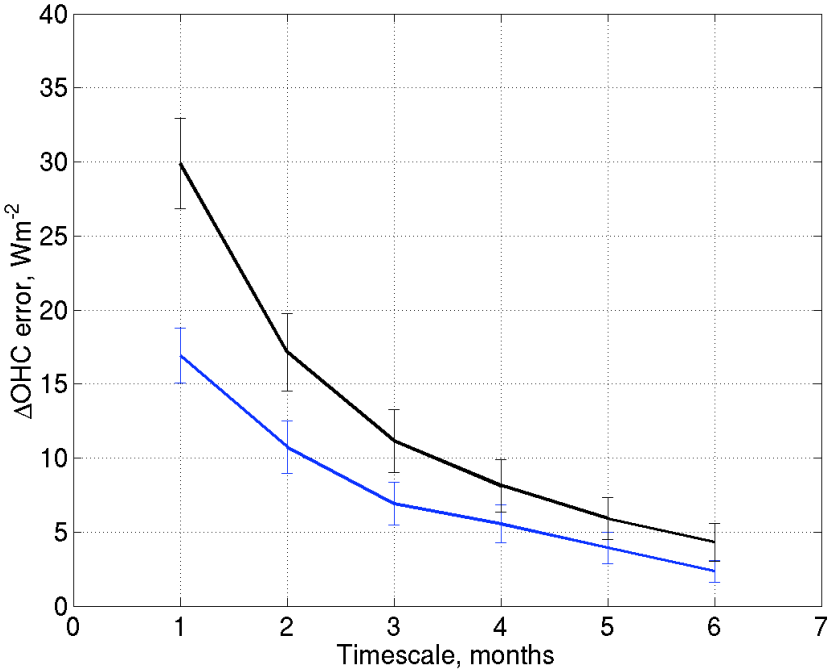


**Figure 4.10** Variations in RMS difference between $HS_{full}$ and $HS_{sub}$ over the mixed layer, with temporal scale over which the storage is estimated. Results are plotted for the main North Atlantic region (black) and the subtropical subset (blue). Error bars show twice the standard error.

In order to further improve the accuracy of heat storage estimates one can increase the time scale over which the storage is calculated. The relationship between heat storage estimates and this time frame is investigated to quantify the reduction in error with time. Again, this analysis is only carried out for the mixed-layer heat storage, but the results are expected to be qualitatively similar for other definitions of the upper ocean. Using all 4 years (2000 – 2003) of fully sampled and subsampled model temperature data the heat storage is estimated over periods ranging from 1 to 6 months. The RMS differences between $HS_{full}$ and $HS_{sub}$ at different temporal resolutions are plotted in Fig. 4.10. For the main North Atlantic region the error in mixed layer heat storage reduces from 29±3 $Wm^{-2}$ at monthly time scales, to 12±2 $Wm^{-2}$ for seasonal (i.e. 3 monthly) heat storage and 4±1

$Wm^{-2}$ at biannual scales. Results in the subtropical subset show mean RMS differences of 17±2 $Wm^{-2}$, 7±1 $Wm^{-2}$ and 2±0.5 $Wm^{-2}$ for heat storage at monthly, seasonal and biannual scales, respectively.

It should be noted that the reduction in RMS differences over time is not linear, rather it exhibits a more exponential decrease. This indicates that the physical processes resolved at monthly time scales differ from those resolved at seasonal, and longer, time scales. In particular the full magnitude of the annual cycle is not captured at seasonal timescales.

### 4.5 Model-based Error Estimation

The inclusion of error estimates is necessary in climate change studies to assess the significance of observed trends. A model-based approach has been used in this chapter to obtain insight into the likely Argo-based heat storage errors. In view of the main aim of this thesis (to quantify all heat budget components), it is also constructive to estimate the errors in the MLD and the temperature field using the same approach. Thus, given additional information on the errors in the velocity field (chapter 5.4.2), the errors in all heat budget components can be determined.

It is possible to use the error variance output from the OI scheme utilized in this study to quantify the uncertainty in various parameters (Böhme and Send, 2005). However, conversion of the error variance to errors at different time and space scales is not elementary (note for example the non-linear reduction in errors with increasing time scales shown in Fig. 4.10). For this reason, error estimates for the heat storage, temperature and MLD are obtained by direct comparison of the full and subsampled model values. Although this method provides only an estimate of the combined sampling and OI error, these are the dominant sources of error (the instrumental was shown to be small in section 4.2).

In view of the magnitude of the heat storage errors discussed in the preceding sections, the focus here is on the errors in seasonal (3-monthly) fields. Comparison of the temperature and MLD from the full sampled model and the subsampled model, indicates that the accuracy of these variables varies spatially and temporally. For simplicity, in this study an average value is used to represent the error in the temperature and MLD at each 10° x 10° box. In order to capture some of the temporal variability, the error in the MLD is

defined as a percentage of the MLD. The uncertainty in the MLD and temperature is smallest in the subtropical North Atlantic. Here the errors are typically less than 10 % for the MLD and around 0.10 °C for the upper ocean temperature. Elsewhere in the North Atlantic the uncertainty in the MLD can exceed 20 %, with largest errors in the Gulf Stream and subpolar regions. Largest errors in the temperature field exceed 1 °C, but are typically less than 0.5 °C.

### 4.6 Summary

In this chapter, the suitability of the Argo profiling float dataset for analysing variability in the North Atlantic has been investigated. In particular, the limitations placed by the number of available floats on the accuracy with which Argo can be used to estimate both the upper ocean temperature field and upper ocean heat storage have been considered.

Observations of the temperature field across 36°N obtained from a hydrographic section have been compared with the corresponding field derived for the same time as the section from Argo using an OI method. The analysis has revealed encouraging agreement, typically to within 0.5 °C, between the Argo based temperature field at 36°N and the corresponding field from a hydrographic section. This is a large improvement over using temperature values from the WOA, which have differences of more than 0.8 °C. Analysis of altimeter data suggests that this is an overestimate of the temperature error on the scales of interest, with the cruise section resolving mesoscale features which cannot be fully captured by Argo.

Subsampled temperature fields from the OCCAM model were used to gain insight into the likely sampling and OI errors associated with Argo-based heat storage estimates. It is recognized that this approach does not provide the actual total heat storage error. However, in view of the small instrumental errors expected from Argo, and given the paucity of independent heat storage estimates, the approach taken is thought to provide both a reasonable estimate of the likely error, and the best possible estimate of the likely errors in heat storage. Throughout the remainder of this study, the results of the model based analysis will be used to provide an indication of the errors in the heat storage and other heat budget components.

Analysis of subsampled temperature fields from the OCCAM model indicates that in the subtropical North Atlantic, the Argo project provides temperature data at a spatial and temporal resolution that results in a sampling uncertainty in monthly mixed layer heat storage of order 10-20 $Wm^{-2}$. This error is higher, with RMS differences between 20 and 50 $Wm^{-2}$, for the heat storage estimates over the upper 300 m and over an isothermal layer. Within the western boundary current and the subpolar North Atlantic the heat storage estimates are less accurate, with RMS differences typically exceeding 100 $Wm^{-2}$ for all definitions of the upper ocean.

The relationship between the accuracy of Argo derived upper ocean heat storage estimates and the number of floats has been investigated. An increase in the number of profiles available for use in the OI reduces the RMS difference between estimates of mixed layer $HS_{full}$ and $HS_{sub}$ by a factor of 1/3 from 18 $Wm^{-2}$ at the 1999 Argo resolution to 12 $Wm^{-2}$ at the target resolution in the subtropics. To improve the accuracy of heat storage estimates, it is necessary to increase the timescale over which storage is calculated. Seasonal mixed layer heat storage estimates in the subtropical North Atlantic are accurate to 7±1.5 $Wm^{-2}$. This error is sufficiently small that it should allow investigations of variability in this region, on these timescales. The reduction in errors associated with increasing the number of observations and the timescale over which the heat storage is calculated is expected to be qualitatively similar for the heat storage over a fixed depth and isothermal layer.

While the application of a 3-month smoothing to all heat budget components will improve the accuracy with which the individual terms can be quantified, some dampening of the seasonal signal will also occur. In order to quantify the effects of this, the difference in the annual range in the net heat flux from monthly fields both before and after a 3-month smoothing is considered. The difference in annual range as a percentage of the annual range from the unsmoothed monthly fields varied for different 10° x 10° boxes, from 4 % to 19 %, with a mean of 11 %.

# CHAPTER 5: The Heat Budget: Terms, Variables and Methodology

## 5.1 Introduction

The variables and methods used to quantify the heat budget components on seasonal scales are outlined in this chapter. The physical processes that need to be considered in an analysis of the upper ocean heat budget include the local heat storage, the horizontal advective heat divergence, the velocity shear covariance, the entrainment heat flux, the horizontal and vertical diffusive heat divergence and the net heat flux. The entrainment heat flux comprises three components, arising from 1) temporal changes in $h$, 2) horizontal gradients in $h$ and 3) vertical advection. These terms are quantified by the heat budget equation (left to right), which was introduced in chapter 1, reiterated below**.** For details on the derivation of equation 5.1 refer to appendix A1.

$$h\frac{\partial T_a}{\partial t} + h\upsilon_a \cdot \nabla T_a + \nabla \cdot \int_{-h}^{0} \hat{\upsilon}\hat{T}dz + (T_a - T_{-h})\left(\frac{\partial h}{\partial t} + \upsilon_{-h} \cdot \nabla h + w_{-h}\right) + hk_{x,y} \cdot \nabla^2 T_a + k_{z,-h}\frac{\partial T}{\partial z} = \frac{Q + Q_{-h}}{\rho C_p} \tag{5.1}$$

where $T$ is temperature, $\upsilon$, horizontal velocity with ($u$,$v$) the eastward and northward components, respectively, $w$, vertical velocity, $h$, depth of the upper ocean, $k_{x,y,}$ horizontal and diffusion coefficient, $k_{z,-h}$, vertical diffusion coefficient across -$h$, $\rho C_p$, specific heat capacity per unit volume (with $C_p$ and $\rho$ set to constants of 3986 J kg$^{-1}$ °C$^{-1}$ and 1027 kg m$^{-3}$, respectively), $Q$, surface heat flux, $Q_{-h}$, penetrative heat flux, $\nabla \equiv (\partial/\partial x, \partial/\partial y)$ the horizontal gradient, $x$, $y$ and $z$ the eastward, northward and downward coordinates respectively and $t$, time. The subscripts $h$ and $a$ are used to indicate variables at depth $-h$ and averaged between depth $h$ and the sea surface, respectively, $\hat{\upsilon}$ is the deviation from the vertically averaged velocity field $\left(\upsilon = \upsilon_a + \hat{\upsilon}\right)$ and $\hat{T}$ is the deviation from the vertically averaged temperature $\left(T = T_a + \hat{T}\right)$.

The main variables required for an analysis of the upper ocean heat budget are the Mixed Layer Depth (MLD - often used to identify the upper ocean), the temperature, the 3-dimensional velocity field and the penetrative heat flux. These terms are derived using the Argo subsurface float dataset alongside atmospheric variables from the National Centers for Environmental Prediction/ National Center for Atmospheric Research (henceforth NCEP) reanalysis and the National Oceanography Centre (NOC) climatology. In this chapter these variables are investigated with the aim of assessing their quality.

In the following, the Argo-based MLD and subsurface temperature field are described in section 5.2 and section 5.3, respectively. The horizontal velocity field is derived in section 5.4 and the vertical velocity is quantified in section 5.5. The methods used to determine the individual heat budget terms are then outlined in section 5.6. A brief summary follows in section 5.7. Before the above analysis is carried out, the sign convention used in this study is outlined.

### 5.1.2 Applied Sign Convention and Terminology

i) A positive surface heat flux indicates ocean heat gain.

ii) Negative advective and diffusive temperature divergence denotes heat import.

iii) The process of entrainment can only cool the upper ocean, except for the rare case where the temperature beneath $h$ is warmer than the upper ocean temperature.

iv) $x$, $y$ and $z$ are positive in an eastward, northward and upward direction, respectively.

v) The phrase ‘heat budget components’ is used to refer to the individual terms in the heat budget such as the heat storage and the absorbed net flux.

vi) The phrase ‘heat budget variables’ is used to refer to the observed quantities such as the temperature and the 3-dimensional velocity field.

vii) The 2° x 2° grid refers to the locations to which individual variables are interpolated. This grid extends from 9.5°N to 69.5°N and from 84.5°W to 0.5°W. The 10° x 10° grid extends from 20 to 60°N, 75 to 5°W. The region north of 60°N and south of 20°N is not considered in this study because of the large amount of land and ice at higher latitudes and the more irregular seasonal cycle in heat storage at low latitudes.

### 5.2 The Argo-Based Mixed Layer Depth

In this study, the MLD is calculated for individual Argo profiles using a critical temperature criterion of 0.2 °C. These MLD values are interpolated onto regular monthly 2° x 2° grids using a modified version of the optimal interpolation scheme described in chapter 3. Rapid changes in the MLD that occur in response to changes in atmospheric forcing will thus not be resolved here. Such variability cannot be fully captured by the Argo dataset and aliasing of this signal may occur. However, the effect of this on the resulting MLD field is expected to be small on the timescales considered (Martin, 1995).

A map of the Argo-based wintertime maximum MLD for the period 1999 – 2005 is shown in Fig. 5.1. The wintertime maximum MLD varies from around 50 m, to more than 500 m. There is a latitudinal variation, with shallowest MLDs in the subtropics and deepest MLDs in the subpolar North Atlantic. Within the Labrador Sea the MLD can exceed 800 m during some years. This spatial trend is driven by buoyancy forcing. Imposed on this simple spatial trend is a more complex pattern with relatively deep MLDs along the path of the NAC and shallow MLDs near the Azores and off the west coast of Africa.

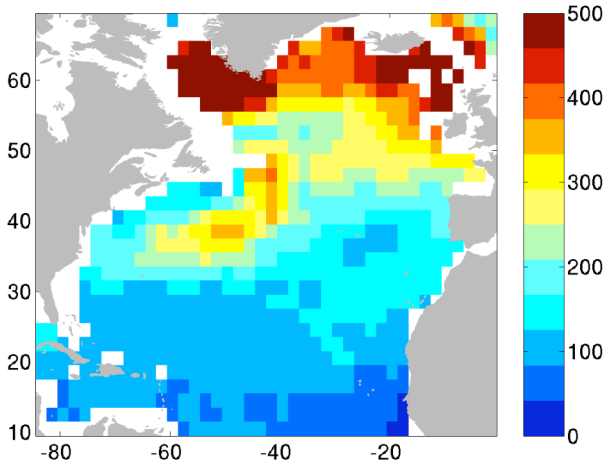


**Figure 5.1** Wintertime maximum Mixed Layer Depth (m) from seven years of Argo data, 1999 – 2005

The 7-year mean seasonal cycle in MLD for 10° x 10° boxes is plotted in Fig. 5.2. The MLD is smoothed by a three-month running mean. All boxes indicate a seasonal cycle

with deepest MLD in February or March and minimum MLD between June and August. This result is consistent with the seasonal signal presented in Montegut et al. (2004). The range of the seasonal cycle increases with latitude, from an average of 60 m at 20-30°N, to more than 230 m at 50-60°N. There is an asymmetry in the seasonal cycle with a more rapid shoaling of the mixed layer between March and May than the subsequent deepening.

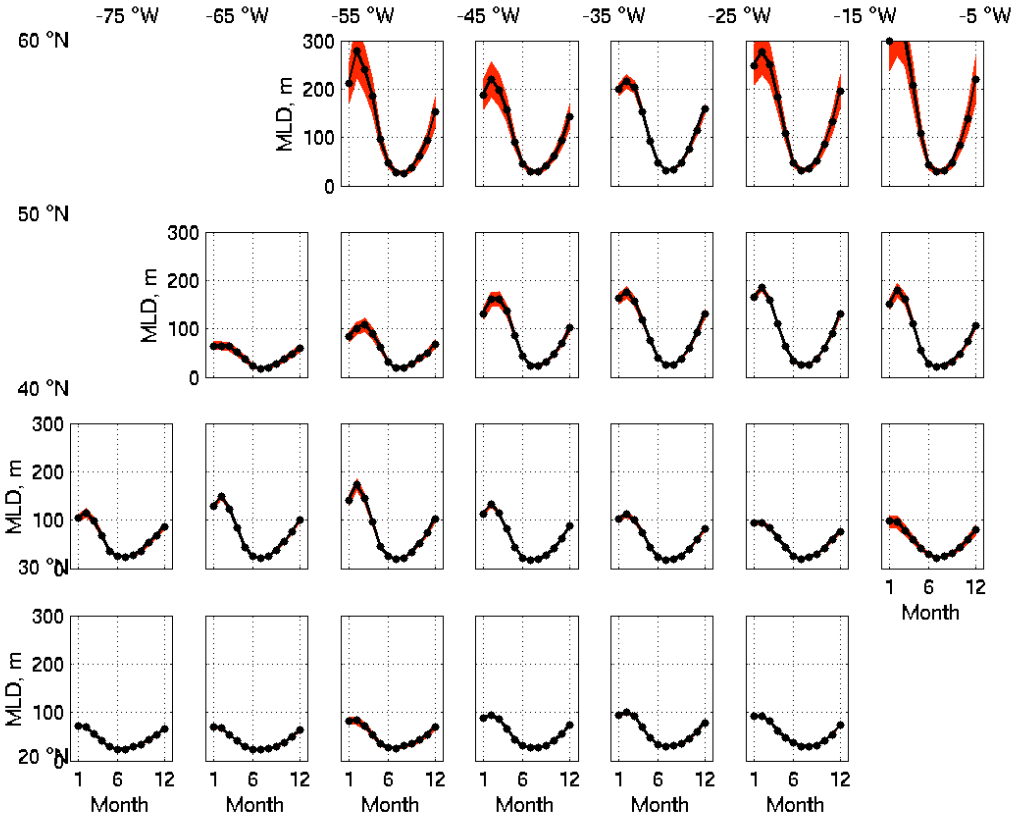


**Figure 5.2** Seasonal cycle in Mixed Layer Depth (m) for different 10° x 10° boxes throughout the North Atlantic. The red shading indicates the estimated seasonal error.

Errors in the MLD are also shown (red shading). These errors are the estimated seasonal errors for an individual year, derived using the sub-sampling model-based analysis described chapter 4.5. Errors in estimating the MLD from Argo are highest (50 - 60 m) in the subpolar North Atlantic during winter and spring and in the 10° x 10° boxes east of 15°W. The regions of high MLD errors reflect the regions of highest spatial variability.

South of 40°N the shading is difficult to identify, indicating the small errors in this region. Additional errors associated with estimating the MLD in the subpolar North Atlantic may arise due to the dependence of the MLD on the salinity, which is not considered in this study. Calculations by Montegut et al. (2004) suggest that the MLD defined using a critical density criterion in the subpolar North Atlantic may be more than 60 m deeper than the MLD defined using a critical temperature criterion.

Comparison of the Argo-based MLD with climatological values in Montegut et al. (2004) indicates similar values throughout most of the year, except during the period of maximum MLD (January to March), north of 30°N. During this time the Argo-based MLD is typically deeper than that from the climatology. This difference can exceed 50 m at high latitudes during wintertime. Montegut et al. (2004) noted that their wintertime MLDs were shallower than previous estimates. It is thought likely that this difference may arise from the limited number of deep profiles used in the climatology, particularly at high latitudes.

### 5.3 The Argo-based Temperature Field

In this section, the Argo-based temperature field covering the period 1999 – 2005 is examined. The quality of the Argo-based temperature field was established in chapter 4, the main aim here is to provide details on the spatial and temporal variability of the North Atlantic temperature field. The time-averaged 10 m in situ temperature field from Argo is plotted in Fig. 5.3 a). Only temperatures at grid points where the water depth exceeds 1000 m are shown. The primary temperature variation exhibits a cooling with increasing latitude, with a secondary east-west temperature gradient. This zonal temperature variation shows cooling from west to east south of 45°N, reversing further north. The warmest mean temperatures of more than 27 °C are found in the Caribbean Sea and coolest temperatures of around 0 °C occur in the Labrador and Norwegian Seas. The meridional pattern in the temperature field can be explained by differential solar heating between low and high latitudes, while the zonal patterns arise from the mean ocean circulation in which relatively warm waters are transported northwards in the western boundary current (which separates from the coast at the Grand Banks, close to 45°N).

The mean Argo-based temperature field at 1000 m is plotted in Fig. 5.3 b). The spatial temperature distribution exhibits warmest temperatures of around 12 °C off Western Europe in the mid latitudes. Cooler water is found to the south and coldest water temperatures of less than -0.5 °C occur in the Norwegian Sea. This temperature distribution results largely from the inflow of warm Mediterranean Water into the Eastern North Atlantic basin. At low latitudes northward flowing Antarctic Intermediate Water may account for the relatively cool temperatures.

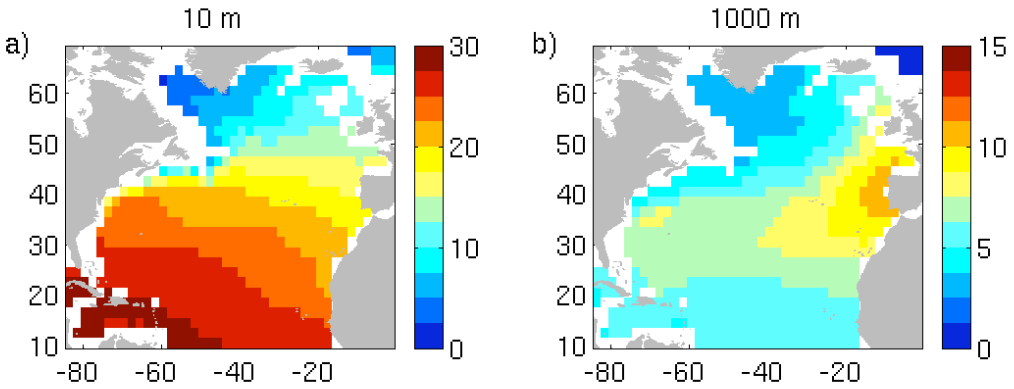


**Figure 5.3** Average temperature (°C) based on seven years of Argo data from 1999 – 2005 at a) 10 m and b) 1000 m.

With regards to the heat budget (equation 5.1), the required temperature terms include $T_a$, the mean temperature of the upper ocean and $T_{-h}$, the entrainment temperature. The entrainment temperature is taken here to be the temperature at the depth bin below $h$. In the following analysis of the heat budget, 2 definitions for the upper ocean are considered; the mixed layer, in which $h$ is the temporally and spatially varying MLD and a fixed depth, in which $h$ is set to 300 m (since seasonal temperature variations are largely confined to this layer). Although discussed in chapter 4, an isothermal definition of the upper ocean is not considered further in this study due to the complications associated with identifying a suitable isotherm for a region of this size.

The mean seasonal cycles in $T_a$ and $T_{-h}$ are plotted for 10° x 10° boxes in Fig. 5.3. Values are smoothed by the application of a three-month running mean. $T_a$ and $T_{-h}$ are

shown for both the MLD and fixed depth definitions of the upper ocean. The seasonal cycle in $T_a$ and $T_{-h}$ varies with the definition of the upper ocean. For the mixed-layer case there is a strong seasonal variation in $T_a$ with an annual range of more than 3 °C throughout the North Atlantic, up to almost 10 °C in the western boundary and with a mean of 5.6 °C. The annual range in $T_{-h}$ for the mixed layer definition is slightly smaller, with an annual mean of 4.6 °C. This difference in annual cycle can be explained by the close coupling of the mixed layer with the overlying atmosphere. By comparison, the annual range in $T_a$ for the fixed depth case is around 1 °C and there is no discernable seasonal signal in $T_{-h}$. The timing of the minimum and maximum upper ocean temperature also varies with the chosen definition, being slightly later for the fixed-depth case. Differences between $T_a$ (and $T_{-h}$) for the mixed layer and fixed depth definitions are most significant at low latitudes where the MLD is much less than 300 m.

With the exception of some 10° x 10° boxes in the mid-to-high latitudes in the western basin, $T_a$ is warmer than $T_{-h}$ throughout the seasonal cycle. For the mixed-layer definition the RMS difference between $T_a$ and $T_{-h}$ is 0.9 °C for the North Atlantic, this increases to 2.0 °C for the fixed-depth definition. For both definitions, the temperature discontinuity ($T_a - T_{-h}$) is largest during later summer/ early autumn when the upper ocean is most strongly stratified. There is also a spatial variation in the temperature discontinuity, with larger values in the eastern basin. The temperature discontinuity is large in this region due to the upwelling of cold water from beneath and strong solar heating from above. The temperature discontinuity is also relatively large within the subtropical gyre, where low turbulent mixing is conducive to strong stratification.

Error estimates in $T_a$ and $T_{-h}$ are included in Fig. 5.4. These errors are obtained from the model-based analysis in chapter 4 and represent seasonal errors for an individual year. This error is typically small, with mean values less than 0.25 °C throughout much of the North Atlantic. As expected, errors are largest in the Gulf Stream region, where mean seasonal errors can reach 1 °C.

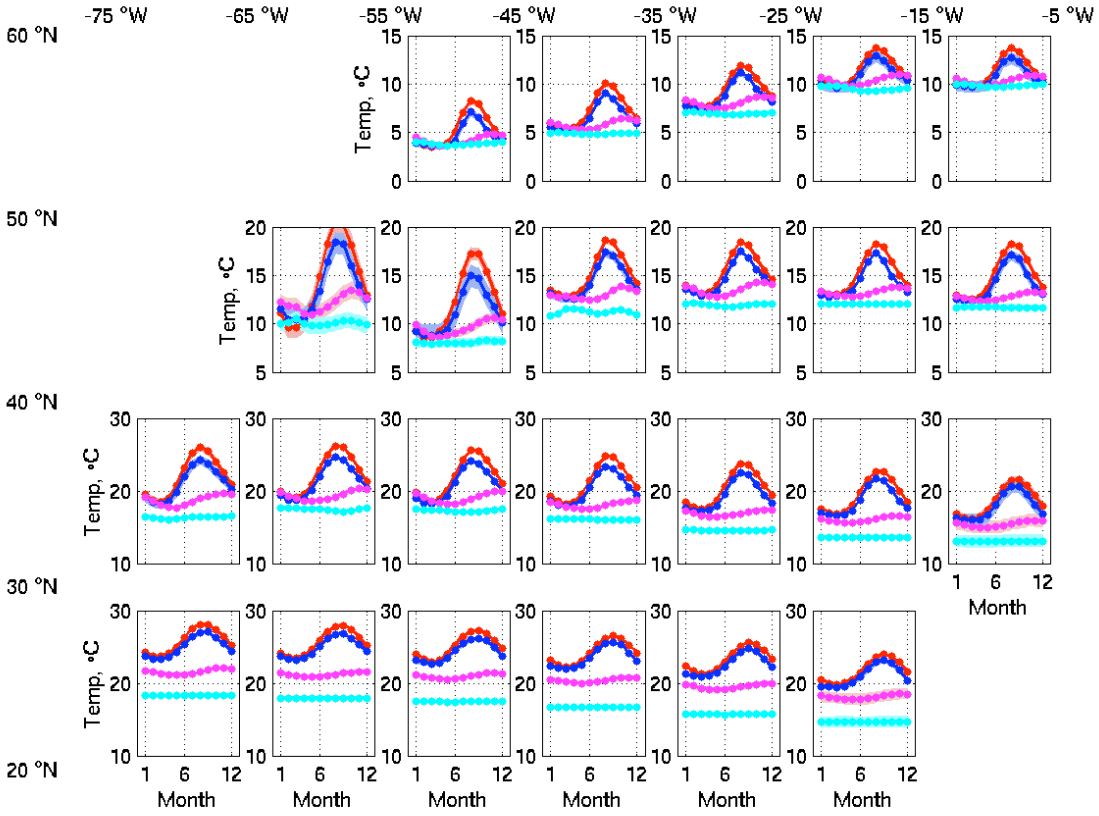


**Figure 5.4** Seasonal cycle in $T_a$ over the mixed layer (red), the upper 300 m (magenta) and $T_{-h}$ for the mixed layer (blue) and fixed depth (cyan) heat budgets for different 10° x 10° boxes in the North Atlantic. The shading indicates the errors associated with estimating the temperature variables from the Argo dataset (refer to chapter 4 for details).

## 5.4 The Horizontal Velocity Field

In this study the horizontal velocity, $\upsilon$, is split into two components; a wind driven, or Ekman, component ($\upsilon_e$) and a density driven, or geostrophic component, ($\upsilon_g$). These components are derived in subsections 5.3.1 and 5.3.2, respectively.

### 5.3.1 The Wind-driven Velocity

Horizontal wind-driven currents are confined to the upper part of the ocean, typically referred to as the Ekman boundary layer. The thickness of this layer, $Z_e$, is given by

$$Z_e = \sqrt{\frac{2A_v}{f}} \tag{5.2}$$

(e.g. Wang and Huang, 2004), where $A_v$ is the coefficient of turbulent viscosity and $f$ is the Coriolis parameter ($2\Omega \sin(\phi)$), $\Omega$ the rotation rate of Earth, $\phi$ the latitude). Typical values for $A_v$ are around 0.1 $m^2s^{-1}$ but can vary by an order of magnitude or more to either side, depending on the stability of the water column. Thus $Z_e$ varies from less than 20 m in well-stratified water columns and at high latitudes, to more than 200 m in well-mixed water in the subtropics. Since strong stratification restricts the depth of the Ekman boundary layer, it is assumed here that it is confined within the mixed-layer. Jones and Leach (1999), Verbrugge and Reverdin (2003) and Dong and Kelly (2004) made this assumption when quantifying the Ekman advective heat flux in the North Atlantic. The errors associated with this assumption are discussed in chapter 6.

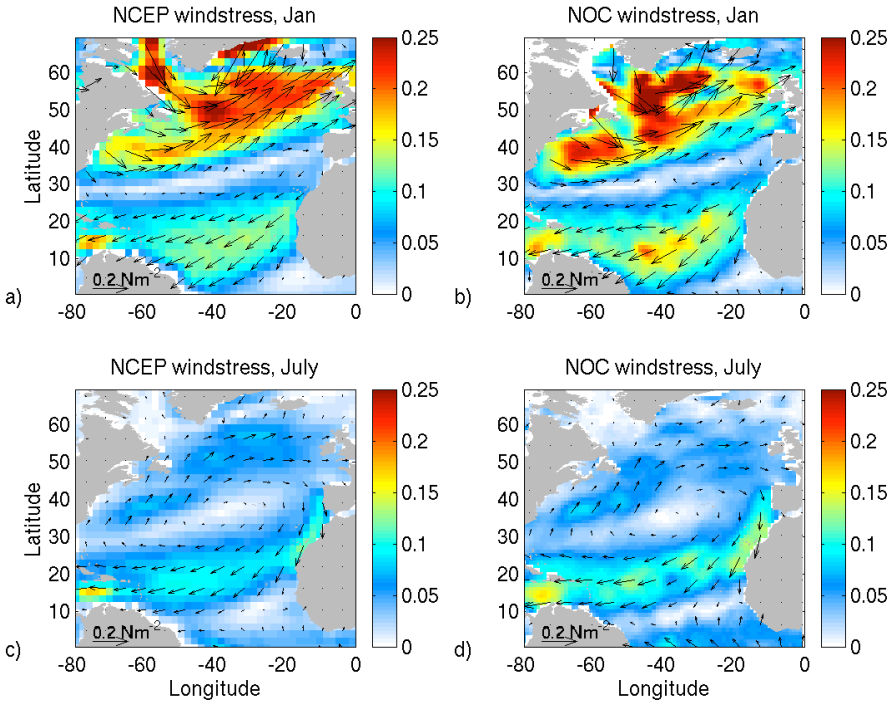


**Figure 5.5** The wind stress field from a) the NCEP reanalysis, January, b) the NOC climatology, January, c) the NCEP reanalysis, July and d) the NOC climatology, July. Units in N $m^{-2}$.

The zonal and meridional wind-driven transports, $M_x$, $M_y$, over the Ekman layer are linked to the wind stress $\tau_x$, $\tau_y$ by the following expressions

$$M_x = \frac{\tau_y}{\rho f} \tag{5.3a}$$

$$M_y = -\frac{\tau_x}{\rho f} \tag{5.3b}$$

Assuming that the depth of the Ekman layer is the depth of the mixed layer, $M_x$ is equal to $hu_{e,a}$, where $u_{e,a}$ is the eastward component of $\upsilon_e$ integrated over the mixed layer. Similarly, $M_y$ is equivalent to $hv_{e,a}$, where $v_{e,a}$ is the the northward component of $\upsilon_e$ integrated over the mixed layer. The mean temperature of the Ekman layer is to good approximation, simply the temperature of the mixed layer. Thus the Ekman heat budget term, $h\upsilon_{e,a} \cdot \nabla T_a$, is equal to $M_x \frac{\partial T_a}{\partial x} + M_y \frac{\partial T_a}{\partial y}$.

The mean wind stress fields from the NCEP reanalysis and NOC climatology during the Argo period (1999 – 2005) are plotted for comparison in Fig. 5.5. Mean values are shown for both January and July. The wind stress field is characterised by a subtropical anticyclonic gyre system which undergoes seasonal variations; the gyre centre is displaced northwards (at roughly 35°N) and is more coherent during summer. Although not clearly identifiable at this resolution, Josey et al. (2002) also note the presence of a subpolar cyclonic gyre centred around 55°N in both the NCEP and NOC wind stress fields.

During summer, differences between the NCEP and NOC wind stress fields are generally small. However, during winter, differences between the two are more evident, particularly north of 40°N. The winds in the NOC climatology are stronger and on a more westerly track off the coast of North America than those in the NCEP reanalysis. In addition, the NOC winds are stronger than those from the NCEP reanalysis in the region south of Greenland, while in the northeast Atlantic, the NCEP winds are stronger than those from NOC. The monthly temporal correlation ($r^2$) between the NCEP and NOC zonal and

meridional wind stress is calculated for individual grid cells and averaged over the North Atlantic region to give mean values of 0.83 and 0.75, respectively.

Smith et al. (2001) compared the wind speeds from the NCEP reanalysis to high-resolution quality controlled ship data. Their results showed that the winds in the reanalysis are significantly underestimated at all latitudes. Josey et al. (2002) compared the NCEP reanalysis wind stress to that from the NOC climatology and found the NCEP wind stress to be underestimated in the tropical North Atlantic. This difference can also be observed here during both summer and winter. By comparison, the NOC wind stress field showed good agreement with Woods Hole Oceanographic Institution research buoy deployments. In view of these results, it is anticipated that use of the NCEP wind stress field may lead to an underestimate of the wind driven heat divergence in some regions, particularly at low latitudes.

### 5.4.2 The Geostrophic Velocity Field

Geostrophic currents arise from the balance between the horizontal pressure gradient force and the Coriolis force. The geostrophic equation describes this balance,

$$f\upsilon_g = g\tan\alpha \tag{5.4}$$

where $g$ is the acceleration due to gravity, set to 9.8 $m^2s^{-1}$ , $\upsilon_g$ is the geostrophic velocity at a given pressure surface and $\alpha$ is the angle of the slope of the pressure surface. In principle the geostrophic equation should permit the speed $\upsilon_{g,i}$ to be obtained by measuring the slope of the isobaric surface. However, since the pressure cannot be measured with the necessary accuracy, the hydrostatic equation

$$p = -\int_{z_2}^{z_1} \rho g dz, \tag{5.5}$$

is typically used. This method gives the difference between $\alpha_1$ at level $z_1$ and $\alpha_2$ at $z_2$, providing a measure of the velocity at depth $z_1$, relative to that at $z_2$, i.e. the baroclinic

velocity. Given the absolute geostrophic velocity at a single level in the water column, the baroclinic velocity can be corrected to give the total geostrophic velocity.

In this study, the geostrophic equation and the hydrostatic equation are used with the Argo temperature field and the WOA salinity field to estimate the baroclinic velocity field. The absolute geostrophic velocity is estimated at two different reference levels; one at 1000 m and one at the sea surface. Both of these velocity reference fields are obtained using Argo float data. At 1000 m, float displacements are used to estimate the velocity, while the velocity at the sea surface is derived using a Sea Surface Height (SSH) field derived from Argo temperature and salinity data and the Bernoulli inverse method (Cunningham, 2000). Given the closer proximity of the upper ocean to the sea surface than to 1000 m, it is expected that the errors in the geostrophic velocity referenced to the surface will be smallest. Thus the total geostrophic velocity will primarily be referenced to the surface. For completeness, both of these methods and their corresponding velocity fields are discussed in more detail in sections a) and b), respectively.

There are other datasets which could be used to obtain the geostrophic velocity field, including altimeter data. However, such datasets are not considered further here since the aim of this study is to assess the usefulness of the Argo datasets in heat budget analyses.

a) The Displacement Method

The velocity field of the ocean's interior can be estimated using the positions of subsequent Argo float profiles and the time lag between them. The calculations performed in this study are relatively simple. Park et al. (2005) propose a more advanced method which uses prior assumptions about the statistics of inertial motions to improve estimates of surfacing and dive times. However, Willis suggests that the error arising from inaccurate surfacing and dive times is small relative to eddy variability (personal communication). Thus no corrections are applied to account for drift at the surface in this study.

For the calculation performed here, only floats programmed to drift at 1000 m are used, thus avoiding the application of depth corrections. The estimated velocities derived from subsequent float profile positions are averaged into 1° bins and interpolated onto a regular 2° x 2° grid using the OI scheme described in chapter 3 and a length scale of 500 km. Only the time mean velocity is discussed here; in chapter 6 time varying currents on

3-monthly scales are used. The time-mean velocity at 1000 m is shown by a vector plot in Fig. 5.6 a). The velocity field at 1000 m exhibits low current velocities, less than 0.01 $ms^{-1}$ in the subtropical gyre and stronger currents near the coastal boundaries in the western basin and along the NAC. Bathymetric steering is evident, with largest NAC velocities across the Mid-Atlantic Ridge in the vicinity of the Charlie Gibbs Fracture Zone.

The general circulation pattern from Argo presented here is in good agreement with the circulation schematic at 800 – 1000 m presented in Schmitz and McCartney (1993) and at 900 m from Kwon and Riser (2005). In addition, the flow speeds, directions and variability presented here are generally consistent with results from Lankhorst and Zenk (2006), who examined the circulation in the North East Atlantic using autonomous floats. At this location velocities range from 0 $ms^{-1}$ to more than 0.07 $ms^{-1}$ and exhibit large directional variability. The mean circulation at 1000 m depth in the Labrador Sea is in good agreement with the mean circulation at 700 m observed by Lavender (2001); strongest flows are along the coastal boundaries, with a cyclonic circulation and mean velocities around 0.05 $ms^{-1}$. However, Lavender (2001) also observed an anticyclonic countercurrent occurring to the interior of the boundary current, which is not evident here. This current is most likely smoothed by the application of 500 km length scales (Lavender, 2001 used a shorter length scale of 185 km), or is not fully resolved by the 2° resolution.

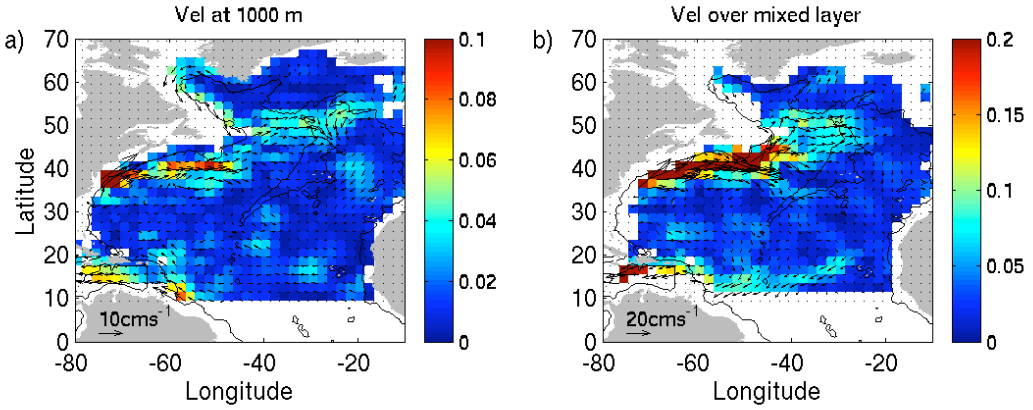


**Figure 5.6** Vector plot of the velocity field at a) 1000 m (i.e. the reference velocity) and b) averaged over the mixed layer. Velocity field derived using float displacements to obtain the reference velocity and temperature data for the baroclinic velocity component. Note the different scales used in a) and b).

The baroclinic velocity field referenced to 1000 m is added to the reference velocity to give the total geostrophic velocity. The mean geostrophic field over the mixed layer ($\upsilon_{ga}$) is shown in Fig. 5.6 b). The mean velocity field exhibits fastest flows in the Gulf Stream region, of more than 0.20 $ms^{-1}$ (note the different scales of the arrows in the subplots). Elsewhere in the North Atlantic the flow is typically less than 0.05 $ms^{-1}$. The circulation presented here is consistent with the circulation presented in Kwon and Riser (2005). This result is perhaps not surprising given the similarity in the methods and data.

Errors in the total geostrophic velocity arise from uncertainty in both the temperature and salinity field; using a reference level at 1000 m results in the integration of these errors over a large depth. The errors in this mixed layer geostrophic velocity field are thus likely to be large in comparison to those in a geostrophic velocity field that is referenced to known velocity at the surface.

b) The Bernoulli Method

The geostrophic velocity field at the oceans surface can be calculated using Sea Surface Height (SSH) data and the geostrophic equation (5.4). In this study a SSH dataset provided by Alderson and Killworth (2005) is used for this purpose. Their dataset is based on the Bernoulli Inverse method, which was first proposed by Killworth (1986) and later adapted by Cunningham (2000). In the original method, it is assumed that the density, potential vorticity and the compressible Bernoulli function, $B$, (equation 5.6) are conserved along streamlines

$$B = \frac{p}{\rho} + gz \tag{5.6}$$

here $p$ is pressure, ρ is density, $g$ is acceleration due to gravity and $z$ is the depth of the point. If the potential vorticity and density on a depth surface at one station are equal to that on a depth surface at a second station, it is assumed that the two stations are joined by a streamline. The requirement that the Bernoulli function also matches at crossings leads to a heavily over-determined problem for the surface pressure field which can be solved using a singular value decomposition. Alderson and Killworth (2005) use the adapted Bernoulli

inverse method (Cunningham, 2000), in which the three properties conserved along streamlines are the compressible Bernoulli function, salinity and the modified potential temperature (modified since potential temperature itself is not a conserved property). This modified potential temperature is a linear combination of potential heat content and salinity (and is thus conserved).

The SSH field provided by Alderson and Killworth covers 36 months between January 2003 and December 2005; there is not sufficient salinity data from the Argo floats to provide reliable SSH estimates prior to this time. It should be noted here that the obtained SSH field is not absolute, but rather is relative to the SSH at all other points. The OI scheme used to interpolate the MLD field (chapter 4) is used here to obtain monthly grids of the SSH. In addition to the SSH field, Alderson and Killworth provide estimates of the error in the SSH (calculated by the singular value decomposition). These error estimates are also interpolated onto a regular grid. As with the interpolated MLD field, some gaps occur in the interpolated SSH field in data sparse regions. The missing values are filled using a simple linear spatial interpolation. The error in SSH at missing data points is set to the maximum error throughout the study region.

The SSH field for an example month (September 2004) is plotted in Fig. 5.7. The interpolated SSH field is shown both before (subplot a) and after (subplot b) any gaps have been filled. There is a spatial trend in the SSH which exhibits similar features to the temperature field, highlighting the dominance of thermosteric expansion in the SSH field. The Argo-based SSH field is consistent with the SSH field in the OCCAM model and with SSH products from altimeter (Alderson and Killworth, 2006). The estimated error in the SSH is plotted in Fig. 5.7 c) and d). The typical error is around 0.02 – 0.04 m, corresponding to around 10 % of the relative SSH field. The error fill values are typically much larger than the error at surrounding grid points. This is deemed desirable given the essentially unknown SSH at such grid points. However, given the relatively smooth nature of the SSH field it is likely that these errors are over-estimates of the actual error.

The variability in the SSH field is investigated to determine the best fill values during the years 1999 to 2002. Examination of the SSH field throughout the 36 months for which data was adequate to provide reliable estimates revealed no dominant seasonal signal in the

SSH field (the SSH field is not absolute, but relative). Variations in SSH between January 2003, January 2004 and January 2005 were as significant as variations in SSH throughout the course of a one-year period. This result is supported using a Fourier analysis in which no dominant peak in amplitude was found to correspond with annual frequency.

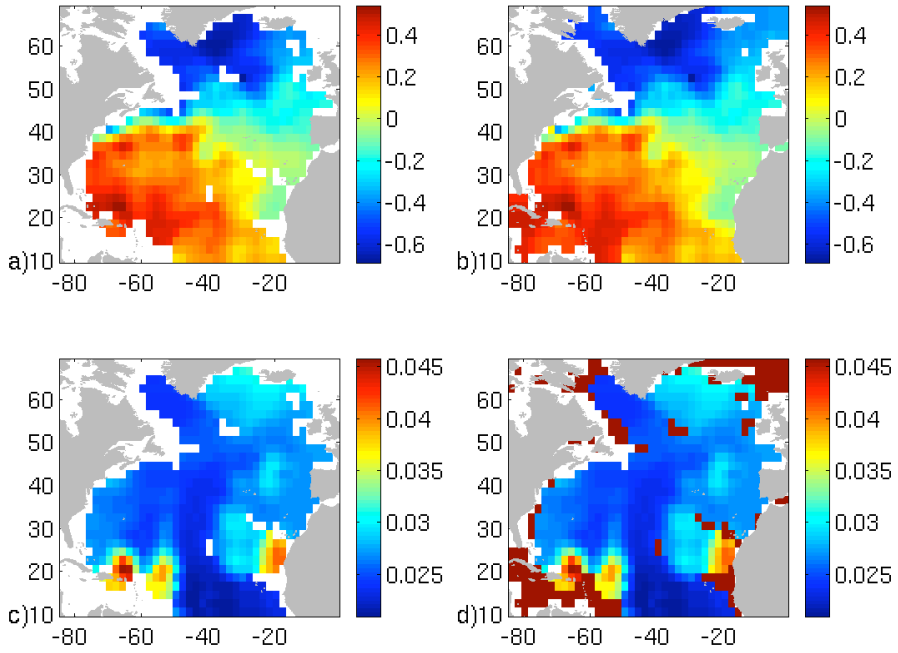


**Figure 5.7** The Sea Surface Height field from the Bernoulli inverse method (Alderson and Killworth, 2005), a) the interpolated SSH field for an example month (September 2004) without gaps, b) as a) but with gaps filled, c) the interpolated error in SSH with gaps and d) as c) but with gaps filled. Gaps in the error field are filled with the maximum SSH error.

The SSH between January 1999 and December 2002 (i.e. prior to available SSH Argo based fields) is thus assumed to have a temporal mean (i.e. constant) value. It is therefore not possible to resolve interannual variations in the barotropic velocity field from this method for the first four years of the study period. Although this may be considered a limitation of this method relative to the displacement method, examination of the amount of data pairs used in the displacement method (shown in Fig. 5.7) showed the amount of available data was low prior to 2003, suggesting significant errors are likely. The number

of data pairs available for estimating the velocity at the sea surface is shown in Fig. 5.8. After 2003, there are typically 100 more profile pairs per month used by this method than by the displacement method.

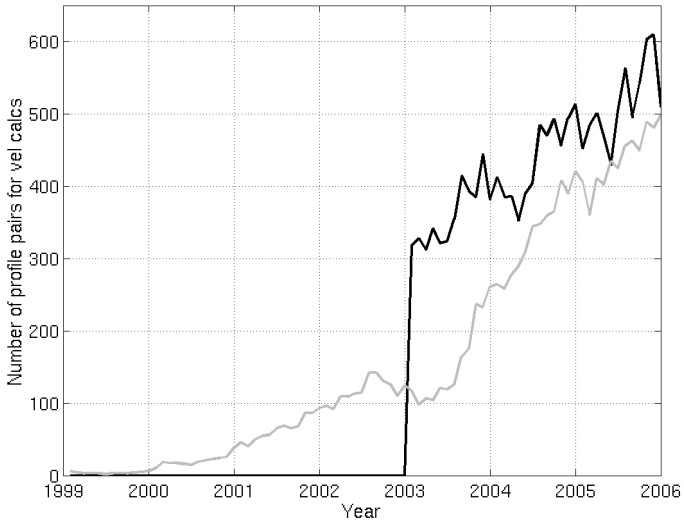


**Figure 5.8** Time series of the number of data pairs used to estimate the surface velocity field (black) and the number of data pairs used to estimate the 1000 m velocity (grey).

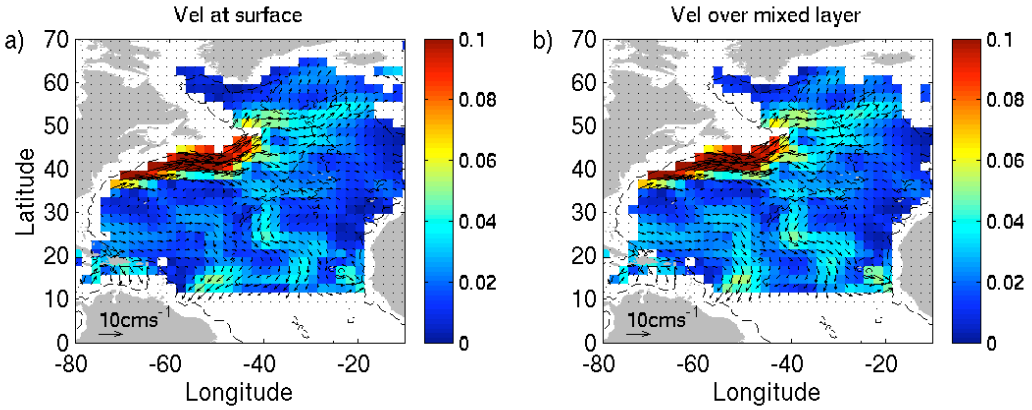


**Figure 5.9** Vector plot of the velocity field at a) the sea surface (i.e. the reference velocity) and b) averaged over the mixed layer. Velocity field derived using the Bernoulli inverse SSH field to obtain the reference velocity and temperature data to obtain the baroclinic flow component.

All SSH data are used to obtain the time mean surface geostrophic velocity field, shown as a vector plot in Fig. 5.9 a). The Gulf Stream and NAC can easily be identified with mean velocities of 0.12 $ms^{-1}$. Velocities are lowest within the central Labrador Sea and off the west coast of Africa. Comparison of the surface geostrophic velocity field with that presented in Kwon and Riser (2005) indicates a good agreement in terms of the general circulation pattern. However, the surface velocities based on the Bernoulli method are typically smaller than those in Kwon and Riser, 2005. The difference within the Gulf Stream is particularly large, exceeding 0.20 $ms^{-1}$. These smaller velocity fields likely result from the larger smoothing in the SSH field than in the displacement method used in Kwon and Riser (2005).

The total geostrophic velocity field (i.e. the barotropic plus baroclinic) averaged over the mixed layer is shown in Fig. 5.9 b). Comparison with Fig. 5.9 a) reveals little or no difference between the two. This is expected since by definition, changes in temperature are small within the mixed layer, resulting in a small baroclinic velocity component. The error in the total geostrophic field is thus dominated by errors in the SSH, while errors arising from the temperature and salinity fields are small. Comparison of the mean mixed layer velocity field based on the Bernoulli method (Fig. 5.9) and based on the displacement method (Fig. 5.6) indicates smaller velocities in the former, particularly in the Gulf Stream region. This likely results from the larger smoothing applied in the Bernoulli method. This over-smoothing will be considered in the heat budget analysis as it may lead to an underestimate of the advective contribution to the heat budget. However, in view of the larges-scales (of the order 1000 km) considered in this study, this over-smoothing is not expected to have a large impact on the results.

### 5.5 The Vertical Velocity Field

As with the horizontal velocity, there is both an Ekman and geostrophic component to the vertical velocity. The Ekman pumping velocity, $w_{e,-h}$, is the vertical velocity at the base of the Ekman layer, induced by the curl of the wind stress. This is given by the following equation

$$w_{e,-h} = -\frac{1}{\rho f}\left(\frac{\partial \tau_y}{\partial x} - \frac{\partial \tau_x}{\partial y}\right) \tag{5.7}$$

(e.g. Josey et al., 2002). Using Stokes' theorem, which states that the integral of the curl of a vector field across a region is equal to the integral of the vector field along the boundary of that region, $w_{e,-h}$, integrated over the 10° x 10° boxes, can be written

$$\iint_A w_{e,-h} = -\frac{1}{\rho f}\oint \tau \cdot n \; dl \tag{5.8}$$

where $A$ is the area of integration. This allows the Ekman pumping velocity to be obtained for any shape region, although in this instance the region considered is roughly rectangular, the northern and southern boundaries are not equal due to the divergence of meridians with latitude. Thus this latter method should provide a more accurate answer than use of equation 5.7. The Ekman pumping velocity is calculated using both the NCEP and NOC wind stress fields (see section 5.4) in equation 5.8. Plots of the time-mean vertical velocity field are shown in Fig. 5.10 a) and b) for NCEP and NOC, respectively. The velocity ranges from -50 m $yr^{-1}$ (i.e. downwelling) south of 40°N, to more than 50 m $yr^{-1}$ (i.e. upwelling) at high latitudes and in the eastern basin, south of 20°N. The Ekman pumping velocities derived from the NCEP and NOC wind stress fields exhibit similar spatial trends. However, the line of zero velocity (corresponding to the line of zero wind stress curl) from the NOC wind stress field is located further south in the eastern North Atlantic than the corresponding line in NCEP. In addition, the Ekman downwelling is stronger when quantified from the NOC wind stress, while the Ekman upwelling is weaker.

The geostrophic component of the vertical velocity field, $w_{g,-h}$, arises from latitudinal variations in $f$ quantified using

$$w_{g,-h} = -\frac{\beta}{f} h v_{ga} \tag{5.9}$$

(Gill, 1982) where β is the gradient in *f* with latitude. β varies from 2.2 x $10^{-11}$ $m^{-1}s^{-1}$ at 20°N to 1.7 x $10^{-11}$ at 60 °N. Here β is assumed to be constant at 2 x $10^{-11}$ $m^{-1}s^{-1}$. The vertical velocity field driven by the latitudinal variations in *f* is plotted in Fig. 5.10 c). The geostrophic vertical velocity is typically smaller than the wind driven vertical velocity with values less than 10 m $yr^{-1}$ throughout most of the North Atlantic. However, it becomes relatively large south of 20°N, exceeding 30 m $yr^{-1}$ where *f* is small. In view of the expected underestimate of the geostrophic velocity field, this term may also be underestimated.

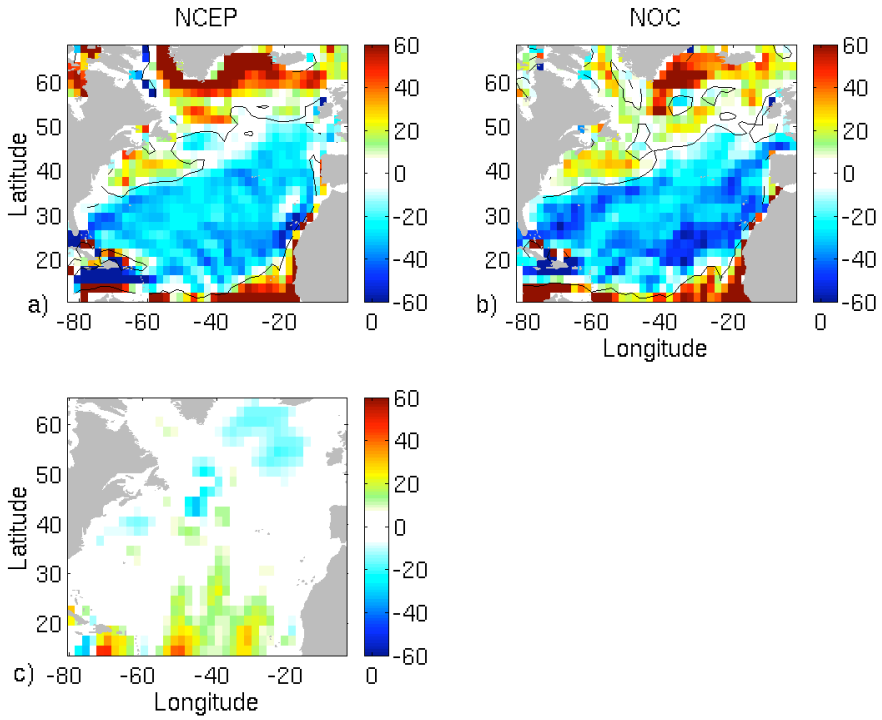


**Figure 5.10** Vertical velocity components, m $year^{-1}$, a) Ekman component based on NCEP wind stress and b) Ekman component based on NOC wind stress field and c) the geostrophic component. Positive values indicate upwelling. Zero contours (black) are also shown on a) and b).

## 5.6 The Heat Budget Components

In this section the methods used to quantify the individual heat budget components are outlined. The required variables (discussed above) are initially interpolated to monthly 2° x 2° grids using the OI scheme outlined in chapter 3. The temperature and the MLD are interpolated to both the start and the middle of each month. All other variables are centred on the middle of each month. As shown in Fig. 5.11, this enables the heat budget components to be calculated so they are centred on the middle of the month. In view of the assessment of the magnitude of errors associated with estimating the heat storage over different time periods (see chapter 4.4), all heat budget variables are smoothed by a 3-month running mean and averaged into 10° x 10° boxes covering 20°N - 60°N, 75°W - 5°W. Quantification of each heat budget component is considered in the subsections below.

### 5.6.1 The Heat Storage

In this thesis the term 'heat storage' refers to the rate of change in upper ocean heat content over time. The seasonal heat storage, $\rho C_p h \frac{\partial T_a}{\partial t}$, is quantified using the interpolated Argo-based temperature fields and a centred differencing scheme. Where $h$ is defined as the MLD, the interpolated Argo-based MLD field is also used. These fields are averaged from their original 2° x 2° grids into 10° x 10° boxes using a weighting function to account for the larger area covered by grid cells at lower latitudes (due to divergence of the meridians). A 3-month running mean is also applied. In order that the heat storage is centred on the middle of each three month period the upper ocean temperature, $T_a$, is quantified using values centred on the 1st of each month. For the mixed depth heat storage, $h$ is quantified using values centred on the middle of the month. For example, in order to obtain the April-centred heat storage, the upper ocean temperature for the 16th January and the 15th of April (taken to be the average of the monthly values centred on February 1st, March 1st and April 1st) is subtracted from the corresponding mean temperature for the 16th of April to the 15th of July. This temperature difference is then divided by the time separating the two periods (3 months) and multiplied by either the mean MLD for the period 1st of March to the 31st of May (i.e. the average of values centred on March the 15th,

April the 15th and May the 15th) for the mixed layer heat storage, or by 300 m for the heat storage over the fixed depth. The schematic in Fig. 5.11 explains this visually.

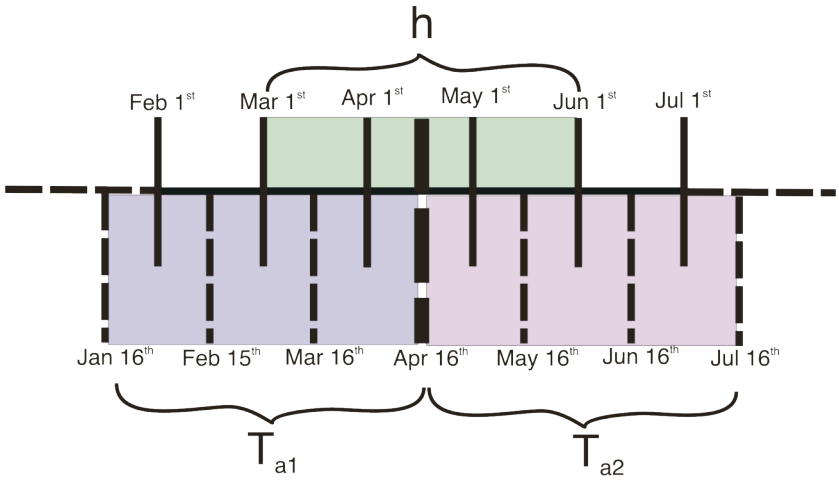


**Figure 5.11** Schematic to provide visual explanation of how the April-centred heat storage is calculated from $T_a$ and $h$. Individual $T_a$ values are calculated for periods bound by dashed bars (using corresponding $h$ values) and centred on solid bars, while individual values for $h$ are calculated for periods bound by solid bars (centred on dashed bars). For the fixed layer heat storage, $h$ is simply 300 m.

5.6.2 Entrainment

The total heat entrainment is given by $\rho C_p (T_a - T_{-h})\left(\frac{\partial h}{\partial t} + \upsilon_{-h} \cdot \nabla h + w_{-h}\right)$. The 1st and 2nd terms are only included in the mixed layer heat budget, where $h$ varies spatially and temporally. All terms are quantified over three-month (seasonal) periods. Here each entrainment component is considered in turn from left to right.

a) The Entrainment Associated with Temporal Changes in $h$

The first heat entrainment component, arising from temporal changes in $h$, $\rho C_p (T_a - T_{-h})\left(\frac{\partial h}{\partial t}\right)$ is referred to as $E_{MLD}$. This term is quantified using the temperature variables $T_a$, $T_{-h}$ centred on the middle of each month, while $h$, is centred on the first of

each month. Hence $\frac{\partial h}{\partial t}$ is also centred on the middle of the month in the same way as shown for $\frac{\partial T_a}{\partial t}$ in subsection 5.6.1.

b) The Entrainment Associated with Spatial Gradients in *h*

The second heat entrainment term, $\rho C_p(T_a - T_{-h})\upsilon_{-h} \cdot \nabla h$, referred to as $E_{adv}$ requires knowledge of the horizontal velocity field at the base of the mixed layer ($\upsilon_{-h}$). Since it is assumed that the Ekman layer is confined within the mixed layer, the wind-driven velocity at the base of the mixed layer is taken to be zero. Therefore only the geostrophic velocity component is considered and $\upsilon_{-h}$ is quantified using the Argo-based SSH field and the thermal wind equations (discussed in section 5.4.2). The gradients in the MLD across the box ($\nabla h$) are quantified using the Argo-based MLD field on a 2° x 2° grid in the same way as the temperature gradient is quantified for the advective heat divergence (discussed in section 5.6.4).

c) The Entrainment Associated with Vertical Advection

The third heat entrainment term, $\rho C_p(T_a - T_{-h})w_{-h}$, referred to as $E_z$, is simply obtained from 10° x 10° seasonal averages of the temperature and vertical velocity field (discussed in section 5.5).

5.6.3 The Absorbed Net Heat Flux

The net heat flux absorbed in the upper ocean, $Q + Q_{-h}$, is quantified using both the flux components from the NCEP reanalysis and the NOC climatology. Details of these flux products can be found in chapter 2, section 4. The heat flux penetrating though the surface layer, $Q_{-h}$, is estimated from

$$Q_{-h} = -\lambda_{PAR} Q_s \exp(-\gamma h) \tag{5.10}$$

where $\lambda_{PAR}$ is the fraction of light available for heating at the surface, $Q_s$ is the shortwave flux component, $\gamma$ is the penetration coefficient and $h$ is the depth of the upper layer (McPhaden, 2002). This penetrative heat flux is largest in regions of low turbidity and productivity (i.e. clear water regions). Rochford et al. (2001) estimated the optical properties of the global oceans using Sea-viewing Wide Field-of-View Sensor (SeaWiFS) data. They found $\lambda_{PAR}$ varied slightly with latitude from 0.49 at the equator to 0.48 at 40°N while $\gamma$ varied from an average of 0.06 $m^{-1}$ at low latitudes to 0.10 $m^{-1}$ at high latitudes. A strong frontal feature between these $\gamma$ values was observed at 30-40°N in the Atlantic Ocean. In view of this, values of 0.06 $m^{-1}$ and 0.10 $m^{-1}$ south and north of 40°N are used for $\gamma$. The applied penetration coefficients correspond to heat extinction depths of 16.5 m and 10 m north and south of 40°N, respectively. $\lambda_{PAR}$ is set to a constant value of 0.48 following Rochford (2001). The combination of $Q$ and $Q_{-h}$, that is $Q + Q_{-h}$, represents the net surface heat flux absorbed in the upper ocean. This term is referred to as the absorbed net surface heat flux.

**Table 5.1** The maximum of NCEP and NOC penetrative heat flux for individual 10° x 10° boxes, $Wm^{-2}$.

| | 75-65°W | 65-55°W | 55-45°W | 45-35°W | 35-25°W | 25-15°W | 15-5°W |
|---|---|---|---|---|---|---|---|
| 50-60°N | - | - | -18 | -15 | -17 | -10 | -14 |
| 40-50°N | - | -46 | -28 | -22 | -18 | -15 | -20 |
| 30-40°N | -50 | -60 | -63 | -62 | -59 | -57 | -50 |
| 20-30°N | -51 | -57 | -67 | -50 | -38 | -40 | - |

None of the net heat flux penetrates deeper than 300 m. Thus for the fixed depth heat budget the absorbed net heat flux is equal to the heat flux. However, for the mixed layer heat budget the penetrative heat flux may be large during summer and autumn when the mixed layer is shallow. The maximum penetrative heat flux, calculated for different 10° x 10° boxes in the North Atlantic, is shown in Table 5.1. $Q_{-h}$ ranges from 0 $Wm^{-2}$ in the winter months, when the mixed layer is deep and the solar heat flux is at a minimum, to

more than 60 $Wm^{-2}$. The largest penetrative heat flux occurs in the subtropical North Atlantic coinciding with the location of shallowest MLD. To be consistent with the heat storage values, three month running means of the absorbed net surface heat flux are used throughout.

5.6.4 The Advective Heat Flux Divergence

The advective heat flux divergence is quantified as $\rho C_p h \upsilon_a \cdot \nabla T_a$. The depth of the upper ocean, ($h$) and the horizontal velocity over $h$, ($\upsilon_a$) represent 3-monthly averages for 10° x 10° boxes throughout the North Atlantic. $\upsilon_a$ is the sum of the wind driven velocity, $\upsilon_{e,a}$ and the geostrophic velocity, $\upsilon_{g,a}$ in the upper ocean. In order to quantify the gradient in the upper ocean temperature, $\nabla T_a$, across the 10° x 10° boxes, the temperature field on the original 2° x 2° grid is used. $\nabla T_a$ is approximated as $\frac{T_{a,x2} - T_{a,x1}}{\delta x}$, $\frac{T_{a,y2} - T_{a,y1}}{\delta y}$ where $T_{a,x1}$, $T_{a,x2}$ represent the average temperature along the boundaries of the box at $x = 1$ and $x = 2$, respectively and $T_{a,y1}$, $T_{a,y2}$ represent the average temperature along the boundaries of the box at $y = 1$ and $y = 2$. $\delta x$, $\delta y$ are the distances between the grid points $x = 1$ and $x = 2$ and $y = 1$ and $y = 2$, respectively. The schematic in Fig. 5.12 depicts how these quantities are defined. Although this is an approximation based on using discrete values to define a continuous variable, the sensitivity of the advective flux divergence to the location of the boundaries was investigated and found to be small.

The schematics in Fig. 5.12 c) and d) show the meridional and zonal boundaries used for calculating the temperature gradient across all 10° x 10° boxes in the study region, respectively. It should be noted that the Argo-based fields are only interpolated to grid points at which the water depth exceeds 1000 m. For an estimate of the advective heat flux to be obtained for a particular 10° x 10° box, each boundary of the box must have at least one grid point in water deeper than 1000 m. Thus the advective heat flux cannot be estimated at several locations in the defined study area. In addition, some boxes have a limited number of grid points along the boundaries from which the temperature gradient can be calculated, for example at 40-50°N, 45-55°W. It can therefore be expected that the heat divergence at these boxes may be of limited accuracy.

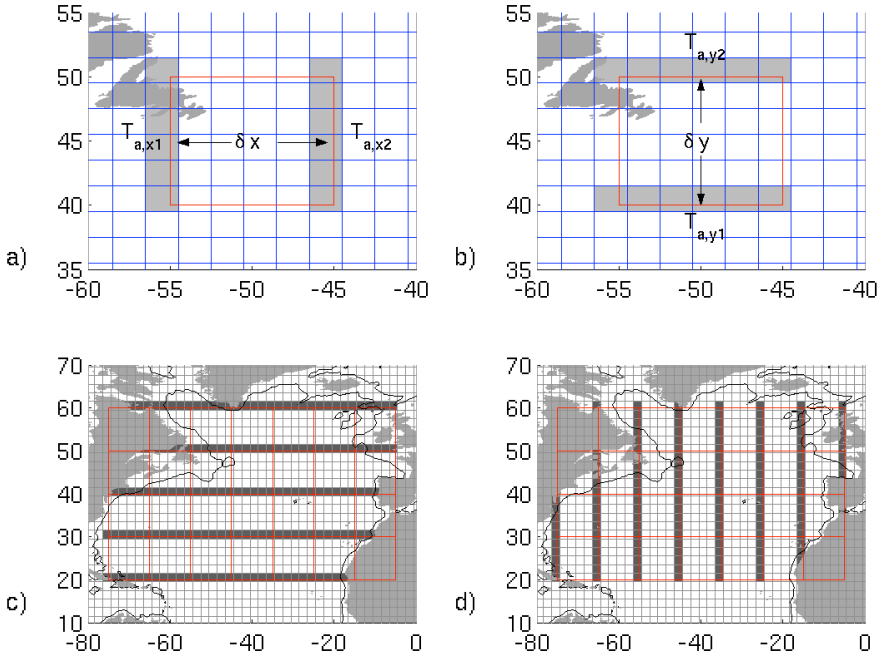


**Figure 5.12** Schematic to show how temperature gradients are quantified, a) and b) give an e.g. of how zonal and meridional gradients are obtained for a particular 10° x 10° box, respectively, c) and d) show the grid cells (thick black lines) in 10° x 10° boxes used for quantifying the zonal and meridional gradients. The 1000 m depth contour is also shown.

### 5.6.5 Diffusion

The diffusive heat flux component, $\rho C_p \left[ k_{x,y} \cdot \nabla^2 T_a + k_{z,-h} \frac{\partial^2 T}{\partial z^2} \right]$, requires knowledge of vertical and horizontal gradients in temperature and of the heat diffusion coefficients. The horizontal temperature gradient needs to be calculated first across the boundaries of individual 10° x 10° boxes and then across each defined 10° x 10° box. These latter gradients are quantified in the same way as for the advective fluxes, while the temperature gradient across the boundaries of individual boxes is approximated as $\frac{T_{a,x(3/2)} - T_{a,x(1/2)}}{\delta x}$, $\frac{T_{a,y(3/2)} - T_{a,y(1/2)}}{\delta y}$, where $T_{a,x(1/2)}$, $T_{a,x(3/2)}$ represent the average temperature

along lines parallel to the boundaries of the box at $x = 1/2$ and $x = 3/2$, respectively, $T_{a,y(1/2)}$, $T_{a,y(3/2)}$ represent the average temperature along the boundaries of the box at $y = 1/2$ and $y = 3/2$. $\delta x$, $\delta y$ are the distances between the grid points $x = 1/2$ and $x = 3/2$ and $y = 1/2$ and $y = 3/2$, respectively (i.e. the distance between the mid-point of two adjacent 10° x 10° boxes). $\frac{\partial T}{\partial z}$ is approximated by $\frac{T_a - T_{-h}}{\delta z}$ with $\delta z$ set to 5 m in view of the thickness of the standard depth surfaces used in this study.

The diffusion coefficients $k_{x,y}$ and $k_{z,-h}$ are set to 5000 $m^2s^{-1}$ and 2 x $10^{-5}$ $m^2s^{-1}$, respectively. These values are used by McCulloch and Leach (1998) in an analysis of the North Atlantic heat budget. This value of $k_{x,y}$ represents the eddy diffusivity estimated from buoys drogued at 100 m (Schäfer and Kraus, 1995), while the applied value of $k_{z,-h}$ is based on vertical diffusion calculations across the thermocline on scales of hundreds of kilometres and several months (Ledwell et al., 1993). Kwon and Riser (2005) also estimated the horizontal eddy diffusivity using velocity observations from Argo floats drogued at a depth of around 1000 m. They found horizontal diffusivities varying from 1000 $m^2s^{-1}$ to more than 13,000 $m^2s^{-1}$ with largest values found in the Gulf Stream. Given the large variability and uncertainty in the diffusion coefficients the error in the diffusion terms is assumed to be 100 %.

### 5.6.6 The Velocity Shear Covariance

The velocity shear covariance term, $\rho C_p \nabla \cdot \left( \int_{-h}^{0} \hat{v}\hat{T} dz \right)$, has often been neglected in the literature due to 1) the difficulty associated with obtaining an accurate estimate and 2) it's small expected magnitude. Given that the upper ocean is typically well mixed, the deviations in the vertically averaged horizontal temperature ($\hat{T}$) and velocity ($\hat{v}$) are expected to be small.

The temporal mean absolute values of $\hat{T}$ and $\hat{v}$ are estimated from the Argo-based velocity and temperature fields. These values were typically smaller than the estimated error, with means of 0.05 °C and 0.001 $ms^{-1}$ for $\hat{T}$ and $\hat{v}$, respectively and the estimated shear covariance flux is zero throughout the North Atlantic, with the exception of four

10° x 10° boxes at high latitudes. The maximum mean velocity shear covariance heat flux is 5 $Wm^{-2}$ at 50-60°N, 35-25°W. Given the large uncertainty in this term and its small magnitude, it is neglected in this study.

**5.7 Summary**

In this chapter the individual variables required and the methods used to quantify the heat budget components are presented and discussed. Thus this chapter provides essential grounding for an analysis of the upper ocean heat budget. It has been shown that when used in conjunction with atmospheric fields from a climatology (or reanalysis), the Argo array may be used to obtain estimates of the individual heat budget components.

In general the heat budget variables quantified from Argo and the NCEP and NOC atmospheric fields exhibit a realistic range of values and the large-scale features of the North Atlantic and the seasonal signal are resolved. Despite this, some discrepancies between the Argo-based results presented here and results published in the literature have been observed and some limitations of the methods used have been highlighted. In particular the Argo-based MLD field is deeper than that presented in Montegut et al. (2004), the geostrophic velocity referenced to the surface is underestimated and the time-span of the geostrophic velocity field is limited to a 3-year period.

The Argo-based MLD is compared with the climatological MLD of Montegut et al. (2004), which is based on the same criterion for defining the MLD as used in this study. The differences between the Argo-based MLD and the climatological MLD are largest during wintertime, when the Argo-based MLD can be more than 50 m deeper than from climatology. It is thought that this difference is due to underestimated MLDs in Montegut et al. (2004) arising from limited data availability during winter.

The geostrophic velocity field based on the Bernoulli method yielded lower velocities than results presented in Kwon and Riser (2005). It is thought that this may be due to over-smoothing of the SSH field. Despite this, the Bernoulli method is used to obtain the geostrophic velocity in this study. The decision to use this method is based on the difficulty in quantifying the errors in the displacement method and the uncertainty associated with using only the temperature to obtain the velocity field 1000 m shallower

than the directly measured velocity. While use of the geostrophic velocity field based on the Bernoulli method may underestimate the magnitude of the velocity, this may not be important on the large spatial scales considered in this study.

# CHAPTER 6. Seasonal Heat Budget Analysis

## 6.1 Introduction

In this chapter, the seasonal heat budget components quantified using the equations and variables defined in chapter 5 are presented. All heat budget components and errors are based on seasonal (3-monthly values). The seasonal cycles in the Argo based heat storage, absorbed net heat flux and the advective and diffusive heat divergence are first considered and the heat budget residual is then examined.

In the following, the seasonal cycle in the heat storage is presented in section 6.2. A comparison of the air-sea heat fluxes from the NCEP reanalysis and NOC climatology is undertaken in section 6.3. This comparison aims to provide some measure of the expected errors in net flux fields (addressing the lack of error estimates in existing atmospheric reanalyses and climatologies). The seasonal cycle in the advective heat divergence is considered in sections 6.4 (the Ekman contribution) and 6.5 (the geostrophic contribution). The diffusive heat divergence is discussed in section 6.6. The level of closure of the heat budget that can be achieved from these terms is then investigated in section 6.7. The error estimates provided in this chapter are derived from the model based analysis in chapter 4. The aim here is to identify the regions where the Argo dataset can usefully be used for investigations of the upper ocean heat budget. A summary of the main findings is given in section 6.8.

## 6.2 The Heat Storage

In this analysis the term 'heat storage' refers to the rate of change in upper ocean heat content over time, with a positive heat storage indicating a warming and negative heat storage, a cooling. Two different definitions for the upper ocean, $h$, are considered here. The heat storage over the mixed layer is presented in section 6.2.1 and the heat storage over a fixed 300 m depth is presented in section 6.2.2. The former definition provides more insight into the physical processes connected with the mixing of the heat in the upper ocean and, while the latter is more useful for comparison with the NCEP/NOC heat fluxes and existing studies in the literature.

### 6.2.1 The mixed layer heat storage

The annual mean mixed layer heat storage, $h\frac{\partial T_a}{\partial t}$ is given for individual 10° x 10° boxes in Table 6.1a. Values are negative throughout the North Atlantic, varying from around -15 $Wm^{-2}$ in the subtropics to less than -40 $Wm^{-2}$ at 30-40°N, 65-45°W. Seasonal heat storage error estimates, $\Delta HS$, are also given in Table 6.1.

$$\Delta HS = \rho C_p \left[ (h + \Delta h) \frac{\partial}{\partial t} \left( T_a + \Delta T_a \right) - h \frac{\partial T_a}{\partial t} \right], \tag{6.1}$$

(Yan et al., 1995), where $\Delta h$ and $\Delta T_a$ are the errors in $h$ and $T_a$, estimated using the model-based approach (chapter 4). Within the subtropics the seasonal heat storage errors are typically around 5 $Wm^{-2}$. Errors are larger in the Gulf Stream region, in the subpolar region and east of 15°W, with values of 20-30 $Wm^{-2}$.

The negative mixed layer heat storage values indicate that more heat is lost from the mixed layer than is gained, suggesting that heat entrainment may be significant. The annual mean entrainment, $(T_a - T_{-h})\left( \frac{\partial h}{\partial t} + \upsilon_{-h} \cdot \nabla h + w_{-h} \right)$ - with the terms from left to right representing the entrainment due to temporal variations in $h$, spatial variations in $h$ and the vertical velocity field is given for individual 10° x 10° boxes in Table 6.1 b. The entrainment contributions associated with temporal and spatial variations in $h$ and the vertical velocity field are not shown individually. However, the contribution from the latter 2 terms is negligible, with an annual mean of less than 3 $Wm^{-2}$ at all 10° x 10° boxes, and temporal variations in $h$ contributing the largest entrainment heat flux. The heat entrainment flux removes heat from the mixed layer, varying from less than 8 $Wm^{-2}$ in the western subtropics to more than 20 $Wm^{-2}$ in the eastern basin at 50-60°N. The regions of smallest entrainment heat flux correspond to the regions of smallest temporal variability in the MLD (Fig. 5.5). The seasonal error associated with the entrainment due to temporal variations in the MLD ($\Delta E$) is also given.

$$\Delta E = \rho C_p \left[ \left[ (T_a + \Delta T_a) - (T_{-h} + \Delta T_{-h}) \right] \left[ \frac{\partial}{\partial t} (h + \Delta h) \right] - (T_a - T_{-h}) \left( \frac{\partial h}{\partial t} \right) \right] \quad (6.2)$$

where $\Delta T_{-h}$ is the error in $T_{-h}$, derived from the model based approach discussed in chapter 4. The seasonal entrainment error in the region south of 40°N is typically 1-10 $Wm^{-2}$. The uncertainty is larger in the region off Newfoundland (up to 16 $Wm^{-2}$) and in the easternmost 10° x 10° boxes (up to 34 $Wm^{-2}$). This error may be underestimated since the uncertainty associated with the depth at which $T_{-h}$ is defined, is not included.

Heat loss through entrainment balances the negative heat storage throughout most of the 10° x 10° boxes. However, at mid-latitudes (30-40°N) the negative heat storage is only partially offset by the heat entrainment. This latitude roughly corresponds the location of the centre of the subtropical gyre. In this region the summertime mixed layer is shallow and atmospheric heating may penetrate beneath $h$. Release of heat from below the summer time mixed layer during periods of mixed layer deepening may account for this offset.

**Table 6.1** Annual mean values of a) mixed layer heat storage and b) heat entrainment, error estimates based on seasonal values for an individual year are also shown, $Wm^{-2}$

| a) | 75-65°W | 65-55°W | 55-45°W | 45-35°W | 35-25°W | 25-15°W | 15-5°W |
|---|---|---|---|---|---|---|---|
| 50-60°N | - | - | -26±27 | -23±21 | -23±10 | -30±24 | -30±29 |
| 40-50°N | - | -33±30 | -14±25 | -19±14 | -26±8 | -25±5 | -24±17 |
| 30-40°N | -33±17 | -44±6 | -47±9 | -34±4 | -25±6 | -22±4 | -21±20 |
| 20-30°N | -16±3 | -15±3 | -14±6 | -16±2 | -17±3 | -15±6 | - |

| b) | 75-65°W | 65-55°W | 55-45°W | 45-35°W | 35-25°W | 25-15°W | 15-5°W |
|---|---|---|---|---|---|---|---|
| 50-60°N | - | - | 18±11 | 23±8 | 21±8 | 23±29 | 20±34 |
| 40-50°N | - | 10±8 | 16±16 | 18±12 | 15±5 | 20±3 | 18±10 |
| 30-40°N | 15±8 | 18±4 | 21±6 | 16±2 | 14±6 | 11±3 | 14±13 |
| 20-30°N | 6±3 | 6±3 | 8±7 | 9±1 | 9±4 | 8±4 | - |

The seasonal cycle in the combined mixed layer heat storage and entrainment (which will be referred to as the total heat storage) is shown in Figure 6.1. Throughout the North Atlantic, the mean seasonal cycle exhibits a heat loss during the winter months and a smaller heat gain in the summer months. This seasonal difference is particularly evident at lower latitudes. For example south of 30°N, the total summer heat storage is less than 60 $Wm^{-2}$ and the total winter heat storage is as low as -100 $Wm^{-2}$ (i.e. the mixed layer loses 40 $Wm^{-2}$ more heat in winter than gained in summer). This imbalance is consistent with the theory that the ocean beneath the mixed layer is heated by incoming solar radiation.

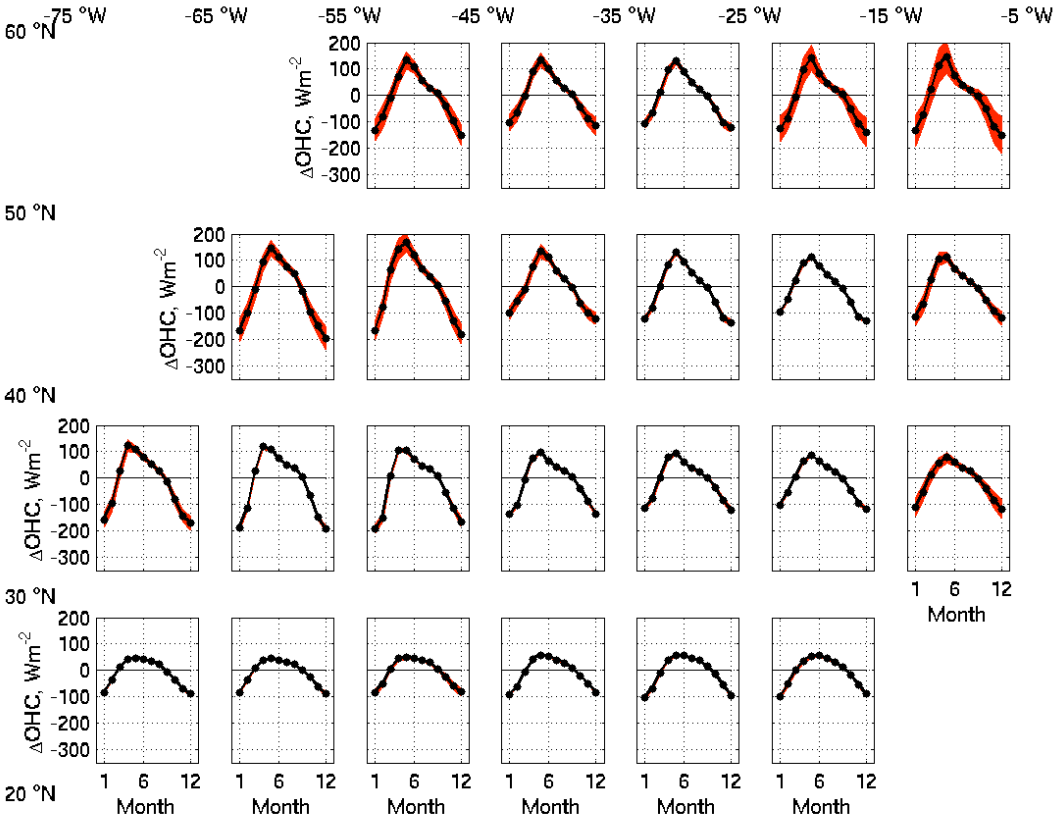


**Figure 6.1** Seasonal cycle in the total mixed layer heat storage ($Wm^{-2}$) for different 10° x 10° boxes in the North Atlantic. Red shading indicates the estimated seasonal error.

There is an asymmetry in the seasonal cycle with a rapid increase in total heat storage to its maximum value in May (or April at 30-40°N in the western basin) and a more gradual

decline during which the mixed layer still gains heat, typically until September. After September the mixed layer begins to cool, with maximum heat loss generally occurring in December. These features of the total mixed layer seasonal heat storage can largely be explained by the seasonal cycle in the MLD (chapter 5.3), which exhibits a rapid shoaling between March and May, to shallowest depths during the summer months. This is followed by a more gradual deepening during the months of August to December. Thus during summer the amount of heat stored in the shallow mixed layer is limited. The seasonal cycle in $T_a$ (discussed in chapter 5, section 3) largely dictates the timing of positive and negative heat storage. The timing of the seasonal cycle in total heat storage over the mixed layer are not consistent with the seasonal cycle in heat storage typically described in the literature; existing studies of the mixed layer heat budget are generally restricted to the tropical oceans where variations in the mixed layer are small. It is therefore concluded that the mixed layer approach is not valid when temporal variations in $h$ are large. In the subtropics and mid-latitudes a fixed depth heat budget analysis is the more conventional approach. However, the mixed layer heat storage presented in this subsection demonstrates the possibility of using the Argo dataset for investigating the ventilation of thermocline waters. A more detailed analysis on this subject is beyond the scope of this study. In the following sections all heat budget components are quantified over a fixed depth.

### 6.2.2 The fixed depth heat storage

The annual mean fixed-depth heat storage, $h\frac{\partial T_a}{\partial t}$ and associated error estimates are given in Table 6.2. $h$ is set to 300 m, since the effects of the seasonal cycle are largely restricted within this layer. For all 10° x 10° boxes the annual mean heat storage is less than the estimated error. The heat storage errors (estimated using the model based approach outlined in chapter 4 and equation 6.1) exhibit significant spatial variations with errors of more than 100 $Wm^{-2}$ in the Gulf Stream region, and less than 10 $Wm^{-2}$ in the eastern basin. Heat storage error estimates provided in the literature typically represent a mean spatial and temporal error. For example Lamb and Bunker (1982) (henceforth LB82) assumed an error

of 15 $Wm^{-2}$ at each latitude band. While the errors presented here exceed those from LB82 for many 10° x 10° boxes, the errors here are based on individual years while the errors in LB82 are based on a climatology compiled from a decade of data.

The seasonal cycle in fixed depth heat storage is shown for all 10° x 10° boxes in Fig. 6.2. The maximum heat storage typically occurs in June or July, being slightly earlier at low latitudes and the maximum heat loss occurs during December and January. The timing of the seasonal cycle is in agreement with results presented in Hsiung et al. (1989) (henceforth H89) and LB82, who also considered the heat storage over a fixed 300 m layer.

**Table 6.2** Annual mean values of fixed depth heat storage with error estimates, $Wm^{-2}$. The error estimates are based on seasonal (three-monthly) heat storage for an individual year.

| | 75-65°W | 65-55°W | 55-45°W | 45-35°W | 35-25°W | 25-15°W | 15-5°W |
|---|---|---|---|---|---|---|---|
| 50-60°N | - | - | 3±17 | 2±41 | 5±34 | 2±16 | 0±20 |
| 40-50°N | - | -18±117 | -5±104 | -1±38 | 8±24 | 0±9 | 0±18 |
| 30-40°N | 1±44 | -6±17 | 1±19 | 2±6 | 1±7 | 1±7 | 0±53 |
| 20-30°N | 0±16 | 0±19 | 3±26 | 1±9 | 3±18 | -1±30 | - |

The annual range in heat storage is given for individual 10° x 10° boxes in Table 6.3. The largest annual range in seasonal heat storage occurs over the Gulf Stream, with a maximum range of almost 550 $Wm^{-2}$ at 40-50°N, 65-55°W. Above average summer heat gain and winter heat loss both contribute to the large annual range at this location. The high summertime heat storage indicates that heat may be supplied to this region through advective or diffusive processes, while the strong wintertime heat loss is likely driven by significant heat exchange with the atmosphere. The mean annual range at 40-50° N is 350 $Wm^{-2}$, larger than the mean annual range at other latitude bands in the North Atlantic. H89 also found a maximum annual range in the upper ocean heat storage at this latitude. Although this reference dates back almost 20 years, it remains one of the most comprehensive observational studies of the annual cycle in ocean heat storage, providing full coverage of the North Atlantic Ocean. They reported a maximum annual range of more

than 300 $Wm^{-2}$, with summertime heat storage exceeding 150 $Wm^{-2}$ and a wintertime heat storage of -150 $Wm^{-2}$. The annual range in heat storage is smallest in the subtropical North Atlantic, less than 150 $Wm^{-2}$ at 20-30°N, 65-55°W.

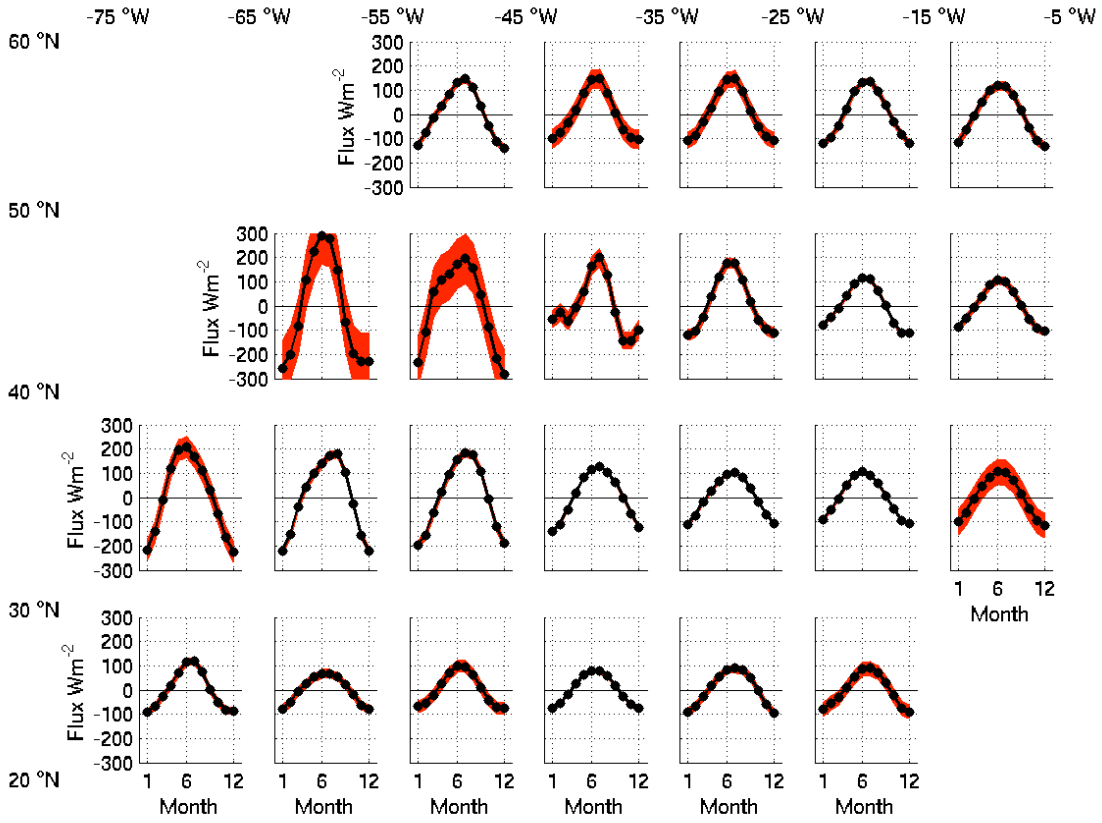


**Figure 6.2** Seasonal cycle in the heat storage of the upper 300 m ($Wm^{-2}$) for different 10° x 10° boxes in the North Atlantic. Red shading indicates the estimated seasonal error.

**Table 6.3** Annual range in seasonal fixed depth heat storage ($Wm^{-2}$)

| | 75-65°W | 65-55°W | 55-45°W | 45-35°W | 35-25°W | 25-15°W | 15-5°W |
|---|---|---|---|---|---|---|---|
| 50-60°N | - | - | 287 | 253 | 254 | 256 | 251 |
| 40-50°N | - | 546 | 477 | 344 | 297 | 226 | 213 |
| 30-40°N | 432 | 400 | 382 | 267 | 217 | 214 | 224 |
| 20-30°N | 210 | 148 | 174 | 156 | 185 | 181 | - |

### 6.3 The NCEP and NOC Fluxes

In this section the absorbed net fluxes from the National Centers for Environmental Prediction/ National Center for Atmospheric Research (henceforth NCEP) reanalysis and the National Oceanography Centre (NOC) climatology are considered. As discussed in chapter 2, there are two versions of the NOC climatology: NOC 1.1 (Josey et al., 1999) and NOC 1.1a (Grist and Josey, 2003). The version NOC 1.1 (henceforth NOC) is used here.

A major limitation of existing air-sea flux climatologies and reanalyses is the lack of accompanying error estimates. The NCEP reanalyses and the NOC climatology are no exception to this. Gleckler and Weare (1997) suggest that the typical error in zonally averaged annual net heat flux in the North Atlantic is 40 $Wm^{-2}$. However, as with the uncertainty in heat storage, this error varies throughout time and space. Comparison of two (semi) independent flux products can be used to provide some information on the expected error and to identify regions and times of high (and low) errors. Although the NCEP and NOC flux fields utilise some of the same observations the NOC climatology is strictly an observational estimate, while the NCEP reanalysis, involves assimilation of observations into a NWP model (Kalnay et al., 1996; Kistler et al., 2001). Kistler et al. (2001) noted that the impact of these observations in the NCEP reanalysis is limited. In addition the methods used to derive the radiative (longwave and shortwave) fluxes are different. Radiative transfer equations are applied in the NCEP reanalysis while much simpler parameterisations, involving knowledge of cloud cover, are employed in the NOC climatology. The variable exchange coefficients applied in the bulk formulae to calculate the turbulent fluxes (equations 2.1 and 2.2) also differ between the NCEP reanalysis and NOC climatology.

The annual mean net heat flux between 1999 and 2005 from the NCEP reanalysis and the NOC climatology is quantified for individual 10° x 10° boxes throughout the study region and given in Table 6.4 a). The annual mean net heat flux is also plotted Fig. 6.3. Before plotting, the higher resolution NOC fluxes (originally on a 1° x 1° grid) are interpolated onto the coarser NCEP grid, which is roughly 2° x 2°.

Table 6.4 a) and Fig. 6.3 a) and b) indicate a weak latitudinal variation in net flux with smaller heat loss or heat gain occurring in the subtropics and larger ocean heat loss at

higher latitudes. Superimposed on this general variation, both flux fields exhibit highest ocean heat loss in the subpolar North Atlantic and over the Gulf Stream and NAC. The largest annual mean heat loss for a 10° x 10° box is -113 $Wm^{-2}$ and -73 $Wm^{-2}$ for NCEP and NOC, respectively occurring at 30-40°N, 75-65°W. In this region oceanic heat loss is large during cold-air outbreaks, which occur when cold, dry air masses from the continent are advected over the relatively warm ocean. Largest positive annual mean heat fluxes of 30 $Wm^{-2}$ in the NOC climatology occur off the west coast of Africa. The strong net heating in this region is due to the shortwave heat gain being only partially offset by latent heat loss, as upwelling of cold water here inhibits evaporation (Bunker and Worthington, 1976).

**Table 6.4** Annual mean absorbed seasonal net heat flux for a) NCEP and NOC, with the latter shown in brackets and b) the RMS difference between the two flux fields.

| a) | 75-65°W | 65-55°W | 55-45°W | 45-35°W | 35-25°W | 25-15°W | 15-5°W |
|---|---|---|---|---|---|---|---|
| 50-60°N | - | - | -19 (-10) | -27 (-27) | -33 (-23) | -50 (-29) | -36 (-18) |
| 40-50°N | - | -20 (-12) | -7 (6) | -84 (-54) | -29 (-15) | -11 (0) | -5 (11) |
| 30-40°N | -113 (-73) | -104 (-57) | -56 (-14) | -21 (12) | -1 (23) | -2 (13) | 3 (30) |
| 20-30°N | -23(22) | -19 (29) | -13 (35) | -10 (39) | -16 (36) | 12 (42) | - |

| b) | 75-65°W | 65-55°W | 55-45°W | 45-35°W | 35-25°W | 25-15°W | 15-5°W |
|---|---|---|---|---|---|---|---|
| 50-60°N | - | - | 23 | 19 | 26 | 30 | 27 |
| 40-50°N | - | 14 | 24 | 35 | 8 | 14 | 18 |
| 30-40°N | 43 | 48 | 43 | 34 | 25 | 17 | 29 |
| 20-30°N | 45 | 49 | 48 | 50 | 52 | 29 | - |

The NCEP annual mean net flux is less than zero throughout most of the Atlantic north of 20°N, with only two 10° x 10° boxes (20-30°N, 25-15°W and 30-40°N, 15-5°W) exhibiting a positive mean flux. Comparatively, the NOC mean absorbed flux is positive southeast of a line extending from Cape Hatteras to Ireland, and negative northeast of this.

Differences between the NCEP and NOC net flux are plotted in Fig. 6.3 c). On average the mean NOC fluxes exceed those from NCEP (i.e. more heat is gained/ less heat is lost by the ocean in NOC). Differences exceed 50 $Wm^{-2}$ in the southern North Atlantic and in the Gulf Stream. In order to further quantify this difference, three-monthly RMS differences for 10° x 10° boxes are given in Table 6.4 b). These RMS differences give an indication of the likely error in the absorbed net flux. Differences are smallest in the eastern mid-latitudes, less than 20 $Wm^{-2}$. The differences between the NCEP and NOC net fluxes are larger than the estimated heat storage error (given in Table 6.2) except in the boxes through which the Gulf Stream and NAC flow. Thus it is anticipated that use of the Argo based heat storage may be useful for identifying the more accurate flux field.

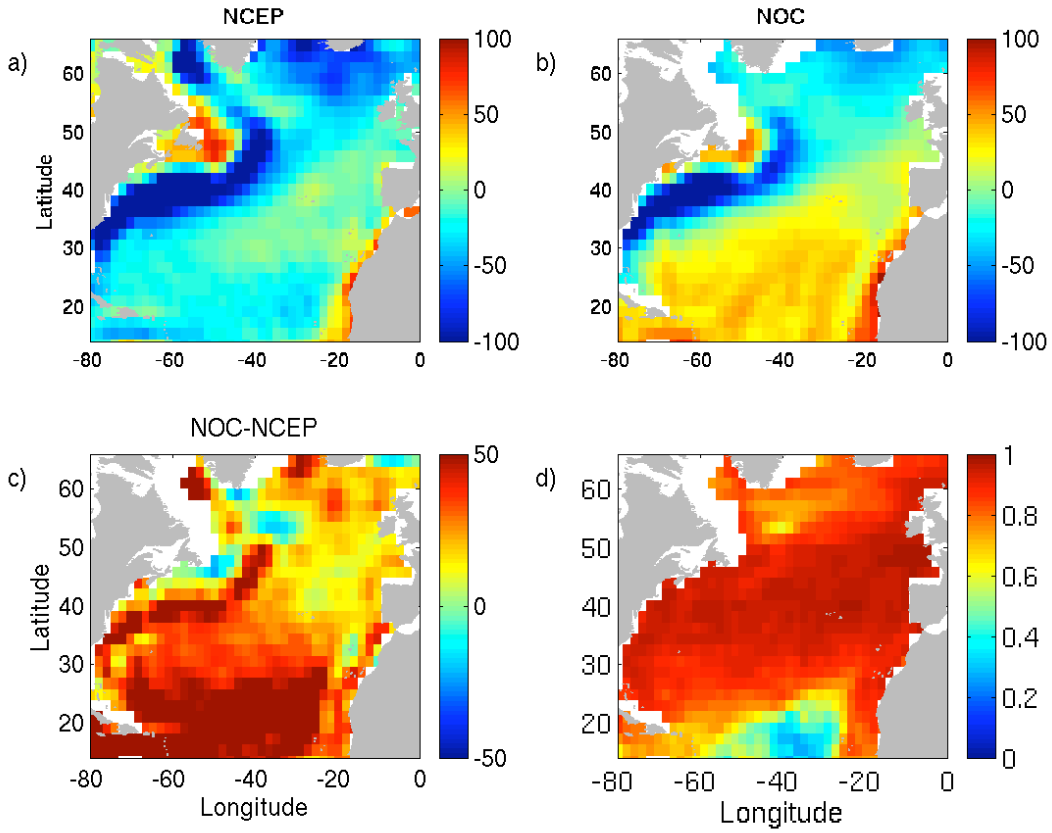


**Figure 6.3** Mean net flux ($Wm^{-2}$) for a) the NCEP reanalysis, b) the NOC climatology and c) the difference between a) and b) (NOC – NCEP): Positive values indicate larger NOC fluxes than NCEP fluxes. Subplot d) shows the correlation ($r^2$) between the NCEP reanalysis and NOC climatology absorbed net flux fields between 1999-2005.

The temporal correlation between the NCEP and NOC absorbed net surface heat flux for January 1999 – December 2005 is calculated at each grid point and plotted in Fig. 6.3 d). Despite the observed differences in the flux fields, the correlation exceeds 0.9 throughout a large area of the North Atlantic. The correlation is lower, around 0.7 in the subpolar North Atlantic (north of 50°N) and around 0.3 south of 20°N. The relatively low correlation in these two regions is expected since at the former location the number of available observations is low (thus higher errors), while at the latter location the seasonal cycle is weaker (shown below). The correlation between the NCEP and NOC absorbed net heat flux after removal of the mean seasonal cycle reduced from an average of 0.95 to 0.56. Both of these correlations are significant, indicating that the two net flux products resolve similar seasonal and interannual features. Interannual variability is discussed in more detail in chapter 7.

The seasonal cycles in absorbed net heat flux from the NCEP reanalysis and the NOC climatology are plotted for all 10° x 10° boxes in the North Atlantic study region in Fig. 6.4. The seasonal cycle in the net flux typically shows ocean heat gain between March and September at lower latitudes and between April and August at high latitudes. The maximum heat gain in the ocean occurs during June or July and the maximum ocean heat loss typically occurs in December. Between 20 and 40°N the absorbed net heat flux is higher in NOC than in NCEP throughout the seasonal cycle. That is, the ocean in the NOC climatology gains more heat during summer and loses less heat during winter than the ocean in the NCEP reanalysis. At 40-60°N, the summertime offset between the NCEP and NOC fluxes is reduced to close to zero and in some cases the ocean in the NCEP reanalysis gains more heat than that in the NOC climatology.

The annual range in absorbed net heat flux (Table 6.5) varies from less than 200 $Wm^{-2}$ in the subtropics, to more than 400 $Wm^{-2}$ in the Gulf Stream region. Throughout most of the North Atlantic the seasonal cycle is more pronounced in the NCEP absorbed net heat flux than the corresponding cycle from the NOC climatology. This is particularly evident over the Gulf Stream and in the subpolar North Atlantic.

Published results in the literature suggest that there is a systematic bias in the NCEP flux in the Labrador Sea, whereby the heat loss from the ocean is overestimated (Renfrew

et al., 2002). In addition, the NCEP shortwave radiation is known to be underestimated over the subduction region of the subtropical North Atlantic (Josey, 2001). By comparison the NOC fluxes are in good agreement with buoy data in this region (Josey, 2001) but underestimate ocean heat loss over the western boundary current compared with in situ data (Moore and Renfrew, 2002). It is therefore expected that in the eastern subtropical North Atlantic the NOC fluxes are more accurate than those from the NCEP reanalysis. Despite this, overall closure of the global heat budget is not obtained in the NOC climatology net flux and regions of bias have been identified (refer to chapter 2.3.2 for more details).

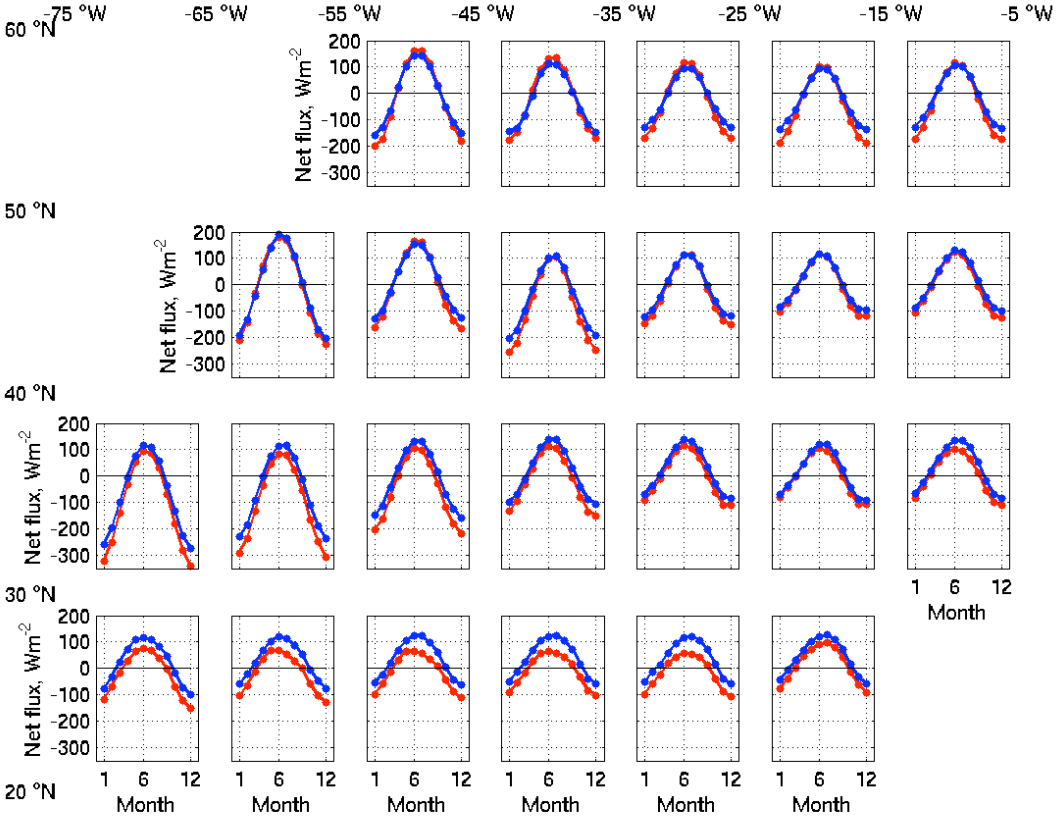


**Figure 6.4** Seasonal cycle in absorbed net flux for NCEP (red) and NOC (blue) derived using monthly averages between 1999 and 2005, values in $Wm^{-2}$.

Comparison of the seasonal cycle in heat storage and absorbed net heat flux (Fig. 6.5) indicates several similarities. In particular both components exhibit maximum ocean heat gain in the summer and maximum ocean heat loss in the winter and the range in each

reaches a maximum at 40-50°N and a minimum at 20-30°N. These results suggest that on these large scales atmospheric forcing plays the dominant role in driving the seasonal cycle in upper ocean temperature, consistent with scaling arguments in Gill and Niiler (1973).

**Table 6.5** Annual range in absorbed net heat flux for NCEP and NOC, with the latter given in brackets, $Wm^{-2}$

| | 75-65°W | 65-55°W | 55-45°W | 45-35°W | 35-25°W | 25-15°W | 15-5°W |
|---|---|---|---|---|---|---|---|
| 50-60°N | - | - | 362 (304) | 312 (258) | 284 (224) | 288 (232) | 291 (234) |
| 40-50°N | - | 404 (392) | 330 (283) | 363 (310) | 262 (235) | 234 (213) | 246 (229) |
| 30-40°N | 433 (340) | 389 (354) | 321 (289) | 261 (246) | 227 (222) | 210 (210) | 212 (219) |
| 20-30°N | 223 (217) | 198 (194) | 174 (188) | 164 (182) | 162 (179) | 187 (187) | - |

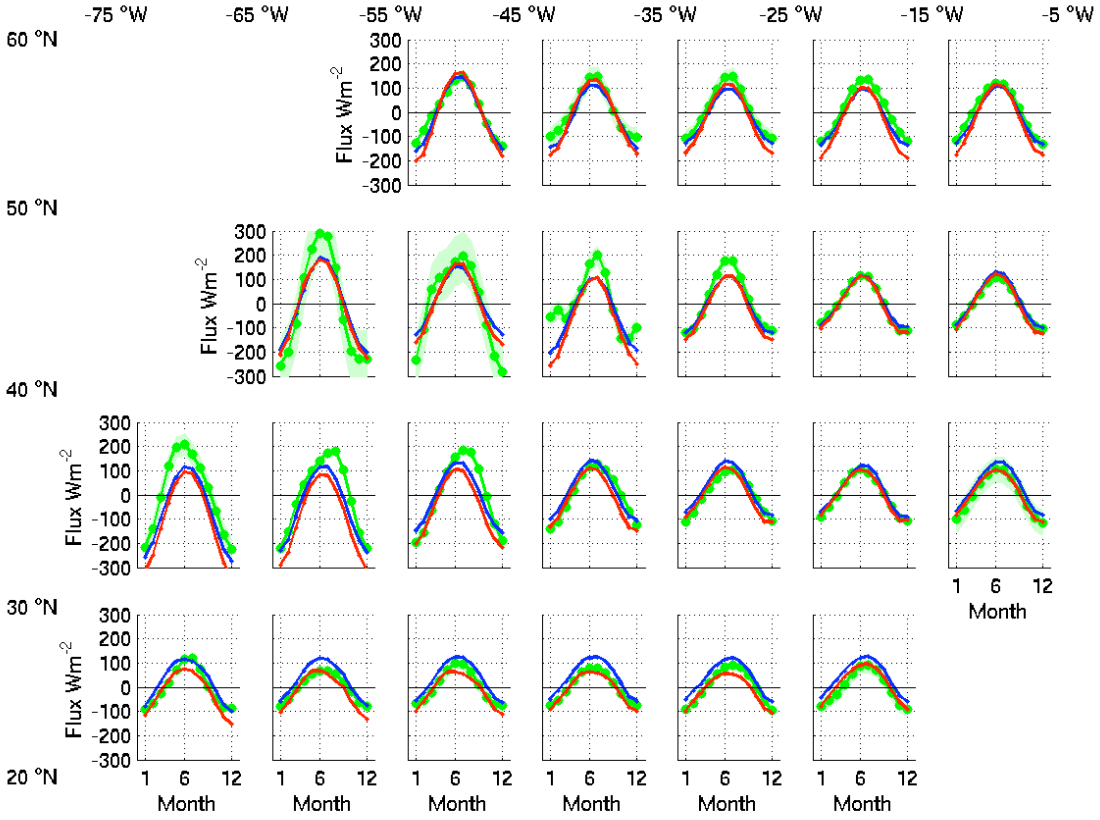


**Figure 6.5** Seasonal cycle in heat storage (green), absorbed net flux for NCEP (red) and NOC (blue) derived using monthly averages between 1999 and 2005, values in $Wm^{-2}$.

Despite this, differences between the seasonal cycle in the upper ocean heat storage and net surface heat flux are apparent. Differences are most notable in the boxes through which the Gulf Stream flows (western basin, 30-50°N). In this region the summertime heat storage is significantly larger (more than 100 $Wm^{-2}$ at some locations) than the observed net heat flux. This indicates that heat is supplied to the upper ocean through some process other than incoming solar radiation.

## 6.4 The Ekman Heat Divergence

In this section the horizontal Ekman heat divergence is quantified using the NCEP and NOC wind stress fields and the Argo-based subsurface temperature field. The annual mean and seasonal cycle are first investigated in subsection 6.4.1. In 6.4.2 the magnitude of the associated errors is quantified.

### 6.4.1 The Annual Mean and Seasonal Cycle

The annual mean Ekman heat divergence has been calculated for 10° x 10° boxes throughout the study region. Values based on the NCEP and NOC wind stress field are given in Table 6.6. In addition, annual mean Ekman heat divergence is also quantified and plotted on a 2° x 2° grid (Fig. 6.6). It can be seen that the northwards Ekman transport warms the upper layer south of 30°N (denoted by a negative heat divergence) while the southward transport cools the upper layer to the north. This heat divergence is typically less than 10 $Wm^{-2}$ throughout the North Atlantic. The main exception to this can be found in the Gulf Stream/NAC region where the wind driven transport divergence cools the upper layer by an annual average of 20-30 $Wm^{-2}$ at 40-50 °N, 55 - 35°W due to strong temperature gradients. The Ekman heat divergence cannot account for the observed discrepancy between the heat storage and net heat flux.

Comparison of the Ekman heat divergence based on the NCEP and NOC wind stress fields indicates little difference between the two. The mean North Atlantic RMS difference is 3 $Wm^{-2}$. Largest RMS differences of 9 $Wm^{-2}$ are found at 40-50°N, 55-45°N. As expected given the underestimate of the subtropical wind stress in NCEP (discussed in chapter 5, section 4.1), the subtropical Ekman heat divergence based on the NCEP wind

stress is smaller than the corresponding value from NOC. However, given the small Ekman heat divergence at this location (typically less than 10 $Wm^{-2}$), the difference is small, less than 2 $Wm^{-2}$ and is only evident in the western basin.

**Table 6.6** Annual mean wind-driven heat divergence for individual 10° x 10° boxes in the North Atlantic based on the NCEP reanalysis wind stress and the NOC climatology wind stress, with the latter given in brackets. Values are in $Wm^{-2}$.

| | 75-65°W | 65-55°W | 55-45°W | 45-35°W | 35-25°W | 25-15°W | 15-5°W |
|---|---|---|---|---|---|---|---|
| 50-60°N | - | - | 1 (1) | 12 (9) | 15 (11) | 9 (8) | 3 (4) |
| 40-50°N | - | - | 28 (29) | 28 (26) | 16 (13) | 9 (8) | 4 (4) |
| 30-40°N | 3 (4) | 5 (7) | 4 (6) | 3 (4) | 2 (2) | 2 (2) | 1 (0) |
| 20-30°N | -6 (-8) | -6 (-7) | -6 (-7) | -5 (-5) | -4 (-4) | 3 (4) | - |

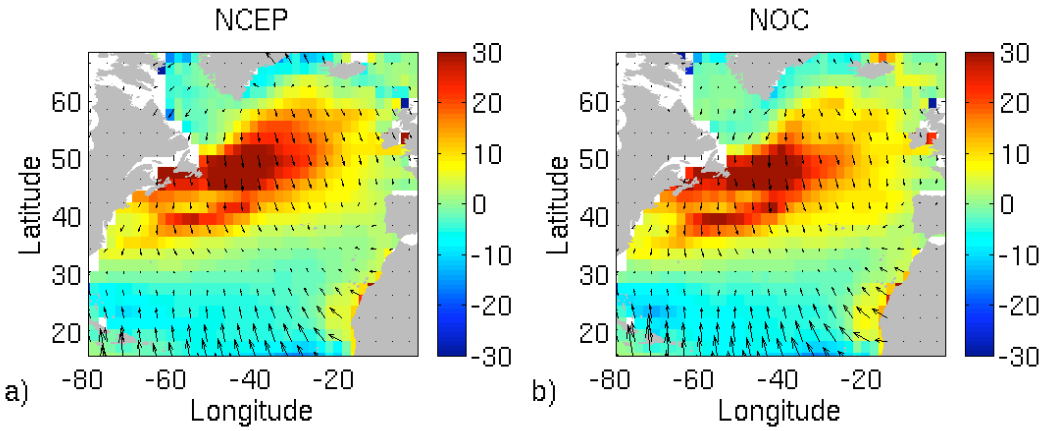


**Figure 6.6** The mean horizontal Ekman heat divergence calculated using a) the NCEP wind stress field and b) the NOC wind stress ($Wm^{-2}$). Vectors indicate the direction of Ekman volume flux.

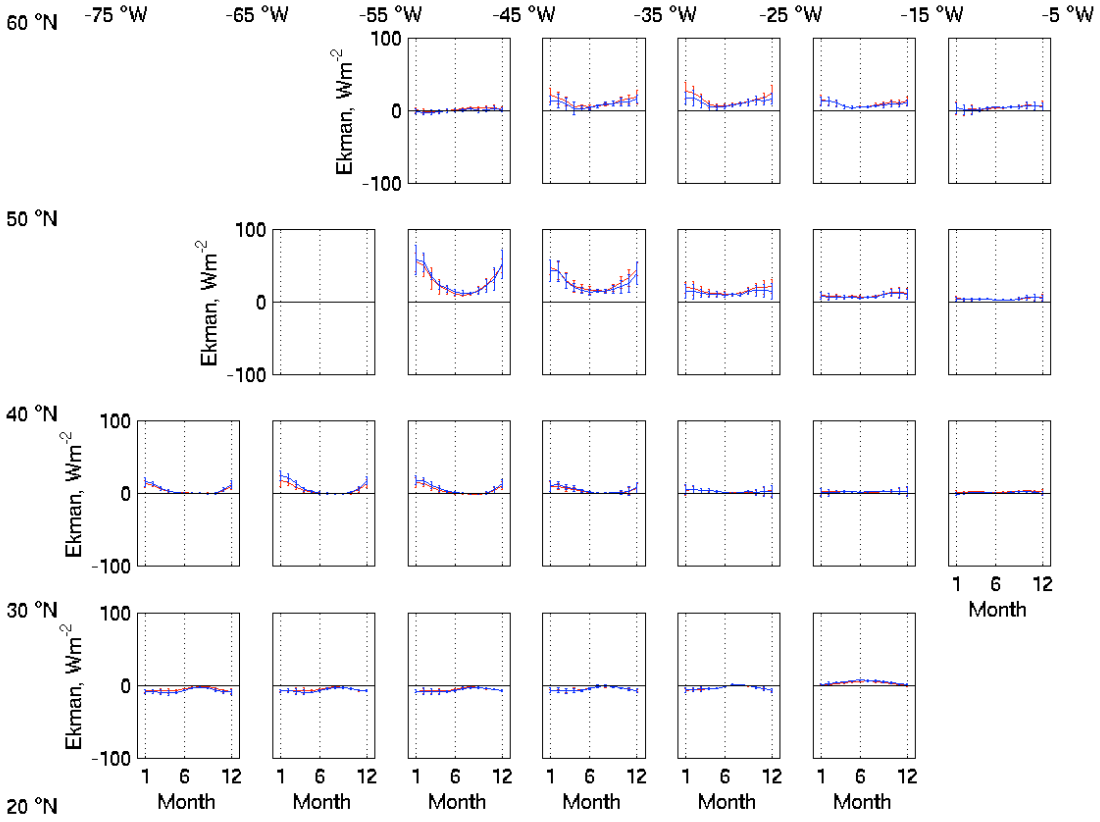


**Figure 6.7** Seasonal cycle in the horizontal Ekman heat divergence for different 10° x 10° boxes in the North Atlantic. Fluxes based on the NCEP (red) and NOC (blue) wind stress fields are shown. The error bars indicate two standard errors of the seasonal values used to obtain the seasonal mean.

The mean seasonal cycle in the Ekman heat divergence is plotted for 10° x 10° boxes in the North Atlantic in Fig 6.7. For ease of comparison, the scale is the same for each subplot. Error bars of two standard errors in seasonal values are also plotted. The strongest seasonal signal in Ekman heat divergence can be found in the Gulf Stream and NAC region with a range of up to 50 $Wm^{-2}$. The annual range is much smaller in the subtropics (< 10 $Wm^{-2}$). However, the seasonal cycle is generally consistent throughout the North Atlantic with strongest heat divergence or divergence (depending on the location) occurring during the winter and spring. The weakest seasonal signal can be found in the centre of the subtropical gyre where the Ekman heat divergence is close to zero throughout the year.

This location roughly corresponds to the centre of the anticyclonic wind stress gyre (chapter 5), where winds are weak and of the opposing sense in the northern and southern parts of the 10° x 10° boxes. As with the annual mean, the seasonal cycle in the Ekman heat divergence from the NCEP and NOC wind stress fields show good agreement with a mean correlation ($r^2$) of 0.82 for all 10° x 10° boxes in the North Atlantic.

### 6.4.2 Sources of Error

There are several sources of error associated with estimating the Ekman heat divergence. In particular, errors arise from uncertainty in i) the depth of the Ekman layer, ii) the temperature field and iii) the wind stress field. Assuming that these three sources of error are independent, the total error, $\Delta Ek$ , can be estimated as

$$\Delta Ek = \sqrt{Er1^2 + Er2^2 + Er3^2} \tag{6.3}$$

where *Er1, Er2* and *Er3* are the Ekman heat divergence errors arising from uncertainty in the different variables. It should be noted that the error arising from uncertainty in the depth of the Ekman layer and the temperature field are actually not independent (since $T_a$ depends on $h$).

The positions of the discrete boundaries used to calculate the temperature gradient (see Fig. 5.12) introduce an additional source of error. However, the sensitivity of the flux to the selected boundaries was investigated and found to be small (ranging from one standard deviation of 0.2 $Wm^{-2}$ in the subtropics, to 1 $Wm^{-2}$ in the subpolar and Gulf Stream regions). This error source is thus excluded here.

The estimated mean error associated with quantifying the seasonal (3-monthly) Ekman heat divergence is given for 10° x 10° boxes in Table 6.7. The total error is generally in the range 1-3 $Wm^{-2}$ south of 40°N, but reaches 10 $Wm^{-2}$ in the 10° x 10° box south of Newfoundland. Although the uncertainty in the Ekman heat divergence is small in comparison to the uncertainty in the heat storage and air-sea flux components, this uncertainty is large relative to the Ekman heat divergence, typically around 30 %.

**Table 6.7** Mean uncertainty in the seasonal Ekman heat divergence, $Wm^{-2}$.

| | 75-65°W | 65-55°W | 55-45°W | 45-35°W | 35-25°W | 25-15°W | 15-5°W |
|---|---|---|---|---|---|---|---|
| 50-60°N | - | - | 3 | 6 | 5 | 3 | - |
| 40-50°N | - | - | 10 | 5 | 3 | 2 | 1 |
| 30-40°N | 3 | 2 | 1 | 1 | 1 | 1 | - |
| 20-30°N | 3 | 2 | 2 | 2 | 2 | 2 | - |

In the following, details are provided on the magnitude of the different error sources and the methods used to derive each error term.

i) Uncertainty in the Depth of the Ekman Boundary Layer

In this study it is assumed that the Ekman layer is confined within the mixed layer. In order to estimate the sensitivity of results to this assumption, the Ekman heat flux is recalculated using a fixed Ekman depth, $Z_e$, set to 40 m (McCulloch and Leach, 1998). Since this may extend below the mixed layer $T_a$ is now calculated using a weighting function to account for the vertical Ekman structure.

$$w(z) = e^{z/Z_e} \sin\left(\frac{-z}{Z_e} + \frac{\pi}{4}\right) \tag{6.4}$$

(e.g. Sato and Rossby 2000; Sato and Polito, 2005) where $w$ is the weighting calculated for each standard depth surface, $z$, normalised to make the sum of the weights equal to 1. The weights $w(z)$ are 0.226 (10 m), 0.213 (15 m), 0.192 (20 m), 0.163 (25 m), 0.124 (30 m), 0.073 (35 m), 0.009 (40 m). The RMS difference between the Ekman heat divergence calculated over the MLD and the fixed 40 m layer provides a measure of the sensitivity to the assumed Ekman depth. The mean RMS difference throughout the North Atlantic is 0.9 $Wm^{-2}$, and the difference ranges from -4 $Wm^{-2}$ to 7 $Wm^{-2}$. Differences are largest during the summer and autumn and at low latitudes corresponding to times and locations of shallow MLD.

ii) Errors in the Temperature Field

The error associated with estimating the temperature, $T_a$, from the Argo dataset is quantified using the model-based analysis, described in chapter 4. To estimate the associated error in $\nabla \cdot T_a$ (and in the Ekman heat flux), it is necessary to know if the sign of the error is the same, or different, at each boundary. Since this is not known, and in view of the fact that this may vary with grid cell and time, it is assumed that the error in the temperature gradient is simply the error in $T_a$ itself ($\Delta T_a$). This represents an average of the extreme cases.

The error in the Ekman heat divergence arising from uncertainty in the temperature field ($E_T$) is thus quantified as

$$E_T = \rho C_p h \upsilon_{e,a} \Delta T_a \tag{6.5}$$

This gives a temporal mean error close to 0 $Wm^{-2}$ in the subtropics and a maximum mean error of 3 $Wm^{-2}$ in the Gulf Stream region. There is a seasonal cycle in the error, with largest uncertainty in the winter months when the fluxes are largest. During this time $E_T$ can reach 13 $Wm^{-2}$.

iii) Errors in the Wind Stress Field.

There are no error estimates for the wind stress fields from the NCEP reanalysis and the NOC climatology. However, comparison of the Ekman heat divergence from these two semi-independent fields provides some indication of the likely errors. The RMS difference in heat divergence calculated from the NCEP and NOC wind stress fields are on average 3 $Wm^{-2}$ for the North Atlantic. Maximum differences occur over the Gulf Stream and NAC and in the subpolar North Atlantic. In these areas, RMS differences between the Ekman heat divergence based on the NCEP and NOC wind stress fields reach 9 $Wm^{-2}$, contributing the largest source of error in estimating the Ekman heat divergence.

In summary, the annual mean wind driven heat divergence for 10° x 10° boxes is typically less than 15 $Wm^{-2}$ except at 40-50°N, 55-25°N where zonal winds are strongest and temperature gradients are large (refer to Figure 5.6). In this region the annual mean heat divergence cools the mixed layer by 15-30 $Wm^{-2}$, with largest values of up to 60 $Wm^{-2}$

in winter and spring. The results indicate that wind-driven heat divergence does not play an important role in the upper ocean heat budget throughout much of the North Atlantic and cannot account for the differences between the heat storage and net heat flux.

### 6.5 The Geostrophic Heat Divergence

The geostrophic velocity field derived using the method in chapter 5.4.2b is used to estimate the geostrophic heat divergence. Annual mean values are given in Table 6.8. The heat divergence can only be calculated for boxes with at least 1 grid point in water deeper than 1000 m along all 4 boundaries (See Fig. 5.12). The values in bold indicate estimates which are based on only a limited number of grid cells around the boundaries, highlighting the values which should be treated with extra caution.

**Table 6.8** Annual mean geostrophic heat divergence for individual 10° x 10° boxes in the North Atlantic, $Wm^{-2}$. Negative values indicate a warming contribution. Bold values should be treated with extra caution.

| | 75-65°W | 65-55°W | 55-45°W | 45-35°W | 35-25°W | 25-15°W | 15-5°W |
|---|---|---|---|---|---|---|---|
| 50-60°N | - | - | **3±2** | 22±10 | -8±9 | **-42±7** | - |
| 40-50°N | - | - | **-161±41** | 3±16 | -24±6 | -21±2 | **-10±2** |
| 30-40°N | 60±16 | -9±4 | -6±3 | 2±3 | 0±2 | 6±2 | - |
| 20-30°N | 13±2 | -9±2 | 8±2 | 27±4 | 11±4 | 5±6 | - |

The annual mean geostrophic divergence typically cools the upper ocean at low latitudes and supplies heat in the boxes through which the Gulf Stream and NAC flow (except for the boxes at 45-35°W where there is strong zonal advection of relatively cool surface waters at the western edge). The mean geostrophic heat divergence varies from 0 to more than 150 $Wm^{-2}$, with largest values in the box east of Newfoundland. There is large variability in the geostrophic heat divergence, with a mean temporal standard deviation of more than 30 $Wm^{-2}$. However, no seasonal signal was evident. Geostrophic driven heat divergence may partially account for the observed difference between the heat storage and net surface heat flux at some locations.

Errors arise in the geostrophic heat divergence from uncertainty in $\upsilon_{ag}$, $T_a$ and $h$. The error arising from uncertainty in $T_a$ was obtained in the same way as for the Ekman heat divergence. The error in $\upsilon_{a,g}$ was estimated from the error in the Sea Surface Height, as provided by Alderson and Killworth (2005). Errors in the velocity field arising from errors in the temperature and (unknown) salinity were assumed to be negligible compared with this error. This assumption is valid since vertical variations in temperature and salinity are small within the upper ocean, minimising the baroclinic velocity component.

The mean magnitude of the error in $\upsilon_{a,g}$ for 10° x 10° boxes on seasonal timescales is 0.001 $ms^{-1}$ (approximately 10 %). However, there is significant spatial variability. In addition, this error estimate presents a lower limit of the uncertainty since it does not include interpolation errors. Thus the mean error in the geostrophic velocity is set to 0.002 $ms^{-1}$. The total estimated error in the geostrophic heat divergence is given for 10° x 10° boxes in Table 6.8. The error is smallest (2-6 $Wm^{-2}$) in the subtropics and largest, up to 41 $Wm^{-2}$, in the Gulf Stream region. This error may be underestimated in view of the large smoothing in the geostrophic velocity field.

### 6.6 The Diffusive Heat Flux

The diffusive heat flux has been quantified using the method outlined in section 5.6.5. Mean values of the total diffusive heat flux for 10° x 10° boxes in the North Atlantic are given in Table 6.9. On average the combined horizontal and vertical diffusion removes around 10-30 $Wm^{-2}$ of heat from the upper 300 m. However, in the northwestern North Atlantic, at 40-60°N, 55-45°W, diffusion can warm the upper ocean by more than 50 $Wm^{-2}$. The seasonal cycle in the diffusive heat divergence is plotted in Fig. 6.8. The heat divergence associated with the horizontal and vertical diffusion are shown separately. The horizontal diffusive heat divergence exhibits no seasonal signal and is most significant in the Gulf Stream region and at high latitudes. The vertical diffusive heat divergence does exhibit a seasonal signal and is typically smaller than the horizontal diffusive heat divergence, except in the subtropics and eastern mid-latitudes. Largest vertical diffusive fluxes occur during late summer when the stratification is strongest. Given the high level of uncertainty in the diffusion coefficients, the error in the diffusive heat divergence is

assumed to be100 %. The diffusive heat divergence is of the wrong sense to account for the observed difference between the heat storage and net heat flux in the western basin.

**Table 6.9** The annual mean combined horizontal and vertical diffusive heat divergence for 10° x 10° boxes in the North Atlantic, based on three-monthly values.

| | 75-65°W | 65-55°W | 55-45°W | 45-35°W | 35-25°W | 25-15°W | 15-5°W |
|---|---|---|---|---|---|---|---|
| 50-60°N | - | - | -55 | -24 | -16 | 27 | 47 |
| 40-50°N | - | 19 | -76 | 34 | 17 | 5 | -3 |
| 30-40°N | - | 29 | 35 | 22 | 4 | 4 | 4 |
| 20-30°N | 10 | 9 | 15 | 21 | 29 | 22 | - |

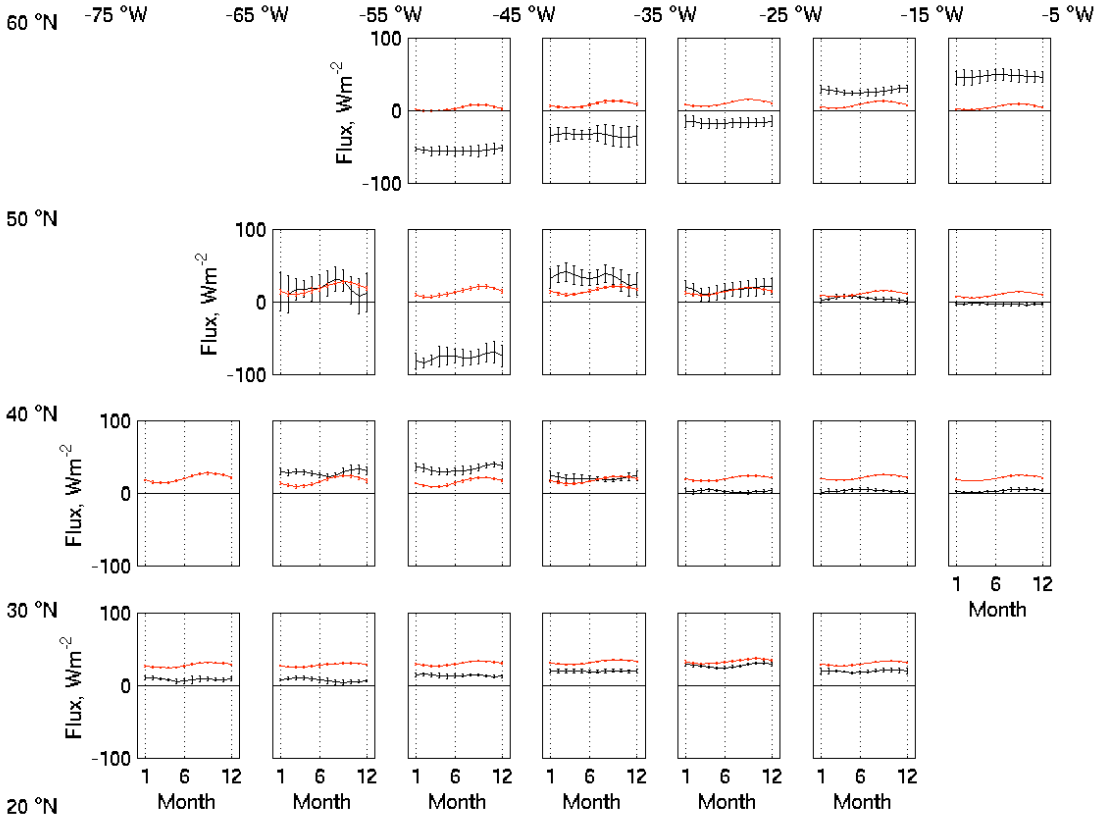


**Figure 6.8** Seasonal cycle in the diffusive heat flux for different 10° x 10° boxes in the North Atlantic ($Wm^{-2}$). Horizontal (black) and vertical diffusion (red) are shown separately. Error bars are two standard errors of the seasonal values used to obtain the seasonal mean.

## 6.7 The Heat Budget

Having presented the heat budget components in the preceding sections, the level of closure of the heat budget is now investigated. This analysis aims to provide further insight into the accuracy of the Argo-based heat budget terms and to yield information on the accuracy of the net heat flux fields. A brief overview of the annual mean heat budget for all 10° x 10° boxes in the North Atlantic is first provided in section 6.7.1. In section 6.7.2 through 6.7.4, the annual mean heat budget and the seasonal cycle in the heat budget components are investigated in more detail for 3 regions of the North Atlantic.

### 6.7.1 The Annual Mean Heat Budget of the North Atlantic

The closure obtained from the annual mean Argo-based heat budget is now investigated. The level of closure obtained by summing all of the components is referred to as the heat budget residual, $R$ (equation 6.6). Although not presented in detail above due to its small magnitude (less than 3 Wm, section 6.2.1), the entrainment associated with vertical advection is included here. $R$ is given for individual 10° x 10° boxes in Tables 6.10 a) and b) for the NCEP and NOC atmospheric variables, respectively. These values are also presented graphically in Fig. 6.9. The total error, which includes an estimate of the heat storage, advective and diffusive errors is also given; the error associated with the net surface heat flux is not included. A positive heat budget residual indicates that the observed heat storage is less than can be accounted for by combined atmospheric, advective and diffusive fluxes of heat.

$$R = Q + Q_{-h} - \rho C_p \left[ h \frac{\partial T_a}{\partial t} - h \upsilon_a \cdot \nabla T_a + (T_a - T_{-h}) w_{-h} - h k_{x,y} \cdot \nabla^2 T_a - k_{z,-h} \frac{\partial T}{\partial z} \right] \qquad (6.6)$$

Comparison of $R$ from the NCEP-based heat budget (i.e. the heat budget based on the Argo float data and the NCEP atmospheric variables) and the NOC-based heat budget reveals smaller values from NOC for 14 out of 20 of the 10° x 10° boxes. The mean residual in the NOC-based heat budget analysis is typically around 20 ± 30 $Wm^{-2}$ south of

30°N. However, *R* is larger over the Gulf Stream and NAC boxes with a maximum value of 219±136 $Wm^{-2}$ at 40-50°N, 55-45°W.

**Table 6.10** The annual mean heat budget residual, ($Wm^{-2}$) based on a) NCEP and b) NOC atmospheric variables. Bold text indicates where closure of the heat budget is obtained to within the quoted error (i.e. residual not significantly different from zero).

| a) | 75-65°W | 65-55°W | 55-45°W | 45-35°W | 35-25°W | 25-15°W | 15-5°W |
|---|---|---|---|---|---|---|---|
| 50-60°N | - | - | **30±57** | **-29±55** | **-29±40** | -46±32 | - |
| 40-50°N | - | - | 206±136 | -148±55 | -47±32 | **-4±12** | **3±18** |
| 30-40°N | - | -128±34 | -89±40 | -49±23 | **-8±9** | -15±9 | - |
| 20-30°N | -40±20 | **-13±22** | **-32±31** | -54±24 | -55±35 | **-16±38** | - |

| b) | 75-65°W | 65-55°W | 55-45°W | 45-35°W | 35-25°W | 25-15°W | 15-5°W |
|---|---|---|---|---|---|---|---|
| 50-60°N | - | - | **40±57** | **-26±55** | **-14±40** | **-25±32** | - |
| 40-50°N | - | - | 219±136 | -116±55 | **-29±32** | **7±12** | 20±18 |
| 30-40°N | - | -78±34 | -49±40 | **-17±23** | 17±9 | **0±9** | - |
| 20-30°N | **7±20** | 36±22 | **16±31** | **-5±24** | **-4±35** | **12±38** | |

The Argo based annual mean heat budget appears accurate in the subtropics and in the eastern basin. In these regions the advective and diffusive heat divergence is expected to be low. Comparison of the heat budget residual based on the NCEP and NOC atmospheric variables in the eastern subtropical North Atlantic suggests that the latter product is the more accurate one. This result is consistent with findings reported in Josey (2001) in which the NCEP and NOC net flux fields were compared to high quality flux data from buoys.

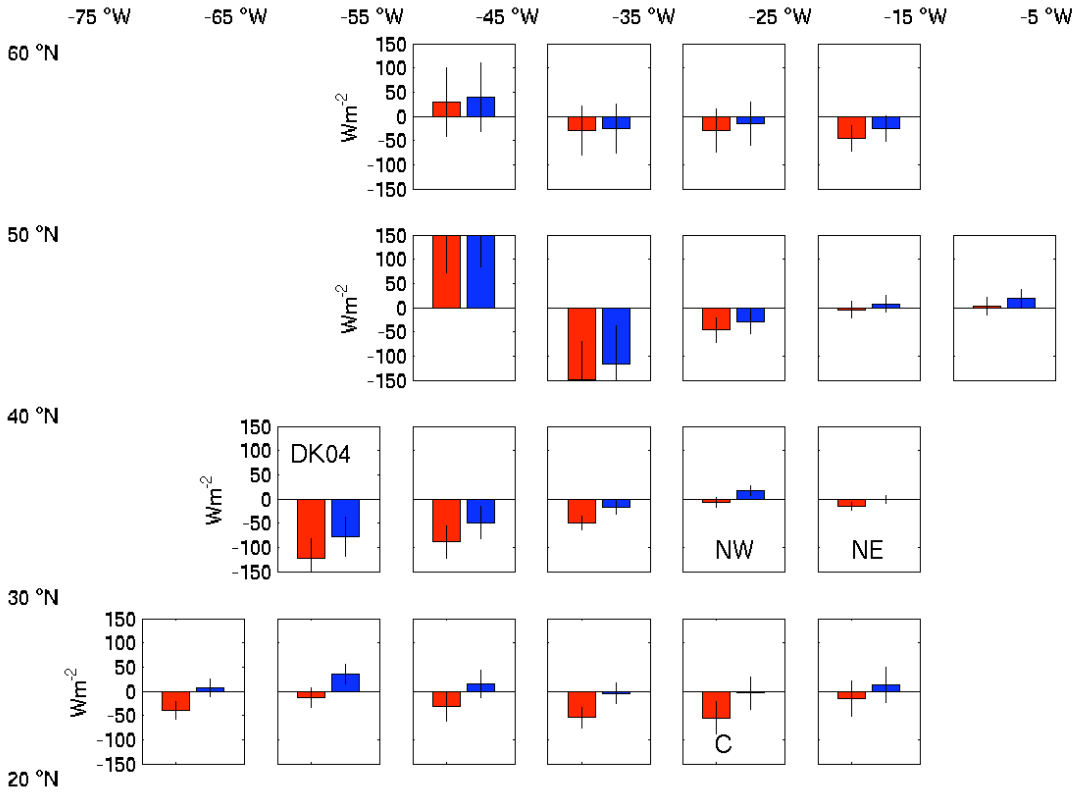


**Figure 6.9** Graphical representation of *R* as given in Table 6. 10. NCEP-based heat budget residual in red, NOC-based values in blue. NW, NE and C represent the 10° x 10° boxes that the northwest, northeast and central subduction buoys lie in. DK04 indicates the study region of Dong and Kelly (2004).

In the Gulf Stream region, where advection and diffusion are likely to play a more important role in the heat budget, there is a much larger residual. It may be that in this region both the NCEP reanalysis and NOC climatology heat fluxes are overestimated. However, results in the literature indicate that although the NCEP reanalysis fluxes do overestimate ocean heat loss in this region, the ocean heat loss in the NOC climatology is underestimated (Moore and Renfrew, 2002). The NCEP and NOC fluxes therefore represent the likely upper and lower limits of heat loss in this region, thus the large negative residual obtained for each suggests a significant bias in the Argo-based terms here.

6.7.2 The Eastern Subtropical North Atlantic

In the eastern subtropical North Atlantic the error in the Argo-based heat storage is relatively small, (typically around 20 $Wm^{-2}$ on seasonal timescales) and the accuracy of the NCEP and NOC heat fluxes has been assessed (Moyer and Weller, 1997; Josey et al., 1999; Josey 2001). Thus, this region provides an ideal location at which to examine the accuracy of the seasonal cycle in the Argo-based heat budget in more detail. Previous assessments of the accuracy of the NCEP and NOC net heat flux have been carried out in the eastern subtropics using data from 3 buoys referred to as the North West subduction buoy (NW), the North East subduction buoy (NE) and the Central subduction buoy (C). The 10° x 10° boxes in which these buoys lie are denoted on Fig. 6.9.

The seasonal cycles in the various heat budget components for the 10° x 10° box covering 20-30°N, 35-25°W (in which lies the central subduction buoy) are plotted in Fig. 6.10. The net heat flux, heat storage and combined advective and diffusive heat divergence (henceforth referred to simply as heat divergence) are all shown. At this location the main processes controlling seasonal variations in the upper ocean heat storage are essentially one dimensional, with largest heat exchange between the atmosphere and the upper ocean and the seasonal cycle of heat storage largely following that of the net heat flux. The advective processes are relatively small, with a mean 4 $Wm^{-2}$ wind-driven heating and an 11 $Wm^{-2}$ geostrophic-driven cooling (Tables 6.6, 6.8). The diffusive contribution is slightly larger, with a mean 29 $Wm^{-2}$ cooling (Table 6.9).

The heat budget residual based on both the NOC and NCEP atmospheric fields is also shown in Fig. 6.10. Despite the better agreement of the seasonal cycle in heat storage with the NCEP net heat flux, the heat budget residual based on the NOC net heat flux is significantly smaller than that from NCEP throughout the year, with the removal of heat through divergence approximately balancing the offset between the heat storage and the NOC net heat flux. Both geostrophic currents and diffusive processes drive this loss of heat from the upper ocean. This result suggests that the NOC net heat flux is more accurate than the NCEP net heat flux at this location. This is consistent with the results of Josey (2001). The seasonal heat budget residual based on the NOC net heat flux is typically around 15-20 $Wm^{-2}$, less than the estimated errors throughout the year. This result

indicates that the Argo dataset can be usefully used for studies of the heat budget in the eastern subtropical North Atlantic.

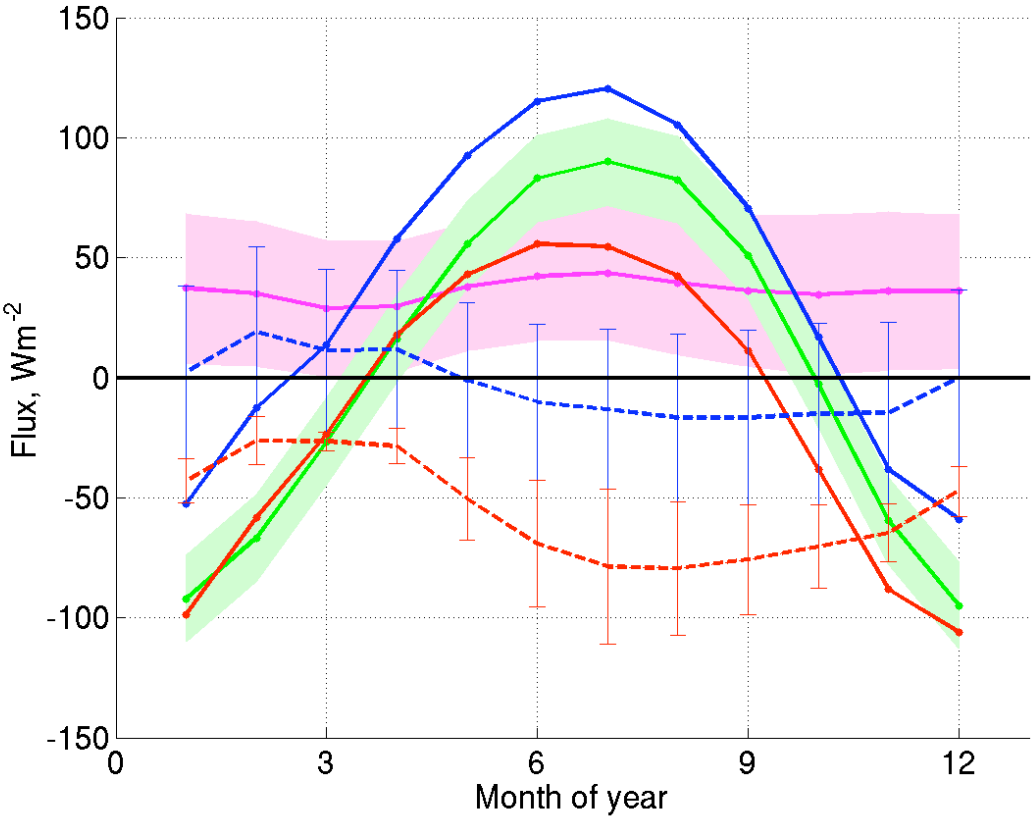


**Figure 6.10** The seasonal cycle in the heat budget components at 20-30°N, 35-25°W. The NCEP net heat flux (red), NOC net heat flux (blue), heat storage (green), heat divergence (pink), the NCEP heat budget residual (red dashed) and the NOC heat budget residual (blue dashed) are shown. Shading indicates estimated errors for each term.

### 6.8.3 Eastern Mid-Latitudes

In the eastern mid-latitudes of the North Atlantic heat fluxes from the NCEP reanalysis and the NOC climatology are in good agreement (Fig. 6.4), with RMS differences of 14 $Wm^{-2}$ at 40-50°N, 25-15°W. This result suggests that the errors in net heat flux are likely to be smaller here than at other locations in the North Atlantic (see Table 6.4 for RMS differences at all 10° x 10° boxes). The Argo-based heat budget components and

the heat budget residual are plotted for the 10° x 10° box covering 40-50°N, 25-15°W in Fig. 6.11. The heat storage and the absorbed net flux have a maximum magnitude of more than 100 $Wm^{-2}$. Comparatively the heat divergence is relatively small with maximum values of 14 ± 6 $Wm^{-2}$.

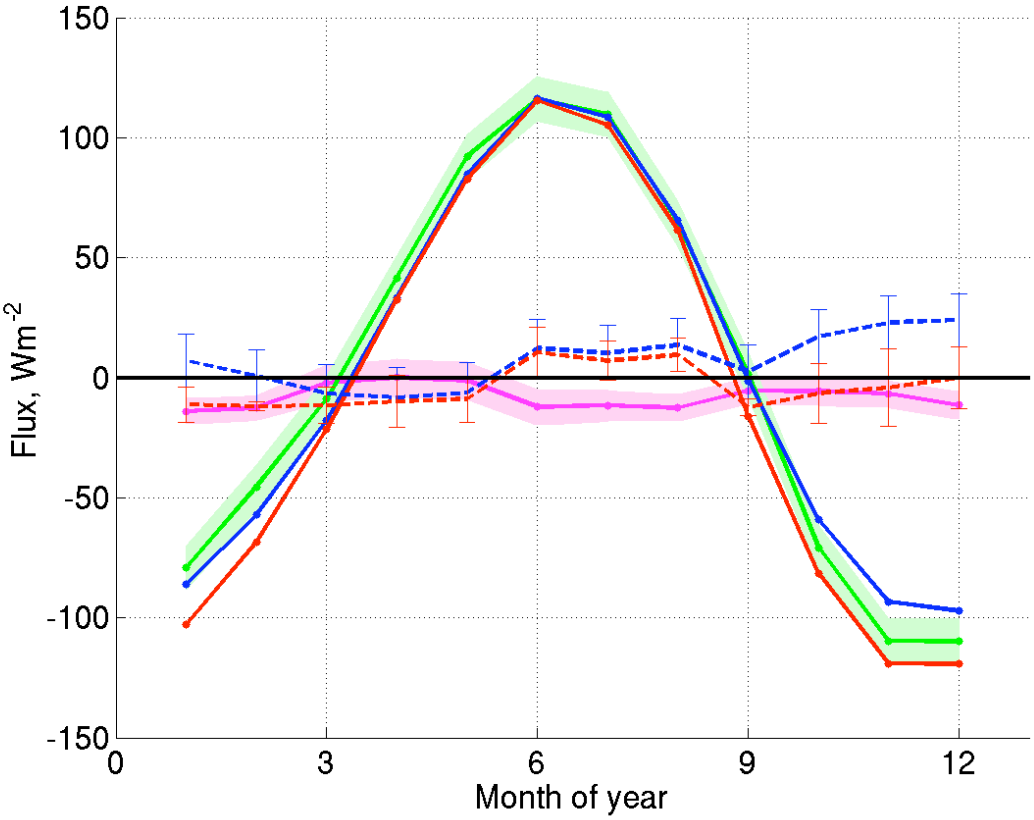


**Figure 6.11** The seasonal cycle in the heat budget components at 40-50°N, 25-15°W. The NCEP net heat flux (red), NOC net heat flux (blue), heat storage (green), heat divergence (pink), the NCEP heat budget residual (red dashed) and the NOC heat budget residual (blue dashed) are shown. Shading indicates estimated errors for each term.

At this location the NCEP annual mean residual is less than that from NOC, being just -4±12 $Wm^{-2}$. Examination of the seasonal signal in the heat budget residual based on the 2 atmospheric fields reveals smaller residuals based on the NOC net heat flux during the 1st half of the year and smaller residuals based on the NCEP net heat flux during the 2nd half of the year. Throughout much of the year the residual based on both the NCEP and

NOC net heat flux is less than the estimated errors, indicating that the reanalysis, climatology and Argo-based heat budget components are of good accuracy in this region. However, at certain times of the year the heat budget residuals do exceed the expected error. For example, between October and December the residual from the NOC net flux is larger than the estimated errors, with a maximum residual of 24 ± 11 $Wm^{-2}$ in December. The nature of this residual indicates that more heat is lost from the upper ocean than can be accounted for by either heat divergence or heat exchange with the atmosphere. McCulloch and Leach (1998) examined the heat budget of the upper 500 m in this region and achieved similar results. In view of this, and the smaller residual attained from the NCEP net heat flux during this time of year (-4 $Wm^{-2}$) it is concluded that the residual is due to an underestimate of the heat loss in the NOC climatology and not errors in the other Argo-based heat budget components. The Argo dataset can therefore be usefully used for studies of the heat budget in the eastern mid-latitudes.

### 6.7.4 The Western Boundary Current

An analysis in the region of the western boundary current is now undertaken to assess the likely accuracy of the Argo-based heat divergence. The heat budget in this region is likely to be significantly different from those previously considered due to the presence of the Gulf Stream. In view of the large heat budget residual and the large uncertainty in the heat budget components at this location, the Argo heat budget cannot be used to derive information on the accuracy of the NCEP and NOC net heat flux.

The heat budget components for the 10° x 10° box 30-40°N, 65-55°W are plotted in Fig. 6.12. The primary balance is between the net heat flux and the heat storage. This result is consistent with a model-based study of the mixed layer temperature tendency in this region (Dong and Kelly, 2004, henceforth DK04). The heat divergence contribution to the heat budget is relatively small, with a mean cooling of 26 $Wm^{-2}$. DK04 also noted the small annual mean contribution of this term, although their results suggest that the heat divergence contributed a net warming.

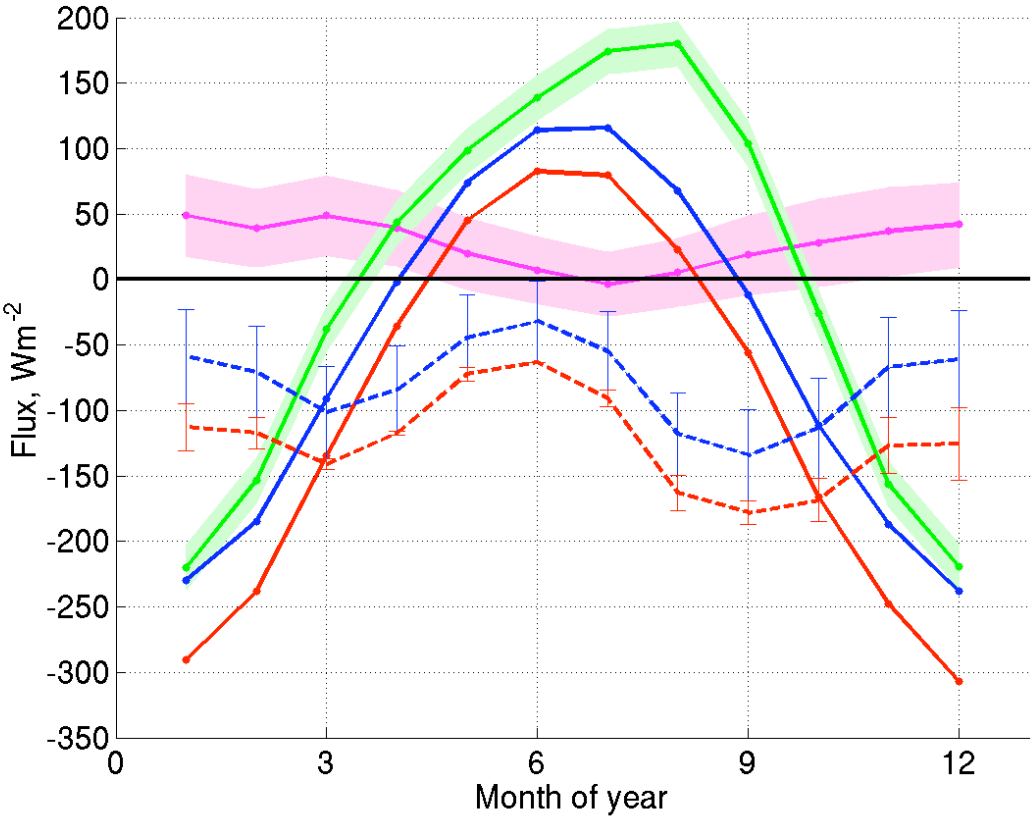


**Figure 6.12** The seasonal cycle in the heat budget components at 30-40°N, 65-55°W. The NCEP surface heat flux (red), NOC surface heat flux (blue), heat storage (green), heat divergence (pink) the NCEP heat budget residual (red dashed) and the NOC heat budget residual (blue dashed) are shown. Shading indicates estimated errors for each term.

Unlike in the subtropical and eastern mid-latitude North Atlantic, the mean heat budget residual is not close to zero, being -128±34 and -78±31 $Wm^{-2}$ based on the NCEP and NOC atmospheric fields, respectively. Examination of the seasonal cycle in the heat budget residual reveals smallest values during May to July and largest values during September when both the NCEP reanalysis and NOC climatology net heat flux is used.

In view of the over-smoothing in the geostrophic velocity field and the uncertainty in the diffusion coefficients it is expected that underestimated heat divergence may account for this residual, with the time and space scales on which this term is important unresolved by the Argo dataset. LB82 and H89 estimated the heat divergence as a residual of the heat

storage and net surface heat flux (referred to as the implied heat divergence). Following this approach an implied heat divergence of -110±17 $Wm^{-2}$ and -63±17 $Wm^{-2}$ is obtained at 30-40°N, 65-55°W using NCEP and NOC atmospheric fields, respectively. Findings presented in the literature indicate that in this region, the wintertime heat loss in NCEP is overestimated, while in NOC it is underestimated (Moore and Renfrew, 2002). It can therefore be expected that the heat divergence lies somewhere between the two implied values quoted above. The implied heat divergence varies throughout the year with maximum heating contributions in March and September of 50-100 $Wm^{-2}$ and 110-160 $Wm^{-2}$, respectively. This seasonal variation is broadly consistent with that presented in LB82 and H89 at this latitude band. However, in view of the large range in implied heat divergence based on the NCEP and NOC atmospheric fields it is concluded here that without additional detailed information on the expected accuracy of atmospheric fields, implied estimates of heat divergence should be interpreted with caution.

### 6.8 Summary

In this chapter the heat storage has been quantified over both the mixed layer and a fixed 300 m layer. While the mixed layer definition minimised the heat storage errors, the seasonal cycle in mixed layer heat storage exhibited asymmetry atypical of the seasonal cycle in heat storage presented in existing studies in the literature. These published studies tend to consider the heat storage over a fixed depth, with mixed-layer heat storage analyses typically restricted to the tropical oceans where temporal variations in the MLD are small. However, analysis of the mixed layer heat storage may provide insight into the processes of upper-ocean mixing and thus accurate derivation of this term is important. While the Argo dataset can be used to quantify this variable to a high degree of accuracy, its asymmetry at high latitudes suggests that all processes associated with this term may not be fully quantified. A more in depth analysis of the mixed layer heat storage and heat budget is beyond the scope of this study, and a fixed depth heat storage is considered in the main part of this chapter.

The fixed depth heat budget analysis presented in this chapter indicates that the net heat flux is the dominant process driving temporal variations in upper ocean heat storage,

with the seasonal cycle in heat storage closely following the net heat flux seasonal cycle. This conclusion is consistent with existing studies in the literature, which have used scaling arguments, observations and models to quantify the magnitude of the heat budget components (Gill and Niiler, 1973; Hsiung et al., 1989; Dong and Kelly, 2004).

Despite the similarities in the seasonal signal of these two heat budget components, on average the annual range in heat storage is larger than the annual range in net heat flux, with values of 351 $Wm^{-2}$, 239 $Wm^{-2}$ and 272 $Wm^{-2}$ for the heat storage, NCEP reanalysis net flux and NOC climatology net flux, respectively. The differences between the heat storage and net heat flux are small in the subtropical and eastern North Atlantic, but become large in the Gulf Stream region. In the 10° x 10° boxes through which the Gulf Stream flows (30-40°N, 75-45°W and 40-50°N, 65-35°W) the summertime heat storage can be more than 100 $Wm^{-2}$ larger than the net heat flux. The nature of this difference suggests that heat divergence may contribute a warming of the upper ocean in this region. Examination of the heat divergence terms is not consistent with this hypothesis; the average -19±9 $Wm^{-2}$ geostrophic heating is offset by the 12±3 $Wm^{-2}$ wind driven cooling and 36±36 $Wm^{-2}$ diffusive heat loss. It is therefore expected that it may not be possible to fully resolve the time and space scales on which the heat divergence is important using the Argo dataset, thus limiting its use for analyses of this nature in regions of high mesoscale variability.

Away from the western boundary and subpolar North Atlantic the heat budget residual was typically less than 20 $Wm^{-2}$ (when the NOC net heat flux was used). This heat budget residual remained small throughout the year in both the eastern subtropics and eastern mid-latitudes. This result highlights the usefulness of the Argo dataset for investigations of seasonal heat budget in this region.

Gleckler and Weare (1997) suggest that the uncertainty in the annual mean net heat flux is approximately 40 $Wm^{-2}$. In view of this high uncertainty and the comparatively low uncertainty in the remaining heat budget components (except in the western mid-latitudes and subpolar regions), the residual in the Argo-based heat budget provides useful insight into which of the flux fields is likely to be the most accurate. The annual mean heat budget was closed (i.e. the residual was zero) to within the estimated error for 13 out of 20 of the 10° x 10° boxes when the NOC atmospheric fields were used. This fell to 9 when the

NCEP atmospheric fields were used, suggesting that in general the NOC atmospheric fields may be more accurate than those from the NCEP reanalysis. Examination of the seasonal cycle in the heat budget residual in 2 regions of the North Atlantic suggested that the NOC fluxes were more accurate than those from NCEP throughout the year in the subtropics. Within the eastern mid-latitudes the differences between the NCEP and NOC net heat flux were small, with both the NCEP and NOC heat budget residual smaller than the estimated error throughout most of the year. However, during the period October-December the NCEP net heat flux is expected to be more accurate than that from NOC, which overestimates the net heat loss.

# Chapter 7: Temporal Changes in the North Atlantic Heat Budget

## 7.1 Introduction

Having investigated the seasonal cycle in the heat budget components in chapter 6, the interannual variability in the North Atlantic heat budget is now considered. Of particular interest is the magnitude of the variability in the heat budget components. In addition, the correlation between the various heat budget components and temporal trends in Argo-based estimates of the temperature are examined. Although this analysis is restricted by the relatively short time series of Argo data currently available, some insight into the utility of the Argo dataset for studies of this nature may be gained.

In the following, variability in the components of the heat budget is first discussed in section 7.2, the main aim being to determine whether the Argo-based heat budget can be usefully employed to identify significant interannual variability. The relationship between interannual variability in the different heat budget components is then investigated. A case study of an interannual event is examined in more detail in section 7.3. The mean trends in temperature between 1999 and 2005 are discussed in section 7.4. The primary purpose of this section is to ascertain whether warming and cooling trends documented in the literature, can be captured by Argo. A summary follows in section 7.5.

## 7.2 Interannual Variability in the North Atlantic Heat Budget

In this section, the interannual variability in the heat budget throughout the seven-year period, 1999 – 2005, is investigated. In view of the smaller errors in heat storage over the mixed layer than over the fixed depth, the focus here is on the mixed layer heat budget. The standard deviation of the anomalous heat budget components (i.e. seasonal cycle removed), which is used to provide a measure of the interannual variability (subsection 7.2.1) is first analysed. The correlation between the various heat budget components is then considered in more detail in subsection 7.2.2.

### 7.2.1 The Magnitude of Variability in the Heat Budget Components

The standard deviation in the heat budget components is used here as an indication of the interannual variability. The mean seasonal cycle is first removed from each component. The standard deviation in each heat budget component is given for various regions of the North Atlantic in Table 7.1.

**Table 7.1** One standard deviation of the various heat budget components after removal of the seven-year mean seasonal cycle. Results are shown for four subregions of the North Atlantic: the subtropics (20-30°N, 75-15°W), the eastern midlatitudes (30-50°N, 35-5°W), the Gulf Stream region (30-50°N, 75-35°W) and the subpolar North Atlantic (north of 50°N).

| Heat budget component | Subregion, values in $Wm^{-2}$ | | | |
|---|---|---|---|---|
| | Subtropics | Eastern midlatitudes | Gulf Stream region | Subpolar North Atlantic |
| Net heat flux: NCEP | 13 | 13 | 23 | 18 |
| Net heat flux: NOC | 14 | 11 | 18 | 24 |
| Heat storage | 11 | 23 | 40 | 38 |
| Heat divergence | 6 | 7 | 23 | 9 |
| Entrainment | 3 | 7 | 10 | 11 |

One standard deviation in the heat storage anomaly for the region 20-30°N, 75-15°W (i.e. where the Argo-based heat budget is expected to be most accurate, see chapter 6) is 11 $Wm^{-2}$, while one standard deviation in the absorbed surface heat flux anomaly in the same region is 14 $Wm^{-2}$. The variability in the heat entrainment, the Ekman, geostrophic and diffusive heat divergence is relatively small, with one standard deviation of less than 5 $Wm^{-2}$ for each individual component. In view of this result it is unlikely that the heat divergence plays a dominant role in driving interannual variations in the temperature of the upper ocean in the subtropical North Atlantic.

Elsewhere in the North Atlantic interannual variability is larger in all heat budget components, with one standard deviation exceeding 20 $Wm^{-2}$ in both the heat storage and net heat flux anomalies over the Gulf Stream region. At this location one standard

deviation in the geostrophic and Ekman heat divergence anomalies is also larger, 19 and 7 $Wm^{-2}$, respectively. Thus heat divergence, in addition to the net surface heat flux, may play a role in driving interannual variations at this location.

The estimated mean subtropical North Atlantic heat storage error (presented in chapter 6) is 4 $Wm^{-2}$. Thus it should be possible to identify significant interannual variations (identified as anomalies exceeding twice the estimated error) in the upper ocean heat storage at this location. Within the Gulf Stream region the heat storage error is of comparable magnitude (around 20 $Wm^{-2}$) to one standard deviation in the heat storage anomaly. Thus investigations of interannual variability from Argo are more limited here.

### 7.2.2 Correlation Between the Heat Budget Components

The correlation between the heat storage anomaly and other heat budget components is investigated to determine which processes may be responsible for driving interannual variability in the upper ocean temperature field. For this analysis the heat budget components are first smoothed by application of a five-point running mean to reduce intra-annual signals. The correlation ($r^2$) between the heat storage anomaly and anomalies of other heat budget components is shown for individual 10° x 10° boxes in Fig. 7.1. Correlations with the NCEP net heat flux, the NOC net heat flux, the heat entrainment and the combined advective and diffusive heat divergence (referred to simply as heat divergence) are shown.

Heat storage anomalies in the North Atlantic are most strongly correlated with net heat flux anomalies, with correlations ($r^2$) reaching a maximum of 0.73. The correlations exhibit large spatial variations and differ for the NCEP and NOC absorbed heat fluxes with NCEP typically better correlated with the heat storage anomaly than NOC; On average for the whole North Atlantic the correlation between heat storage anomaly and the NCEP net heat flux anomaly is 0.28, compared to 0.17 for the NOC net heat flux anomaly. Thus, despite a systematic bias in the NCEP heat fluxes, the interannual variability in this flux product is better resolved than in the ship-based NOC fields.

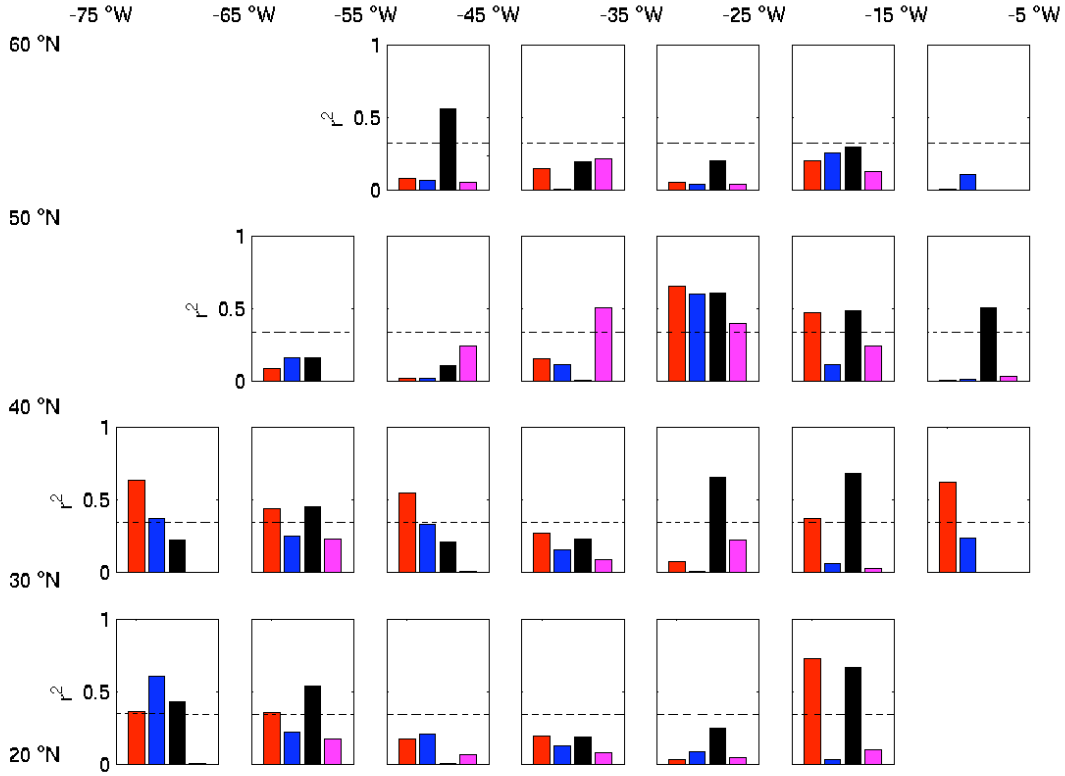


**Figure 7.1** Correlation between heat storage anomaly and heat budget components for 10° x 10° boxes in the North Atlantic. Correlation with anomalies of NCEP absorbed net heat flux (red), NOC absorbed net heat flux (blue), heat entrainment (black) and heat divergence (pink). The dashed line indicates the 95 % significance level.

The correlation between the heat storage anomaly and the heat entrainment anomaly is largest in the eastern basin and in the Labrador Sea. In these regions, the atmosphere drives temperature variations in the thermocline and deeper waters. Comparatively the correlation between the heat storage and heat divergence anomalies is typically small. Largest correlations between the heat storage and heat divergence anomalies occur in the central basin at 40-50°N, along the path of the NAC.

In summary these results suggest that the major contributor to interannual variations in the temperature of the mixed layer is interannual variability in the net surface heat flux. However, anomalies in entrainment are also well correlated with heat storage anomalies in

some regions, particularly in the eastern basin and the Labrador Sea. At 40-50°N, correlation with heat divergence is also significant. It is important to note that the seven-year time series from Argo limits the accuracy of this analysis. Analysis of the relationship between advective heat divergence and upper ocean heat storage is further restricted by the short period for which the geostrophic velocity fields are available.

### 7.3 A Case-Study of Interannual Variability

A case study of an interannual event is considered in this section. The aim here is to provide further analysis of the processes responsible for observed interannual variability in the temperature of the upper ocean. The 10° x 10° box covering 20-30°N, 25-15°W is used here. At this location the uncertainty in the heat storage is small, with estimated mean errors of 6 $Wm^{-2}$. Interannual events at other 10° x 10° boxes could also be considered here**.** However, the errors in heat storage and the heat budget residual are larger at other locations and thus it can be expected that an analysis of this nature elsewhere in the North Atlantic may be less accurate.

The heat budget components throughout the seven-year time series are shown for the 10° x 10° box covering 20-30°N, 25-15°W in Fig. 7.2 a). The anomalous heat budget components (i.e. seasonal cycle removed) are filtered by a 5-point running mean and plotted in Fig. 7.2 b and c). The anomalies indicate the dominant role of the absorbed heat flux in driving interannual variations in the mixed layer heat storage, as noted in the previous section. There is particularly good coherence between the NCEP heat flux and the mixed layer heat storage anomalies, with a correlation of 0.73. It should be noted that in this location the NOC fluxes are not well correlated with the heat storage anomaly. This probably reflects the relatively low numbers of observations available here for use in the climatology (Josey et al., 1998).

The time series exhibits a significant interannual event in winter 2004/2005, in which the ocean cooled by 23 $Wm^{-2}$ (or 44 $Wm^{-2}$ from unsmoothed values) more than the average 117 $Wm^{-2}$ winter heat loss. The expected wintertime heat storage error in this region is comparatively small, 10 $Wm^{-2}$. This interannual event was also evident in the fixed-depth heat storage, with a similar magnitude. The NCEP net heat flux, heat entrainment and

geostrophic heat divergence all exhibit above average heat loss during this time, while the Ekman and diffusive heat divergence are not significantly anomalous.

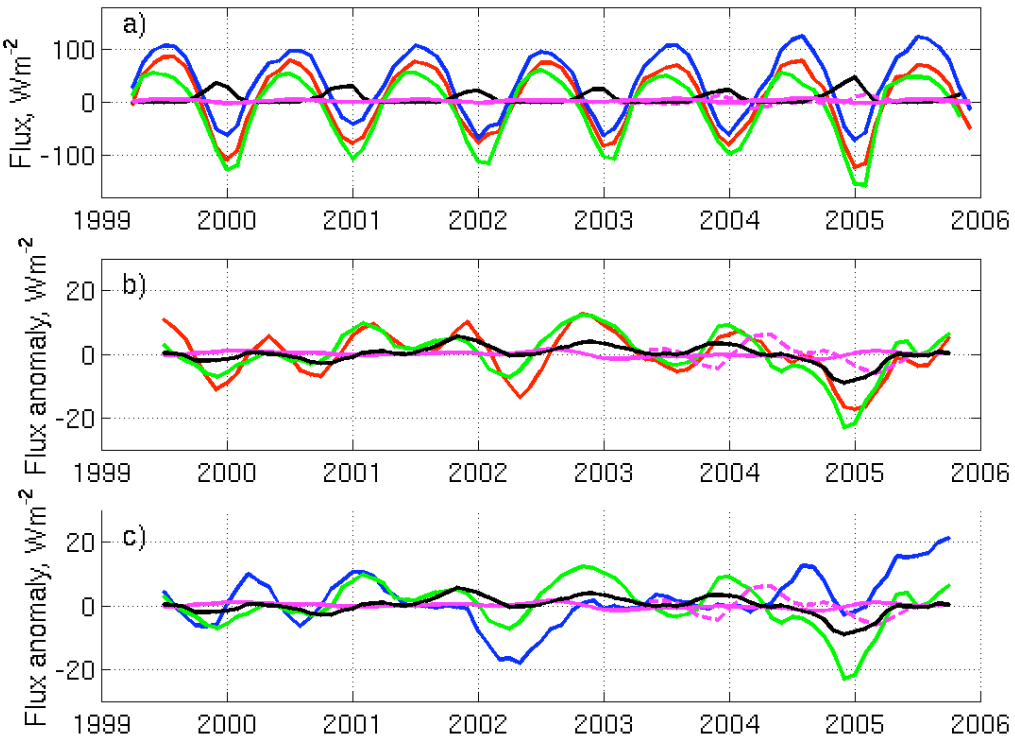


**Figure 7.2** Time series of the heat budget components at 20-30°N, 25-15°W. The NCEP net heat flux (red), NOC net heat flux (blue), heat storage (green), heat entrainment (black) and advective heat divergence (pink) are shown. The Ekman (solid) and geostrophic (dashed) advective divergence are plotted separately. Absolute values are shown in a), anomalies are given in b) and c) for the NCEP reanalysis fluxes and the NOC climatology fluxes, respectively. The heat divergence and entrainment anomalies are plotted with reversed sign (i.e. a negative anomaly indicates an anomalous cooling).

Further investigation of this anomalous event reveals that the NCEP net heat flux anomaly arises primarily from increased latent heat loss, which appears to be driven by anomalously strong dry winds coming off Africa. The NCEP latent heat flux anomaly and

wind stress anomaly are plotted in Fig. 7.3. The anomaly in latent heat flux covers much of the eastern subtropics, with largest values of more than 60 $Wm^{-2}$.

The anomalously high ocean heat loss in January 2005 drives a deeper mixed layer and exposes deeper waters to the atmosphere. Thus it appears that this particular interannual event is driven by atmospheric forcing. The observed anomaly in the geostrophic heat divergence lags the anomaly in net heat flux by several months. Anomalously high easterly and northerly currents coincide with the timing of the geostrophic heat divergence anomaly. The 10° x 10° boxes to the north and east also exhibit a negative anomaly in heat storage at this time.

In summary, the anomalous event in winter 2004/2005 appears to be driven by atmospheric forcing. Anomalously high wind stress increased the latent heat loss from the ocean to the atmosphere. These stronger winds increase the depth of the mixed layer, further increasing heat loss through entrainment. The geostrophic heat divergence also contributes anomalous cooling at this time, arising from increased westward and southward velocities. This case study indicates that the Argo data can be used to identify interannual variability in the mixed layer heat storage, coincident with atmospheric forcing.

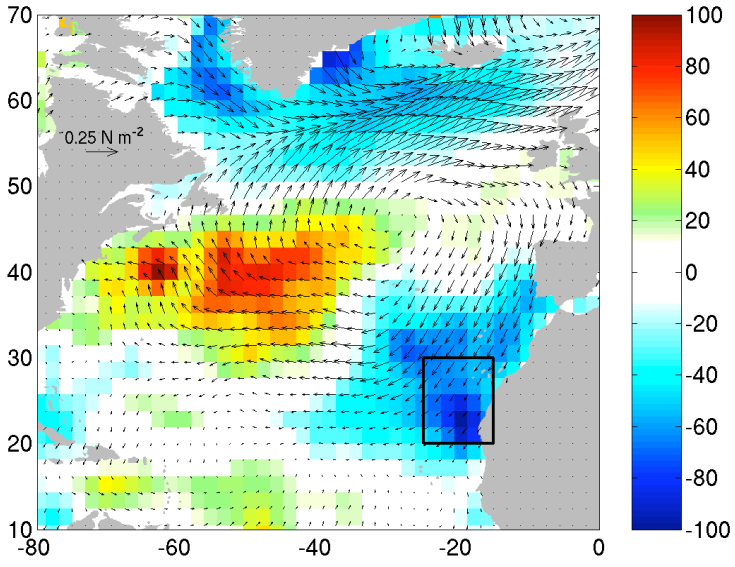


**Figure 7.3** Composite plot of NCEP latent heat flux anomaly and wind stress anomaly vectors for December 2004. The 10° x 10° box 20-30°N, 25-15°W is also shown (black).

### 7.4 Trends of temperature and MLD in the North Atlantic

In this section, temporal trends in the temperature between 1999 and 2005 are investigated. To this end, linear regressions are fitted to the data. The mean seasonal cycle is removed before fitting. Mapped values of the gradient of the fitted regression line (henceforth referred to as the trend) are shown in Fig. 7.4. Subplots show the trends for temperature at 10 m, 100 m, 400 m, 1000 m and a mean between 500 and 1000 m. Contours indicate regions of significant trends at the 95 % certainty level. In view of the short timescale used here, many of the observed trends are not significant.

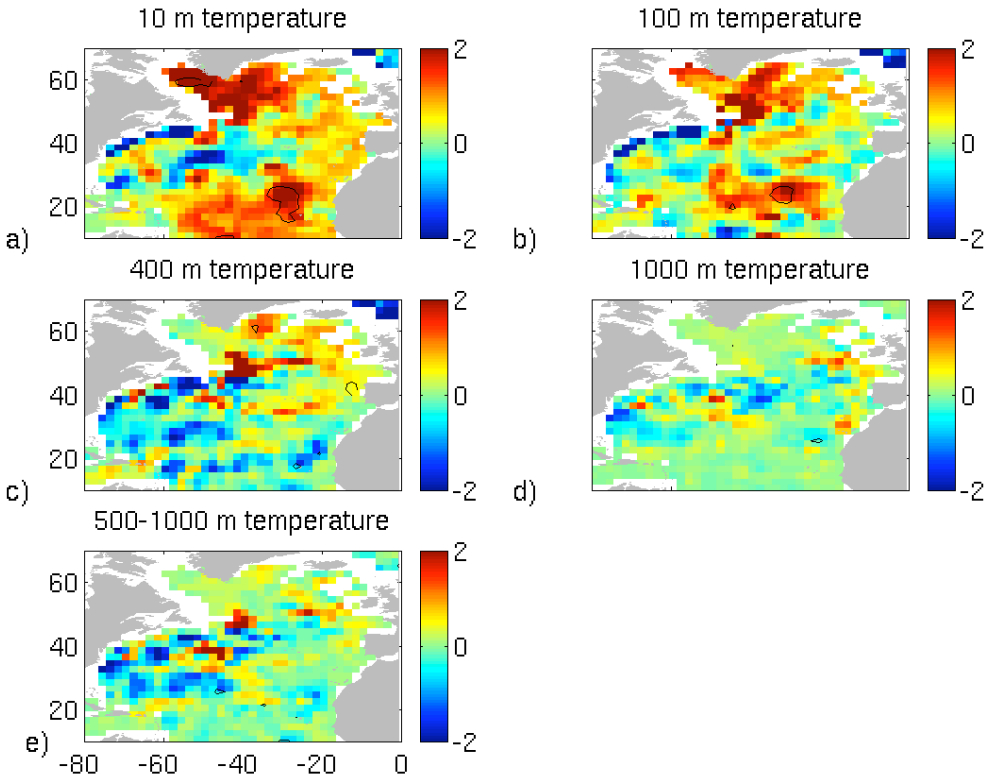


**Figure 7.4** Mean temporal trends in a) 10 m temperature, b) 100 m temperature, c) 400 m temperature, d) 1000 m temperature and e) mean temperature between 500 and 1000 m throughout the Argo period, 1999 – 2005, in °C per decade. Contours show significant trends at the 95 % level.

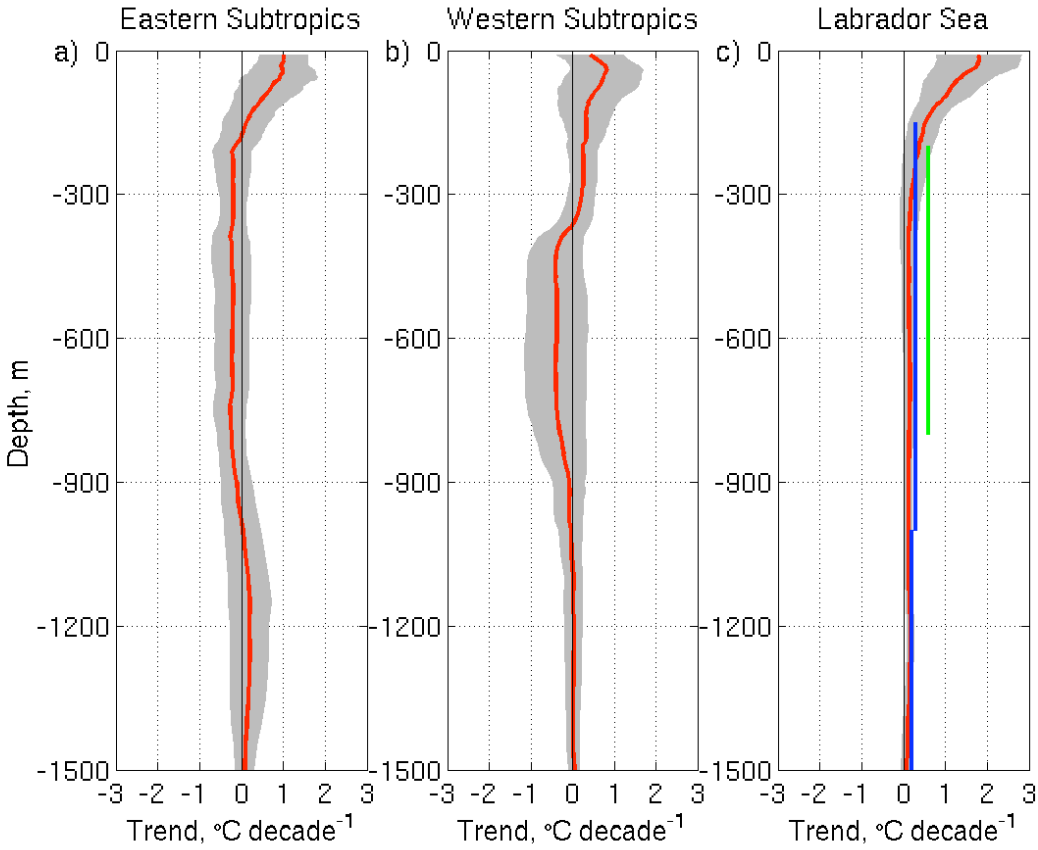


**Figure 7.5** Temporal trends throughout the water column in a) the eastern subtropical North Atlantic, between 20-30°N, east of 30°W, b) the western subtropical North Atlantic, between 20-30°N, west of 30°W and c) the Labrador Sea, north of 52°N, west of 45°W. Shading indicates one standard deviation in the trend, the red line is the mean trend for the region. The blue and green lines indicate the subpolar warming trends documented in Lazier et al. (2002) and Yashayaev and Clarke (2005), respectively.

The 10 m temperature field exhibits positive trends (indicating a mean warming between 1999 and 2005) throughout most of the North Atlantic. Significant warming (at the 95 % level) occurs in the subpolar region (namely the Labrador Sea and Irminger Basin) and in the eastern subtropics. Deeper than 400 m in the subtropical North Atlantic, a mean cooling is apparent. Comparatively, in the subpolar regions, the warming extends to 1000 m, weakening with depth. These changes with depth are shown in more detail for the eastern subtropics (between 20-30°N, east of 30°W), the western subtropics (between 20-

30°N, west of 30°W) and the Labrador Sea (north of 52°N, west of 45°W) in Fig. 7.5. A mean cooling along the path of the Gulf Stream, particularly in the upper 400 m is also apparent (Fig. 7.4). This cooling trend is not significant and has not been documented previously in the literature.

Historical results (discussed in chapter 1) indicate a persistent warming in the subtropics at a depth of 600-1000 m throughout much of the 20$^{th}$ Century (Joyce and Robbins, 1996). Joyce et al. (1999) reported the warming to have ended by 1997 in the western basin, while Vargas-Yáñez et al. (2004) observed a continued warming (relative to hydrographic sections sampled during the preceding 50 years) in a 2002 survey of the eastern subtropics. The results presented here suggest that the more recent trend is one of cooling. This result is consistent with Ivchenko et al. (2006), who also observe a cooling across the basin in the subtropical North Atlantic from Argo floats. The cooling rate in Ivchenko is equivalent to a cooling of the order 0.02 °C decade$^{-1}$ over the upper 1500 m. This is similar to the depth average cooling of 0.03 °C decade$^{-1}$ observed in this study. This trend is small in comparison to the estimated errors. In addition, in February 2007 (after this analysis was undertaken) issues with the pressure sensors on some Argo floats were reported. Recalculation of the trends after the exclusion of almost 4000 profiles that may be affected by this problem suggested no mean cooling or warming in the subtropical North Atlantic. The pressure problems are discussed in more detail in Appendix 2.

Several recent published studies have observed a warming in the Labrador Sea, extending back to 1994 (Lazier et al., 2002; Yashayaev and Clarke, 2005; Ivchenko et al., 2006; Avsic et al., 2006). Lazier et al. (2002) suggested warming at a rate of 0.3 °C per decade at 150 – 1000 m and 0.2 °C per decade at 1000 – 2000 m. Yashayaev and Clarke (2005) and Avsic et al. (2006) found higher rates of warming, 0.6 °C per decade at 200 – 800 m depth along a transect at the southern edge of the Labrador Sea. Warming in the subpolar North Atlantic is also observed in this study. The observed subpolar warming is occurring at a rate of around 2 °C per decade in the surface waters, decreasing to 0.2 °C per decade at 300 m in the Labrador Sea (north of 52°W, west of 45°W) (Fig. 7.5 c). Warming occurs at a roughly constant rate between 400 and 1500 m. The temperature trends

observed using Argo are thus not dramatically different to results published in the literature from other data sources.

The results presented in this section indicate that the trends recorded by the Argo dataset are in agreement with limited published studies based on both Argo and independent datasets. In particular a warming of the Labrador Sea has been observed in this thesis. Although these trends were generally insignificant at the time scales presented here, continued funding of the Argo array could extend the time series available for analysis of this nature and reduce our uncertainty in observed trends. It is thus concluded that the Argo dataset provides an invaluable monitoring tool for identifying significant temporal changes in the North Atlantic.

### 7.5 Summary

Although on the short side, the seven-year Argo dataset exploited in this study has been used to investigate variability in the North Atlantic. Given the variability and expected errors in the heat budget components, the Argo dataset spanning 1999 to 2005 is likely to be useful for investigations of interannual events in the subtropical North Atlantic. In this region one standard deviation in the heat storage anomaly (i.e. mean seasonal cycle removed) is 10 $Wm^{-2}$ and the expected error is just 4 $Wm^{-2}$. An analysis of this nature is expected to be more restricted in the western and subpolar North Atlantic where the errors are larger.

Correlation between heat budget anomaly components is generally strongest between the absorbed net heat flux and the heat storage. Correlations are particularly high when the NCEP atmospheric field is considered, with a maximum correlation of 0.76 attained at 20-30°N, 25-15°W. At the same location the correlation between the NOC absorbed heat flux and the heat storage is insignificant, probably reflecting the low number of observations (Josey et al., 1998). A case study of interannual variability at 20-30°N, 25-15°W further highlights the close coupling between the heat storage and the NCEP net heat flux. A strong anomalous heat loss to the atmosphere in winter 2004/2005, which was driven by anomalously high northeasterly winds, decreased the mixed layer temperature and resulted

in stronger entrainment. Correlation between the heat storage anomaly and heat entrainment anomaly is also significant in the eastern basin.

A model-based study of the interannual variability in the various heat budget components suggests that advective processes play a significant role in the generation of heat storage anomalies only in the region between Cape Hatteras and Nova Scotia (Battisti et al., 1995). This region is within the 1000 m depth contour and thus is not sampled by Argo. However, 10° x 10° boxes with relatively high correlations between the heat storage anomaly and heat divergence anomaly have been identified. These boxes correspond to the region through which the Gulf Stream and NAC flow. This result indicates that heat divergence may play a role in generating heat storage anomalies over a more extended area than suggested by Battisti et al. (1995).

Trends in the temperature during the seven-year time period were investigated. The existing dataset reveals a warming in the subpolar North Atlantic and a cooling within the subtropics. The rate of this latter cooling is strongest in the western basin with maximum rates of cooling of 0.42 °C decade$^{-1}$ at 600 m. The subpolar warming is strongest at the surface where it exceeds 1 °C decade$^{-1}$, decreasing to 0.2 °C decade$^{-1}$ at 400 m. However, it should be noted that these observed trends are generally insignificant and should be interpreted with caution. In addition, the trends observed in the subtropical North Atlantic in particular, may be the result of the inclusion of profiles with pressure offsets. Details of this can be found in Appendix 2.

# Chapter 8: Discussion and Conclusions

## 8.1 Introduction

The main aim of this thesis is to investigate the usefulness of the Argo array in studies of the seasonal heat budget. To this end the Argo dataset was used alongside atmospheric data from the NCEP reanalysis and the NOC climatology to obtain estimates of the individual heat budget components. The accuracy of these heat budget components was then assessed using a model based approach, by examination of the heat budget closure attained and through comparison with existing studies in the literature.

In this discussion chapter the main findings of the study are reviewed in the context of the aims and objectives outlined in chapter 1 and in relation to existing studies. In the following sections the length scales which can be resolved using Argo are first discussed in section 8.2, the accuracy of the Argo-based temperature and heat storage fields are considered in 8.3 and the closure obtained by the Argo-based heat budget is discussed in section 8.4. The usefulness of the Argo dataset for investigations of interannual variability in the heat budget is then discussed in section 8.5. A conclusion follows in section 8.6. Subject matter for further related work is explored in section 8.7.

## 8.2 The Scales That Can Be Resolved Using Argo

The Argo array, which at the time of writing comprised almost 2800 profiling floats, contributes a valuable data source for oceanographic research. Between January 1999 and December 2005 the array provided an average of 590 temperature profiles in the North Atlantic per month. Despite this relatively high sampling rate, the multiscale ocean is under-sampled with the available observations imposing a limit on the length and timescales that can be resolved. There is a trade off between the temporal and spatial resolution that can be achieved. The aim of this study is to assess the usefulness of Argo for analyses of the seasonal heat budget and interannual variability. In order that the seasonal signal in heat budget components is resolved, the temporal interpolation scale is set to 30 days. The number of points on a 2° x 2° grid that contain data within 30 days and different distances was computed to determine the length scales which can be reliably

resolved using the Argo dataset. Around 89 % and 98 % of the 2° x 2° grid points are located within one month and 500 km of an observation in 1999 and 2005, respectively. Comparatively, only 20 % of grid points contain an Argo observation within one month and 100 km. This result indicates that Argo cannot typically resolve length scales of less than 500 km if both the seasonal and interannual signals are to be resolved. This 500 km scale represents a mean scale for the North Atlantic, throughout the study period. However, due to the large variability in sampling, the resolvable scale will vary and it mat be possible to resolve smaller scales in well sampled regions.

### 8.3 The Accuracy of the Argo-based Temperature and Heat Storage Fields

The accuracy of North Atlantic temperature and heat storage fields from the Argo profiling float dataset has been investigated to determine the suitability of using the Argo dataset to analyse the North Atlantic heat budget. Observations of the temperature field across 36°N obtained from a hydrographic section were compared with the corresponding field derived from Argo using an optimal interpolation method. Agreement between the hydrographic and Argo based temperature fields to within 0.5 °C was typically found in the eastern basin, with higher differences in the western basin, particularly within the boundary current where errors exceed 2 °C. The difference between the hydrographic and Argo values was significantly smaller than the difference between hydrography and values from the monthly WOA climatology. The improvement was particularly large in the upper 100 m, where the WOA RMS differences were more than twice as large as those from Argo. This result indicates that Argo data are useful for capturing variability in the temperature field across zonal sections in the absence of a dedicated research cruise and thus demonstrates the potential for using Argo to monitor changes in ocean properties. It is anticipated that this result will hold for other regions of the North Atlantic with similar sampling densities, thus Argo offers exciting possibilities for investigating temperature variability that may be linked to changes in the meridional overturning circulation (Bryden et al., 2005).

The accuracy of Argo based estimates of the upper ocean heat storage was assessed using subsampled temperature fields from the OCCAM model. Three different definitions

for the upper ocean were considered; a mixed layer, a fixed depth and an isothermal layer definition. Each of these methods has its own merits and limitations. In the subtropical North Atlantic where temporal variations in the MLD are relatively small, the uncertainty in the upper ocean heat storage was smallest for the mixed layer definition. In this region the Argo array provides temperature data at a spatial and temporal resolution that results in a mixed layer heat storage error of 10-20 $Wm^{-2}$ over 10° x 10°. For the fixed depth and isothermal definitions the monthly error was typically between 20 and 50 $Wm^{-2}$ in the same region.

Randomly subsampled output from OCCAM was used to simulate varying numbers of Argo floats in order to investigate how the accuracy of Argo derived heat storage estimates is likely to vary with the number of floats. This analysis was only carried out for the mixed layer but results are expected to be similar for other upper ocean definitions. As anticipated, an increase in the number of profiles available for use in the optimal interpolation reduces the RMS difference between estimates of the heat storage from the fully sampled and subsampled versions of OCCAM. In the subtropics, this reduction is by a factor of 1/3 (from 18 to 12 $Wm^{-2}$) from the 1999 Argo resolution to the target resolution.

To achieve an accuracy of around 10 $Wm^{-2}$ (a desirable level of accuracy in view of the magnitude of interannual variability, which is of the order 10s of $Wm^{-2}$, WGASF, 2000) it is necessary to increase the time frame over which heat storage is quantified. At seasonal timescales the mixed layer heat storage error is reduced to 7±2 $Wm^{-2}$ in the subtropical North Atlantic. Errors of this magnitude should enable investigations of variability using the Argo dataset. Within the Gulf Stream and subpolar regions the sampling errors are much larger and thus the Argo dataset will be less useful at these locations for investigating variability in the mixed layer heat storage. The application of this 3-month smoothing will dampen the seasonal cycle in the heat budget components, with an expected amplitude decrease of approximately 10 %.

Other published studies have employed a model-based approach to investigate the extent to which various sampling arrays can resolve the temperature field. Schiller et al. (2004) used a global version of MOM with an average resolution of 2° x 1°, while Guinehut et al. (2003) employed a 1/3° primitive equation model, which was subsequently

extended to 1/6° by Guinehut et al. (2004). All three studies found that the target Argo array could replicate a large amount of the seasonal variability in the temperature field, in particular Guinehut et al. (2003) found that 82 % of the signal variance could be accounted for by using a 3° x 3° sampling grid. However, unlike our analysis, these earlier studies all adopted a regular sampling array in their experiments. This is an unrealistic assumption and the results presented in this thesis are the first to employ a sampling technique that reflects the actual float distribution.

### 8.4 Heat Budget Closure

The seasonal cycle in each heat budget component was examined to assess the usefulness of the Argo dataset for investigations of the North Atlantic heat budget. To enable comparison with existing published studies and for ease of comparison with the net heat flux field, a fixed depth definition of the upper ocean was used in this analysis. Thetfixed depth 3-monthly heat storage errors are typically less than 20 $Wm^{-2}$ away from the western boundary. These errors are for individual years and can thus be expected to be smaller for the 7-year climatology presented. Regional analysis could further reduce this uncertainty by enabling shallower fixed depths to be applied in some regions. For example, south of 30°N, the MLD remains shallower than 100 m throughout the year, reducing the errors to 6 $Wm^{-2}$. The characteristics of the seasonal cycle in heat storage from Argo were found to be similar to the independent results presented in LB82 and H89, further accrediting the Argo-based heat storage estimates.

In agreement with scaling arguments presented in Gill and Niiler (1973), an observational study by Hsiung et al. (1989) and a model-based study by Dong and Kelly (2004), it is found here that air-sea exchanges represent the dominant mechanism driving the seasonal cycle in upper ocean heat storage. These two heat budget components are well correlated throughout the annual cycle and exhibit similar annual ranges at many of the 10° x 10° boxes. However, the domain-average annual range in heat storage is higher than the range in net heat flux, being 351 $Wm^{-2}$ compared to the 239 $Wm^{-2}$ and 272 $Wm^{-2}$ range in the NCEP and NOC net flux, respectively. This is primarily due to differences in the western basin during summer. The nature of this difference suggests that advective or

diffusive heating may be significant at this time and location. Estimates of the heat divergence did not support this theory with a net cooling contribution of 29 $Wm^{-2}$. Dong and Kelly (2004) used a model to investigate the heat divergence in this region and found a small net heat heating contribution. The imbalance in the heat budget terms, which reaches a maximum of 206±136 $Wm^{-2}$ and 219±136 $Wm^{-2}$ (based on the NCEP and NOC atmospheric fields) at 40-50°N, 55-45°W, indicates that either the heat gain from the net flux or divergence is underestimated or that the heat storage is overestimated. It is hypothesised here that heat divergence may be significant at scales that cannot be resolved using the Argo dataset. Implied heat divergence estimates (based on the difference in the heat storage and net heat flux) exhibit a broad range due to the large difference between the NCEP and NOC net heat flux in this region. It is therefore concluded that estimates of implied heat divergence such as that presented in LB82 and H89 should be treated with caution.

The level of heat budget closure attained using the Argo dataset and atmospheric fields from NCEP and NOC was used to further assess the accuracy of the Argo-based heat budget analysis. Consistent with the model-based results on the accuracy of the heat storage, the magnitude of the heat budget residual indicates that the Argo-based analysis is most accurate at low latitudes and in the eastern basin. In these regions the heat budget residual was typically less than the estimated errors, with smaller residuals typically obtained when the NOC net heat flux was used. The errors in this region were typically between 20-30 $Wm^{-2}$, smaller than the expected uncertainty in the net heat flux. Thus the seasonal cycle in the heat budget residual at this location was used to gain further insight into the accuracy of the net heat flux fields. The NOC net heat flux was found to be more accurate than the NCEP net heat flux throughout the year in the subtropical North Atlantic and during the first half of the year in the eastern mid-latitudes. Consistent with Josey (2001), errors in the NCEP net heat flux were found to be large (more than 50 $Wm^{-2}$) in the eastern subtropics. However, in the eastern mid-latitudes the heat budget residual based on the NCEP net heat flux was small throughout the year and was found to be more accurate than the NOC net heat flux in the eastern mid-latitudes during late autumn/ early winter.

In view of the large differences in the heat budget characteristics and accuracy in the eastern and western North Atlantic, the analysis for 10° x 10° boxes presented here is thought to be more insightful than the zonal means used in LB82 and H89.

### 8.5 Using Argo to Investigate Interannual Variability

Although on the short side, the seven-year time series of temperature and heat budget components derived from Argo presents an opportunity to investigate interannual variability. The suitability of using Argo to this end has been investigated in this study. The focus here is on the mixed layer heat budget. Results indicate that data collected by the Argo array may already be useful for identifying and studying interannual events in the heat budget at some locations. Within the subtropical North Atlantic the heat storage error is 4 $Wm^{-2}$, smaller than the standard deviation in the interannual variability of 11 $Wm^{-2}$. However, within the western boundary current, NAC and subpolar regions the heat storage error is higher, up to 30 $Wm^{-2}$, thus limiting the investigations of interannual variability in this region. Observational studies of interannual variability in the large-scale North Atlantic heat budget have previously been limited by the availability of observations and the high levels of variability in sampling from one year to the next.

Correlations between the anomaly heat budget components (i.e. mean seasonal cycle removed) have been investigated to identify which processes may be responsible for interannual variability in the heat content of the upper ocean. Correlations were typically largest between the heat storage and the NCEP reanalysis net heat flux. This result is consistent with model-based studies (Dong and Kelly, 2004; Battisti et al., 1995). Dong and Kelly (2004) focused on the Gulf Stream region and found that the effects of advection on interannual variability only became dominant beneath the mixed layer, with net heat fluxes dominating in the mixed layer. Battisti et al. (1995) found that oceanic advection only played a role in the generation of interannual sea surface temperature anomalies in a small region extending along the US coast from Cape Hatteras to Nova Scotia. The water depth in this region is less than 1000 m and thus the Argo-based heat budget analysis does not cover this location. Correlations between the heat storage and NOC climatology net heat flux were lower than the correlation between the heat storage and NCEP reanalysis net

heat flux, particularly in the regions away from main shipping routes, where the number of atmospheric observations may be lower.

Examination of the Argo based temperature trend revealed a warming within the subpolar North Atlantic and a cooling in the subtropical North Atlantic. The observed subtropical cooling may be an artefact introduced by pressure offsets in some of the profiling floats (appendix 2). The subpolar warming is more significant, particularly in the upper 150 m. The mean warming rate here exceeds 1 °C decade$^{-1}$. The trends observed here are consistent with the findings of Lazier et al. (2002); Yashayaev and Clarke (2005) and Ivchenko et al. (2006).

The IPCC report (2007) investigates the likely warming trends under various greenhouse gas emissions. Future warming trends equivalent to 0.4 °C decade$^{-1}$ are predicted under high emission scenarios. Mean warming trends of this magnitude were observed from the Argo dataset spanning 1999-2005 in the mid-latitude eastern basin (shown in Fig. 8.2). However, these trends were generally not significant. In order to asses sthe time series required to observe significant trends of this magnitude the temperature time series over the upper 750 m at 50°N, 36°W has been projected forward in time. This projection is plotted in Fig. 8.1a). The mean warming trend and variability about this trend are assumed to be constant with time. The significance of the trend (based on a one-tailed t-test) with the length of the time series is plotted in Fig. 8.1b). Given a time series of 168 months (14 years) the significance of the warming trend is above the 95 % significance level (also shown in Fig. 8.1b). The length of the time-series required before significant changes are observed may be reduced by increasing the number of Argo floats in this region (assuming that some of the variability in the trend arises from under-sampling).

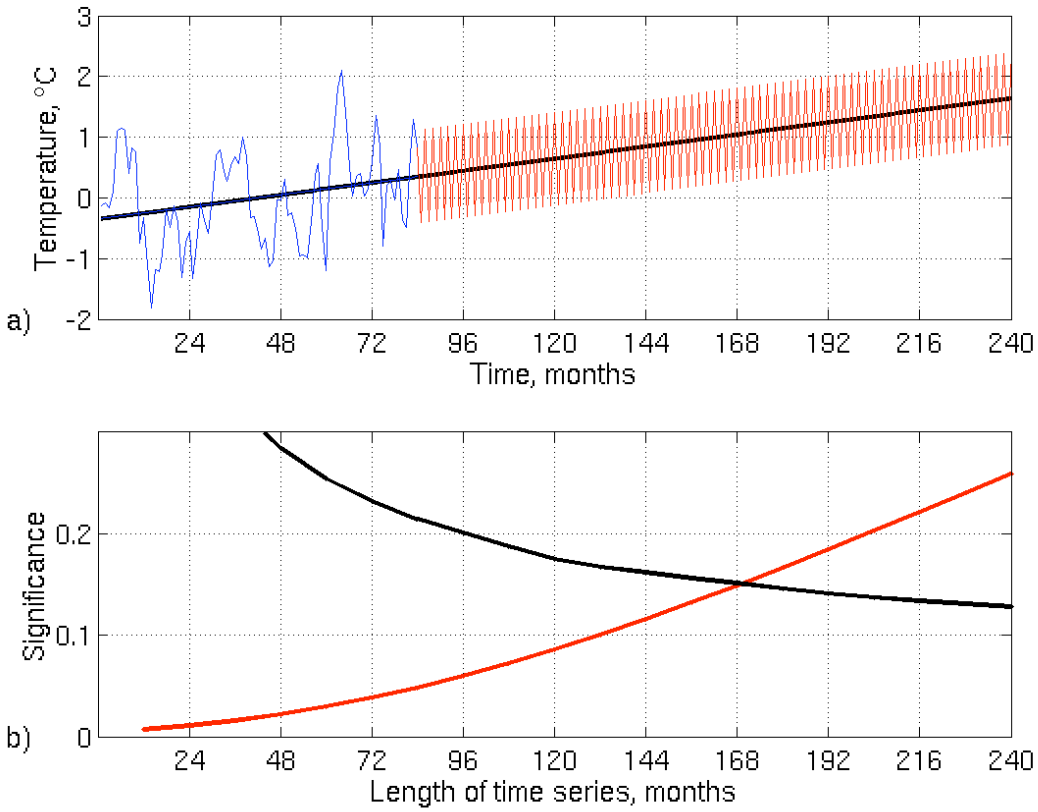


**Figure 8.1** a) the warming trend in the mean temperature of the upper 750 m at 50°N, -36°W as measured by Argo (blue) and b) projected temperature changes over a longer time period using the same mean and variability as measured between 1999 and 2005 (red). The significance of the trend with the length of the time series (red) is plotted in b). The 95 % significance level (black) is also shown.

## 8.6 Conclusion

The results presented in this thesis provide new insight into the usefulness of the Argo dataset in investigations of the North Atlantic heat budget. In particular the study indicates which heat budget components may accurately be quantified using Argo and in what regions the accuracy of the terms enables investigations of the seasonal cycle and interannual variability.

Assessment of the mean sampling between 1999 and 2005 indicated that the Argo array is capable of resolving spatial scales of the order of 500 km on monthly timescales. The heat storage can be quantified to a relatively high degree of accuracy using data from the Argo array on these scales. This is particularly true within the subtropical and eastern North Atlantic where errors in monthly and seasonal mixed layer heat storage are expected to be around 15 $Wm^{-2}$ and 7 $Wm^{-2}$, respectively. The errors in the fixed-depth heat storage are slightly larger, but remain less than 20 $Wm^{-2}$ on seasonal timescales for most of the 10° x 10° boxes in this region. Although these errors exceed the estimated bimonthly heat storage error of 15 $Wm^{-2}$ given in LB82, the values presented here are for individual years, while those in LB82 are based on a 10-year climatological mean. The level of climatological heat budget closure attained in the North Atlantic is smaller than the estimated error estimates for many of the 10° x 10° boxes outside of the Gulf Stream region. In view of the low errors in these regions, the heat budget residual may be used to provide insight into the accuracy of the NCEP and NOC net heat fluxes throughout the year. It is concluded that in the eastern subtropics the NOC net heat flux is more accurate than the NCEP net heat flux throughout the year. Within the eastern mid-latitudes the NCEP and NOC net heat flux are both of reasonable accuracy, however the net heat loss appears to be slightly underestimated from NOC during the late autumn/ early winter.

In the western boundary the errors in heat storage and heat divergence are large, exceeding 100 $Wm^{-2}$ at 40-50°N, 55-45°W. This restricts the usefulness of the Argo dataset for analyses of the heat budget in this region. The heat budget residual is typically larger than the estimated error suggesting that the errors may be underestimated here. Estimates of heat divergence from Argo are of more limited accuracy than temperature and heat storage estimates. This may be due to the high spatial and temporal variability in the geostrophic velocity field (particularly in the western boundary), which cannot be fully resolved using the Argo array.

In view of the low seasonal mixed layer heat storage errors, which are smaller than the expected interannual variability, investigations of temporal variability at time scales of more than one year should be possible using Argo in the subtropics. A case-study of an interannual event successfully resolved by Argo was presented. While the seven-year

dataset used in this study is on the short side for analyses of this nature, if the Argo array is maintained, future investigations may be more comprehensive and insightful.

### 8.7 Further Work

While this thesis has provided valuable insight into the capabilities of the Argo dataset for investigations of the North Atlantic heat budget, several limitations of this study have been identified and there is considerable scope for further work in this subject area. Some ideas for further study are discussed here.

This study is the first observational study to undertake a large-scale analysis of directly quantified heat divergence in the North Atlantic. However, the analysis here was limited by over-smoothing and the short time period over which the geostrophic heat divergence could be quantified from Argo. In view of the imbalance in the Argo-based heat budget within the western boundary, warming through advection and diffusion, is thought to be underestimated. The errors in the velocity field associated with under-sampling and smoothing have not been fully investigated here. A model-based approach as undertaken to estimate the sampling errors associated with quantification of the heat storage from Argo would provide useful insight into the expected magnitude of such errors. An eddy resolving model would be required for such an analysis. While the Argo array is expected to be of limited use for quantifying the heat divergence, the Argo array is only one component of the present day global observing system. Estimates of the geostrophic heat divergence could be improved through an integrated approach in which Argo based SSH fields are combined with satellite altimeter data and/or surface drifter datasets.

In view of the average sampling rate provided by the Argo array throughout the study region and time, length scales of 500 km were used during interpolation of the data. In some well-sampled regions it may be possible to reduce the length scales used. Böhme and Send (2005) employed a two-step OI scheme during interpolation of historical salinity data, to enable finer scales to be resolved in regions with higher sampling density. The application of this scheme to the Argo dataset may enable smaller scale features to be resolved. The effects of this scheme on 1) the interpolated fields and 2) the results of the heat budget analysis would provide an interesting study.

An analysis of the mixed layer heat budget may be useful for providing insight into the mechanisms of water mass transformation which are a key component of the thermohaline circulation. During an analysis of the mixed layer heat budget, accurate determination of the ocean mixed layer is essential. Ideally, the MLD should be defined using a density criterion. However, due to the limitations of the Argo-based salinity field at the time of writing, this was not possible and instead the MLD was estimated using a temperature criterion. This may limit the accuracy of the MLD estimates, particularly in the subpolar North Atlantic where salinity plays an important role in stratifying the water column (Montegut et al., 2004). The Argo profiling floats sample conductivity as well as temperature, theoretically enabling salinity to be derived. However, the conductivity sensors typically exhibit significant drift caused by biofouling. Given that the floats are not recovered, calibration is not a trivial matter. Several studies have focused on this issue (Wong et al., 2003; Böhme and Send, 2005; Oka, 2005) and DMQC procedures implemented at the Argo data centres aim to improve the quality of this dataset. It is expected that in the near future (with the broad-scale implementation of these procedures) Argo floats will provide an invaluable salinity data source without the need for extensive time consuming quality control by the user.

The Argo array provides global coverage, offering exciting opportunities to extend the analysis presented here to other regions of the worlds oceans. Thus the Argo array provides an invaluable data source for investigating changes not only in the North Atlantic, but over the global oceans.

# APPENDIX 1: DERIVATION OF THE HEAT BUDGET EQUATION

In this appendix, the heat budget equation is derived using the equations for the conservation of heat and mass, given in 1.1a and 1.1b, respectively.

$$\rho C_p \left( \frac{\partial T}{\partial t} + \upsilon \cdot \nabla T + w \frac{\partial T}{\partial z} \right) = \frac{\partial q}{\partial z} \tag{1.1a}$$

$$\nabla \cdot \upsilon + \frac{\partial w}{\partial z} = 0 \tag{1.1b}$$

In this manuscript the heat budget of the upper ocean is investigated. The upper ocean is defined as the layer extending from the surface to depth $h$. Vertically integrating equation 1.1b over this surface layer and separating the zonal ($u$) and meridional ($v$) velocity components gives

$$\int_{-h}^{0} \frac{\partial u}{\partial x} dz + \int_{-h}^{0} \frac{\partial v}{\partial y} dz + \int_{-h}^{0} \frac{\partial w}{\partial z} dz = 0 \tag{A1.1}$$

The identity for integrating across a discontinuous surface was given in Whittaker and Watson (1929) as

$$\frac{\partial}{\partial x}\int_{a(x)}^{b(x)} f(x,z)dz = \int_{a(x)}^{b(x)} \frac{\partial f}{\partial x}dz + \frac{\partial b}{\partial x} f(x,b(x)) - \frac{\partial a}{\partial x} f(x,a(x)) \tag{A1.2}$$

the different terms in equation A1.1 can thus be rewritten as

$$\int_{-h}^{0} \frac{\partial u}{\partial x}dz = \frac{\partial}{\partial x}\int_{-h}^{0} u dz - u_0 \frac{\partial(0)}{\partial x} + u_{-h} \frac{\partial(-h)}{\partial x} \tag{A1.3}$$

$$\int_{-h}^{0} \frac{\partial v}{\partial y}dz = \frac{\partial}{\partial y}\int_{-h}^{0} v dz - v_0 \frac{\partial(0)}{\partial y} + v_{-h} \frac{\partial(-h)}{\partial y} \tag{A1.4}$$

$$\int_{-h}^{0} \frac{\partial w}{\partial z}dz = -w_{-h} \tag{A1.5}$$

Substituting these terms into A1.1 gives

$$\frac{\partial}{\partial x}\int_{-h}^{0} u dz - u_{-h}\frac{\partial h}{\partial x} + \frac{\partial}{\partial y}\int_{-h}^{0} v dz - v_{-h}\frac{\partial h}{\partial y} + w_{-h} = 0 \tag{A1.6}$$

Defining the terms $u_a$, $v_a$ as the average velocity of the surface layer

$$u_a = \frac{1}{h}\int_{-h}^{0} u dz \tag{A1.7}$$

$$v_a = \frac{1}{h}\int_{-h}^{0} v\,dz \tag{A1.8}$$

Substitution of these terms into A1.6 gives

$$\frac{\partial(hu_a)}{\partial x} - u_{-h}\frac{\partial h}{\partial x} + \frac{\partial(hv_a)}{\partial y} - v_{-h}\frac{\partial h}{\partial y} - w_{-h} = 0 \tag{A1.9}$$

Thus, equation 1.1b integrated over the layer *h* gives equation 1.2

$$w_{-h} + \upsilon_{-h}\cdot\nabla h = \nabla\cdot h\upsilon_a \tag{1.2}$$

The integration of equation 1.1a over the upper layer is now considered. For clarity, this integration is done term-by-term. Using the identity given in A1.2 gives

$$\int_{-h}^{0}\frac{\partial T}{\partial t}dz = \frac{\partial}{\partial t}\int_{-h}^{0} T dz - T_{-h}\frac{\partial h}{\partial t} \tag{A1.10}$$

for the integration of $\frac{\partial T}{\partial t}$ over depth *h* The second term decomposed into *u* and *v* components and integrated over *h* can likewise be written

$$\int_{-h}^{0} u\frac{\partial T}{\partial x}dz = \frac{\partial}{\partial x}\int_{-h}^{0} uT dz - (uT)_{-h}\frac{\partial h}{\partial x} \tag{A1.11}$$

and

$$\int_{-h}^{0} v\frac{\partial T}{\partial y}dz = \frac{\partial}{\partial y}\int_{-h}^{0} vTdz - (vT)_{-h}\frac{\partial h}{\partial y}. \tag{A1.12}$$

Given

$$T_a = \frac{1}{h}\int_{-h}^{0} Tdz, \tag{A1.13}$$

A1.10 can be rewritten

$$\int_{-h}^{0} \frac{\partial T}{\partial t}dz = \frac{\partial}{\partial t}(hT_a) - T_{-h}\frac{\partial h}{\partial t}, \tag{A1.14}$$

using the product rule to differentiate the first term on the right hand side this can be rewritten

$$\int_{-h}^{0} \frac{\partial T}{\partial t}dz = h\frac{\partial T_a}{\partial t} + T_a\frac{\partial h}{\partial t} - T_{-h}\frac{\partial h}{\partial t}. \tag{A1.15}$$

Defining

$u = u_a + \hat{u}$ and $T = T_a + \hat{T}$, $\frac{\partial}{\partial x}\int_{-h}^{0} uTdz$ can be rewritten using

$$\int_{-h}^{0} uTdz = \int_{-h}^{0} (\hat{u}\hat{T} + u_a\hat{T} + \hat{u}T_a + u_aT_a)dz = \int_{-h}^{0} (\hat{u}\hat{T} + u_aT_a)dz \quad \text{(A1.16)}$$

Thus equation A1.11 can be rewritten

$$\int_{-h}^{0} u\frac{\partial T}{\partial x}dz = \frac{\partial}{\partial x}\int_{-h}^{0} \hat{u}\hat{T}dz + \frac{\partial}{\partial x}\int_{-h}^{0} u_aT_a dz - (uT)_{-h}\frac{\partial h}{\partial x} \quad \text{(A1.17)}$$

which can be rewritten using A1.6 to give

$$\int_{-h}^{0} u\frac{\partial T}{\partial x}dz = \frac{\partial}{\partial x}\int_{-h}^{0} \hat{u}\hat{T}dz + \frac{\partial}{\partial x}(hu_aT_a) - (uT)_{-h}\frac{\partial h}{\partial x} \quad \text{(A1.18)}$$

Differentiating using the product rule gives

$$\int_{-h}^{0} u\frac{\partial T}{\partial x}dz = \frac{\partial}{\partial x}\int_{-h}^{0} \hat{u}\hat{T}dz + hu_a\frac{\partial T_a}{\partial x} + T_a\frac{\partial (hu_a)}{\partial x} - (uT)_{-h}\frac{\partial h}{\partial x}. \quad \text{(A1.19)}$$

Likewise, it can be shown that equation A1.12 can be rewritten

$$\int_{-h}^{0} v\frac{\partial T}{\partial y}dz = \frac{\partial}{\partial y}\int_{-h}^{0}\hat{v}\hat{T}dz + hv_a\frac{\partial T_a}{\partial y} + T_a\frac{\partial(hv_a)}{\partial y} - (vT)_{-h}\frac{\partial h}{\partial y} \tag{A1.20}$$

and the remaining term in equation A1.1a can be written

$$\int_{-h}^{0} w\frac{\partial T}{\partial z}dz = (wT)_0 - (wT)_{-h} \tag{A1.21}$$

Gathering the terms (A1.15 and A1.19 - A1.21) gives

$$\begin{aligned} &h\frac{\partial T_a}{\partial t} + T_a\frac{\partial h}{\partial t} - T_{-h}\frac{\partial h}{\partial t} + \frac{\partial}{\partial x}\int_{-h}^{0}\hat{u}\hat{T}dz + hu_a\frac{\partial T_a}{\partial x} + T_a\frac{\partial(hu_a)}{\partial x} - (uT)_{-h}\frac{\partial h}{\partial x} + \\ &\frac{\partial}{\partial y}\int_{-h}^{0}\hat{v}\hat{T}dz + hv_a\frac{\partial T_a}{\partial y} + T_a\frac{\partial(hv_a)}{\partial y} - (vT)_{-h}\frac{\partial h}{\partial y} - (wT)_{-h} \end{aligned} \tag{A1.22}$$

Using mass conservation (equation 1.2), which can be written as

$$\frac{\partial(hu_a)}{\partial x} + \frac{\partial(hv_a)}{\partial y} = w_{-h} + u_{-h}\frac{\partial h}{\partial x} + v_{-h}\frac{\partial h}{\partial y} \tag{A1.23}$$

in A1.22 gives

$$h\frac{\partial T_a}{\partial t} + T_a\frac{\partial h}{\partial t} - T_{-h}\frac{\partial h}{\partial t} + \frac{\partial}{\partial x}\int_{-h}^{0}\hat{u}\hat{T}dz + hu_a\frac{\partial T_a}{\partial x} - (uT)_{-h}\frac{\partial h}{\partial x} + \frac{\partial}{\partial y}\int_{-h}^{0}\hat{v}\hat{T}dz + hv_a\frac{\partial T_a}{\partial y} - (vT)_{-h}\frac{\partial h}{\partial y} - (wT)_{-h} + T_a w_{-h} + T_a u_{-h}\frac{\partial h}{\partial x} + T_a v_{-h}\frac{\partial h}{\partial y} \quad \text{(A1.24)}$$

collecting terms gives

$$h\frac{\partial T_a}{\partial t} + (T_a - T_{-h})\frac{\partial h}{\partial t} + (T_a - T_{-h})w_{-h} + (T_a - T_{-h})\left(u_{-h}\frac{\partial h}{\partial x} + v_{-h}\frac{\partial h}{\partial y}\right) + \frac{\partial}{\partial x}\int_{-h}^{0}\hat{u}\hat{T}dz + \frac{\partial}{\partial y}\int_{-h}^{0}\hat{v}\hat{T}dz + hu_a\frac{\partial T_a}{\partial x} + hv_a\frac{\partial T_a}{\partial y} \quad \text{(A1.25)}$$

Rewriting A1.25 and substituting terms back into A1.1a gives

$$\rho C_p\left(h\frac{\partial T_a}{\partial t} + hv\cdot\nabla T_a + \nabla\cdot\int_{-h}^{0}\hat{v}\hat{T}dz + (T_a - T_{-h})\times\left(\frac{\partial h}{\partial t} + v_{-h}\cdot\nabla h + w_{-h}\right)\right) = \frac{\partial q}{\partial z} \quad \text{(A1.26)}$$

Including diffusion terms and rewriting $\partial q/\partial z$ as $Q + Q_{-h}$, (where $Q$ is the net heat gain of the upper ocean and $Q_{-h}$ is the heat loss through the layer $h$) in equation A1.26 gives the heat budget equation 1.3 (and 5.1).

$$h\frac{\partial T_a}{\partial t} + hv\cdot\nabla T_a + \nabla\cdot\int_{-h}^{0}\hat{v}\hat{T}dz + (T_a - T_{-h})\times\left(\frac{\partial h}{\partial t} + v_{-h}\cdot\nabla h + w_{-h}\right) + hk_{x,y}\cdot\nabla^2 T_a + k_{z,-h}\frac{\partial T}{\partial z} = \frac{Q + Q_{-h}}{\rho C_p}$$

# APPENDIX 2: PRESSURE SENSOR ISSUES WITH SOLO FSI FLOATS

In February 2007, as this thesis was being finalised, the Argo data centre reported possible issues with the pressure sensors on a number of Argo floats operating in the North Atlantic. It was revealed that SOLO floats fitted with FSI sensors may be offset upward by one or more pressure levels, resulting in a cold bias for these instruments. The pressure offset only resulted in subtle changes to the temperature profile and thus typically went un-flagged by quality control procedures. At the time of writing the Argo data centre is still analyzing the problem. In order to assess how such a pressure offset may affect the results of this study, all SOLO floats fitted with FSI sensors were removed from the database and the Argo based temperature and MLD were briefly reanalysed.

A total of 107 of the 285 floats used in this study are SOLO floats fitted with FSI sensors. These 107 floats sampled 3901 temperature profiles between November 2001 and December 2005 in the North Atlantic. The spatial distribution of these profiles is shown in Figure A2.1. These floats are predominantly concentrated in the western subtropical and mid-latitude North Atlantic.

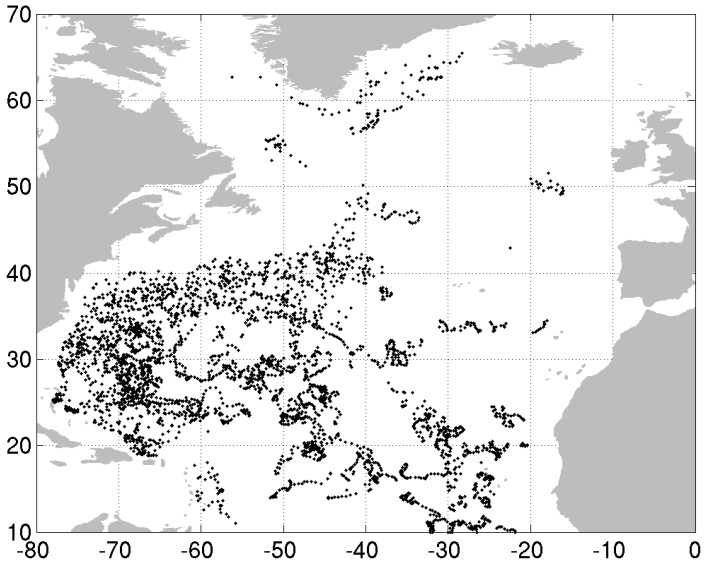


**Figure A2.1** Distribution of profiles collected by SOLO floats fitted with FSI sensors.

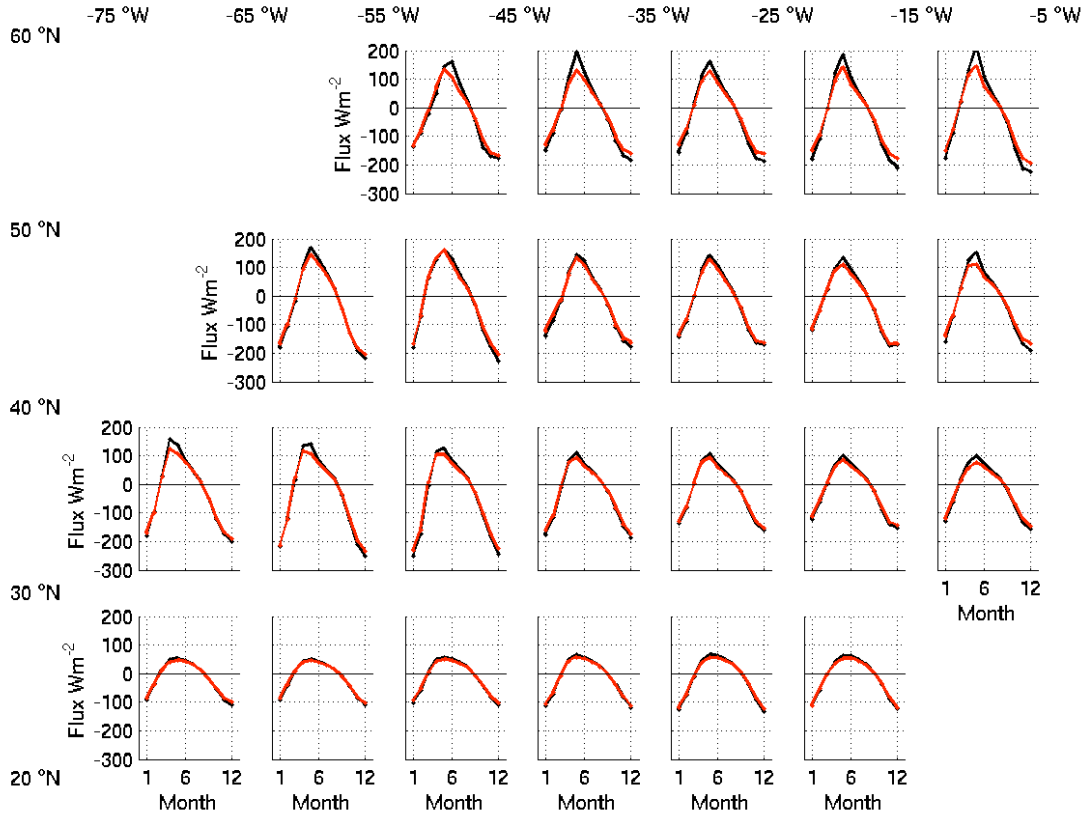


**Figure A2.2** The mixed layer heat storage based on the full Argo dataset (red) and on the Argo dataset with profiles from the SOLO floats fitted with FSI sensors removed (black) at various 10° x 10° boxes in the North Atlantic.

The average RMS difference between the 10 m temperature field based on the original Argo dataset (which included SOLO floats with FSI sensors) and the updated Argo dataset is 0.07 °C. This reduces to 0.04 °C for the average temperature over the upper 1500 m. RMS differences between the MLD before and after removal of these floats from the dataset were also relatively small with an average of 11.5 m; the wintertime mixed layers were slightly deeper after the removal of profiles from the SOLO FSI floats. In view of these small differences it is unlikely that the results on the heat budget components would be significantly affected by the pressure offsets. The mean RMS difference in mixed layer heat storage is 22 $Wm^{-2}$, with larger summertime heat storage when the SOLO FSI floats are included in the database. The mean seasonal cycle in mixed layer heat storage is shown

for the original Argo database and the updated Argo database (with profiles from SOLO floats fitted with FSI sensors removed) in Fig. A2.2.

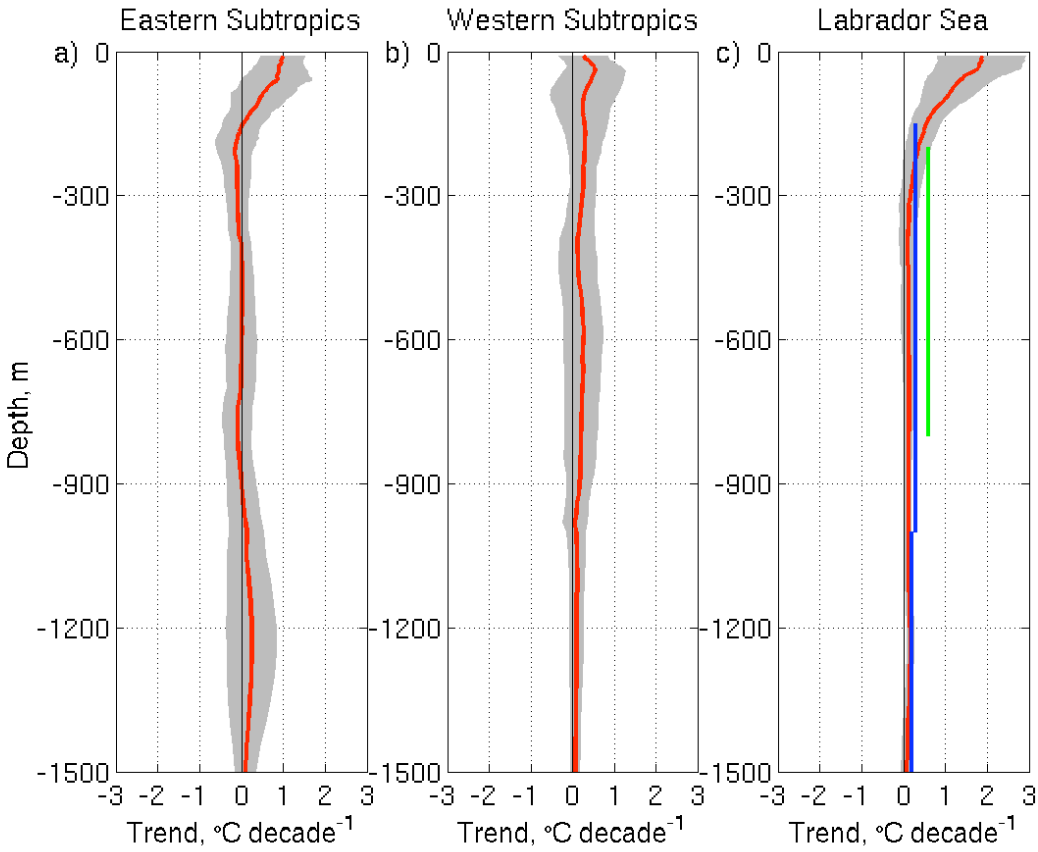


**Figure A2.3** Temporal trends throughout the water column in a) the eastern subtropical North Atlantic, between 20-30°N, east of 30°W b) the western subtropical North Atlantic, between 20-30°Nm west of 30°W and c) the Labrador Sea, north of 52°N, west of 45°W. Shading indicates one standard deviation in the trend, the red line is the mean trend for the region. These trends are based on the updated Argo dataset with the SOLO floats fitted with FSI sensors removed.

The interannual variability in heat storage was unchanged by removing the SOLO FSI floats from the Argo dataset and the interannual event discussed in section 7.3 was still apparent. However, comparison of the temperature trends observed using the full dataset (Fig. 7.5) and the updated dataset (i.e. without SOLO FSI temperature profiles) were not fully consistent. The trends from the updated dataset (Fig. A2.3) indicate a slight warming

trend in the subtropics, which is a reversal of the cooling trend observed in chapter 7. Trends observed in the subpolar North Atlantic were unchanged by the removal of profiles sampled by the SOLO floats fitted with FSI sensors.

With the exception of the temperature trends observed with Argo, the main results of this study are unchanged by omitting profiles with suspected pressure offsets. Thus the key results on the usefulness of the Argo array for investigating the seasonal cycle and interannual variability in the North Atlantic heat budget still stand. However, the need for careful quality control is highlighted.

# References

Alderson, S.G. and P.D. Killworth (2005), A preoperational scheme for calculating sea surface height by Bernoulli inverse of Argo float data in the North Atlantic. *Journal of Atmospheric and Oceanic Technology 22(9),* 1416-1422.

Arbic, B.K. and W.B. Owens (2001), Climate warming of Atlantic Intermediate Waters. *Journal of Climate 14,* 4091-4108.

Avsic, T., J, Karstensen, U. Send and J. Fischer (2006), Interannual variability of newly formed Labrador Sea Water from 1994 to 2005. *Geophysical Research Letters 33,* L21s02, doi:10.1029/2006GL026913.

Bacon, S. (1997), Circulation and fluxes in the North Atlantic between Greenland and Ireland. *Journal of Physical Oceanography 27,* 1420-1435.

Bacon, S., L. Centurioni and W.J. Gould (2001), The evaluation of salinity measurements from PALACE floats. *Journal of Atmospheric Technology 18,* 1258-1266.

Barnes, S. (1964), A technique for maximising details in numerical map analysis. *Journal of Applied Meteorology 3,* 395-409.

Barnett, T.P., D.W. Pierce, K.M. AchutaRao, P.J. Gleckler, B.D. Santer, J.M. Gregory and W.M. Washington (2005), Penetration of human-induced warming into the World's Oceans. *Science 309*, 284-287.

Banks, H and R.A. Wood (2001), Where to look for anthropogenic climate change in the ocean. *Journal of Climate 15*, 879-893.

Battisti, D.S., U.S. Bhatt and M.A. Alexander (1995), A modelling study of he interannual variability in the wintertime North Atlantic Ocean. *Journal of Climate 8,* 3067-3082.

Böhme, L. and U. Send (2005), Objective analyses of hydrographic data for referencing profiling float salinities in highly variable environments. *Deep Sea Research II, 52(3-4),* 651-664.

Böning, C.W. and P. Herrmann (1994), Annual cycle of poleward heat transport in the ocean: Results from high resolution modelling of the North and Equatorial Atlantic. *Journal of Physical Oceanography 24,* 91-107.

Bower, A.S., B. Le Cann, T. Rossby, W. Zenk, W.J. Gould, K. Spear, P.L. Richardson, M.D. Prater and H-M Zhang (2002). Directly measured mid-depth circulation in the north eastern North Atlantic Ocean. *Nature 419*, 603-607.

Bretherton, F.P. R.E. Davis and C.B. Fandry (1976), A technique for objective analysis and design of oceanographic experiments applies to MODE-73. *Deep-Sea Research, 23,* 559-582.

Bryan, K. (1969), A numerical method for the study of the circulation of the world ocean. *Journal of computer Physics 4,* 347-376.

Bryan, K. and E. Schroeder (1960), Seasonal Heat Storage in the North Atlantic Ocean. *Journal of Meteorology 17*, 670-674.

Bryden, H.L., H.R. Longworth and S.A. Cunningham (2005), Slowing of the Atlantic Meridional Overturning Circulation at 25°N. *Nature 438*, 655-657.

Bryden, H.L. and S. Imawaki (2001), Ocean heat transport. P 455-474 in Ocean circulation and climate. G. Siedler (Ed), Academic Press.

Bryden, H.L., M.A. Griffiths, A.L Lavin, R.C. Millard, G. Parilla and W.M. Smethie (1996), Decadal changes in water mass characteristics at 24°N in the Subtropical North Atlantic Ocean. *Journal of Climate 9(12),* 3162-3186.

Bryden, H.L. (1993), Ocean heat transport across 24°N latitude. Interactions between Global climate subsystems: The Legacy of Hann. M. G.A. and M. Hantel. 75: 65-75.

Budyko, M. (1963), Atlas of heat balance of the World." Glabnaia Geofiz. Observ.

Bunker, A. F. (1975), Energy exchange at the surface of the Western North Atlantic Ocean, WHOI manuscript 75-3, 107pp.

Bunker, A. F. (1976), Computations of surface energy flux and annual air-sea interaction cycles of the North Atlantic Ocean. *Mon, Wea. Rev 104,* 1122-1140.

Bunker, A. F. and L. V. Worthington (1976), Energy exchange charts of the North Atlantic Ocean. *Bulletin of American Meteorological Society 57,* 670-678.

Buzzi A., D. Gomis, M.A. Pedder and S. Alonso (1991), A method to reduce the adverse impact that inhomogenous station distributions have on spatial interpolation. *Monthly Weather Review 119,* 2465-2491.

Carrisimo, B.C., A.H. Oort and T.H. Vonder Haar (1985), Estimates of meridional energy transports in the atmosphere and ocean. *Journal of Physical Oceanography 15,* 82-91.

Carval, T., B. Keeley, Y. Takatsuki, T. Yoshida, S. Loch, C. Schmid, R. Goldsmith, A. Wong, R. McCreadie, A. Thresher and A. Tran (2006), Argo data management, users handbook, Version 2.1. IFREMER report cor-do/dti-mut/02-084.

Centurioni, R., and J. Gould (2004), Winter Conditions in the Irminger Sea Observed With Profiling Floats, *Journal of Marine Research 62*, 313-336.

Chambers, D.P., B.D. Tapley and R.H. Stewart (1997), Long-period ocean heat storage rates and basin-scale heat fluxes from TOPEX. *Journal of Geophysical Research 102(C5)*, 10525-10533.

Clarke, R.A. and J.C. Gascard (1983), The formation of Labrador Sea Water, part 1: Large scale processes. *Journal of Physical Oceanography 14,* 1764-1778.

Conkwright, M.E., J.I. Antonov, O.K. Baranova, T.P. Boyer, H.E. Garcia, R. Gelfeld, D. Johnson, R.A. Locarnini, P.P. Murphey, T.D. O'Brien, I. Smolyar and C. Stephens (2002), The World Ocean Database, 2001. Levitus, S (Ed), NOAA Atlas NESDIS 42.

Cox, M.D. (1984), A primitive equation 2-dimensional model of the ocean. GFDL Ocean Group, Technical Report No 1. Geophysical Fluid Dynamics Laboratory/NOAA, Princeton University, Princeton, H.J. 08542, USA, 143 pp.

Coward, A.C. P.D. Killworth and J.R. Blundell (1994), Tests of a two grid world ocean model. *Journal of Geophysical Research 99,* 22,725-22,735.

Coward, A.C and B.A de Cuevas (2005), The OCCAM 66 level model: physics, initial conditions and external forcing. SOC internal report 99.

Cressman, G.P. (1959), An operational objective analysis system. *Monthly Weather Review 87,* 367-374.

Cunningham, S.A. (2000), Circulation and volume flux of the North Atlantic using synoptic hydrographic data in a Bernoulli inverse. *Journal of Marine Research 58(1),* 1-35.

Cunningham, S.A. and S. G. Alderson (2006), Transatlantic temperature and salinity changes at 24.5°N from 1957 to 2004. *In preparation*.

Curry, R.G. and M.S. McCartney (2001), Ocean gyre circulation changes associated with the North Atlantic Oscillation. *Journal of Physical Oceanography 31*, 3374-3400.

Davis, R.E. and W. Zenk (2001), Subsurface Lagrangian observations during the 1990s (pp123-139, Chapter 3.2). In: Siedler, G. J. Church and J. Gould (eds), Ocean circulation and climate – observing and modelling the global ocean. Academic press, International Geophysics Seriers, volume 77, 712 pp.

Davis, R.E. (1998), Preliminary results from directly measuring mid-depth circulation in the Tropical and South Pacific. *Journal of Geophysical Research 103,* 24,619-24,639.

Davis, R.E., J.T. Sherman and J. Dufour (2001), Profiling ALACEs and other advances in autonomous subsurface floats. *Journal of atmospheric and oceanic technology 18(6)*, 982-993.

Davis, R.E., D.C. Webb, L.A. Regier and J. Dufour (1992), The autonomous Lagrangian circulation explorer (ALACE). *Journal of atmospheric and oceanic technology 9,* 264-285.

DeCosmo, J., K. B. Katsaros, S.D. Smith, R.J. Anderson, W.A. Oost, K. Bumke and H. Chadwick (1996), Air-sea exchange of water vapour and sensible heat: The Humidity Exchange Over the Sea (HEXOS) results. *Journal of Geophysical Research 101*, 12001-12016.

Dixon, K.W. and J.R. Lanzante (1999), Global mean surface air temperature and North Atlantic overturning in a suite of coupled GCM climate change experiments. *Geophysical Research Letters 26,* 1885-1888.

Dong, S. and K.A. Kelly (2004), Heat budget in the Gulf Stream region: The importance of heat storage and advection. *Journal of Physical Oceanography 34,* 1214-1231.

Douglas, B.C. (1997), Global sea level rise: a redetermination. *Surveys in geophysics 18 (2-3)*, 279-292.

Durand, F. and G. Reverdin (2005), A statistical method for correcting salinity observations from autonomous profiling floats: an Argo perspective. *Journal of Atmospheric and Oceanic Technology 22*, 292-301.

Fairall, C. W., E. F. Bradley, J.E. Hare, A.A. Grachev, J.B. Edson (2003), Bulk parameterisation of air-sea fluxes: Updates and verification for the COARE algorithm. *Journal of Climate 16,* 571-591.

Fairall, C. W., E. F. Bradley, D.P. Rogers, J.B. Edson, G.S. Young, (1996), Bulk parameterization of air-sea fluxes for TOGA-COARE. *Journal of Geophysical Research 101,* 3747–3764.

Folland, C.K., T.R. Karl and M.J. Salinger (2002), Observed climate variability and change. *Weather 57(8)*, 269-278.

Foltz, G.R., S.A. Grodsky, J.A. Carton and M.J. McPhaden (2003), Seasonal mixed layer heat budget in the tropical Atlantic Ocean. *Journal of Geophysical Research 108 (C5).* doi:10.1029/2002JC001584.

Foltz, G.R. and M.J. McPhaden (2005), Mixed layer heat balance on intraseasonal time scales in the Northwestern tropical Atlantic Ocean. *Journal of Climate 18*, 4168-4184.

Freeland, H. (1997), Calibration of the conductivity cells on P-ALACE floats. U.S. WOCE Implementation report 9, 64 pp.

Gabites, J. F., 1950: Seasonal variations in the atmospheric heat balance. ScD, MIT.

Ganachaud, A. and C. Wunsch (2003), Large-scale ocean heat and freshwater transports during the World Ocean Circulation Experiment. *Journal of Climate 16(4),* 696-705.

Gandin, L. S. (1963). Objective Analysis of Meteorological Fields. Leningrad, Gidrometeorol Izdat, 242pp.

Gellers-Barkman, S. and N. C. Wells (1992). Gridding of XBT and CTD datasets. Southampton, Department of Oceanography, University of Southampton.

Gill, A.E. and P.P Niiler (1979), The theory of the seasonal variability in the ocean. *Deep-Sea Research 20*, 141-177.

Gill, A.E. (1982), Atmospheric Ocean Dynamics, Academic Press, London, 662 pages. *International Geophysical Series, Vol. 30.*

Gille, S (2002), Warming of the Southern Ocean since the 1950s, *Science 295 (5558)*, 1275-1277.

Gleckler, P.J. and B.C. Weare (1997), Uncertainties in global ocean surface heat flux climatologies derived from ship observations. *Journal of Climate 10*, 2764-2781.

Godfrey, J.S., E.F. Bradley, P.A. Coppin, L.F. Pender, T.J. McDougall, E.W. Schulz and I. Helmond (1999), Measurements of Upper Ocean Heat and Freshwater Budgets Near a Drifting Buoy in the Equatorial Indian Ocean. *Journal of Geophysical Research 104 (C6),* 13,269-13,302.

Gregory, J.M., H.T. Banks, P.A. Stott and J.A. Lowe (2004), Simulated and observed decadal variability in ocean heat content. *Geophysical Research Letters 31*, doi 10.1029/2004GL020258.

Grist, J. P. and S. A. Josey (2003), Inverse analysis adjustment of the SOC air-sea flux climatology using ocean heat transport constraints. *Journal of Climate 16,* 3274-3295.

Guinehut, S., P.Y. Le Traon, G. Larnicol and S. Philipps (2004), Combining Argo and remote-sensing data to estimate the ocean 3-dimensional temperature fields – a first approach based on simulated observations. *Journal of Marine Systems 46*, 85-98.

Gulev, S. K. (1995), Long-term variability of sea-air heat transfer in the North Atlantic Ocean. *International Journal of Climatology 15*, 825-852.

Hadfield, R.E., N.C Wells, S.A. Josey and J. J-M. Hirschi (2006), On the accuracy of North Atlantic temperature and heat storage fields from Argo. *Journal of Geophysical Reasearch,* in press.

Hall M.M., and H.L. Bryden (1982), Direct estimates and mechanisms of ocean heat transport. *Deep Sea Research 29*, 339-360.

Hirschi, J.J-M, P.D. Killworth and J.R. Blundell (2006), Subannual, seasonal and interannual variability of the North Atlantic Meridional Overturning Circulation. Submitted to *Journal of Physical Oceanography.*

Hsiung, J, R.E. Newell and T. Houghtby (1989), The annual cycle of oceanic heat storage and oceanic meridional heat transport. *Quarterly Journal of the Royal Meteorological Society 115*, 1-28.

IPCC (2001). Climate Change 2001: The Scientific Basis. Contribution of Working Group I to the Third Assessment Report of the Intergovernmental Panel on Climate Change. J. T. Houghton, Y. Ding, D. J. Griggset al. Cambridge, 881 pp.

Ivchenko, V.O., N.C. Wells and D.I. Aleynik (2006), Anomaly of heat content in the last 7 years: is the ocean warming or cooling? Submitted, *Geophysical Research Letters.*

Johnson, G.C. (2006), Generation and initial evolution of a mode water potential temperature – salinity anomaly. *Journal of Physical Oceanography 36*, 739-751.

Jones, I. and H. Leach (1999), Isopycnic modeling of the North Atlantic heat budget. *Journal of Geophysical Research 104(C1*), 1377-1392.

Jones, P.D., T.J. Osborn and K.R. Briffa (2001), The evolution of climate over the last millennium. *Science 292*, 662-667.

Josey, S. A., E. C. Kent and P.K. Taylor (1998), The Southampton Oceanography Centre (SOC) ocean-atmosphere heat, momentum and freshwater flux atlas. National Oceanography Centre, Southampton report number 6, 30 pp plus figures. Southampton, U.K.

Josey, S. A., E. C. Kent and P.K. Taylor (1999), New insights into the ocean heat budget closure problem from the analysis of the SOC air-sea flux climatology. *Journal of Climate 12(9),* 2856-2880.

Josey, S.A., (2001), A comparison of ECMWF, NCEP-NCAR and SOC surface heat fluxes with moored buoy measurements in the subduction region of the Northeast Atlantic. *Journal of Climate 14,* 1780-1789.

Josey, S.A., E.C.Kent and P.K. Taylor (2002), Wind stress forcing of the ocean in the SOC climatology: Comparisons with the NCEP-NCAR, ECMWF, UWM/COADS, and Hellerman and Rosenstein datasets. *Journal of Physical Oceanography 32(7*), 1993-2019.

Joyce, T.M., R.S. Pickart and R.C. Millard (1999), Long-term hydrodynamic changes at 52 and 66°W in the North Atlantic Subtropical Gyre and Caribbean. *Deep Sea Research II 46(2),* 245-278.

Joyce, T.M. and P. Robbins (1996), The long-term hydrographic section at Bermuda." *Journal of Climate 9(12),* 1.

Kalnay, E. et al. (1996), The NCEP/NCAR 40 year reanalysis project. *Bulletein of the American Met. Soc. 77,* 437-471.

Kanzow, T., S. Cunningham, D. Rayner, J.J-M.Hirschi, W.E. Johns, M. Barringer, H.L. Bryden, L. Beal, C.S. Meinen and J. Marotzke (2007), Observed flow compensation associated with the Meridional Overturning Circulation at 26.5 °N in the Atlantic. *Science 17*, 938-941, doi:10.1126/Science.1141293.

Keith, D.W., (1995), Meridional energy transport: uncertainty in zonal means. *Tellus 47A,* 30-44.

Kent, E. C., P. G. Challenor and P.K. Taylor (1999), A statistical determination of the random observational errors present in voluntary observing ships' meteorological reports. *Journal of Atmospheric and Oceanic Technology 16* 920-929.

Kent, E.C., P.K. Taylor, B.S. Truscott and J.S Hopkins (1993), The accuracy of voluntary observing ships meteorological observations – results of the VSOP-NA. *Journal of Atmospheric and Oceanic Technology 10*, 591-608.

Killworth, P.D., (1986), A Bernoulli inverse method for determining the ocean circulation. *Journal of Physical Oceanography 16*, 2031-2051.

King, B.A. and E.L. McDonagh (2005), Decadal changes in ocean properties revealed by Argo floats. *Geophysical Research Letters 32*, doi:10.1029/2005GL023145.

Kistler, R., E. Kalnay, et al. (2001), The NCEP-NCAR 50-year reanalysis: monthly means CD-ROM and documentation. *Bulletin of American Meteorological Society 82(2),* 247-267.

Klein, B., R.L. Molinari, T.J. Müller and G. Siedler (1995), A transatlantic section at 14.5°N: Meridional volume and heat fluxes. *Journal of Marine Research 53*, 929-957.

Koltermann, K.P., A.V. Solov, V.P. Tereschenkov, S.A. Dobroliubov, K. Lorbacher and A. Sy (1999), Decadal changes in the thermohaline circulation of the North Atlantic. *Deep Sea Research II 46(2),* 109-138.

Kwon, Y-O and S.C. Riser (2005), General circulation of the western subtropical North Atlantic observed using profiling floats. *Journal of Geophyiscal Research 110 (C12),* 10.1029/2005JC002909.

Lamb, P.J. and A.F. Bunker (1982), The annual march of the heat budget of the nor th and tropical Atlantic oceans. *Journal of Physical Oceanography 12(12)*, 1388-1410.

Lankhorst, M., and W. Zenk (2006), Lagrangian observations of the middepth and deep velocity fields of the Northeastern Atlantic Ocean. *Journal of Physical Oceanography 36,* 43-63.

Latif, M., E. Roeckner U. Mikolajewicz and R. Voss (2000), Tropical stabilisation of thermohaline circulation in a greenhouse warming simulation. *Journal of Climate 13,* 1809-1813.

Lavender, K.L. (2001), The general circulation and open-ocean deep convection in the Labrador Sea: A study using subsurface floats. PhD Thesis, University of California, San Diego, 131 pp.

Lavender, K.L., W.B. Owens and R.E. Davis (2005), The mid-depth circulation of the subpolar North Atlantic Ocean as measured by subsurface floats. *Deep-Sea Research 52*, 767-785.

Lavin, A.L., H.L. Bryden and G. Parrilla (1998), Meridional transport and heat flux variations in the Subtropical North Atlantic. *Global Atmosphere and Ocean Systems 6*, 269-293.

Lazier, J., R. Hendry, A. Clarke, I. Yashayaev and P. Rhines (2002), Convection and restratification in the Labrador Sea, 1999-2000. *Deep Sea Research 49,* 1819-1835.

Ledwell, J.R., A.J. Watson and C.S. Law (1993), Evidence for slow mixing across the pycnocline from an open-ocean tracer-release experiment. *Nature 364(6439),* 701-703.

Levitus, S. (1982), Climatological Atlas of the World, NOAA report 13, 173pp.

Levitus, S., J. Antonov and T. Boyer (2005), Warming of the ocean, 1955-2003. *Geophysical Research Letters 32*, L02604, doi:10.1029/2004GL021592.

Lozier, M.S., W.B Owens and R.G Curry (1995), The climatology of the North Atlantic. *Progress in Oceanography 36(1)*, 1-44.

Lynch, D.R. and D.J. McGillicuddy (2001), Objective analysis for coastal regimes. *Continental Shelf Research 21(11/12),* 1299-1315.

Maddox, R.A. (1980), An objective technique for separating macroscale and mesoscale features in meteorological data. *Monthly Weather Review 108*, 1108-1121.

Marsh, R., B.A. de Cuevas, A.C. Coward, H.L. Bryden and M. Alvarez (2005), Thermohaline circulation at 3 key sections in the North Atlantic over 1985-2002. *Geophysical Research Letters 32(10),* L10604, DOI:10.1029/2004GL022281.

Marshall, J. and F. Schott (1999), Open-ocean convection: Observations, theory and models. *Reviews of Geophysics 37,* 1-64.

Marshall, J.C., A.J.G. Nurser and R.G. Williams (1993), Inferring the subduction rate and period over the North Atlantic. *Journal of Physical Oceanography 23(7)*, 1315-1329.

Martin, P., (1995), Hindcasting changes in upper ocean thermal structure on short time scales with data from MILE and Ocean Weather Station - Papa. *Journal of Atmospheric and Oceanic Technology 12(4)*, 871-880.

McCulloch, M.E. and H. Leach (1998), Air-sea fluxes inferred from an upper ocean heat budget north east of the Azores. *Quarterly Journal of the Royal Meteorological Society 124,* 2465-2476.

McDonagh, E.L. et al., (2006), RRS *Charles Darwin* Cruise 171, 01 May-15 Jun 2005. Trans-Atlantic Hydrographic Section across 36°N. National Oceanography Centre, Southampton Cruise report, in preparation.

McPhaden, M. (2002), Mixed layer temperature balance on Intraseasonal timescales in the Equatorial Pacific Ocean. *Journal of Climate 15,* 2632-2647.

MODE group (1978), The mid-ocean dynamics experiment. *Deep Sea Research 25*, 859-910.

Moisan, J.R. and P.P. Niiler (1998), The seasonal heat budget of the North Pacific: Net heat flux and heat storage rates (1950-1990). *Journal of Physical Oceanography 28*, 401-421.

Molinari, R.L. (2004), Annual and decadal variability in the western subtropical North Atlantic; signal characteristics and sampling methodologies. *Progress in Oceanography 62,* 33-66.

Montegut, C.D., G. Madec, A. Fischer, A. Lazar and D. Iudicone (2004), Mixed layer depth over the Global Ocean: an examination of profile data and a profile-based climatology. *Journal of Geophysical Research 109(C12),* C12003, DOI: 10.1029/2004JC002378.

Moore, G.W.K. and I.A. Renfrew (2001), An assessment of the subsurface turbulent heat fluxes from the NCEP reanalysis over western boundary currents. *Journal of Climate 15*, 2020-2037.

Moyer, K.A. and R.A. Weller (1997), Observations of surface forcing from the Subduction Experiment: A comparison with global model products and climatological datasets. *Journal of Climate 10,* 2725-2742.

Nerem, R.S., (1999), Measuring very low frequency sea level variations using satellite altimeter data. *Global and planetary change 20 (2-3)*, 157-171.

Oka, E., (2005), Long term sensor drift found in Argo profiling floats. *Journal of Oceanography 61(4),* 775-581.

Oort, A.H. and T.H. Vonder Haar (1976), The observed annual cycle in the ocean-atmosphere heat balance over the Northern Hemisphere. *Journal of Physical Oceanography 6*, 781-800.

Pacanowski, R.C., K. Dixon and A. Rosati (1990), The GFDL Modular Ocean model users guide, Version 1.0. GFDL ocean group technical report 3, Geophysical Fluid Dynamics Laboratory, NOAA, Princeton University, Princeton NJ 08542, USA, pp 18.

Park, J.J., K. Kim, B.A. King and S.C. Riser (2005), An advanced method to estimate deep currents from profiling floats. *Journal of Atmospheric and Oceanic Technology 22(8)*, 1294-1304.

Parrilla, G., A.L. Lavin, H.L. Bryden, M. Garcia and R.C. Millard (1994), Rising temperatures in the Subtropical North Atlantic Ocean. *Nature 369,* 48-51.

Perez-Brunius, P., T. Rossby and D.R. Watts (2004), Transformation of the warm waters of the North Atlantic from a geostrophic stream function perspective. *Journal of Physical Oceanography 34(10)*, 2238-2256.

Pickart, R.S., F. Straneo and G.W.K. Moore (2003), Is Labrador Sea Water formed in the Irminger Basin? *Deep Sea Research 50,* 23-52.

Pickart, R.S., D.J. Torres and R.A. Clarke (2002), Hydrography of the Labrador Sea during active convection. *Journal of Physical Oceanography 32(2),* 428-457.

Piterbarg, L. I., G. M. Reznik and Y.B. Filyushkin (1991), Optimum interpolation of hydrophysical fields. *Oceanology 31(5),* 630-636.

Rahmstorf, S. (1995), Bifurcations of the Atlantic thermohaline circulation in response to changes in the hydrological cycle. *Nature 378,* 145-149.

Rapid (2006). http://www.soc.soton.ac.uk/rapid/rapid.php.

Read, J.F. and W.J. Gould (1992), Cooling and freshening of the Subpolar North Atlantic Ocean since the 1960's. *Nature 360,* 55-57.

Renfrew, I. A., P. S. Guest and K. Bumke (2002), A comparison of surface layer and surface turbulent flux observations over the Labrador Sea with ECMWF analyses and NCEP reanalyses. *Journal of Physical Oceanography 32*, 383-400.

Richardson, P.L., (1983), Gulf Stream Rings. Pp19-45 in Eddies in Marine Science, Ed. A.R. Robinson. Springer-Verlag, Berlin, 609 pp.

Rochford, P.A., B.A. Kara, A.J. Wallcraft and R.A. Arnone (2001), Importance of solar subsurface heating in ocean general circulation models, *Journal of Geophysical Research 106 (C11)*, 30,923-30,938.

Roemmich, D., J. Gilson and J. Willis (2005), Closing the time varying mass and heat budgets for large ocean areas: the Tasman box. *Journal of Climate 18*, 2330-2343.

Roemmich, D. and C.D. Wunsch (1985), Two transatlantic sections-meridional circulation and heat flux in the subtropical North Atlantic ocean. *Deep Sea Research A 32(6)*, 619-664.

Roemmich, D. and C.D. Wunsch (1984), Apparent changes in the climatic state of the deep North Atlantic Ocean. *Nature 307,* 447-450.

Rossby, T., S. C. Riser and A.J. Mariano (1983), The Western North Atlantic - A Lagrangian view point. Eddies in Marine Sciences. A. R. Robinson. New York, Springer-Verlag: 66-91.

Rossby, T. and D. Webb (1970), Observing abyssal motions by tracking Swallow floats in SOFAR channel. *Deep Sea Research 17(2)*, 359.

Sarmiento, J.L. (1986), On the North and tropical Atlantic heat balance. *Journal of Geophysical Research 91*, 11677-11689.

Sato, O.T. and P.S. Polito, (2005), Comparison of the global meridional Ekman heat flux estimated from four wind sources. *Journal of Physical Oceanography 35(1),* 94-108.

Sato, O.T and T. Rossby. (2000), Seasonal and low-frequency variability of the meridional heat flux at 36N in the North Atlantic. *Journal of Physical Oceanography 30(3),* 606-621.

Schäfer, H. and W. Kraus (1995), Eddy statistics in the South Atlantic as derived from drifters drogued at 100 m. *Journal of Marine Research 53*, 403-431.

Schiller, A., S.E. Wijffels and G.A. Meyers (2004), Design requirements for an Argo float array in the Indian Ocean inferred from observing system simulation experiments. *Journal of Atmospheric and Oceanic Technology 21,* 1598-1620.

Schmitz, W.J. and M.S. McCartney (1993), On the North Atlantic circulation. *Reviews in geophysics 31*, 29-49.

Semtner, A.J., (1976), A model for the thermodynamic growth of sea ice in numerical investigations of climate. *Journal of Physical Oceanography 6,* 379-389.

Smith, S.R., D.M Legler and K.V. Verzone (2001), Quantifying uncertainties in NCEP reanalyses using high quality research vessel observations. *Journal of Climate 14*, 4062-4072.

Stammer, D., C.D. Wunsch, R. Giering, C. Eckert, P. Jeimbach, J. Marotzke, A. Asdcroft, C.N. Hill and J. Marshall (2003), Volume, heat and freshwater transports of the global ocean circulation 1992-1997, estimated from a General Circulation Model constrained by WOCE data. *Journal of Geophysical Research 108(C1),* art. no.-3007 (DOI 10.1029/2001JC001115).

Stephens, C., J.I. Antonov, T.P. Boyer, M.E. Conkright, R.A. Locarnini, T.D. O'Brien, H.E. Garcia and S. Levitus (2001), World Ocean Atlas 2001, volume 1: temperature. NOAA atlas NESDIS 49, 176 pp.

Stern, N., (2006), The Stern review on the economics of climate change. Cambridge University Press.

Stevenson, J.W. and P.P. Niiler (1983), Upper ocean heat budget during the Hawaii-to-Tahiti Shuttle Experiment. *Journal of Physical Oceanography 13*, 1895-1907.

Straneo, F., (2006), Heat and freshwater transport through the central Labrador Sea. *Journal of Physical Oceanography 36 (4),* 606-628.

Swallow, J.C., (1955), A neutral-buoyant float for measuring deep currents. *Deep Sea Research 3,* 74-81.

Swallow, J.C., (1957), Some further deep current measurements using neutrally buoyant floats. *Deep Sea Research 4,* 93-104.

Swallow, J.C. (1971) The Aries current measurements in the western North Atlantic. *Philosophical Transactions of the Royal Society London A 270,* 451-460.

Taylor, P.K. and M.J Yelland (2001), The dependence of sea surface roughness on the height and steepness of waves. *Journal of Physical Oceanography 31*, 572-590.

Thiebaux, H. J. and M. A. Pedder (1987). Spatial Objective Analysis: with Applications in Atmospheric Science. London, Academic Press.

Tourre, Y.M., B. Rajagopalan and Y. Kushnir (1998), Dominant patterns of climate variability in the Atlantic Ocean region during the last 136 years. *Journal of Climate 12(8),* 2285-2299.

Trenberth, K.E. and J.M. Caron (2001), Estimates of meridional atmosphere and ocean heat transports. *Journal of Climate 14,* 3433-3443.

Trenberth, K.E. and A. Solomon (1994), The Global heat balance: Heat transports in the atmosphere and ocean. *Climate Dynamics 10,* 107-134.

UNESCO (1983), Algorithms for computation of fundamental properties of seawater. UNESCO technical paper in marine sciences 44, 53 pp.

Vargas-Yáñez, M., G. Parrilla, A. Lavin, P. Velez-Belchi and C. Gonzalez-Pola (2004), Temperature and salinity increase in the Eastern North Atlantic along the 24.5°N during the last 10 years. *Geophysical Research Letters 31(6).* L06210, DOI:10.1029/2003GL019308.

Verbrugge, N. and G. Reverdin (2003), Contribution of horizontal advection to the interannual variability of sea surface temperature in the North Atlantic. *Journal of Physical Oceanography 33(5),* 964-978.

Vonder Haar, T.H. and A.H. Oort (1973), New estimate of annual pole ward energy transport by northern hemisphere oceans. *Journal of Physical Oceanography 2,* 169-172.

Wang, J. and J.A. Carton (2002), Seasonal heat budgets of the North Pacific and North Atlantic Oceans. *Journal of Physical Oceanography 32,* 3474-3489.

Wang, W. and M.J. McPhaden (1999), The surface-layer heat balance in the equatorial Pacific Ocean. Part 1: Mean seasonal cycle. *Journal of Physical Oceanography 29*, 1812 – 1831.

Wang, W. and R.X. Huang (2004), Wind energy input to the Ekman layer. *Journal of Physical Oceanography 34 (5),* 1267 – 1275.

WGASF (2000), Final report of the joint WCRP/SCOR Working Group on Air-Sea Fluxes, Intercomparison and validation of ocean-atmosphere energy flux fields. November 2000, WCRP 112.

Webster, P. J. and R. Lukas (1992), TOGA COARE: The Coupled Ocean - Atmosphere Response Experiment. *Bulletin of American Meteorological Society 73(9),* 1377-1416.

White, W.B (1995), Design of a global observing system for gyre-scale upper ocean temperature variability. *Progress in Oceanography 36(3)*, 169-217.

White, W and C.K. Tai (1995), Inferring interannual changes in global upper ocean heat storage from TOPEX altimetry, *Journal of Geophysical Research 100(C12),* 24,943-24,954.

Willis, J.K., D. Roemmich and B. Cornuelle (2004), Interannual variability in upper ocean heat content, temperature and thermosteric expansion on global scales. *Journal of Geophysical Research 109*, doi:10.1029/2003JC002260.

Willis, J.K., D. Roemmich and B. Cornuelle (2003), Combining altimetric height with broadscale profile data to estimate steric height, heat storage, subsurface temperature and sea-surface temperature variability. *Journal of Geophysical Research 108 (C9)*, doi:10.1029/2002JC001755.

Wirts, A. and G.C. Johnson (2005), Recent interannual upper ocean variability in the deep southeastern Bering Sea. *Journal of Marine Research 63,* 381-405.

WMO (1993), International list of selected, supplementary and auxiliary ships. WMO Report, WMO Geneva.

Wong, A., R. Keeley, T. Carval and the Argo data management team (2002), Argo quality control manual.

Wong, A., G.C. Johnson and W.B. Owens (2003), Delayed-mode calibration of autonomous CTD profiling float salinity data by T-S climatology. *Journal of Atmosphere and Oceanic Technology 20(2),* 308-318.

Wood, R.A., A.B. Keen, J.F.B. Mitchell and J.M. Gregory (1999), Changing spatial structure in the thermohaline circulation in response to atmospheric $CO_2$ forcing in a climate model. *Nature 399,* 572-575.

Woodruff, S.D., S.J. Lubker, K. Wolter, S.J. Worley and J.D. Elms (1993), Comprehensive Ocean-Atmosphere Data Set (COADS) release 1a; 1980-92. *Earth System Monitoring 4,* 4-8.

Yan, X-H., P.P. Niiler, S.K. Nadiga, R.H. Stewart and D.R. Cayan (1995), Seasonal heat storage in the North Pacific: 1976-1989. *Journal of Geophysical Research 100(C4)*, 6899-6926.

Yashayaev, I. and A. Clarke (2005), Recent warming of the Labrador Sea. *ASOF Newsletter, issue 4*, 17-18, November 2005.

Yoshida, T. and N. Hoshimoto (2006), Heat content change in the surface isothermal layer of a warm core ring in the sea east of Japan. *Journal of Oceanography 62(3)*, 283-287.

Yu, L., R. A. Weller and B. Sun (2004), Improving latent and sensible heat flux estimates for the Atlantic Ocean (1988-99) by a synthesis approach. *Journal of Climate 17(2),* 373-393.

Zang, X. and C. Wunsch (2001), Spectral description of low-frequency oceanic variability. *Journal of Physical Oceanography 31,* 3073-3095.

**Personal Communication**

Kanzow, T. (2006), National Oceanography Centre, Southampton.

McDonagh, E. (2006), National Oceanography Centre, Southampton.

**Web site references**

Argo bibliography, http://www.argo.ucsd.edu/FrBibliography.html (April, 2006).

Coriolis, Argo European Global Data Assembly Centre, www.coriolis.eu.org (March, 2006).

Aviso website (2006), Live access server, http://www.aviso.oceanobs.com/html/donnees/ welcome_uk.html

NCEP/NCAR: http://ingrid.Ideo.columbia.edu/SOURCES/.NOAA/.NCEP-NCAR/. (Feb 2006)